

# UNIVERSITÀ DEGLI STUDI DI MILANO

**DEPARTMENT OF MEDICAL BIOTECHNOLOGY AND TRANSLATIONAL MEDICINE**

**PHD SCHOOL IN PHYSICS, ASTROPHYSICS AND APPLIED PHYSICS**

**CYCLE XXXII**


# THE MICROSCOPIC SIGNATURE OF THE RHEOLOGY OF AMORPHOUS SOFT MATERIALS: FROM LINEAR RESPONSE TO FAILURE

Disciplinary Scientific Sector FIS/03


**PhD Thesis of:**
Paolo Edera

**Director of the school:** Prof. Matteo Paris
**Supervisor of the Thesis:** Prof. Roberto Cerbino


**A.Y. 2019-2020**

# Contents

# Chapter 1

# Yielding in soft materials: state of the art

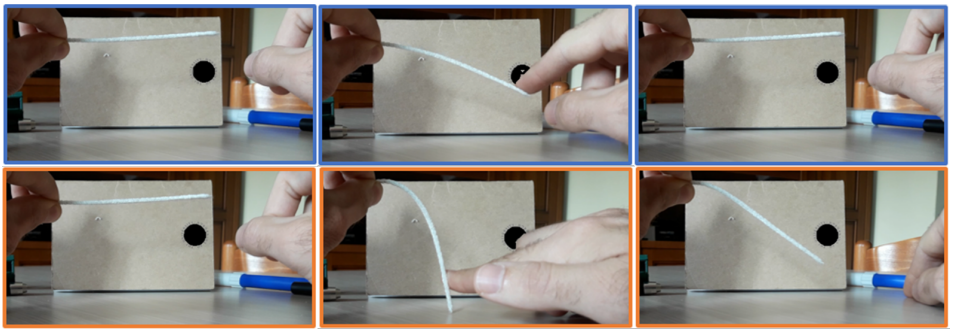

**Figure 1.1:** Metallic wire deformed below (top series) and above (bottom series) its yielding point.

## 1.1 Yielding: a solid to fluid transition

This thesis is devoted to the study of **yielding**, a mechanical phenomenon common to all solids and particularly relevant for *ductile* materials: those materials exhibiting a wide plastic regime. In solids' mechanics yielding can be defined as the onset of an *irreversible* deformation due to the application of a *load*. Differently from *fracture*, during yielding the material does not break in pieces but both its shape and its mechanical properties are irreversibly modified Fig.1.1.

In Fig.1.2 we sketch a simplified *load vs deformation* curve for a ductile and a fragile solid. We can divide the response curve in three parts. For small enough loads the deformation grows linearly: this corresponds to an elastic (spring-like) behavior. Increasing the load we observe a deviation from linear elasticity, not necessarily related to an *irreversible* process. In the

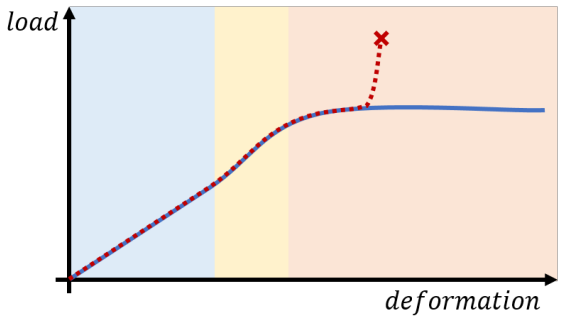


**Figure 1.2:** Load *vs* deformation response for a ductile (blue line) and brittle (red dotted line) material. Both of the curves exhibit an initial elastic region. From the yield point on, the deformation increases with no change in load. Fragile materials break at relatively small deformation after passing a narrow ductile region. The x in the fragile curve marks the *failure* point, when the material breaks in two, or more, pieces and opposes no more resistance.

third region, the deformation increases even if a constant load is maintained: this is what is called yielding. The extent of the yielding region depends on the material ductility: it is very narrow for fragile materials that break at relatively small deformation. Despite the fact that we are considering solid samples, the mechanical behavior in the yielding region closely resembles the behavior of a fluid. We can ask how deep is this analogy, in particular with reference to the microscopic structure and dynamics of the material in this peculiar state, will they resemble that of a solid or that of a liquid?
Moreover yielding occurs with common features across very different materials, this suggests that there is an underlying common mechanism and, to some extent, this *universality* allows us to arbitrarily choose our favorite model system, with a reasonable hope that what we will learn on that system will teach us something that will be applicable to a wider class of materials. The focus of this work is on the **mechanical yielding** of **soft materials** and more specifically of **yield stress fluids**. This category includes different systems with very diverse applications and compositions: foodstuff [63], cosmetics [20], paints [68], drilling fluids [75], fresh concrete [113] etc.

The advantages coming from studying the yielding transition in soft materials are numerous. One of them is reproducibility: in yield stress fluids, after yielding occurred and the load is removed, the initial condition, in terms of mechanical properties, is quite easily resetted. Another relevant consideration is that soft materials are usually composed of elementary "building blocks" that have dimensions comprised between tens of nanometers and few microns. This makes their structures and microscopic dynamics accessible by means of optical techniques, such as microscopy or light scattering. This is particularly important for the sake of this work, since we are interested in investigating the connection between macroscopic and microscopic behaviors.

To give a more precise definition of yielding we need to go through the definition of the specific mechanical tests. Since yielding is a non-linear property of the material its occurrence depends on the way in which the material is tested, and there is no straightforward way to connect the result of an experimental protocol to a different one. We will go through three different mechanical tests commenting on how yielding occurs in the different conditions, with a particular attention to the definition of the *yield stress* and the *yield strain*: the values that marks the onset of the yielding transition.

Afterwards, we will review some recent experimental studies that probe the microscopic structure and dynamics during the mechanical tests.

**Boxes**

The main test is accompanied by **boxes** where some basic concepts of **rheology**, **microscopy** and **scattering**, are introduced. These concepts are necessary for the understanding of the discussion, but the reader that is already familiar with the topics can safely skip them.

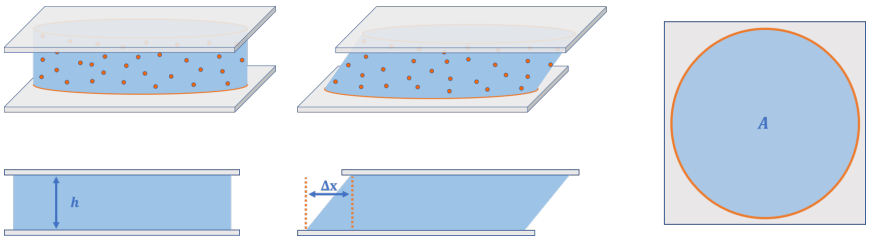


**Figure 1.3:** Parallel sliding plates shear experiments. Views in prospective (top left and center), from the side (bottom left and center) and from the top (right). The **shear deformation** $\gamma$ is defined as the displacement $\Delta x$ divided by the sample thickness $h$. $F$ is a **shear force** (parallel to the plates) applied to induce the shear deformation $\gamma$. **Shear stress** is defined as $\sigma = \frac{F}{A}$, where $A$ is the area of of the sample.

## Rheology

A mechanical test is the combination of a force application and a deformation measurement (or *vice versa*). Shear rheology experiments are those mechanical experiments where **shear forces** (or **shear deformations**) are applied. Referring to Fig.1.3, which represents a shear experiment in **parallel sliding plates** conditions 1.4.1, we define the **relative deformation** $\gamma = \frac{\Delta x}{h}$, the **deformation rate** as the time derivative of the relative deformation $\dot{\gamma}$ and the **shear stress** $\sigma = \frac{F}{A}$ *i.e.* the applied shear force divided by the area $A$ of the sample surface portion to which the force $F$ is applied.
The two simplest examples of materials that one can consider are **ideal elastic solids** and **Newtonian liquids**.
For the former the mechanical response is

$$\sigma = G_E \gamma \tag{1.1}$$

where $G_E$ is, by definition, the **linear elastic modulus**. In this case the stress is linear with the *instantaneous* deformation $\gamma$.
In the case of Newtonian fluids

$$\sigma = \eta \dot{\gamma} \tag{1.2}$$

where $\eta$ is fluid's **viscosity**. In this case the stress only depends on the shear rate $\dot{\gamma}$. Equations 1.1 and 1.2 introduce useful concepts to describe the response of a wide class of materials to small perturbations.

**Rheology: Linear visco-elastic moduli**

In the linear regime, the mechanical response of a general visco-elastic material in the temporal domain is described by the equation

$$\sigma(t) = \int dt' G^*(t-t')\gamma(t').$$

In the Fourier domain $\tilde{\sigma}(\omega) = \tilde{G}^*(\omega)\tilde{\gamma}(\omega)$. The symbol $\tilde{.}$ represents the *Fourier transform*.
In the case of a harmonic perturbation $\gamma = \gamma_0 \cos(\omega_0 t)$ transforming back in the temporal domain the equation 1.1 we obtain

$$\sigma(t) = G'\gamma_0 \cos(\omega_0 t) - G''\gamma_0 \sin(\omega_0 t) \tag{1.3}$$

where $G'$ is the real part of $\tilde{G}(\omega_0)$ and $G''$ is the imaginary one. The physical interpretation of these quantities is straightforward:

- $G'$ is the *elastic* (or *storage*) *modulus*. It is the generalization of the elastic modulus introduced in 1.1: it's the part of the stress proportional to the shear deformation.
- $G''$ is the *viscous* (or *loss*) *modulus*, it is related to the viscosity by the relation $G'' = \omega\eta$: it's the part of the stress proportional to the shear rate.

## 1.2 Creep experiments

A very natural way to define the yield stress is to measure the response to the sudden application of a homogeneous constant stress. This kind of test is called *creep test* and in this approach the yield stress is defined as the critical value $\sigma_y$ such that:

- for $\sigma < \sigma_y$ the system displays a solid like behavior,
- for $\sigma > \sigma_y$ the system behaves like a fluid.

In Fig.1.4 is reported, in a *log-log* scale, the expected behavior of a creep experiment. Initially, the deformation grows quadratically because of inertial effects [5], at longer times we observe two possible responses: if the applied stress is smaller than $\sigma_y$ the deformation $\gamma$ reaches a plateau, the deformation velocity goes to zero and the apparent viscosity diverges, indicating that such a system can't be described as a liquid; if $\sigma > \sigma_y$ the deformation grows linearly with time, the deformation velocity and the viscosity reach a finite value.
In 2002 Coussot and colleagues proposed a model to rationalize the yielding

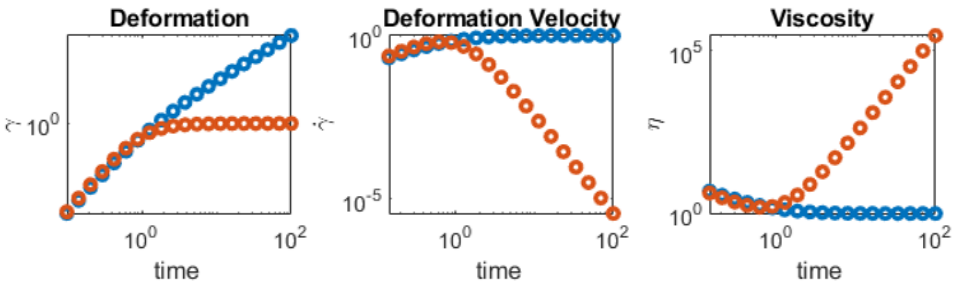


**Figure 1.4:** Response to a creep test for a yield stress fluid in the solid (red symbols) and in the liquid (blue symbols) region in a log-log scale. The initial regime is dominated by inertial effects and $\gamma \propto t^2$, then the material reaches a state of constant deformation if the stress is smaller than the yield stress, while if the stress exceeds the yield stress the shear rate reaches a constant value. The initial decrease of the viscosity is not a genuine effect and it is just the effect of the inertia of the measurement system, while the divergence for long times for the solid regime simply indicates the fact that the mechanical state can't be described in terms of the viscosity.

transition in terms of *viscosity bifurcation* (infinite viscosity in the solid state versus finite viscosity in the fluidized state) [31]. In this work the authors show viscosity data, obtained by creep experiments, for three yield stress fluids with quite diverse microscopic structures: a bentonite clay suspension, a hair gel (polymer gel) and a colloidal glass (Laponite RD).

The three systems are yield stress fluids and indeed they exhibit a yielding

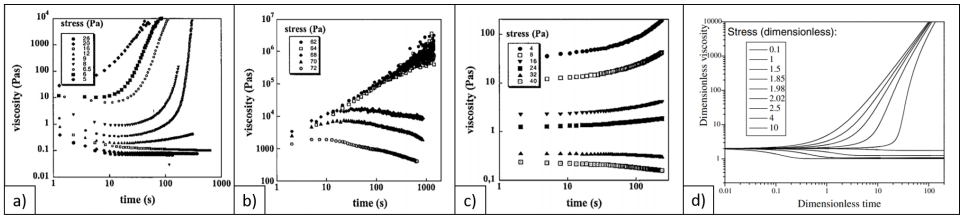


**Figure 1.5:** Panel a)-c) Viscosity bifurcation observed by *creep experiments* for (from left to right) bentonite in water, polymer gel, colloidal glass. Panel d) Viscosity as a function of time for different stress values as predicted by the model presented in the main text (all the quantities are made dimensionless). Adapted from [31].

transition depending on the applied stress Fig.1.5. The authors propose a very simple physical model to describe, with a unique mechanism, the **viscosity bifurcation**. In the model, the viscosity is attributed to the presence of a structure parametrized by a "structure parameter" $\lambda$ that indicates, for example, the degree of flocculation, or the fraction of bonded particles; the relation between the viscosity and $\lambda$ is phenomenologically assumed to be a

non-homogeneous power law

$$\eta = \eta_0(1 + \lambda^n) \tag{1.4}$$

In the model, the structure may change because of the shearing condition: it is partially destroyed by the flow but it is also able to heal because of the reversibility of its bonds. A straightforward implementation of these mechanisms is provided by the following equation:

$$\frac{d\lambda}{dt} = \frac{1}{\tau} - \alpha\lambda\dot{\gamma} \tag{1.5}$$

where $\tau$ is the structure recovery time, and $\alpha$ describes the *destructuration* effect of the shear. The shear rate, of course, depends both on the viscosity and on the applied stress:

$$\sigma = \eta(\lambda)\dot{\gamma}. \tag{1.6}$$

We end up with a closed system of equations that can be solved to obtain the evolution of the viscosity for different applied stresses. In particular a critical value of the stress $\sigma_c$, that marks the transition, emerges from the model. The results reported in Fig.1.5 (d) well capture the qualitative behavior of the viscosity that diverges for $\sigma < \sigma_c$ and reaches a finite plateaus for $\sigma > \sigma_c$.
In this example we can see how a microscopic description based on few parameters, with a clear physical meaning, gives a great insight on the mechanism that rules such a complex non-linear mechanical behavior.

If we could access experimentally these, or equivalent, microscopic features, we would have a deeper understanding of the yielding transition and a better control of the mechanical behavior of yield stress fluids.

**Beyond viscosity bifurcation:** Before moving to the discussion of the microscopic side of yielding, let us mention some very interesting and important phenomena that are not captured by the viscosity bifurcation picture. Even though we will not discuss these phenomena in detail, it is worth to go through them because they are good examples of interesting mechanical phenomena that would benefit from a deeper microscopic understanding.
First of all, yielding is not a sharp transition: in Fig.1.6 adapted from another work of Coussot and colleagues [30], we can see some intermediate behaviors incompatible either with a solid or with a fluid. An important intermediate behavior is found when the deformation increases sub-linearly, implying no plateau in the deformation $\gamma \to \infty$ and, at the same time, a vanishing velocity $\dot{\gamma} \to 0$: this is called **creep** regime. The creep regime can, or can not, be followed by a **delayed yielding**: an abrupt speed up of the deformation taking to a flow with a finite deformation rate. Both creep and

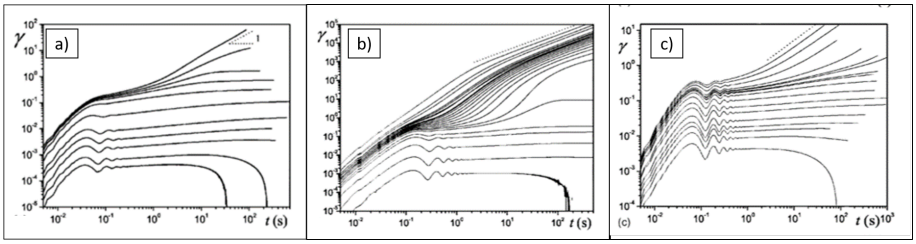


**Figure 1.6:** Creep test for a) Mustard, b) Bentonite suspension, c) Hair gel. From the bottom to the top the applied stress increases. The three different samples show an elastic plateau for small stress, a fluid region for the highest stresses and a transition region showing *delayed yielding* and non stationary flow (*creep*) at intermediate stress. Adapted from [30].

delayed yielding observed here for soft materials have their analog in hard materials, from metals to the Earth crust. When subjected to a continuous stress, after a period of latency, they abruptly start deforming and eventually break. Since from a macroscopic point of view there are no clear signs of the imminent yielding, precursors are sought in the microscopic structure and dynamics [4], [62], [81].

After briefly covering the macroscopic signatures of yielding in creep experiments, we can move to a microscopic inspection and we will do it by reviewing a series of works that combine mechanical tests and microscopical observations.
The latter were carried out using different techniques, *e.g.* **ultrasound speckle velocimetry**, **light scattering** and **confocal microscopy**. For the reader that is not familiar with these techniques, their brief sketch can be found in boxes accompanying the main text.

Scattering: General features

In scattering experiments, a coherent field is sent onto a sample and interacts with it to then be scattered in directions different from the incoming one. From the analysis of the scattered signal one can learn about the microscopic configuration and dynamics of the scatterers. The more widespread probe field that are used in the investigation of soft materials are: electromagnetic fields at different frequencies (visible light and x-rays), particles (such as neutrons), acoustic fields. Despite some peculiarities of the different scattering techniques, we can list some of their common features:

- the signal is an average over the *scattering volume*, determined by the beam size, and the inspected length scale is roughly fixed by the scattering vector $q$.

- quantities such as *structure function*, *mean square displacement* (MSD[a]) and higher order moments of the displacement probability distribution are accessible using different correlation functions.

[a]Defined by equation 1.12, and discussed in Chapt. 3.

### 1.2.1 Creep and flow inhomogeneities

Rheological experiments probe macroscopic samples and make assumptions on the shape of the deformation field[1]. This assumption relies on the homogeneity of the material. We will see that close to the yielding point even small inhomogeneities have a dramatic effect and lead to big inhomogeneities in the deformation field: different part of the sample are subjected to different local deformations $\gamma(x)$. Addressing this point is very important: first of all we need to know the *local* value of the **macroscopic quantities** if we want to relate them to some **microscopic** behaviors.

**Rheology: Deformation field**

The application of a macroscopic deformation $\Delta x$ does not produce, in general, a uniform deformation field. We can describe the process triggered by the application of a deformation and leading to the stress response as follows: one imposes a macroscopic deformation, that produces a heterogeneous deformation field $\gamma(\mathbf{x})$. Each part of the deformed material reacts with a certain stress $\sigma(\mathbf{x})$, whose *sum* over the sample volume gives the macroscopic stress

$$\Delta x \rightarrow \gamma(\mathbf{x}) \rightarrow \sigma(\mathbf{x}) \rightarrow \sigma_T.$$

One controls the *macroscopic* quantities: $\Delta x$ and $\sigma_T$ and wants to infer the relation between *local* quantities: $\gamma(\mathbf{x})$ and $\sigma(\mathbf{x})$.
Clearly, if the deformation field is homogeneous, the *local* and the *macroscopic* quantities coincides.

A series of works from Manneville and coworkers systematically addresses the assumption of *flow homogeneity* and shows how this is often violated in correspondence with the yielding transition.
In Ref. [39] the authors combine creep experiments, carried out in a "small-gap" Couette geometry [1.7], with ultrasonic speckle velocimetry (USV) observing at the same time the evolution of the rheological response and the evolution of the velocity profile within the rheometer gap.

[1]See also **deformation field** box1.2.1.

**Scattering: Ultrasonic Speckle Velocimetry**

**USV** is a space-resolved ultrasound scattering technique. An ultrasound coherent pulse is sent into a sample that was previously seeded with glass beads. The beads scatter the sound wave, producing a speckle field reflecting the scatterers distribution along the beam. Cross-correlation over various pulses allows the reconstruction of a 2D velocity profile. This technique has been adapted to rheological experiments performed in Couette geometry [77].

**Rheology: Couette**

In this geometry, the material is confined between two coaxial cylinders of radii $R_i$ and $R_o$. Usually the inner cylinder is the rotating one Fig.1.7. The shear stress field is:

$$\sigma(r) = \frac{T}{2\pi H r^2}, \tag{1.7}$$

where $T$ is the total torque, $H$ is the height of the cylinder and $r$ the distance from the center. In the simple case of an oscillatory experiment in the linear regime (if $max(\sigma) << \sigma_y$) deformation amplitude will be linearly proportional to the stress

$$\gamma_0(r) \propto \sigma(r)$$

Things become much more complicated in the non-linear regime.
In the limit of *small-gap Couette*, usually defined as $\frac{R_o - R_i}{R_i} < 5\%$, both the stress and the shear rate are considered homogeneous.

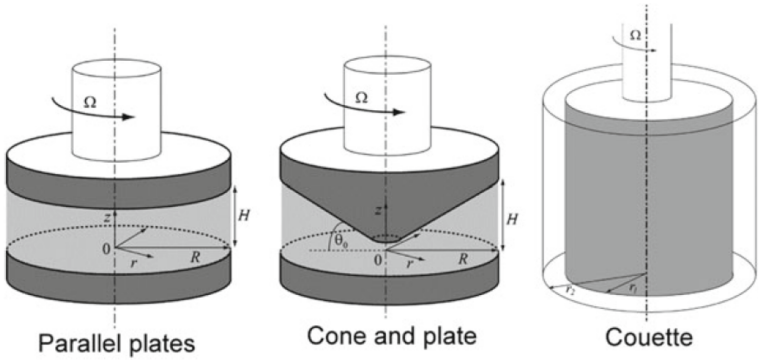


**Figure 1.7:** Typical geometries for shear rheology experiments. The sample is confined between a fixed surface and a moving one. Adapted from [87], [29].

The studied sample is a soft glass: Carbopol ETD 2050, a model system for yield stress fluids. Panel one of Fig.1.8 shows the temporal evolution of the *mean* shear rate, measured by assuming an affine deformation field. From the study of this macroscopic observable we can highlight three different

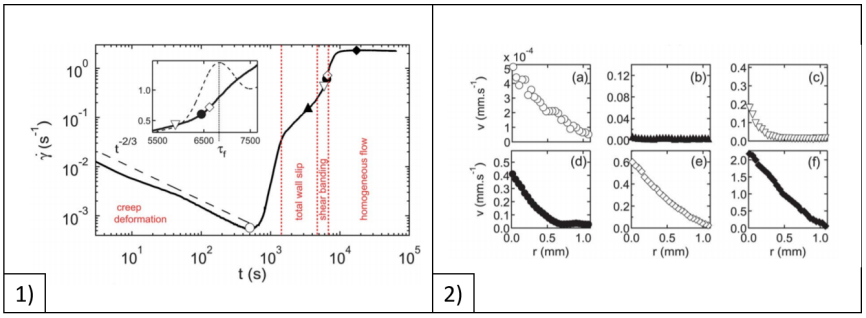


**Figure 1.8:** Creep experiment on Carbopol ETD 2050. Panel 1. Temporal evolution of the *macroscopic* shear rate $\dot{\gamma}(t)$ after the application of a constant stress $\sigma$ at time $t = 0$. Panel 2): velocity profiles $v(r)$, where $r$ is the distance from the rotor, at different times, symbol corresponds to Panel 1). On each profile, the upper value of the velocity scale is set to the current rotor velocity $v_0$ so that the slip velocity $v_s$ at the rotor can be read directly as $v_s = v_0 - v(r = 0)$. Adapted from [39].

regimes: an initial creep regime, where $\gamma \propto t^{1/3}$ and $\dot{\gamma} \propto t^{-2/3}$; followed by a "multi-step" yielding regime; eventually a stationary flow condition is reached. Panel two of Fig.1.8 shows the velocity profiles obtained with USV. Interestingly, while at the beginning and at the end of the experiment the velocity profile $v(r)$ is linear in $r$ (affine deformation field), during the yielding process the deformation field is markedly non-affine, implying a non-homogeneous shear deformation $\gamma(r)$ and shear rate $\dot{\gamma}(r)$ that do not correspond to the values measured with the rheometer. Thanks to USV it is possible to observe that only part of the sample is fluidized and that the fluidization process starts from the inner cylinder (rotor) and progressively invades all the gap.
It is very well known that Couette geometry produces an inhomogeneous stress field, with a stress concentration at the inner surface [87]:

$$\sigma \propto \frac{1}{r^2} \tag{1.8}$$

and so one can expect yielding to occur at the inner surface at first. The geometry used in ref. [39] had a gap of 1.1 $mm$, an inner radius $R_i \simeq 24\ mm$, a percentage difference of $\frac{\Delta r}{r} \simeq 4\%$ taking to a stress percentage difference of $\frac{\Delta \sigma}{\sigma} \simeq 8\%$. Surprisingly enough, such a small difference in the stress leads to very different local deformations. During this transition process the percentage of fluidized sample increases and a progressive speed up of the deformation is observed. We also point out that the stress inhomogeneity does not produce such dramatic effects at the beginning and at the end of the experiment: *i.e.* when the whole sample is either *unyielded* or *yielded*. Qualitatively similar behavior is observed for a Couette geometry with smooth boundaries.

These experiments show that in the proximity of yielding the assumption of homogeneous stress field is very delicate and even small deviations can have a dramatic impact on how the solid to fluid transition occurs. Every time we want to build a connection between the macroscopic and the microscopic sides of yielding we have to be sure that, at list macroscopically, the system can be treated as homogeneous. If this is not the case the microscopic observation won't be representative of the whole system.

For a microscopic description of yielding we now want to study the system's dynamics at the length-scales of its elementary components.

### 1.2.2 Creep and microscopy

An increasingly popular technique that can be combined with mechanical tests is **confocal microscopy**: with this technique it is possible to identify in three dimensions the positions of single micrometric particles and reconstruct their motion with high spatial and relatively high temporal resolutions. In this way, not only information on the mesoscopic flow, but also on the microscopic rearrangements becomes accessible. The main drawback of this approach is that the high spatial resolution is obtained at the expense of the probed volume extension: only a *small* part of the sample is inspected and so one has to necessarily assume that both the macroscopic and the microscopic behaviour are homogeneous in the different parts of the sample, but, as we have just seen in the previous section, this is not always the case.

**Confocal Microscopy**

*Confocal microscopy* is a fluorescent microscopy technique that, thanks to its extraordinary resolution in the direction of the optical axis ($\sim 1\mu m$), can be used to scan the sample in 3D and to build a 3D image of the sample. A classical technique to achieve this resolution is the so called **laser scanning microscopy**, in which the main idea is to illuminate the sample "point-by-point", the main drawback of this strategy is the relatively long time required to scan a certain volume, which makes confocal microscopy suitable for slowly-evolving samples. An important advantage of fluorescent microscopy is that, working in reflection, requires only one optical entrance. This allows to couple it with a rheometer mounting a cone plate geometry Fig.1.7, that produces a homogeneous deformation field.

In a recent work, Sentjabraskaja and coworkers [107] use confocal microscopy to study the microscopic shear-induced dynamics in a *colloidal glass* at various stages of a creep test.

**PMMA Colloidal Glasses**

Colloidal glasses are model systems of amorphous soft materials. A widely used system is a dispersion of PMMA (PolyMethyl Methacrylate) colloidal particles in organic solvent (typically Decalin). The interest in this system is motivated by a number of factors: from an experimental point of view PMMA particles are quite easily synthesized, their interaction can be easily tuned (making them attractive or repulsive) and, varying the particles' concentration and interaction, a very rich phase diagram can be explored. PMMA can be fluorescently labeled in such a way to be individually imaged even at high concentrations using confocal microscopy [38].
The possibility of experimentally tune these microscopic parameters motivated a number of theoretical works and simulations, making PMMA colloids the ideal benchmark for the study of many phenomena in the soft matter field [99], [94], [73], [8], [66], [53].

The rheological measurements are performed in a cone-plate geometry that ideally produces a perfectly homogeneous stress and deformation field.

**Rheology: parallel rotating plates & cone-plate**

- The sample is confined between two **parallel plates**, at a distance $H$, one of them is fixed and the other rotates Fig.1.7. In this geometry the local deformation depends on the distance from the center of the disks. If the moving plate rotates of an angle $\Omega$ the resulting inhomogeneous deformation field is:
$$\gamma(r) = \Omega \frac{r}{H}. \tag{1.9}$$
- In a **cone and plate** geometry the top plate is substituted with a truncated cone, whose virtual vertex exactly falls on the bottom plate. This way the gap depth $H(r)$ depends on the distance form the center. As a consequence, a homogeneous deformation field is produced:
$$\gamma(r) = \Omega \frac{r}{H(r)} = \Omega \frac{r}{r \sin(\theta_0)} = \frac{\Omega}{\sin(\theta_0)} \tag{1.10}$$
where $\theta_0$ is the angle of the cone.

The authors explore **flow** ($\gamma \propto t$) and **creep** conditions ($\gamma \propto t^{1/2}$) Fig.1.9] comparing the macroscopic shear deformation and the **non-affine mean square displacement** $\Delta r^2_{\mathrm{NA}}$ measured with particle tracking.

Particle Tracking (PT)

The principle of PT is to *track* the position of a particle at different times to reconstruct its trajectory and compute, for example, the particle's mean square displacement. This is done in a almost completely automated by way acquiring a microscopy movie with a digital camera, and analysing it with specific algorithms. Once $\vec{x}_j(t)$ the series of positions assumed in time from a certain particle, is available, one can compute quantities such as the mean displacement in a time lag $\Delta t$:

$$\Delta\vec{x}(\Delta t) = \langle \vec{x}(t) - \vec{x}(t+\Delta t)\rangle_{t,j}, \tag{1.11}$$

or the **mean squared displacement**

$$\Delta\vec{x}(\Delta t) = \langle |\vec{x}(t) - \vec{x}(t+\Delta t)|^2\rangle_{t,j}, \tag{1.12}$$

or the complete **displacement probability distribution** $P(\Delta\vec{x}(\Delta t))$, also known as the **van Hove distribution function**.
Also static quantities, such as the **pair correlation function** $g(r)$, can be measured

$$g(r) = \frac{1}{N^2}\int dr'\ c(r')\cdot c(r'+r) \tag{1.13}$$

where $c(r)$ is the probability to find a particle in position $r$.
The particles need to be individually resolved to apply this technique. This limits the size and the concentration of the traced particles.

The displacement of each particle $\Delta\vec{x}_i$ can be decomposed in two parts: the **affine** and the **non-affine**. The affine displacement, in a parallel-sliding-plates geometry or in a cone-plate geometry, is linear with $z$ the distance from the fixed plane and is parallel to the shearing direction ($\hat{u}_S = \hat{x}$ in parallel sliding plates, $\hat{u}_S = \hat{\theta}$ in cone-plate ): $\Delta\vec{x}_A = z\cdot\gamma\cdot\hat{u}_S$. Microscopic deviations from the affine displacement are due to the fact that the material is not homogeneous on the length-scale of its own structure. The affine part is measured by averaging the displacements over all the particles: $\Delta\vec{x}_A = \langle\Delta\vec{x}_i\rangle_i$. The non-affine displacement is : $\Delta\vec{x}_{i,\mathrm{NA}} = \Delta\vec{x}_i - \Delta\vec{x}_A$. In their work Sentjabrskaja and colleagues consider non-affine displacements only in the vorticity direction $\hat{y}$, since there is no affine displacement along $\hat{y}$: $\Delta y = \Delta y_{\mathrm{NA}}$.
The deformation $\gamma$ follows the expected behavior: an initial quadratic inertia-dominated response and then $\gamma$ follows either a linear or a sub-linear increase with time, depending on the value of the applied shear stress $\sigma$ as compared to the yield stress $\sigma_y$. Remarkably, also the $\Delta x^2_{\mathrm{NA}}$, for large enough time, follows a power law dependence on time, with the same exponent as the shear deformation $\gamma$. The link between the microscopic dynamics and the

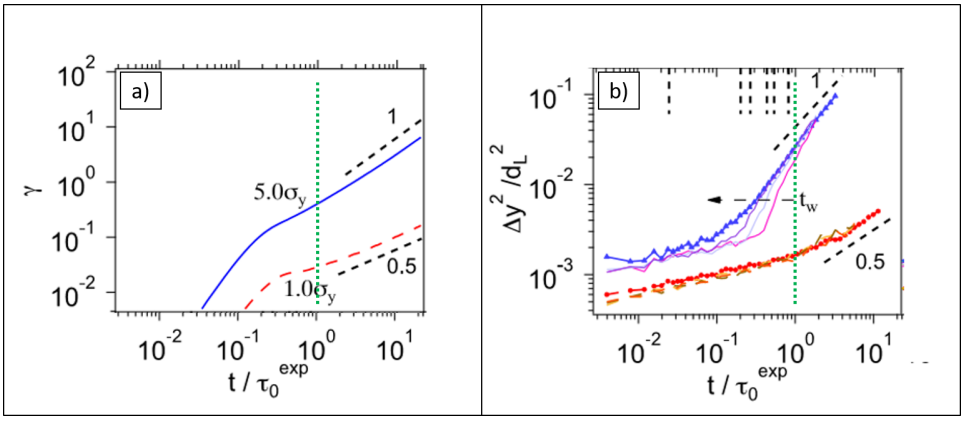


**Figure 1.9:** Creep test for colloidal glass. a) Deformation $\gamma$ as a function of time, in the flow regime (blue) and in the creep regime (red) b) Correspondent non-affine mean square displacement. The green vertical line marks $t = \tau_0$, approximately where the linear behavior sets in. Adapted from [107].

deformation remains elusive during the initial part of the experiment and the transition times are different for the macroscopic and the microscopic responses (the vertical green line in Fig.1.9 marks the macroscopic transition time $\tau_0$ ). The experimental observation is striking but the understanding of this correspondence remains unclear.
The authors define a space-resolved activity $\Phi(R)$ as the integral

$$\Phi(R) = \int_{V(R)} \Delta x^2_{\mathrm{NA}}(t_0) \tag{1.14}$$

where $\Delta x^2_{\mathrm{NA}}(t_0)$ is the non-affine MSD at the shortest time delay and $V(R)$ is a volume centered in $R$ Fig.1.10. From the temporal evolution of these maps in the initial regime (before $\tau_0$) an interesting distinction between the creep and the flow conditions emerges: in the first case the extent of the regions involved in the non-affine rearrangements $\xi$ is constant, while in the second case ($\sigma = 5\sigma_y$) it grows sub-linearly $\xi \propto t^{2/3}$ Fig.1.10 (g).

This difference is intriguing and intuitively could be related to the system flow (or deformation) properties, but at this stage the interpretation of the connection between the microscopic and macroscopic properties is not straightforward.

A better understanding of the early stages of the process would be particularly interesting in the spirit of predicting the solid to liquid transition, but the data obtained in that region are very noisy and this is likely due to the fact that the initial behavior is non-stationary, which precludes the possibility (or questions the opportunity) of performing temporal averages. The poor statistics in the transient region is an important limitation that is

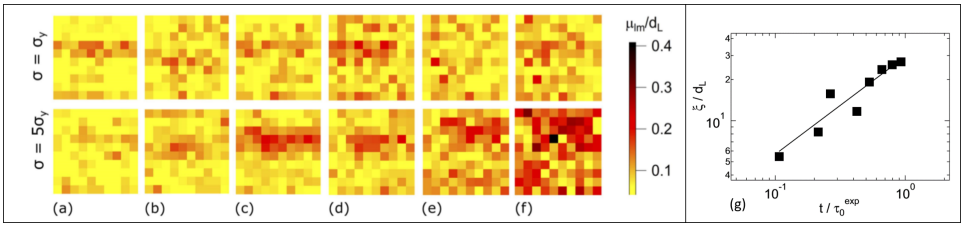


**Figure 1.10:** Panels (a) to (f): activity maps before reaching the steady state condition: for $t/\tau_0 = 0.025; 0.20; 0.27; 0.43; 0.53; 0.8$. The size of the active zones does not increase for $\sigma = \sigma_y$ (*yield stress*) while it does for $\sigma = 5\sigma_y$. (g) Width of the activity correlation function for $\sigma = 5\sigma_y$. Adapted from [107]

intrinsic of *creep tests*. It would be interesting to check whether other mechanical protocols provide better conditions for a microscopic investigation.

## 1.3 Stress growth experiments

Creep is not the only method to study yielding[2]: an alternative approach is provided by **stress growth experiments**. In this case, instead of applying a constant stress, one applies a deformation at constant strain rate. These experiments are usually done at relatively low shear rates in order to minimize the shear rate-dependent effects. These tests are usually faster than creep tests. The typical response is sketched in Fig.1.11 a). Initially, we

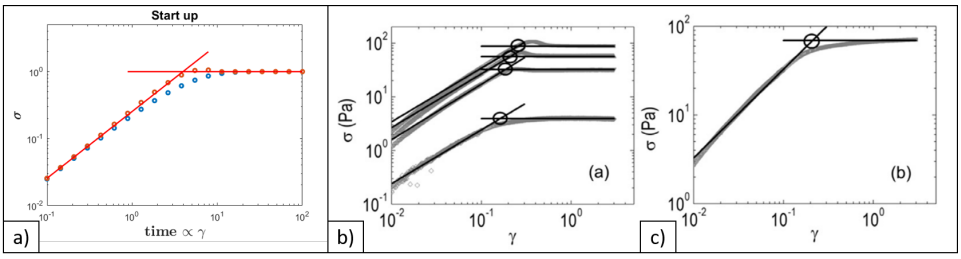


**Figure 1.11:** Panel a) Schematics of stress vs strain in a Stress Growth shear experiment. In these experiments the strain rate is imposed, so that strain grows linearly with time, and the stress evolution is followed in time. Depending on the sample and on the strain rate the stress may, or may not, exhibit an overshoot. Panel b) Data for Carbopol Ultrez U10 at different weight fractions ([1.5, 0.75, 0.5, 0.1] %) c) Data for a commercial hair gel (*Albert Heijn*) based on Carbopol. b) and c) adapted from [36]

observe a linear increase of the stress: this is the linear elastic contribution $\sigma = G\gamma$. At a certain point the stress deviates from linearity, in this phase a stress overshoot may or may not be observed (the origin of this overshoot is

[2] A short review of the more commonly used methods can be found in ref. [36]

still matter of debate). At longer times the stress $\sigma$ reaches a plateau: this is the stationary flow condition. As reported by Bonn and coworkers [36], it is difficult to locate the point where deviation from elastic behavior starts, the main reason being the difficulty in discriminating between *non-linear elasticity* and *plasticity*. Both produces deviations from the linear behaviour but, while the former is a reversible process, the latter is not and its occurrence deteriorates the material's mechanical properties. A pragmatic way to estimate the yield stress $\sigma_y$ and the yield strain $\gamma_y$ is from the intersection of the linear elastic behavior with the asymptotic value of $\sigma$. The physical interpretation of the so defined quantities is not straightforward as compared to the yield stress and strains defined in *creep* tests and the discussion on how the results obtained for different yielding test can be matched is a matter of debate[3] [36], [39].

### 1.3.1 Stress growth and flow inhomogeneities

Manneville and coworkers combine the same USV approach used in ref. [39] with stress growth experiments [40]. The geometry is again a Couette, the velocity map spans the whole gap with a resolution of $R \sim 100\ \mu m$ (pixel size) and a sensitivity to displacements up to $\delta x \sim 1\ m$.

Similarly to what previously seen in creep experiments, the velocity field is far from being affine and the change of slope in the velocity profile indicates the presence of **shear bands**: different parts of the sample are characterized by different velocity gradients (local $\gamma$ and $\dot{\gamma}$). Shear banding is known to occur for thixotropic samples[4] even at steady state. What is somehow surprising in these experiments is that the authors observe transient shear bands for **simple yield stress fluids** (*i.e.* non-thixotropic). In Fig.1.12, panel 1. the evolution of stress versus time is reported for $\dot{\gamma} = 0.7\ s^{-1}$. The measured stress shows a long time transient before stabilizing, analogously to what observed for the strain rate in Ref. [39]. In the insets the velocity profiles are reported for different phases of the transient of Fig.1.12 1. Similarly to what happens for thixotropic samples, the gap is roughly divided in two zones with two different velocity gradients. The portion of fluidized sample gets larger with time Fig.1.12 2. and the total stress decreases proportionally. We notice that a relatively weak stress evolution corresponds to a quite dramatic change in the local velocity gradient and also in this case the assumption of homogeneous flow is found to be inappropriate. The authors exclude stress inhomogeneities as a possible cause of the transient

[3] This debate is not the main focus of our attention: we are looking for the best experimental condition that allows us to learn something on the microscopic mechanism ruling yielding and a faster and more reproducible test may help to this end.

[4] Thixotropic yield stress fluids are characterized by a critical shear rate $\dot{\gamma}_c$ below which they can not flow. If one tries two impose a strain rate $\dot{\gamma} < \dot{\gamma}_c$ the sample naturally separates in two bands: a solid one with a zero *local* shear rate: $\dot{\gamma}_L = 0$ and a fluidized one with a *local* shear rate larger that the critical one: $\dot{\gamma}_L > \dot{\gamma}_c$ [88],[31]

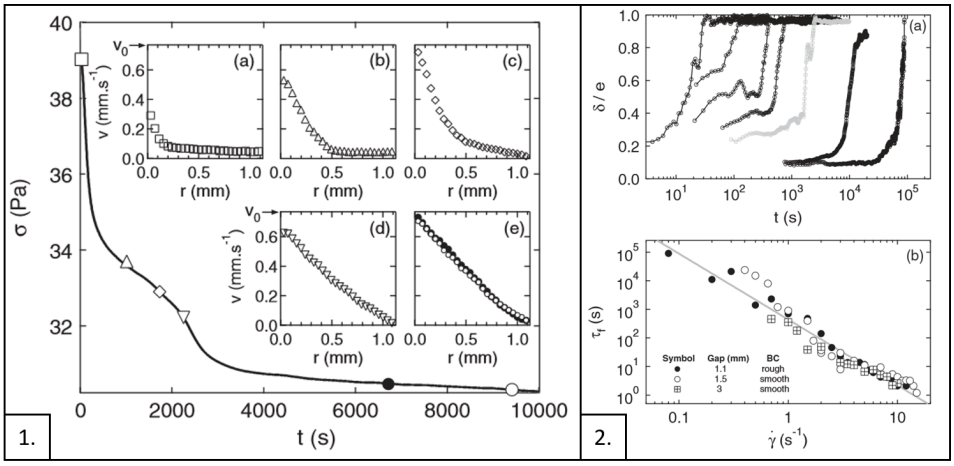


**Figure 1.12:** 1. Stress growth experiments in Carbopol $ETD2050$, strained at $\dot{\gamma} = 0.7s^{-1}$. In the main plot stress vs time. Notice that the focus here is on the long time behavior (the stress growth Fig.1.11 happens in the initial part of the experiment that is not reported in this graph). In the insets of panel 1 the velocity profiles $v(r)$ at different temporal stages of the experiment, inset's symbols corresponds to symbols in the main plot. 2. a) Temporal evolution of the width of the fluidized band $\delta$ normalized by the gap width $e$, $\delta/e = 1$ defines the fluidization time $\tau_f$. b) Fluidization time $\tau_f$ as a function of the imposed shear rate, for different gap width and boundary conditions. Adapted from [40].

shear band, stating that the same scenario is observed with a cone-plate geometry, but they don't show data to support this statement. On the other hand, they show that the fluidization time does not change for different gap widths and so for different stress inhomogeneities since $\frac{\Delta\sigma}{\sigma} \simeq 2\frac{w_{gap}}{R_{in}}$ Fig.1.12, panel 2. (b).

### 1.3.2 Stress growth and microscopy

In a recent work, Laurati and colleagues use a phenomenological model to connect microscopic behaviour and mechanical response of a colloidal glass in a stress growth experiment [70]. The model, originally developed to describe linear elasticity in amorphous materials [117], predicts the elastic modulus $G$ from the number of long-lived neighbours. Two particles are defined to be long lived neighbours if their distance remains below a certain threshold $\Delta r_0$ while they are strained for a certain deformation interval from $(\gamma - \gamma_w/2)$ to $(\gamma + \gamma_w/2)$, where $\gamma_w$ is simply the width of the deformation interval. A confocal microscope is coupled with the rheometer. Particles are imaged and individually tracked in order to extract the number of long-lived neighbours $n(\gamma)$ at different stages of the deformation Fig.1.13 and the instantaneous pair correlation function $g(r)$[5]. Differently from $USV$, confocal microscopy

[5]Reference to **Particle Tracking** box 1.13.

can be combined with a cone-plate geometry, that ideally produces a perfectly homogeneous displacement field. The total stress is modeled as the

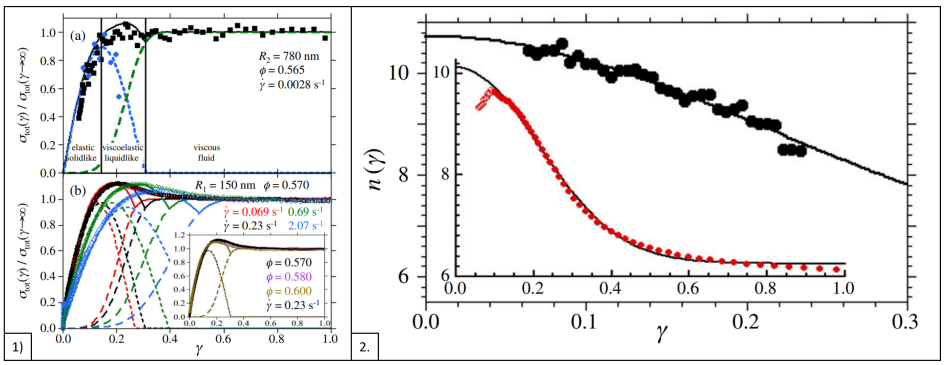


**Figure 1.13:** Stress growth experiments on colloidal glass. Panel 1. Stress $\sigma$ as function of $\gamma$, symbols correspond to rheological data, dotted line is the modeled elastic contribution to the stress $\sigma_E$, dashed lines are the modeled visco-elastic contribution $\sigma_V$, continuous lines are the modeled total stress values $\sigma = \sigma_E + \sigma_V$. The stress is normalized with its asymptotic value. Panel 2.Number of long-lived neighbours as a function of $\gamma$ for $\dot{\gamma} = 0.0028 s^{-1}$. Black dots are confocal microscopy direct measures, red dots are values extracted by rheology, black lines represents an exponential fit with compressing exponent $n(\gamma) = (n_0 - n_\infty)e^{-(\gamma/\xi)^2} + n_\infty$. Adapted from [70].

sum of two parts: $\sigma = \sigma_E + \sigma_V$. The first one is an elastic part that depends on both $g(r)$ and $n(\gamma)$ (dotted blue line in Fig.1.13). Note that the model, originally meant to describe the *linear* elastic shear modulus, is here generalized to predict also the *non-linear* one. This is done introducing the dependence of the number of long-lived neighbours on the deformation $G(n(\gamma))$. The second contribution to the stress is a linear visco-elastic term whose effective viscosity is extracted with a fit of the stress at high deformations (in the steady state regime) green dashed line in Fig.1.13 1.(a). The agreement between the predicted and the measured stress is impressive, apart from the intermediate region where the model predicts an unphysical kink (continuous lines in Fig.1.13), the transition between the elastic-dominated and viscous-dominated regions could be made smoother at the expense of a more complex model. Similarly to the *creep* experiments the more elusive part of the response is the transition one, where both the non-linear elastic and linear visco-elastic descriptions fail.
We also notice that $n(\gamma)$ can be directly measured only for small deformations, see Fig.1.13 2. black symbols, in confocal microscopy, in fact, there is a trade-off between resolution, acquisition velocity and extension of the field of view. The authors assume a model for $n(\gamma) = (n_0 - n_\infty)e^{-(\gamma/\xi)^2} + n_\infty$, but the extent of the $\gamma$ interval where $n$ can be measured directly is not enough to unambiguously determine the fit parameters. Since the elastic part of the

stress is related to $\gamma$, one can infer $n(\gamma)$ from $\sigma_E$, (Figure:1.13, panel 2. red symbols). The inferred $n(\gamma)$ agrees with the model and the fitted curve well overlaps also with microscopy data.
In this example, together with the power of confocal microscopy, some of its limitations emerge: the price to have detailed and high resolution information are the poor statistics and the impossibility to follow the microscopic behavior over large displacements or too large shear rates.

**About continuous shear experiments -** At the microscopic level too we have to deal with the same difficulty that we encounter at a macroscopic level in discriminating between **non-linear elasticity** and **plasticity**, which microscopically corresponds to the difficulty in discriminating between reversible and irreversible events. In fact, at the microscopic level, we can define

- affine displacements, that in a parallel sliding planes geometry Fig.1.17 are $\Delta\vec{x}_A = z\gamma\hat{u}_x$
- non-affine displacements: $\Delta\vec{x}_{\mathrm{NA}} = \Delta\vec{x}_{\mathrm{Tot}} - \Delta\vec{x}_A$

But this distinction does not correspond to the distinction between *reversible* and *irreversible* displacements.
The only way to distinguish reversible and irreversible rearrangements due to a certain transformation is to *remove* the applied stress and observe how much of the deformation is recovered.
The mechanical test where a stress is applied for a finite time, the stress is removed and the deformation recovery is observed, is called **creep and recovery**. While this methodology would allow a clear distinction between reversible and irreversible displacement, it will suffer the same lack of statistics as creep test.

A different approach that helps spotting irreversible rearrangements and, at the same time, provides a stationary condition in the proximity of the yielding point is the **oscillatory** approach.

## 1.4 Large amplitude oscillatory shear (LAOS) experiments

The yielding transition can be studied also under oscillatory condition: one imposes a sinusoidal deformation at a given frequency and amplitude and records the stress as a function of time. The graphs of the stress as a function of the deformation $\sigma(\gamma)$ or of the stress as a function of the deformation rate $\sigma(\dot{\gamma})$ are called Lissajous plots Fig.1.14 1. After some deformations cycles a

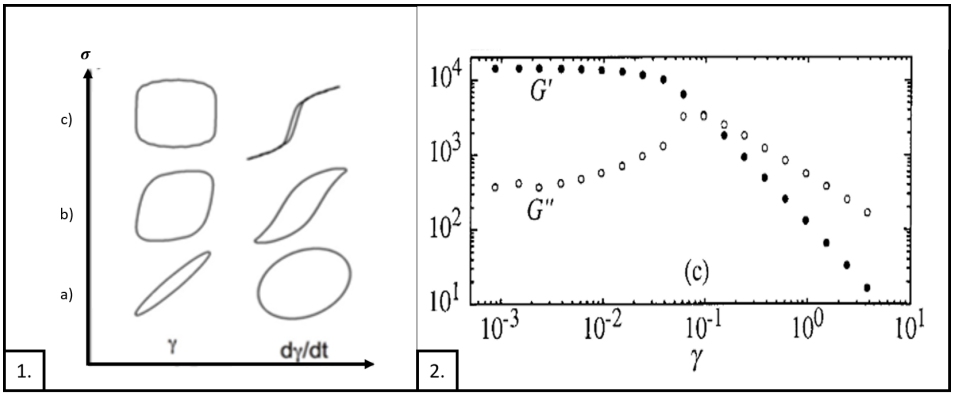


**Figure 1.14:** Typical response of an yield stress fluid in LAOS experiments. 1. Lissajous plots: $\sigma(\gamma)$, $\sigma(\dot{\gamma})$ for different stages of the yielding transition for a *colloidal gel*. a) *unyielded*: the plots are elliptic, the system has a linear visco-elastic response. b) *yielding*: the shape of the plots is far from being elliptic, sign of non-linear response. c) *yielded*: $\sigma$ is almost a function of $\dot{\gamma}$ alone, meaning that the elastic contribution is negligible. Also different phases of the cycle has different effective viscosity $\partial_{\dot{\gamma}}\sigma$. 2. First harmonic of the elastic ($G'$) and viscous ($G''$) moduli as function of $\gamma$. For the smaller $\gamma$, $G'$ an $G''$ are $\gamma$ independent. For increasing deformation $G''$ grows, hallmark of an increasingly dissipative response. Adapted from [69] and [79].

stationary condition is reached, *i.e.* the stress does not depend on the cycle number but only on the *phase* within the deformation cycle

$$\sigma(t + nT) = \sigma(t) \tag{1.15}$$

where $T$ is the deformation period and $n$ is an integer number. The stress is a function of both the strain and the strain rate. In the small amplitude limit, *i.e.* when the system response is linear, the stress response to a sinusoidal deformation

$$\gamma(t) = \gamma_0 sin(\omega t) \tag{1.16}$$

will be sinusoidal as well

$$\sigma(t) = |G^*(\omega)|\gamma_0 sin(\omega t + \delta) \tag{1.17}$$

and the Lissajous figures are ellipses. When linearity is violated (i.e. when the presence of the imposed perturbation alters the response of the material), harmonicity is not guaranteed and non-elliptical Lissajous plots are observed and the stress can be decomposed in Fourier Series

$$\sigma(t) = \sum_{n=0}^{\infty} G'_n \sin((2n+1)\omega t) + G''_n \cos((2n+1)\omega t) \tag{1.18}$$

The Fourier Series only contains odd harmonics, this is due to basic symmetry reasons, according to which if the strain is reverted ($\gamma \to -\gamma$) also the

shear stress must revert ($\sigma \to -\sigma$), from this is straightforward to show that the even terms of the Fourier Series necessarily vanish. Yielding is studied in oscillatory conditions by measuring the response for different imposed shear amplitudes (or shear stresses) Fig. 1.14 1.

A first output of the test is provided by the **first harmonic** of the visco-elastic moduli 1.18 Fig.1.14, panel 2: for the smaller deformations $G'$ an $G''$ are $\gamma$ independent: this is the linear part of the response. For increasing deformation $G''$ grows, hallmark of an increasingly dissipative response and $G'$ decreases. Typically, $G''$ reaches a maximum and for larger $\gamma$ the material becomes weaker and weaker. As discussed in ref. [36] the identification of the yielding point is not unique: three candidates to define the yield point are

- when $G''$ starts to increase
- when $G'' > G'$.
- when the total stress $(G' + G'')\gamma$ deviated from linearity

As we will discuss this in more detail later (2.3.2) also in this case, the physical interpretation of these points is not straightforward[6].

We have learned that, despite of the kind of test they are subjected to, yield stress fluids can be described as visco-elastic solids in their *unyielded* state and as visco-elastic liquids in their *yielded* state, but the more intriguing, yet elusive, regime is the *transition* one. In this regime, the attempted approximated descriptions in terms of linear visco-elastic material generally fails [70], and the non stationarity of this condition prevent a robust experimental characterization [107]. LAOS tests provide a **stationary condition in the transition regimes**, and this is a great advantage as compared to *creep* and *stress growth* tests.
Clearly also this approach has limitations: while in linear regime it is very easy to divide the *elastic* (conservative) and the *viscous* (dissipative) responses, this is more difficult in the non-linear regime. However, given the potential of this approach, several attempts have been made to generalize the concepts of elastic and viscous moduli in the non-linear regime. Particularly appealing is the approach of Rogers and colleagues [103], [43] who introduced *phase* dependent elastic ($G'_t$) and viscous ($G''_t$) moduli. Differently from the linear viscoelastic moduli, $G'_t$ and $G''_t$ relate the deformation $\gamma$ with the *whole* stress $\sigma$ and not just with its projection on the first harmonic

[6]It is worth noticing that this kind of test has an interest also in connection with fatigue tests aimed to characterize the progressive weakening of a material due to the application of a stress (continuous or cyclic), but this phenomenology, intrinsic non-stationary lie outside our current main interest.

$\sigma_0 = \sigma(t) \cdot \sin(\omega t + \delta)$[7].

Another important remark regarding the generality of the results obtained with a specific experimental protocol should be made. As long as the linear part of the response is considered, all the above mentioned experimental procedures (*creep*, *stress growth*, *oscillation*) are equivalent and the response functions of a certain experiment can be perfectly translated in the response of the other [76]. When the non-linear regime is explored, things become much more complicated and it is generally unknown how to map the yielding point obtained with a protocol to one obtained with another one. In a recent work of the group of Daniel Bonn [36] similarities and differences between different yielding tests were reviewed.

### 1.4.1 LAOS and microscopic investigation

Many different techniques has been used to investigate the microscopical features of yielding in oscillatory condition. Most of them use an **echo** approach: the microscopic configuration at time $t$ is compared with the one at time $t + nT$, where $T$ is the period of the oscillatory perturbation. The echo scheme is ideal to single out the signal arising from irreversible changes caused by the perturbation. Another advantage, as compared to continuous deformation protocols, regards the range of shear amplitudes that one can access: in creep or stress growth experiments one wants to detect a non-affine displacement on top of a, generally larger, affine displacement and therefore the dynamical range is usually a limiting factor. In the echo approach the compared microscopic configurations have the same macroscopic deformation and so only the non-affine displacement emerges. As a result, the range of shearing amplitudes that one can explore is way larger.

An interesting example of the potential of this approach is represented by the work of Gibaud et al.[51], where the spatially inomogeneous rearrangments induced in a sample subjected to large amplitude oscillations are investigated with USV. In this paper a carbon black gel is subjected to oscillator shear experiments at fixed stress amplitudes in a Couette geometry. Carbon black gel is composed by polydispersed colloidal particles with diameters of the order of few hundreds of nanometers. The first harmonic of the response function is reported as a function of time for a stress value close to yielding Fig.1.15, panel 1. A multiple yielding process emerges from the series of drops in the mechanical moduli. Simultaneously to the mechanical response, the irreversible displacements occurred during one cycle are monitored, comparing the ultra-sound field scattered at time $t_0$ with the one scattered at time $t_0 + T$ Fig.1.15, panel 2. Similarly to creep [40] and stress

[7] For a more in-depth discussion see Sect. 2.3.2.

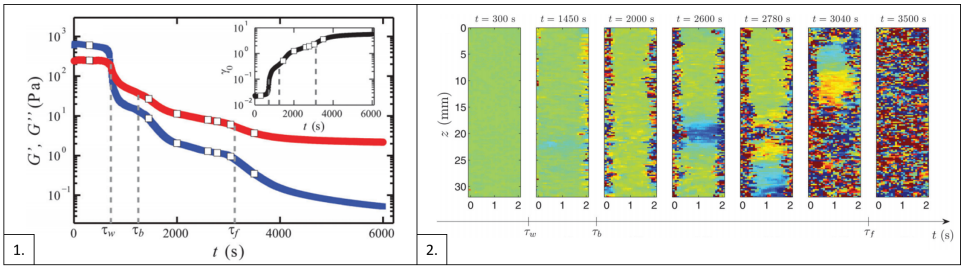


**Figure 1.15:** Panel 1. First harmonic of visco-elastic moduli in stress controlled LAOS test on carbon black gels. In the inset the evolution of the stain amplitude. The macroscopic response shows progressive yielding processes. Panel 2. Spatial map of displacements after one cycle for different stages of the LAOS. The different yielding observed by the evolution of the macroscopic strain correspond to different localized yielding: progressive yielding at the walls starting from $\tau_w$; at $\tau_b$ the walls has been eroded completely; erosion progresses and completes fluidization at $\tau_f$. Adapted from [51].

growth [39] experiments also in this case the progressive fluidization of the sample is observed. Each of these local yielding events is characterized by a waiting time before its occurrence. Thanks to USV three different yielding processes are identified: after a first latency time ($\tau_w$), progressive yielding at the walls starts , that, differently from the continuous shear case, occurs symmetrically at the inner and outer boundaries; once the yielding at the walls is complete ($\tau_b$), the fluidized zones start growing and progressively invade the whole gap ($\tau_f$). Remarkably each of these characteristic times exhibits a specific power law dependence on the stress. The authors make an interesting connection with the Basquin failure criterion [11], [67], an empiric law used in hard materials to describe the relation between the number of stress cycles that a material can stand and the amplitude of the stress.
One important difference with previous studies from the same research group (Refs. [40], [39]), is that in the present case the sample is thixotropic. Thixotropic yield stress fluids are those fluids where the mechanical properties do not depend only on the instantaneous deformation state but also on their shear history. Understanding and modeling the yielding scenario for these systems is way more complex than for simple YSF. It is also known that thixotropic samples present flow inhomogeneities close to the yielding point. For these reasons it is not easy to understand if the phenomenology presented in [51] should be considered as a general feature also for non-thixotropic samples in LAOS conditions or not.
In the same paper the authors also refer to a theoretical work that motivates the validity of Basquin law from a microscopic stand point [67]. Similarly to the model used in ref. [31] the main ingredients are the occurrence of *microscopic fracture* and *healing events*. In our view, the main obstacle that impair the experimental test of the model is, once again, the **non-stationarity** of

the experimental condition.

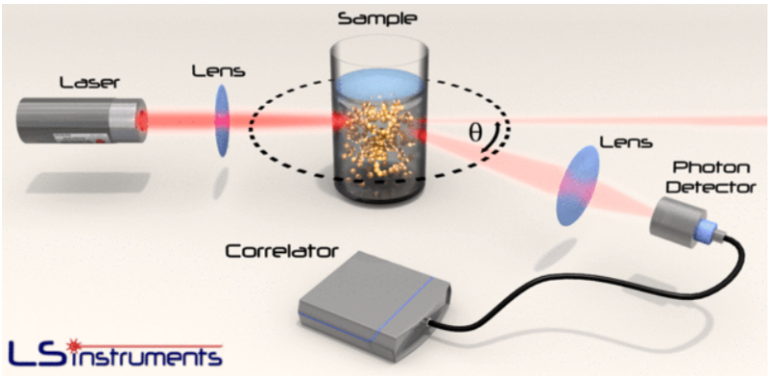


**Figure 1.16:** Representation of a Dynamic Light Scattering experimental setup. A collimated beam impinges on the sample. Light scattered in direction $\theta$ is collected by a detector and a correlator computes the temporal correlation function $g_2(\theta, \Delta t)$(for a more detailed discussion see the following boxes and Sec.3.3). Adapted from [42].

**Dynamic Light Scattering**

**DLS** is a optical techniques enabling to probe small displacements of the elementary constituents (scatterers) of a sample. In a typical DLS experiment a collimated laser is shed on a sample and the intensity of the light scattered at a certain angle $\theta$ with respect to the beam propagation direction is collected. This intensity signal $I(\theta, t)$ fluctuates if the position of the *scatterers* changes in time and one can characterize the dynamics of the scatterers computing the intensity correlation function

$$g_2(\theta, \Delta t) = \frac{\langle I(\theta, t) \cdot I(\theta, t + \Delta t) \rangle_t}{\langle I(\theta, t) \rangle_t^2} \tag{1.19}$$

**Diffusive Wave Spectroscopy**

Light scattering experiments in the strong **multiple scattering** regime are usually referred to as **Diffusive Wave Spectroscopy**(DWS) [98]. In the limit, where the probability of a scattering event is very high, a simple relation holds between the correlation function and the scatterers' *mean square displacement*:

$$g_2(\theta = 0, t) = 1 + \Big(exp\big(-\frac{1}{6}nk^2\langle\Delta r^2(t)\rangle\big)\Big)^2 \tag{1.20}$$

Two peculiarities of the multiple scattering regime:

- the presence of the number of scattering events $n$, meaning that the correlation function is sensitive to displacement of the order of

$$d \sim \frac{\lambda}{\sqrt{n}} \tag{1.21}$$

- there is no $q$ resolution: 1.20 equation is valid in transmission ($\theta = 0$) and $k = 2\pi/\lambda$.

The first experiment using DWS to microscopically probe yielding dates back to 1997 [55]: in this work the examined sample is an emulsion of hexadecane in water and the deformation is applied with a custom-made, parallel-sliding-plate (Fig.1.17) shear-cell that does not allow for a stress measurement. The mechanical properties are obtained by separate experiments [78].

**Parallel sliding plates**

This geometry produces a uniform field, given a global deformation $A$, each element is displaced of a quantity $\Delta x(z) = z \cdot A/H$ where z is the coordinate perpendicular to the two plates and $H$ is the gap width, *i.e.* the distance between the two plates. The local deformation of a small volume coincides with the *mean* deformation $\partial_z \Delta x(z) = \gamma$ Fig.1.17.

The quantity measured in DWS experiments is an intensity correlation function:

$$g_2(\Delta t) = \frac{\langle I(t)I(t+\Delta t)\rangle}{\langle I(t)\rangle^2}.$$

The correlation function is quantitatively modeled in terms of both affine and non-affine displacements, both within the period Fig.1.18 b) and across several periods Fig.1.18 a). The authors consider to the height of the peaks corresponding to following echos and observe that the majority of the rearrangements occurs during the first cycle. $g_2$ drops by an amount that depends on the strain amplitude. This experimental observation has been interpreted

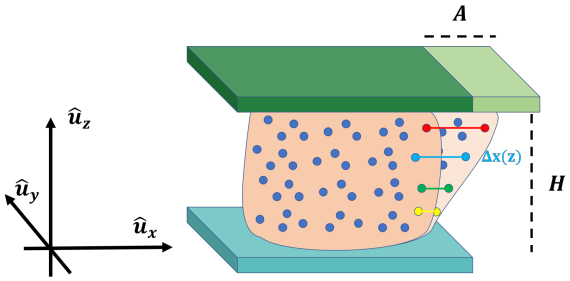


**Figure 1.17:** Cartoon of a parallel sliding plates geometry. $\hat{u}_x$ is the *shear direction*, $\hat{u}_z$ is the *deformation gradient* direction and $\hat{u}_y$ is the *vorticity direction*. $A$ is the macroscopic imposed displacement, $H$ is the *gap*. If the material is homogeneous this geometry produces an affine displacement field, where a portion of material is displaced by an amount $\Delta x(z) = z \cdot A/H$ (four particles at different vertical position $z$ and their affine displacements are labeled with different colors).

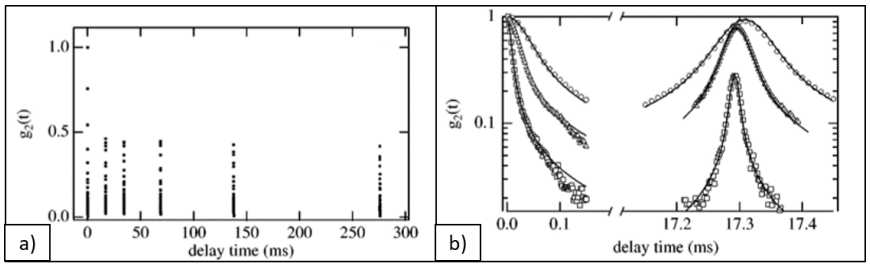


**Figure 1.18:** Correlation functions $g_2(\Delta t)$ for DWS echo experiments with water-in-oil emulsions. a) 1st, 2nd, 4th, 8th and 16th echo peaks: almost all the plastic activity is observed in the first oscillation cycle: the amplitude of the higher orders peaks is unchanged. b) Envelope of 0th and 1st echo peaks, continuous lines correspond to the model accounting for affine motion plus plastic activity, for different shearing amplitude:$\gamma_0 = 1\%$. $\gamma_0 = 2\%$, $\gamma_0 = 6\%$. Thermal motion appears negligible. Adapted from [55].

as follows. There are two distinct families of particles: one involved in the rearrangement dynamics, having a correlation time shorter than one period, and another one whose dynamics is completely reversible even after many cycles. The number of particles involved in the rearrangements depends on the strain amplitude. Quite surprisingly only a small fraction of particles is involved in the rearrangements: even at the higher explored strain rate, the volume fraction occupied by particles involved in the rearrangements, $\Phi$, never exceeds 10%. This suggests that the fluidization is not complete.

Some years later, the same approach was used in an important series of studies on colloidal hard sphere glasses from Petekidis and coworkers [92], [95], [93], [94]. A relevant difference with Ref. [55] is the observation of rearrangements involving also higher order peaks Fig.1.19 a). And, as one would

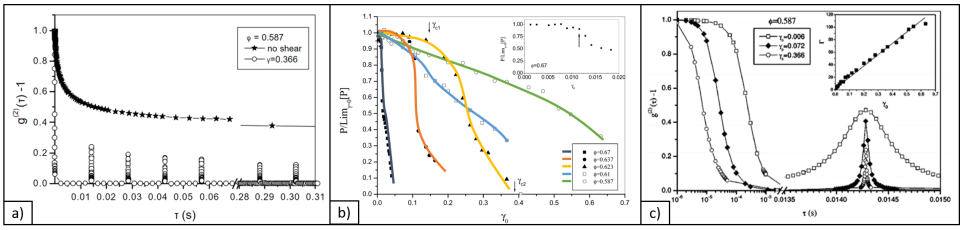


**Figure 1.19:** Echo DWS experiments on a colloidal glass. a) Stars represent the decay of $g_2$ due to thermal dynamics, empty dots the decay of $g_2$ both for thermal dynamics and shear-induced dynamics. Assuming their independence one can separate the contribution. b) Correlation $g_{2Shear}(\Delta t = T, \gamma_0)$ after one deformation cycle for different volume fractions. The correlation functions are normalized in order to account only for the shear-induced dynamics and not for the thermal one. Colored lines have been added as guidelines. c) Envelope of the echo for different shear amplitudes. Inset: inverse width of the envelope $\Gamma$ as a function of the imposed shear amplitude. The observed linear scaling indicates absence of slip. Adapted from [92], [95], [93]

expect, the correlation goes to zero at large enough deformation amplitude. The authors separated the decorrelation due to the thermal agitation from the one due to shear-induced rearrangements, assuming that the thermal and the shear-induced mean square displacements are independent:

$$\langle \Delta r^2 \rangle = \langle \Delta r^2_{shear} \rangle + \langle \Delta r^2_{therm} \rangle. \tag{1.22}$$

This way the correlation function $(g_2 - 1)$ is factorized in two terms, one containing $\Delta r^2_{shear}$ and one $\Delta r^2_{therm}$. From now on we will refer to $g_{2shear}$ as the correlation function from which the thermally-induced contribution has been removed. The shear-induced dynamics is assumed to be diffusive-like but no fitting or modeling of the relaxation dynamics is attempted to prove this assumption. All the analysis is done considering the intensity correlation $g_{2shear}(T, \gamma_0)$ after one cycle as a function of the imposed deformation amplitude.

Using colloidal glasses at different volume fraction, Petekidis and colleagues were able to compare systems with different yielding behaviors: at higher volume fractions glasses are more fragile than at lower volume fractions Fig.1.19, b). This is reflected in a more abrupt microscopic decorrelation: $g_2(T, \gamma_0)$ has a stronger dependence on the shearing amplitude $\gamma_0$ as compared to what observed at lower volume fraction. From the width of the $0th$ order peak one can measure the affine displacement speed. In the absence of slip, the width is expected to be inversely proportional to the imposed deformation amplitude and in fact a good linear scaling is found Fig.1.19 c).

The authors propose an interesting argument concerning the deformation amplitude for which one expects the onset of non-linear behaviour for hard spheres glasses. The arguments is based on the idea that above a certain

deformation amplitude one particle necessarily collides with a neighbour, inducing an irreversible rearrangement. The critical deformation amplitude depends on the free volume per particle, a quantity that can be easily computed for a hard sphere system, known the volume fraction. The authors find that the glasses can tolerate deformation almost one order of magnitude larger than the one predicted by this argument, which led them to hypothesize that the elastic stress is carried by groups of particles (cages of roughly 12 units) that can undergo larger deformation without losing their connectivity.
The results of these experiments are very promising even though their comparison with the macroscopic behavior is remained mostly qualitative.

In a more recent study, Laurati, Egelhaaf and Petekidis [69] used echo DWS to study the yielding of colloidal depletion gels, in which the colloidal particles interacts attractively because of the presence of a polymer. The polymer-coil's diameter sets the interaction range and its concentration sets the interaction strength [7]. The Lissajous plots that we have previously reported in Fig.1.14 1. show the stress within the period of oscillation as a function of the shear $\gamma(t)$ and of the shear rate $\dot{\gamma}(t)$. The non-linear rheological response is analyzed considering different methods and, depending on the deformation amplitude and also on the phase of the deformation cycle, different non-linear mechanisms are identified. The observed viscosity decrease (*shear thinning*) or increase (*shear thickening*) and the elasticity increase (*strain hardening*) are attributed to the formation or disruption of some structures in the gel Fig.1.14 1, but no strong microscopic evidence proves the suggested link between the different non-linear behaviors and a microscopic origin, like the formation or disruption of specific structures.
The correlation functions Fig.1.20 are computed for delays up to hundreds of oscillations (a number considerably larger than the one considered in previous experiments [55]) and for a range of amplitudes going roughly from 1% to 20%. The shear-induced relaxation is fitted with a stretched exponential function and the relaxation time is reported as a function of the shear amplitude. Interestingly, the correlation time $\tau$ changes drastically (4 decades) in a relatively narrow interval of shearing amplitudes. Unfortunately, with echo-DWS there is no way to discriminate between a diffusive-like or a ballistic-like (or others) rearrangement dynamics because of the limited spatio-temporal experimental range.

Few years later, in a work of Moghimi et al. the same system is studied combining rheology with Brownian Dynamics simulations [85]. In this work, rheological data for the visco-elastic moduli $G'$ and $G''$ are compared with the same quantities computed in simulations. From the very same simulations, a detailed configurational information can be also accessed. In Fig.1.21, together with the visco-elastic moduli (both experimental and simulated), cor-

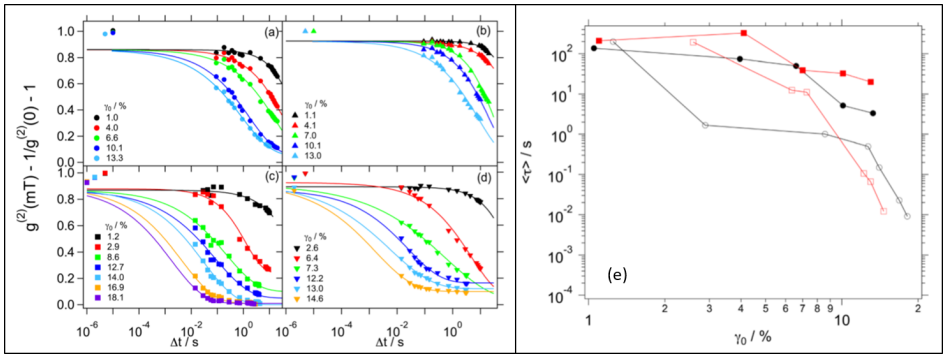


**Figure 1.20:** Correlation functions obtained by Echo-DWS, for PMMA-PS samples with polymer concentrations $c = c^*/2$ [(a) and (c)]; and $c = c^*$ [(b) and (d)]; and frequencies $f = 11Hz$ [(a) and (b)], and $70Hz$ [(c) and (d)]. Lines indicate fits to a stretched-exponential function describing the long-time decay. (e) Relaxation time as a function of the shear amplitude. Dots correspond to $c = c^*/2$ and squares $c = c^*$. Full symbols correspond to $f = 11Hz$, empty symbols to $f = 70Hz$. Adapted from [69].

responding snapshots from the simulation are reported. The insight gained

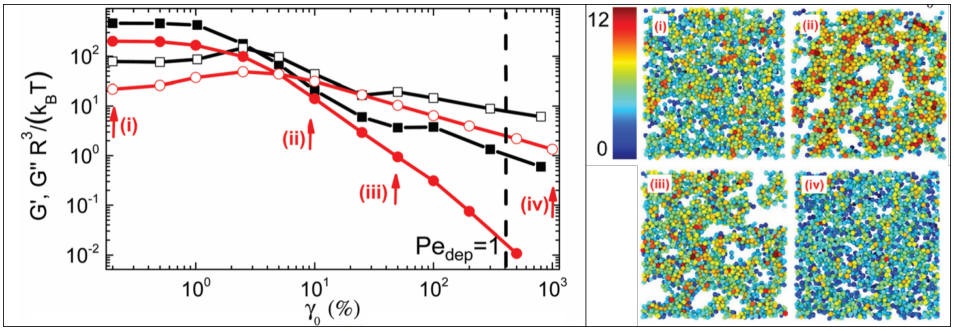


**Figure 1.21:** $G'$ (solid symbols) and $G''$ (open symbols) for colloidal gel, comparison between rheological data for amplitude sweep (in black) and BD simulations (in red). Simulation snapshots corresponding to the arrows in the amplitude sweep. Color labels the number of neighbour. The initial effect of shear is to increase heterogeneity and to promote the formation of more connected clusters(ii). Adapted from [85]

by simulations is extraordinarily rich. Even from the snapshots of Fig.1.21 it is possible to appreciate how the heterogeneity increases passing from i) to ii) and iii), supporting the hypothesis proposed by Laurati and coworkers [69] that shear thickening can be attributed to the formation of clusters of particles. At the highest considered strain amplitudes the systems is more homogeneous and the connectivity is minimal, compatibly with a mainly liquid like response and with a reduction of higher harmonic contributions observed by Laurati and coworkers. The real rheological behaviour is a bit

more complex than the one captured by Brownian Dynamics simulations and this is reflected, for example, in the absence of the second maximum for $G''$, present in the experimental data. The presence of the second maximum of $G''$ in LAOS has been recognized as a robust feature of the yielding of attractive systems [64]. The difference is attributed by the authors to the absence of hydrodynamic interactions which are known to play a role in the formation of clusters, even in quiescent conditions [115].
It is worth mentioning that all the Echo DWS experiments presented hitherto are always performed at relatively high frequencies ($f \simeq 70Hz$) that are not accessible by regular rheometers. The reason is twofold:

- for long enough delays the thermal dynamics can lead to complete decorrelation of the spatial length scales accessible by DWS, even in absence of shear.
- the presence of wall slip would be more pronounced at smaller frequencies [8], [9] and would impair the experimental observations. This problem is cured in rheological experiments increasing the roughness of the boundaries but it is particularly relevant for *all* optical experiments that need transparent and smooth surfaces.

Nevertheless, echo-DWS experiments show that a combined study of mechanical and microscopical yielding in stationary condition is feasible and very interesting. With this approach clear data can be collected even at intermediate shearing amplitude, where the mechanical behavior is already non-linear and intermediate between liquid and solid. There is still large margin of improvement regarding microscopic data interpretation, modeling and connection with mechanical properties. The range of length scales probed with DWS is not wide enough to access all the relevant temporal and spatial scales that needs to be considered to model the mechanical response.

With a similar spirit, Leheny and coworkers studied the yielding transition by combining oscillatory shear to x-ray scattering in single scattering regime. In a first work [101] they studied colloidal depletion gels with particle radius $R \simeq 16\ nm$. In a more recent one [102] the studied system is a stabilized nano-emulsions of silicon oil in water, the size of the droplets being $R \simeq 25\ nm$. In the following we will discuss these two studies together, as they share the same experimental approach. The samples are loaded in a shear cell placed on an x-ray beam line, the signal is collected with a two dimensional CCD. This way both static and dynamics $\vec{q}$-resolved information are acquired during shear. The range of probed wave vectors is $q \in [0.03, 0.22] nm^{-1}$. Both static and dynamics over some tens of cycles are considered.
For both the systems, a super-diffusive $q$-scaling is observed Fig.1.22 3. This kind of information, in particular the measurement of the relaxation

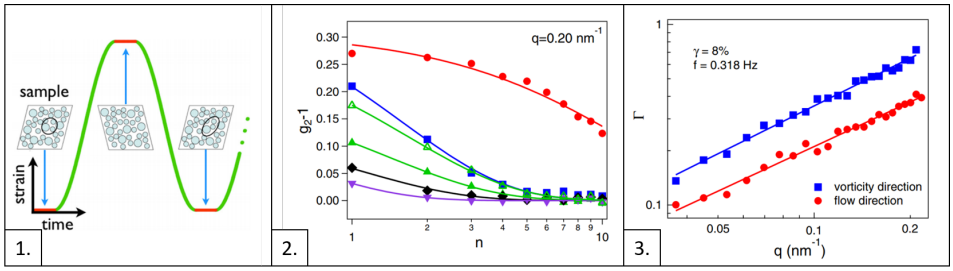


**Figure 1.22:** Echo x-ray experiments on colloidal gels. Panel 1. Representation of the oscillatory strain profile. The strain follows a sinusoidal for half a period between the maximum and the minimum. At the extremes the strain is hold constant for a short time (red) during which a coherent x-ray exposure was obtained, after that the deformation profile starts again harmonic. 2) Intensity correlation functions $g_2(q, n_{cycle})$ for fixed $q$ and different deformation amplitudes. 3) Relaxation rate for a fixed deformation amplitude as a function of the wave vector $q$ in the *vorticity* and *flow* directions Fig.1.17, continuous line are power-law fits with exponents $\alpha \simeq 0.8$ (red),$\alpha \simeq 0.9$ (blue). Adapted from [101].

rate as a function of the wave vector, is very rare in the literature. The authors observe that a diffusive scaling $\Gamma \propto q^2$ would be more naturally expected, also according to some theoretical predictions and computer simulations [84], [15], but they justify the observed behavior with an argument based on the spatial-size distribution of zones involved in the plastic rearrangements. It is worth noticing that even though the majority of the theoretical predictions and simulations supports a diffusive-like behavior, the presence of super-diffusive dynamics should not be excluded *a priori* since it has been observed in other systems in similar condition. Super diffusive dynamics in fact has been observed in systems where some internal elastic energy is progressively released, either because in the initial condition the system is not in mechanical equilibrium or because of an applied stress. This is a well established fact proved by a series of experiments [4] and simulations [52]. Anyway, for large enough shear, when the sample is completely fluidized ($G' \simeq 0$), a diffusive behavior should be expected. The experiments in the shear cell are performed at a frequency $\nu = 0.318Hz$. This allow a more direct comparison with rheology. Slip is restrained increasing the roughness of the shear cell diamond plates by the application of a polyamide sheet. In Ref. [102] a drastic speed up of the shear-induced dynamics is observed: the rate $\Gamma(\gamma_0)$ shows a super-linear dependence on the shearing amplitude $\gamma_0$. The dependence is not as strong as observed in Ref. [69].
From the comparison with rheology an apparent contradiction emerges: the microscopic plastic rearrangements seem to appear quite late as compared to the increase of $G''$. This fact has been observed in other experiments [57], as well as in simulations [105].

To interpret this apparent contradiction the concept of *reversible plastic*

*rearrangements* has been proposed. A *reversible plastic rearrangements* is a periodic plastic displacement, *i.e.* $\Delta x_{\mathrm{NA}}(t)$ is so that

$$\Delta x_{\mathrm{NA}}(t+T) = \Delta x_{\mathrm{NA}}(t)$$

such events dissipates energy but do not emerge in echo experiments.

The LAOS approach has been complemented also with microscopy: the first work in this spirit is the study of Pickering emulsions from Hermes and Clegg [56]. The experiments are performed with a confocal microscope coupled with a rheometer, enabling a more direct comparison with the mechanical response as compared to the works presented so far.
Apart from the remarkable qualitative insight given by visual inspection of the sheared sample, the amount of plasticity is quantified computing the Pearson correlation coefficient between two images separated by a whole period. The Pearson coefficient gives an information integrated over the all image so it does not exploit in the best way the spatial resolution capability of microscopy. Moreover the fact that $G''$ does not increase as the system yields questions the opportunity of considering only the first harmonic of the viscoelastic moduli to follow the yielding process. Nevertheless in the two cases where the correlation functions are also computed, the onset of plasticity occurs quite lately in comparison with the onset of non-linearity, compatibly with the just mentioned plastic reversibility picture. The heterogeneity of the composition and the choice to compute the integrated correlation makes it hard to relate the correlation function to the dynamics of the system in a quantitative way and more is gained from the visual inspection of the movies.

Very relevant contribution comes from Knowlton, Pine and Cipelletti [61]. The authors analyzed microscopy images of periodically sheared emulsions with Image Correlation Velocimetry (ICV)[114] to examine their yielding behavior. With ICV they measure the root mean square displacement RMSD $\langle \Delta y^2 \rangle^{0.5}$ after one cycle in the direction orthogonal to the shear. Longer delays and the dynamics in the shear direction are not considered to avoid spurious effects due to imperfect synchronization between the shear cell and the camera.
The measurements are performed in the proximity of the macroscopic yielding point $\gamma_{y,r}$ defined as the deformation amplitude for which the stress start showing a non-linear dependence on the deformation amplitude [79] Fig.1.23 1. The information obtained from these data is very rich and the microscopic picture is really detailed. From RMSD($\gamma$) the authors detect a very sharp microscopic transition Fig.1.23 2. at a critical deformation value $\gamma_{y,micro}$ that follows very closely $\gamma_{y,r}$ for all the five different samples (different volume fractions).
From the study of the displacement distribution $P(|\Delta y|)$ two families of

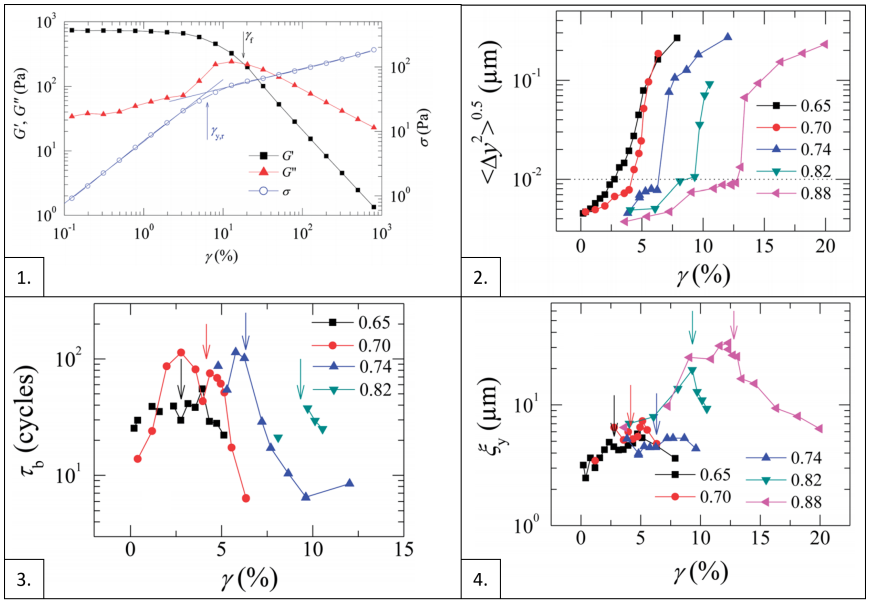


**Figure 1.23:** Panel 1. $G'(\gamma), G''(\gamma)$ first harmonics of viscoelastic moduli, and shear stress $\sigma(\gamma)$, oscillation frequency $1Hz$ for $\phi = 0.83$. The arrows defines the fluidization strain $\gamma_f$: $G'' > G'$ and $\gamma_{y\ Rheo}$ as defined by [78] and in the main text. 2. RMSD $\sqrt{\langle \Delta y^2 \rangle}$ for different concentrations. The horizontal line has been identified as the transition value for the highest volume fraction. 3. Burst duration $\tau_b$ extracted from the temporal correlation function, see the main text for details. 4. Dynamical spatial correlation-length $\xi(\gamma)$, see the main text for details. Adapted from [61].

droplets with different motility are found: *mobile* and *supermobile* droplets. Together with the RMSD, also the fraction of supermobile droplets grows drastically close to $\gamma = \gamma_{y,r}$. Similarly to [92], the microscopic yielding transition is sharper for higher volume fractions.
The plastic rearrangements show both temporal and spatial correlations, typical of glassy dynamics. The duration of the activity bursts $\tau_b$ is evaluated by considering the correlation function

$$c(\tau) = \langle \langle |\Delta y(t, \mathbf{R})||\Delta y(t+\tau, \mathbf{R})| \rangle_t \rangle_{\mathbf{R}} \tag{1.23}$$

across hundreds of cycles. The characteristic time $\tau_b$ exhibits a maximum when examined as a function of $\gamma$ Fig.1.23,3 . The maximum position corresponds, for the majority of the samples, to $\gamma_{y,micro}$. The value of $\tau_b$ is always finite, even at the transition point, this means that an active particle is active for a finite time, and so the two motility families are not separated: a motile droplet can become supermotile and *viceversa*. The spatial correlation is quantified by the four point correlation

$$G_4(\Delta \mathbf{r}) = \langle \langle |\Delta y(t, \mathbf{R})||\Delta y(t, \mathbf{R}+\Delta \mathbf{r})| \rangle_t \rangle_{\mathbf{R}} \tag{1.24}$$

$G_4(\Delta\mathbf{r})$ decays to zero with a characteristic length scale $\xi(\gamma)$ Fig.1.23 4. This correlation-length-scale increases as a function of the volume fraction, indicating a longer range of stress transmission for more solid like samples. For the higher volume fraction samples, $\xi(\gamma_0)$ decreases for $\gamma_0 > \gamma_{y,micro}$, This decrease can be interpreted as a progressive fluidization of the sample according to the same argument used to compare different volume fractions.

The correspondence between $\gamma_{y,micro}$ and $\gamma_{y,r}$ is striking, but the physical interpretation of $\gamma_{y,r}$ (which marks the transition from linear to non-linear response) and its connection with yielding is not straightforward. In fact, non-linearity is in general a necessary, yet not sufficient condition for yielding. As a consequence this close correspondence between the microscopic and macroscopic yield strains shouldn't be considered as a general feature of yielding.
The microscopic transition is remarkably sharp: the RMSD changes by a factor ten in an interval of $\Delta\gamma \sim 1\%$. This is quite contrasting with the rheological response that exhibits a solid to fluid transition, in this case parametrized by $tan\delta = G''/G'$, in an interval $\Delta\gamma_r \simeq 16\%$. How such a sharp microscopic transition gives origin to a way smoother mechanical response is still to be understood, as a model that quantitatively links the observed microscopic plasticity with the mechanical response is missing.
Even though the study is limited to a relatively small shearing amplitude interval the general picture emerging from this detailed analysis is consistent and encouraging for further application of similar methods.

In a following work, Tamborini and coworkers studied the plastic behavior of a periodically sheared polycrystal Fig.1.24 (a) [112]. A polycrystal is an ensemble of crystalline domains separated by amorphous *Grain Boundaries* (GB). In this case the crystalline domains are transparent and their characteristic size is $\sim 10\ \mu m$. The GB are formed by fluorescently labeled polystyrene nanoparticles (NPs) Fig.1.24 (b), (c). The microscopic investigation, performed by means of both confocal microscopy and multi-angle dynamic light scattering, was aimed at monitoring the rearrangements of the Grain Boundaries, because of the optical properties of the sample Fig.1.24 (b),(c),(d).
The dynamics are studied with DLS over a quite wide range of wave vectors: $q \in (0.1, 4)\mu m^{-1}$. The first observation regards the non-stationarity of the process: in Fig.1.24(e) the correlation function for a fixed wave vector and different waiting time is reported. In this case it is possible to observe a slow down of the dynamics in the first $50 - 100s$. The time for reaching the stationary condition depends on the wave vector $q$. In Fig.1.24(f) are reported the correlation functions for different wave vectors once the stationary condition is reached. In the inset of the same figure the temporal axis has been rescaled with $q$, in this way it is possible to appreciate that,

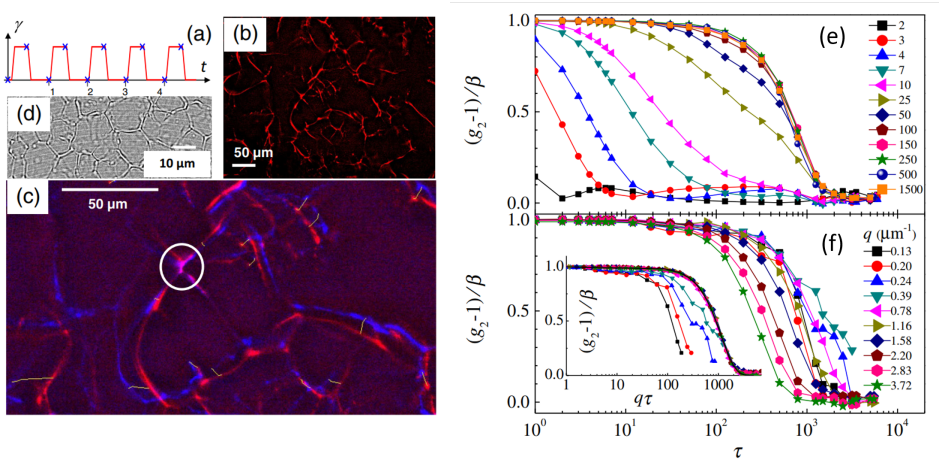


**Figure 1.24:** Periodically sheared polycrystal. The system comprises a water-based thermosensitive block copolymers (Pluronics F108) forming micelles arranged on a face-centered cubic lattice to which a small amount of nanoparticles (NPs) is added. The NPs act as impurities, segregated in the GBs upon crystallization. The source of contrast in both scattering and confocal microscopy observation are the Grain Boudaries. (a) Schematic of the shearing protocol. (b) Confocal image of the polycrystal. (c) Superposition of two images (one in blue and the other in red) separated by almost 4000 shear cycles at ampltude $\gamma = 3.6\%$. Note that even though the overlap between the two images is very small (white circle), the two images looks very similar: the displacement of the grains is not big as compared to their size. (d) bright field image. (e) Intensity correlation function at $q = 1.58\mu m^-1$ for various waiting times. (f) Intensity correlation for different scattering vectors. Inset: intermediate scattering function as a function of the rescaled variable $q\tau$. Functions for $q > q^* = 0.39\mu m^{-1}$ nicely collapse when plotted as a function of the rescaled variable. Adapted from [112].

for $q > q^* \simeq 0.39\ \mu m^{-1}$, the correlation functions nicely collapse on a single master curve. This indicates that at the corresponding length scales the dynamics are ballistic.

The authors point out that the nature of the dynamics is connected to the microscopic mechanism that relaxes the stress: the ballistic relaxation is connected to the presence of stress dipoles [18], in contrast with the vision proposed by Soft Glassy Rheology [108] and other theoretical models, that describes the stress release mechanism in terms of an effective temperature, and thus with completely spatially and temporally uncorrelated events.

The shear amplitude interval is quite narrow and centred around the peak of the viscous modulus: $\gamma \in [1\%, 5\%]$ and, unlike what reported in Ref. [61], the plasticity emerges at deformation amplitude considerably larger than $\gamma_{y,r}$, defined in terms of deviation from a linear behaviour, as shown in Fig.1.23. Extending a similar characterization to other systems would be very interesting, as it would allow to assess the generality of the observed behavior.

Relevant progresses on the topic of coupling shear experiment to microscopic characterization has been recently made in a series of works of Aime, Cipelletti and colleagues. We summarize them briefly. In Ref. [5] the authors describe a home made stress-controlled shear-cell. The cell produces a parallel sliding plates geometry and is designed to be compatible with light scattering (and microscopy) experiments, the laser beam propagates in the *deformation gradient* direction Fig.1.25 i). The cell is also suitable for a mechanical characterization of the sample properties, differently from the majority of the shear cell used in precedent works, that are strain controlled and, not including a force sensor, they are not suited to characterize the mechanical response.
With this setup they were able to prove the existence of microscopic precursors that precedes the, otherwise unpredictable, delayed failure of a colloidal gel [4].
Their approach exploits the possibility for Dynamic Light Scattering to accurately decouple affine deformation from non-affine rearrangements. A rigorous description of the decoupling method is presented in two recent companion papers [2], [3], where the authors present models for the DLS and DDM[8] correlation and structure functions for sheared samples. In particular they clarify the experimental condition where the smaller (but more relevant in the context of the yielding transition) non-affine displacements can be measure and distinguished from generally larger affine displacements.
The authors highlight an interesting difference between DLS and DDM that concerns the probed longitudinal portion of the sample. In DLS the signal is collected from a scattering volume whose limits in the beam propagation direction are given by the sample itself. In DDM the volume that gives rise to the signal is generally smaller than the sample, as shown in Fig.1.25. The "effective scattering volume" depends on the wave vector $q$, and is easily tunable modifying the numerical aperture of the aperture diaphragm[9]. If, on one hand, this means that a generally smaller volume is probed in DDM, with consequently loss of statistics, on the other hand the possibility of a vertical selection on the probed volume gives important advantages when phenomena of heterogeneous deformation field (like wall slip or shear banding, [77],[40],[39]) are present.

**Conclusion -** From this review emerges how much a microscopic physical picture could help in the rationalization of the inherent complexity of

[8]Differential Dynamic Microscopy (DDM) is a technique that combines microscopy and computation of *structure functions*, leading to results similar to Dynamic Light Scattering experiments. This technique is the principal technique used in this work of thesis, and will be presented in the third chapter 3.4.

[9]See Sect. 3.4.

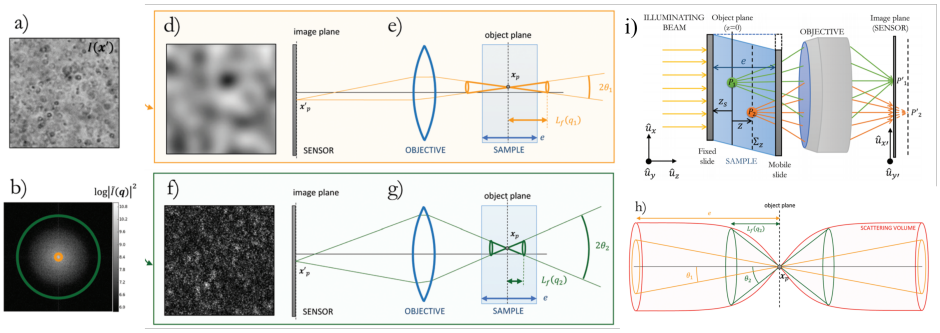


**Figure 1.25:** (i) Representation of the experimental geometry of shear experiment coupled with microscopy: the sample is confined between parallel sliding plates. The optical axis is aligned with the *deformation gradient* direction $\hat{u}_z$ (the same holds for DLS experiments). An image is a projection on the $\hat{u}_x, \hat{u}_y$ directions. (a) Bright field microscopy image (b) Image power spectrum, the orange (green) circle marks the wave vectors with modulus $|\vec{q}| = q_1$ ($q_2$). (d) Same image as in (a), but filtered in Fourier space so as to retain only the contribution of scattering vectors close to $q_1$. (e) Optical layout of the rays contributing to the filtered image shown in (d). $L_f(q_1)$ is the q-dependent depth-of-focus. (f and g) Same as (d) and (e), but for scattering vector $q_2 > q_1$. Notice that, depending on different parameters (such the numerical apertures of the objective and of the aperture diaphragm), the q-dependent depth-of-focus can be longer or shorter of the gap. (h) Effective scattering volume obtained by integrating the conical surfaces associated to all scattering vectors accepted by the objective. All particles within the effective scattering volume contribute to the overall signal observed in position $x'_p$ of image (a). Adapted from [3].

yielding. A series of phenomena, occurring at different length scales, need to be taken into account to have a reliable picture. We think that Large Amplitude Oscillatory Shear represent a very convenient option to explore intermediate stages of the yielding process in stationary conditions.

In this work we apply Differential Dynamic Microscopy (DDM) [21] to the study of shear-induced dynamics in LAOS conditions. DDM was demonstrated to provide information equivalent to a multi-angle DLS experiment form a series of microscopy images even for particles below the microscope optical resolution [22]. This approach combines the easiness of optical microscopy in the coupling with a rheometer and a DLS-like characterization of the dynamics, that do not require to satisfy stringent constrains typical of a particle tracking based approach.

## 1.5 Thesis' outline

The rest of the work is organized as follows: in the Chapter II we present the standard rheological methods used to study the yielding transition for

yield stress fluids.
In Chapter III we discuss real space microscopy, light scattering and digital Fourier microscopy as techniques to characterize the microscopic state of a sheared samples.
In Chapter IV we present some innovations of DDM developed in this work and we describe the analysis methods necessary to apply DDM to sheared samples.
Chapter V regards samples, instruments and experimental protocols.
In Chapter VI we present and discuss all the experimental results regarding the link between the mechanical properties and the microscopic observables, both in the linear and in the *yielding* regime. A conclusive chapter, with a summary of the most important results extracted from this work, follows.

# Chapter 2

# Macroscopic investigation of yielding with shear rheometry

In this chapter we provide a description of shear rheology as a tool for probing the process of material yielding at the macroscopic scale. Yielding occurs when the material is mechanically brought out of its linear response regime, which causes the mechanical response of the material to become very sensitive to the way the mechanical tests are conducted. This sensitivity requires choosing a suitable definition of mechanical response, which will be different for different types of tests. We will focus here on two types of mechanical tests that are quite popular: the creep test, which is intrinsically a stress-controlled test, and the strain controlled oscillation test. In both cases we will describe first the response in the linear regime to then focus on the transition to non-linearity and yielding.

## 2.1 Rotational shear rheometers

Mechanical shear tests on soft materials are typically conducted with rotational shear rheometers, very sophisticated instruments that are nowadays used both in academic and industrial laboratories. In a rotational shear rheometer, the sample is typically confined between a fixed surface and a free-to-rotate surface Fig.2.1, whose rotation implies a shear deformation of the material sample comprised between the two surfaces. In a stress-controlled experiment, the rheometer can exert a controlled torque $\vec{T}$ on the mobile surface and measure its angular displacement $\Theta$, whereas in a strain-controlled experiment the angular displacement is imposed and the reaction torque is measured.
If $\vec{T}$ is the momentum applied by the rheometer and $\vec{T}_R$ is the reaction momentum developed by the deformed material, the equation for the force momenta is

$$\vec{T} + \vec{T}_R = I\ddot{\vec{\Theta}} \tag{2.1}$$

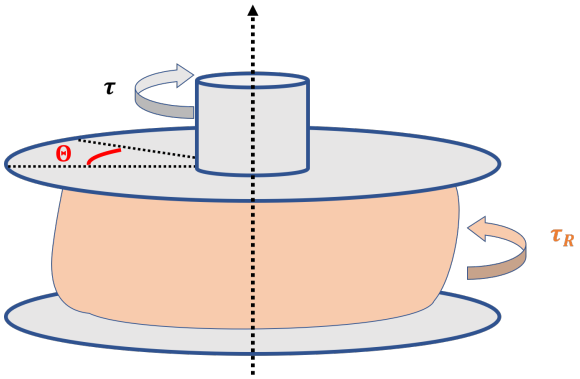


**Figure 2.1:** Schematic of a shear rheological experiment in a **parallel rotating plate** geometry. $\vec{T}$ is the torque applied (or measured) by the rheometer, $\Theta$ is the angular displacement, $\vec{T}_R$ is the reaction torque of the material, these quantities are related by $\vec{T} + \vec{T}_R = I\ddot{\vec{\Theta}}$.

where $I$ mirrors the inertia of the instrument (the inertia of the material is usually negligible). Imposing $\vec{T}$ (or $\Theta$) and measuring $\Theta$ (or $\vec{T}$) one can obtain $\vec{T}_R$ as a characterization of the material response. The relation between the raw quantities $\{\vec{T}_R, \Theta, \dot{\Theta}\}$ and the quantities used in the material's constituent equations $\{\sigma, \gamma, \dot{\gamma}\}$ depends on the experimental geometry.
The relation between the reaction torque $\vec{T}_R$ and the local reaction stress $\sigma_R$ is

$$\vec{T}_R = \int_0^R 2\pi r^2 \sigma_R(r) dr \tag{2.2}$$

and we generally talk of stress-controlled (rather than torque controlled) experiments. Moreover for the following discussion we will consider only that geometries producing homogeneous stress and strain fields, if the material is not heterogeneous. If this hypothesis is verified the relations $\vec{T} \rightarrow \sigma_R$ and $\Theta \rightarrow \gamma$ are straightforward, and we will refer directly to the quantities of interest $(\sigma, \gamma, etc...)$ rather than the raw quantities that one really controls in a rheological experiment.

## 2.2 Stress-controlled experiments

### 2.2.1 Linear Creep Compliance

For sufficiently small applied stresses the equation describing the material response *i.e.* the relation between the stress and the strain is given by

$$\gamma(t) = \int dt' J(t - t')\dot{\sigma}(t') \tag{2.3}$$

where the system response is encoded in the **linear creep compliance** $J$. The linearity of Eq.2.3 means that if $\gamma_1(t)$ is the response to an applied

stress $\sigma_1(t)$, and $\gamma_2(t)$ the response to $\sigma_2(t)$, the response to $\sigma_1(t) + \sigma_2(t)$ is $\gamma_1(t) + \gamma_2(t)$. In this regime, the response function does not depend on the perturbation. By contrast, during *yielding* the applied perturbation is so strong to drive the system out of equilibrium, and system's response does depend on the perturbation.

The simplest case one can imagine is the imposition of a **step stress** of amplitude $\sigma_0$, which is described by the function $\sigma = \sigma_0 \Theta_H(t)$, where $\Theta_H$ is the Heaviside step function. The time-derivative of the imposed stress is then easily written as $\dot{\sigma} = \sigma_0 \delta_D(t)$ where $\delta_D$ is Dirac's delta function. If we insert this expression in Eq. 2.3 we immediately obtain

$$\gamma(t) = \int dt' J(t - t') \delta_D(t') \sigma_0 = J(t) \sigma_0, \tag{2.4}$$

which provides a direct connection between the strain and the stress amplitude. Once the strain is measured one can estimate the linear creep compliance $J(t)$ of the material by calculating the ratio between $\gamma(t)$ and the stress amplitude $\sigma_0$.

**Ideal solid response -** For a Hookean solid the response to a stress step is simply a strain step. Equation 2.3 becomes:

$$\gamma = J_s \sigma_0 \tag{2.5}$$

i.e. the creep compliance for an ideal solid is a constant.

**Ideal liquid response -** For a Newtonian liquid the response to a step stress is a flow at constant strain rate:

$$\gamma(t) = \dot{\gamma}_0 t = J_f \sigma_0 \tag{2.6}$$

the creep compliance is a linear function of time

$$J_f = \frac{\dot{\gamma}_0}{\sigma_0} t$$

and it's slope is the inverse of the viscosity:

$$\dot{J}_f = \frac{\dot{\gamma}_0}{\sigma_0} = \frac{1}{\eta} \tag{2.7}$$

A richer mechanical model is obtained combining $n$ simple (solid or liquid) elements in *series* and/or in *parallel*:

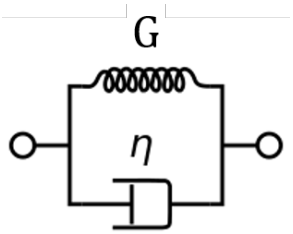


**Figure 2.2:** The Kelvin-Voigth model is obtained combining in parallel an ideal liquid with viscosity $\eta$ and an ideal solid with elasticity $G$.

**Kelvin-Voigt model's response -** The Kelvin-Voigt model is obtained as an elastic (elasticity $G$) and a liquid (viscosity $\eta$) elements joined in parallel Fig.2.2. For this element it is easy to compute the deformation response when a stress $\sigma_0$ is applied. Through simple calculation

$$\begin{cases} \gamma_{liquid} = \gamma_{solid} \\ \sigma_{liquid} + \sigma_{solid} = \sigma_0 \end{cases}$$

results in

$$\gamma(t) = \gamma_\infty\left(1 - e^{-\frac{t}{\eta/G}}\right) = \sigma_0/G \cdot \left(1 - e^{-\frac{t}{\eta/G}}\right). \tag{2.8}$$

The ratio between viscosity and elasticity defines a characteristic time of the system $\tau = \eta/G$ :when $t/\tau \ll 1$ the system behaves like a liquid:

$$\gamma(t) = \frac{\sigma_0}{\eta} t$$

when $t/\tau \gg 1$ the system behaves like a solid:

$$\gamma_\infty = \sigma_0/G$$

### 2.2.2 Non-Linear Creep Compliance

While the creep compliance defined in the previous paragraph is a *linear* property of the material, the phenomenon of yielding is strictly *non-linear*. In Chapter 1, we have seen that for small stress an Yield Stress Fluids (YSF) behave like solids, whereas for larger stresses they behave like liquids. In terms of creep compliance we can say that the creep compliance of an YSF

$$J(t) = \frac{\gamma(t)}{\sigma_0}$$

**does** depend on the applied stress $\sigma_0$. On the other hand, the generalization of equation 2.3 to the yielding regime is not trivial, will clearly be non-linear and will exhibit features of both the solid- and the liquid-like state.

Another issue, which is intrinsic of non-linear creep tests, is the loss of stationarity, as the properties of the material keep changing over time. In particular, the same value of the applied stress produces different deformation effects depending on the application time. As a consequence, while the *linear creep compliance* $J_L$ is a function of the time difference $(t - t')$, the *non-linear creep compliance* will depend on both times i.e. $J_{NL}(t, t')$. As already mentioned (Chapter 1) this fact impairs a statistically robust microscopic characterization of the phenomenon.

## 2.3 Strain controlled experiments

In these experiments, a controlled strain profile is imposed and the reaction stress is measured.

### 2.3.1 Linear visco-elastic moduli

For a *small* imposed *strain* we can write a relation analogous to 2.3:

$$\sigma(t) = \int dt' G(t - t')\dot{\gamma}(t') \tag{2.9}$$

where $G$ is called the **stress relaxation modulus**, and has analogous mathematical properties of the linear creep compliance $J$. The name of the response function $G$ comes from the fact that it describes how the stress relaxes after a sudden strain step $\gamma(t) = \gamma_0 \Theta_H(t)$ is applied at time $t = 0$:

$$\sigma(t) = G(t)\gamma_0.$$

In the Fourier domain, thanks to linearity and stationarity, Eq. 2.9 simplifies to:

$$\tilde{\sigma}(\omega) = \tilde{G}(\omega)\tilde{\dot{\gamma}}(\omega) = \tilde{G}(\omega)i\omega\tilde{\gamma}(\omega). \tag{2.10}$$

We now define $\tilde{G}^*(\omega) = \tilde{G}(\omega)i\omega$ obtaining:

$$\tilde{\sigma}(\omega) = \tilde{G}^*(\omega)\tilde{\gamma}(\omega) \tag{2.11}$$

and the real and imaginary parts of $\tilde{G}^*$ are the **elastic** and the **viscous moduli** already defined in the first chapter 1.1.

Relation 2.11 depends only on one frequency: this means that if the deformation is an harmonic function with frequency $\omega$ also the stress will be an harmonic function with the same frequency. This implies that, as long as the linear response is considered, we can study the response to a harmonic perturbation without loss of generality. If a harmonic deformation

$$\gamma(t) = \gamma_0 \cos(\omega t)$$

is applied, the stress response in the linear regime will be sinusoidal, with an amplitude $\sigma_0 = |G(\omega)|\gamma_0$, and will have a delay $\delta$ such that

$$\delta = \text{atan}\Big(\frac{\mathcal{I}m\big(G(\omega)\big)}{\mathcal{R}e\big(G(\omega)\big)}\Big)$$

$$\sigma(t) = |G(\omega)|\gamma_0 \cos(\omega t - \delta)$$

We will now discuss some paradigmatic cases for which the corresponding response functions $G^*(\omega)$ will be provided.

**Solid response -** For a Hookean solid in the linear regime, the stress is proportional to the strain and there is no effect of the shear rate. This implies that the stress and the deformation are perfectly in phase, *i.e.* that $G^*$ is real:

$$\sigma(t) = G'\gamma_0 \cos(\omega t). \tag{2.12}$$

So an ideal elastic solid has a *real* and *frequency-independent* response function

$$G^* = G' \in \mathbb{R} \tag{2.13}$$

**Liquid response -** A Newtonian liquid exerts an opposing stress proportional to the strain rate $\dot{\gamma}$. For a harmonic deformation we have

$$\sigma(t) = \eta\dot{\gamma} = -\eta\omega\gamma_0 \sin(\omega t) \tag{2.14}$$

meaning that Newtonian liquids have *imaginary* response functions $G^*(\omega)$ and the dependence on frequency is linear:

$$G^* = iG'' = i\eta\omega \in \mathbb{I}. \tag{2.15}$$

**Maxwell fluid response -** A Maxwell fluid is obtained combining an ideal liquid and an ideal solid element in series Fig.2.3. The response to an

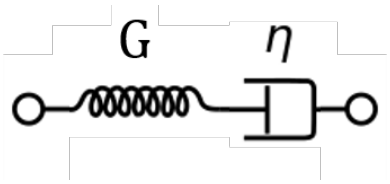


**Figure 2.3:** Schematic mechanical model of a Maxwell fluid obtained combining in series an ideal liquid (viscosity $\eta$) and an ideal solid (elasticity $G$).

imposed deformation is straightforward to compute

$$\begin{cases} \gamma_{liquid} + \gamma_{solid} = \gamma \\ \sigma_{liquid} = \sigma_{solid} = \sigma_0 \end{cases}$$

the system is easily solved in the Fourier space and with few algebraic passages results in

$$\begin{cases} G' = \frac{G\eta^2\omega^2}{G^2+\omega^2\eta^2} \\ G'' = \frac{G^2\eta\omega}{G^2+\omega^2\eta^2} \end{cases}$$

and in particular the phase $\delta$:

$$tan(\delta) = \frac{G}{\omega\eta}. \tag{2.16}$$

In the high frequency limit $\delta \to 0$ the system has a solid-like behavior, while at low frequency $\delta \to \pi/2$ the system has a liquid-like behavior.

**Lissajous plots** A convenient way to look at the response function in oscillatory condition is to plot the stress as a function of the strain or as a function of the strain rate. This type of plot is commonly referred to as Lissajous plot. In the linear regime, the plots $(\sigma/\sigma_0)$ as a function of $(\gamma/\gamma_0)$

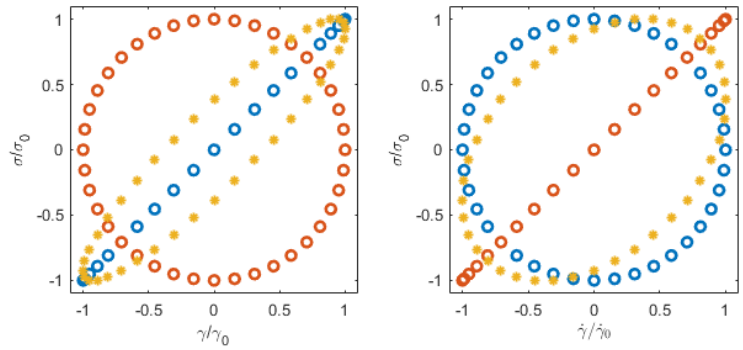


**Figure 2.4:** Schematic of the Lissajous plots for an ideal solid (●) $\delta = 0$, for a Newtonian fluid (●) $\delta = \pi/2$, and for a generic visco-elastic material ( ●) $\delta \in (0, \pi/2)$.

are ellipses described by the equations of the form:

$$\left(\frac{\sigma}{\sigma_0}\right)^2 + \left(\frac{\gamma}{\gamma}\right)^2 = (\sin\delta)^2 + 2\left(\frac{\sigma}{\sigma_0}\right)\left(\frac{\gamma}{\gamma_0}\right)\cos\delta \tag{2.17}$$

Where $\delta$ is the *dephasing* between the strain $\gamma$ and the stress $\sigma$.
Interestingly, the dissipated work per unit volume during a deformation cycle can be estimated as the area enclosed by the curve $\sigma(\gamma)$ equals :

$$W_D = \int \sigma(\gamma) d\gamma \tag{2.18}$$

that in the linear regime gives

$$W_D = A = \pi\sigma_0\gamma_0 \sin\delta \tag{2.19}$$

from which it appears clearly how an ideal solid ($\delta = 0$) and an ideal liquid ($\delta = \pi/2$) correspond to zero and maximum dissipation, respectively.

### 2.3.2 Non-linear oscillatory test: LAOS

When the deformation amplitude exceeds a certain threshold $\gamma_{lin}$ the stress response ceases to be linear, and, in case of oscillatory strain, frequencies larger than the imposed one may appear.

Interestingly, LAOS tests make it possible to reach a stationary condition even when the response is non-linear, which is a considerable advantage over non-linear creep experiments. When the stationary condition is reached, $\sigma(t)$ is a periodic function with the same period of the imposed deformation, which is a very appealing property for a statistically consistent characterization of the microscopic dynamics in the *non-linear regime*.On the other hand the mathematical description of the response function in the non-linear regime is much more complex than in the linear regime, the separation of the viscous and elastic parts becomes more tricky, since the functional form of the response is generally unknown, and the physical interpretation of the data may be controversial. We briefly sketch in the following some of the possible approaches.

**The series expansion approach -** In a series expansion approach one usually chooses a suitable set of functions that are used to reconstruct, by summing consecutive terms of a series, the original function. Usually, in non-linear rheology one considers a limited number of terms and attempts a physical interpretation of the non-linear moduli.

A first possibility is to expand the stress in powers of the strain $\gamma$

$$\sigma(t) = \sum_{p,odd}^{} \sum_{q,odd}^{p} \gamma_0^p [a_{pq}(\omega)\sin(q\omega t) + b_{pq}(\omega)\cos(q\omega t)]. \tag{2.20}$$

The base of this expansion has the form $\gamma_0^p$ times $\sin(q\omega t)$ (or $\cos(q\omega t)$) where $p$ and $q$ are integer odd numbers, and the coefficients $a_{pq}(\omega)$ and $b_{pq}(\omega)$ are the result of the projection of the stress on the basis' elements. Because of symmetry properties of $\sigma(\gamma, \dot{\gamma})$, only odd powers of $\gamma$ and $\dot{\gamma}$ have non-zero coefficients.

Another possibility is to expand the stress by using a *Fourier series*

$$\sigma(t) = \gamma_0 \sum_{n,odd} [G'_n(\omega,\gamma)\sin n\omega t + G''_n(\omega,\gamma)\cos n\omega t] \tag{2.21}$$

where the moduli $G'_n$ and $G''_n$ depends on both $\omega$ and $\gamma$.

Other series expansions are possible but we will not enter a more detailed discussion of this approach for reasons that will be soon clearer.

**The first harmonic approach -** Some insight in the non-linear response is obtained by inspecting the behaviour of the first harmonic of the visco-elastic moduli $G'_1(\gamma_0)$ and $G''_1(\gamma_0)$ in Eq. 2.21 as a function of $\gamma$ Fig.2.5. These quantities are obtained projecting the stress on the strain and on the strain rate:

$$G'_1(\gamma_0) = \frac{1}{\gamma_0}\oint \sigma(t)\cdot\gamma(t)dt \tag{2.22}$$

and

$$G''_1(\gamma_0) = \frac{1}{\omega\gamma_0}\oint \sigma(t)\cdot\dot{\gamma}(t)dt \tag{2.23}$$

The linear region is where the visco-elastic moduli do not depend on the amplitude of the imposed strain $\gamma_0$. Yielding is expected to be accompanied by an increase in the dissipative response. While deviations from the linearity in the elastic modulus may just indicate non-linear elasticity.

There are different ways to identify the yielding point with this test, that

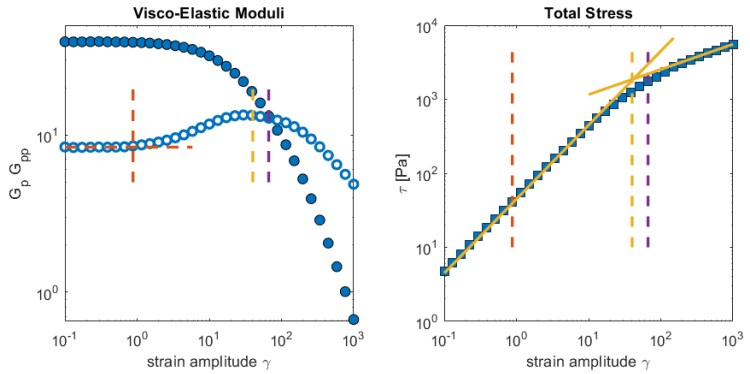


**Figure 2.5:** Left panel: viscoelastic moduli for a typical LAOS test, the red dashes lines sign (in both panel) deviation of $G''$ from linearity, the violet lines sign (in both panel) where $G' = G''$. In the right panel total stress as function of $\gamma$, the yellow line are a linear fit for small amplitudes and a power law fit at high amplitude, the vertical dashed lines marks the interception of the two fits.

are marked by vertical dashed lines in Fig.2.5 and described below[1]:

[1]We are assuming that the first harmonic of the visco-elastic moduli well represents the complete mechanical response of the material.

- We can identify the value $\gamma_P$ as the shear amplitude **for which we observe a deviation of $G''$ from its constant low-$\gamma$ value** (dashed red line). This point marks the onset of increased dissipation. Conversely, deviation from linearity of $G'$ does not necessarily imply the presence of plasticity (see for instance the right panel in Fig.2.5).

- Another possible criterion is to mark the onset of yielding at the **crossover point**: the strain value $\gamma_c$ for which $G'' > G'$, the justification being that the system is more liquid-like than solid-like. In our view, this criterion is not ideal, as all we can say about this point is that the energy stored elastically is equal to the energy dissipated on the other hand it is a quite widespread criterion.

- Another possibility is to consider the stress-strain relation (right panel). The relation $\sigma(\gamma)$ has a starting linear regime ans it deviates at $\gamma_{NL}$. At larger $\gamma$ we can fit the stress-strain relation with a power-law Fig.2.5, right panel continuous yellow lines]. We can define $\gamma_{NL}$ as the point where the two fits intersect (vertical yellow dashed line) [79],[61]. This point marks the transition from linear to non-linear, but this not necessarily correspond to the onset of plastic behaviour. The interpretation of the meaning of this point is not clear since it is more an operational than a physical definition.

**The symmetry approach:** A different approach consists of exploiting the symmetry of the stress-strain relation to separate the stress in a single valued function of the *strain* and a single valued function of the *strain rate*:[2]

$$\sigma(\gamma, \dot{\gamma}) = \sigma_E(\gamma) + \sigma_V(\dot{\gamma}) \tag{2.31}$$

[2]Since

$$\sigma(\gamma, \dot{\gamma}) = -\sigma(-\gamma, -\dot{\gamma}) \tag{2.24}$$

one can define

$$\sigma_E(\gamma, \dot{\gamma}) = \frac{\sigma(\gamma, \dot{\gamma}) + \sigma(\gamma, -\dot{\gamma})}{2} \tag{2.25}$$

that is an even function of the strain rate and an odd function of the strain amplitude:

$$\sigma_E(x, y) = \sigma(x, y) + \sigma(x, -y) = \sigma(x, -y) + \sigma(x, y) = \sigma_E(x, -y) \tag{2.26}$$

$$\sigma_E(-x, y) = \sigma_E(-x, -y) = \sigma(-x, -y) + \sigma(-x, y) = -\sigma_E(x, y) \tag{2.27}$$

Similarly

$$\sigma_V(\gamma, \dot{\gamma}) = \frac{\sigma(\gamma, \dot{\gamma}) + \sigma(-\gamma, \dot{\gamma})}{2} \tag{2.28}$$

is an odd function in the stain rate and an even function in the strain amplitude. From these symmetry properties it follows that

$$\oint \sigma_E(\gamma, \dot{\gamma}) d\gamma = 0 \tag{2.29}$$

implying that $\sigma_E$ is indeed a function of $\gamma$ alone and the same argument can be applied on $\sigma_V$ to show that it is a function of $\dot{\gamma}$. In this way one has a recipe to decompose the

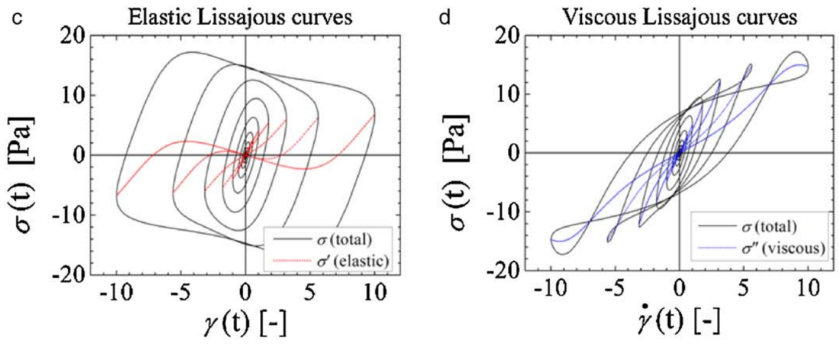


**Figure 2.6:** Lissajous Plots and stress decomposition . If the Lissajous plots are symmetric it is possible to decompose the stress as a sum of two single valued functions $\sigma = \sigma_E(\gamma) + \sigma_V(\dot{\gamma})$. In the left panel in red the elastic stress, in the right panel in blue the viscous stress. Adapted from [58].

where the strain amplitude dependent part coincides with the **elastic** part $\sigma_E$, and the strain rate dependent part with the **viscous** one $\sigma_V$.
Once the stress is decomposed into an elastic and a viscous part one could attempt defining some phase-dependent non-linear response moduli

$$\sigma(t) = G'(t)\gamma_0 + G''(t)\dot{\gamma}_0 \tag{2.32}$$

but this definition leads to some contradictions such as negative valued elastic moduli Fig.2.6, left panel.

**The equilibrium point approach -** The just-mentioned contradictory result may be due to the fact that the equilibrium point defined by:

$$\gamma_{eq}: \qquad \sigma(\gamma_{eq}, 0) = 0 \tag{2.33}$$

is continuously changing during the non-linear deformation cycle. This concept has been clarified by Rogers and coworkers [103], who distinguished between the *macroscopic strain*, or strain in the lab frame of reference $\gamma_{\text{Lab}}$ and the *microscopic strain*, or strain in the sample frame of reference $\gamma_{\text{Samp}}$. Rogers and coworkers describe the stress strain relation with this equation:

$$\sigma(t) = G'(t) \cdot \big(\gamma(t) - \gamma_{eq}(t)\big) + G''(t) \cdot \frac{\dot{\gamma}(t)}{\omega} + \sigma_y(t) \tag{2.34}$$

where all the functions are periodic in time with periodicity $\mathcal{T}$. $G'(t)$ and $G''(t)$ are functions of time, to account for the fact that at different phases

stress in its elastic and viscous parts.

$$\sigma = \sigma_E(\gamma) + \sigma_V(\dot{\gamma}) \tag{2.30}$$

of the deformation cycle the sample's response function changes. $\sigma_y$ is the yield stress, meant as the elastically stored stress, that is also a function of the phase. And $\gamma_{eq}$ defined by 2.33. The equation is now complete but undetermined since we have four phase dependent unknown quantities: $\gamma_{eq}$, $\sigma_y$, $G'(t)$ and $G''(t)$.

We notice that whenever $\gamma_{eq} \neq 0$, as likely is the case in yielding experiments, any approach attempting to define an in cycle response is impaired.

Even though a description of the mechanical response of the material within the cycle may be out of reach, we can still describe the mechanical response on a whole cycle without loss of information due to an approximated description of the stress.
It is thus possible to refer to non-projected, period-averaged quantities, such as the dissipated energy per unit volume per cycle

$$W_D = \int \sigma(\gamma) d\gamma$$

or analogously the *elastic work* per unit volume per cycle

$$W_E = \int \sigma(\dot{\gamma}) d\dot{\gamma} \tag{2.35}$$

From these we can define, in analogy with the linear regime, non-linear elastic and viscous moduli:

$$G'_{NL} = \frac{W_E}{\pi \gamma_0^2} \qquad G''_{NL} = \frac{W_D}{\pi \gamma_0^2} \tag{2.36}$$

# Chapter 3

# Optical probes of the microscopic side of yielding

For a physical system at finite temperature, physical quantities fluctuate both in space and in time. These fluctuations are particularly relevant for soft matter. For example, fluctuations in the position of the elementary constituents of a soft material may change considerably compared to their size ($\sim \mu m$) during the observation time ($\sim s$). As a consequence, any treatment of soft materials needs to consider average quantities, as well as their fluctuations. A typical example is the position of a particle, for which, beyond the average $\langle \vec{x}(t) \rangle_t$, we often consider the mean squared displacement $\langle |\Delta\vec{x}(t, \Delta t)|^2 \rangle_t = \langle |\vec{x}(t) - \vec{x}(t + \Delta t)|^2 \rangle_t$.

In this chapter, we will discuss selected optical approaches for the characterization of the microscopic state of order and activity of soft materials, by focusing in particular on those observables that can be connected to the mechanical properties of the materials. The first part of the chapter will be devoted to providing the needed definitions, while in the second one we will present and compare selected optical methodologies to quantify the observables of interest. Concerning optical approaches we can mainly distinguish two families: imaging (operating in the *real-space*) and scattering (operating in the *reciprocal-space*). As far as real-space is concerned, we will present the microscopy approach with a Particle Tracking-oriented point of view. We will then describe light scattering to eventually outline an intermediate approach that allows to extract light-scattering-like information from microscopy videos: Differential Dynamic Microscopy (DDM).

## 3.1 Microscopic observables for the description of soft materials

In this section, we define the typical observables used to describe the microscopic state of a soft matter system. As a guiding thread, we will use throughout the section a *colloidal glass* of hard-spheres.

**Structural observables:** Every material is composed of elementary building blocks. Molecular materials are made of molecules. Our colloidal glass is made of colloidal particles. Without loss of generality we can refer to the elementary constituents as particles. As long as the number of particles is large enough, statistical mechanical tools can be used for their description. One example is the *particle number density*

$$c(\vec{x},t) = \sum_{n=1,\dots,N} \delta_D(\vec{x} - \vec{x}_n(t)) \tag{3.1}$$

where $\delta_D(\vec{x})$ is the Dirac's delta function, $N$ is the total number of particles and $\vec{x}_n(t)$ is the position of the n-th particle at time $t$. The probability of finding two particles at a distance $\Delta\vec{x}$ from each other is given by the **pair correlation function**:

$$g(\vec{r}) = \frac{1}{\langle c \rangle} \Big\langle c(\vec{x}+\vec{r},t)c(\vec{x},t) \Big\rangle \tag{3.2}$$

where $\langle ... \rangle$ is an ensemble average.

The pair correlation function captures important configurational features

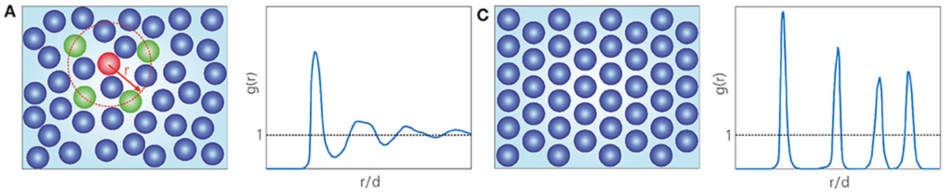


**Figure 3.1:** Configuration (first and third panel) and pair-correlation function (second and fourth) for the molecules of a liquid (A) and of a crystal (C). The pair correlation function exhibits some oscillation. The configurations where $g(r) > 1$ are more likely compared to a random distribution of distances, the ones with $g(r) < 1$ and some that are less likely compared to random distribution. In the liquid state the pair correlation function goes to an asymptotic value of 1 for $r >> d$, sign of lack of long range order. Crystalline solids show long range ordering and long range correlation and anti-correlations continue to alternate for $r$ indefinitely large. Adapted from [59].

of the system. In Fig.3.1 we sketch the configuration of a liquid (A) and of a crystalline solid (C), accompanied by respective pair correlation functions. For randomly distributed independent particles $g \equiv 1$; if $g(r)$ is larger

(smaller) than one two particles are more (less) likely to stay at distance $r$ compared to the random case. The $g(r)$ of a crystal has long-ranged oscillations, mirroring positional order over large distance, whereas in fluids $g(r)$ goes to one for large $r$.
Equivalent information is carried by the **static structure factor**, which is a close relative of the Fourier transform of $g(r)$ Fig.3.2, right panel:

$$S(\vec{q}) = 1 + \langle c \rangle \int_V d\vec{r}\; e^{-i\vec{q}\cdot\vec{r}} g(\vec{r}) \tag{3.3}$$

For an equilibrium system of diluted particles interacting *via* a two-body potential $w(r)$, one can derive $w(r)$ from

$$w(r) = -k_B T\ \log g(r). \tag{3.4}$$

From $g(r)$ we can also derive the **isothermal compressibility** $\chi_T$, which gives the macroscopic response in terms of pressure to a change of volume at fixed temperature:

$$\chi_T = \left.\frac{\partial P}{\partial V}\right|_T = \frac{1}{\rho k_B T}\left(1 + \rho \int_V d\vec{r}[g(\vec{r}) - 1]\right) \tag{3.5}$$

Similar expressions can be written also for the shear modulus and for other linear response properties [86], providing an overall robust link between macroscopic properties of the system and the microscopic structure. However, the hypotheses for the validity of these results are violated in our cases of interest. In particular:

- our systems (glasses, gels etc.) are typically **out-of-equilibrium** and in a kinetically arrested state
- our systems are close to yielding, which is an **intrinsically non-linear** phenomenon

To get a feeling about how much the violation of the equilibrium hypothesis can impair the validity of 3.5 (and similar) we can consider the example of the liquid-glass transition. Across liquid-glass transition the shear modulus changes of several orders of magnitude, while the microscopic static features are essentially unchanged Fig.3.2.

By contrast, a qualitative difference is observed in the particle dynamics: in a solid, the particles are bound and neighbour particles are not allowed to exchange their position, whereas in a system exhibiting a liquid-like behaviour, thermal fluctuations can induce reciprocal motion and positional exchanges between particles.

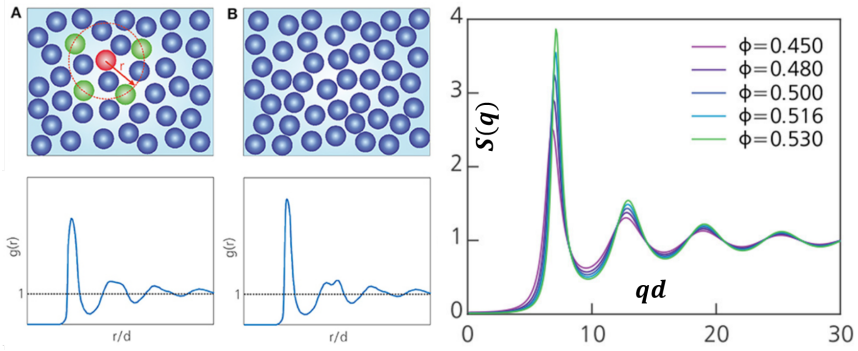


**Figure 3.2:** Configuration (A,B top line) and pair-correlation function (A,B bottom line) for a liquid (A) and a glass (B). The liquid and the glass are indistinguishable from a structural point of view. Right column: Static structure factor across the glass transition. The transition, defined as that point of the phase diagram where the viscosity reaches $\eta = 10^{12} Pa \cdot s$, occurs at $\phi = 0.516$. For lower density the system is in a fluid state ($\phi = 0.450$), and in a glass state for higher density $\phi = 0.530$. The glass transition occurs with no structural sign, since the structure factor has the same qualitative features above and below it. Adapted from [59].

**Dynamic observables:** The generalization of Eq.3.2, which gives the probability of finding two particles at a certain distance after a certain time delay, is the **van Hove distribution function**:

$$g(\vec{r}, \Delta t) = \frac{1}{\langle c \rangle} \langle c(\vec{x} + \vec{r}, t + \Delta t) c(\vec{x}, t) \rangle. \tag{3.6}$$

The van Hove distribution function is generally written as the sum $g = g_{\text{self}} + g_{\text{distinct}}$ of two contributions: the *self* part, that gives the probability for a particle to undergo a displacement $\vec{r}$ in a time lag $\Delta t$, and a *distinct* part, that accounts for inter-particle correlations. The standard output of a **Single Particle Tracking** experiment is $g_{\text{self}} \equiv P(\vec{r}, \Delta t)$, *i.e.* the particle displacement probability distribution[1]. A good proxy of the colloidal glass transition is the width of $P$ as a function of time Fig.3.3, the so called **mean square displacement** (MSD)

$$\langle |\Delta \vec{x}(\Delta t)|^2 \rangle = \langle |\vec{x}(t) - \vec{x}(t + \Delta t)|^2 \rangle \tag{3.7}$$

where $\langle ... \rangle$ stands for an average over the distribution $P(\vec{r}, \Delta t)$. We represent in Fig.3.3 different dynamical regimes for a super-cooled colloidal liquid, a state with features that are intermediate between those of a liquid and a solid. On time-scales shorter than the so-called $\beta$-relaxation time $\tau_\beta$, the particles are caged by their neighbours, as we can see from the plateau in the mean square displacement: positional exchanges are not likely and on these time-scales the system has a solid-like behaviour. On longer time-scales,

[1] See Sect. 3.2 below.

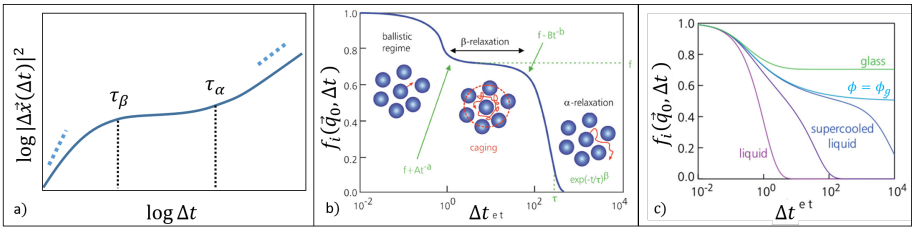


**Figure 3.3:** Dynamics of the particles in a supercooled colloidal liquid represented by (a) the *mean square displacement*, and (b) the intermediate scattering function $f_i(q_0, \Delta t)$ 3.9, $q_0$ corresponds to the peak of the structure factor $S(q)$ Fig.3.2, right panel. The mean square displacement is a *single particle* property, while the intermediate scattering function usually[2] quantifies the *collective* dynamics. In both correlators, it is possible to appreciate the initial *in-cage* ballistic dynamics and the cage confinement, referred to as $\beta$-*relaxation* process, after very long time a particle is able to diffuse away from the cage $\alpha$-*relaxation*. (c) Across the liquid-glass transition, the intermediate scattering function at $q = q_0$ shows qualitative differences. A supercooled liquid is an out-of-equilibrium state where the ergodicity is not broken yet. Upon deeper cooling, the system becomes a glass, ergodicity is lost and no out of cage diffusion is observed within the experimental time. Adapted from [59].

inter-particle positional exchanges are allowed, the mean square displacement has a diffusive-like behaviour and the system flows like a liquid. The lifetime of this intermediate plateau is the so-called $\alpha$-relaxation time $\tau_\alpha$, which exceeds any reasonable experimental time when the system reaches the *non-ergodic* state that we define as glass. We note that for volume fractions smaller than the glass transition value, when the system is a liquid, no intermediate plateau is observed.

Despite the appeal of a *real-space* description it is often more convenient to describe the system in terms of the density Fourier modes, which are encoded in the spatial Fourier transform of the van Hove distribution function, known as the **intermediate scattering function**:

$$F(\vec{q}, \Delta t) = \frac{1}{\langle c \rangle} \langle c(\vec{q}, t + \Delta t) c^*(\vec{q}, t) \rangle \tag{3.8}$$

and in its normalized version

$$f_i(\vec{q}, \Delta t) = \frac{F(\vec{q}, \Delta t)}{F(\vec{q}, 0)} \tag{3.9}$$

The intermediate scattering function that is defined by Eqs. 3.8 and 3.9, which is the typical output of scattering experiments (see 3.3), contains both self and distinct contributions. As a consequence, it carries information on the relaxation of the *collective modes* of the system, quantifying how much the system at time $t + \Delta t$ resembles the system at time $t$ on a certain length scale $\Lambda = 2\pi/q$.

**Passive microrheology:** It is interesting to note that the connection between the microscopic dynamics and the mechanical properties of a soft system can in some circumstances be made fully quantitative. This is the case of **microrheology**. To understand what microrheology is, let us consider the simple example of a micrometric particle dispersed in a Newtonian liquid. Such particle will undergo a Brownian motion characterized by a mean square displacement increasing linearly with $\Delta t$

$$\langle |\Delta \vec{x}(\Delta t)|^2 \rangle_t = 2ND\ \Delta t \tag{3.10}$$

where $N$ is the number of dimensions considered in the calculation of the mean square displacement and $D$ the diffusion coefficient, that follows the Stokes Einstein relation

$$D = \frac{k_B T}{6\pi\eta a} \tag{3.11}$$

where $k_B$ is Boltzmann's constant, $T$ is the temperature, $a$ is the particle radius and $\eta$ is the viscosity of the Newtonian liquid.
Eq.3.11 can be inverted to give

$$\eta = \frac{k_B T}{6\pi D a} \tag{3.12}$$

which enables one obtaining an estimate of the viscosity from the study of the Brownian motion of a probe particle of known radius. This result is telling us that, even though the viscosity characterizes the macroscopic response of the system to a macroscopic shear deformation, we can measure it also when the mechanical perturbation is induced microscopically by thermal fluctuations.

This result was generalized in a seminal work of Mason and Weitz [80], who proved that the erratic motion of a micrometric particle embedded in a visco-elastic material is ruled by the *Generalized Stokes-Einstein relation* (GSER):

$$\langle \Delta \mathbf{r}^2(\Delta t) \rangle = 2N \frac{k_B T}{6\pi a} J(\Delta t) \tag{3.13}$$

where the inverse of the viscosity has been replaced by the linear creep compliance $J(t)$ 2.3.
This result holds if the *tracers particles* are identical, monodisperse, non-interacting spheres and if they are large enough with respect to material's micro structure, so that they interact with an homogeneous medium. This is the essence of **passive microrheology** that enables one characterizing the linear mechanical properties of soft materials by measuring mean square displacements in a micro-scale rheometer "fueled" by thermal fluctuations.

## 3.2 Microscopy and Particle Tracking

Microscopy is an imaging technique, as it is meant to provide a faithful reconstruction of the spatial configuration of the system on a suitable two-dimensional detector. Following [49], we can describe our sample via a suitable concentration $c(\vec{x})$ that, under quite general and non-restricting hypotheses (basically that the sample is a weakly scattering object) is mapped onto the image intensity

$$I(\mathbf{x}, t) = \int dz' \int d\mathbf{x}' \; c(\mathbf{x}', z', t) K(\mathbf{x} - \mathbf{x}', z') \tag{3.14}$$

recorded by the detector. Here, $\vec{x} = [\mathbf{x}, z] = [x, y, z]$, where the $z$ axis is parallel to the optical axis, and $K$ is the Point Spread Function (PSF). Eq.3.14 states that the image is the result of

- a convolution of the PSF with the source of signal (integral on $d\mathbf{x}'$ )
- a projection (integral on $dz$ ).

In particular the PSF sets the maximum image resolution (the minimum spatial detail that one can distinguish in the image), which for optical wavelengths is of the order of a few hundred $nm$. If we are in conditions for which we can clearly *distinguish the single particles* in the image, a series of images separated by a time-gap $t_0$

$$I(\mathbf{x}, t_i) \qquad \text{with} \quad t_i = t_0 + n \cdot \tau \tag{3.15}$$

can be analyzed to obtain, for each image frame, an accurate estimate of the position of a large number (if not all) of particles in the sample. This procedure is named **Particle Tracking** [32] and occurs in practice via a sequence of steps. The first step is to identify the particles, which requires to set some parameters to identify correctly the particles of interest. Typical examples of such parameters are:

- the maximum particle diameter
- the minimum intensity for an image feature to be considered a particle (both per pixel and overall)
- the maximum aspect ratio of the particle

In practice, setting these parameters is critical and the results can change considerably for small changes in the parameters. Under typical experimental circumstances the choice of parameters is made difficult by several issues. For instance, the image of a particle depends on its position along $z$ and in particular from its distance from the focal plane Fig.3.4, central panel.
Once the position of the particles for each frame is obtained, the next step is

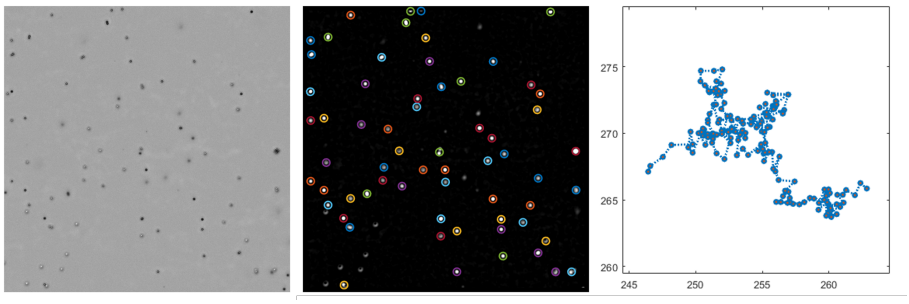


**Figure 3.4:** Microscope image of $r = 1\mu m$ colloidal particles. The image of the particles (size, contrast etc.) changes depending on their position along the optical axis: they appear white if they are above the focal plane, and black if they are below it. The objective magnification is $20X$ and the size of the image is $(121\mu m)^2$. In the central panel the same image preprocessed for the application of the tracking algorithm, the circles mark the tracked particles. In the third panel the zoom of a trajectory: the temporal series of position acquired by a certain particle.

to *link* the particles positions in order to build the trajectories,Fig.3.4, right panel. This is also a crucial step: the algorithm has a series of positions $R_i$ at time $t_n$ and $R'_i$ at time $t_{n+1}$, and all the particles at time $t_{n+1}$ need to be matched with the ones at time $t_n$. A general matching is a two-way correspondence $R_i \leftrightarrow R'_i$; and a global distance $\Delta R = \sum_i |R_i(t_n) - R'_i(t_n + 1)|^2$ is associated to each possible match. Correspondence between $R_i$ and $R'_i$ is usually found by minimizing $\Delta R$ on all the possible matches. To speed up the process one usually considers only the matches with $|R_i - R'_j| < d_{cutoff}$, which requires the definition of another user-dependent parameter.
If all these passages are correctly implemented, one obtains eventually the particles' trajectories for $N_{part}$ particles Fig.3.4:

$$\{R_j(t_i)\} \qquad\qquad j \in [1, N_{part}]$$

At this stage, the quantities that are typically computed are single particles properties, such as the self part of the van Hove distribution function, or the mean square displacement. In general one can compute also more complex correlators, like the distinct part of $g(\Delta\vec{x}, \Delta t)$, or the structure factor, the main limit being the limited statistics arising from the fact that the number of imaged particles is limited by the need of imaging a particle with several pixels.

A very popular variant of microscopy is confocal fluorescence microscopy, which offers a largely improved axial (*i.e.* in the direction of the optical axis $z$) resolution, of the order of $\sim 1\mu m$. As a result, confocal microscopy can be used to scan the sample in 3D and to build 3D images. The main idea that makes possible such a high resolution is to illuminate and collect light from the sample *"point-by-point"* [72]. The main drawback of this strategy is the relatively long time required to scan a certain volume, which makes

confocal microscopy suitable for slowly-evolving samples.

## 3.3 Light Scattering

**Figure 3.5:** Grand Central Terminal NY 1930 (photograph by Hal Morey). The sunlight, coming through the windows of Grand Central terminal, is scattered in the direction of the observer by dust particles suspended in the air.

Light Scattering is an alternative family of techniques that allow the study of microscopic structure and dynamics of a variety of systems including colloids. When light passes through refractive index inhomogeneities its propagation direction is altered Fig.3.5.
In Fig.3.6 we sketch the setup of a typical scattering experiment, in which a coherent radiation is sent onto the sample and a detector receives the intensity of the light scattered in a certain direction. A quantitative treatment of a light scattering experiment on a colloidal suspension can be provided by considering the sample as a collection of secondary sources coinciding with the particles. On a far away detector, the waves scattered by each particle superpose forming a complex interference pattern. Referring to Fig.3.6 the field scattered by two particles produce a constructive or destructive interference depending on the phase difference

$$\Delta\phi = \vec{r} \cdot (\vec{k}_s - \vec{k}_i) = \vec{r} \cdot \vec{q} \tag{3.16}$$

that is a function of the scalar product of the particle distance $\vec{r}$ with the

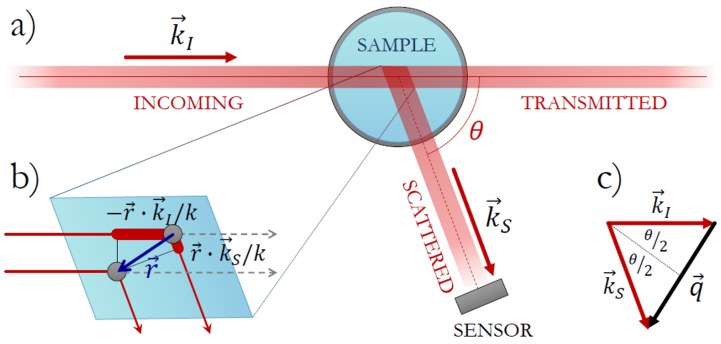


**Figure 3.6:** Scheme of a light scattering experiments as seen from the top. A coherent beam propagating along the direction of the incident wave vector $\vec{k}_I$ is sent onto a sample confined in a cylindrical capillary. Part of the incoming light is scattered by the sample in the direction of the scattered wave vector $\vec{k}_S$. In the *elastic scattering process* the modulus of the wave vectors does not change: $k_I = k_S = 2\pi/\lambda$, where $\lambda$ is the wavelength of the radiation in the solvent medium (e.g. water if the sample is aqueous colloid). The difference between the incoming and the scattered wave vectors defines the transmitted wave vector: $\vec{q} = \vec{k}_S - \vec{k}_I$ . Adapted from [1].

scattering vector $\vec{q} = \vec{k}_s - \vec{k}_i = \frac{2\pi}{\lambda}\sin(\theta/2)$.

**Static Light Scattering** If we now consider the field scattered by N particles (labeled by $j$), each one containing $M_j$ elementary scatterers

$$\vec{E}(\vec{q}) = \sum_{j=1}^{N}\sum_{l=1}^{M_j}\vec{E}_{jl}(\vec{q})e^{i\vec{q}\cdot(\vec{r}_j+\vec{r}_l^{(j)})} = \sum_{j=1}^{N}\vec{E}_j(\vec{q})e^{i\vec{q}\cdot\vec{r}_j} \tag{3.17}$$

where $\vec{r}_j$ is the position of the center of mass of the particle $j$ and $\vec{r}_l^{(j)}$ the position of the $l-th$ elementary scatterer belonging to particle $j$ with respect to $\vec{r}_j$. And $\vec{E}_j(\vec{q}) = \sum_{l=1}^{M_j}\vec{E}_{jl}(\vec{q})e^{i\vec{q}\cdot\vec{r}_l^{(j)}}$ is the field scattered by the j-th particle. Now if all the particles are identical and identically stimulated the scattered field $\vec{E}_j(\vec{q}) = \vec{E}_P(\vec{q})$ can be taken outside of the sum and the scattered intensity results in

$$I(\vec{q}) = \vec{E}(\vec{q})\cdot\vec{E}^*(\vec{q}) = |\vec{E}_P(\vec{q})|^2\sum_{j,l=1}^{N}e^{i\vec{q}\cdot(\vec{r}_j-\vec{r}_l)} = AP(\vec{q})S(\vec{q}) \tag{3.18}$$

where A is a constant depending on both instrumental (such as laser beam size and intensity) and physical quantities (such as the particle size, number density and refractive index contrast),

$$P(\vec{q}) = |\vec{E}_P(\vec{q})|^2/|\vec{E}_P(0)|^2 \tag{3.19}$$

is the particle **form factor**, accounting for particle's shape and size and

$$S(\vec{q}) = N^{-1} \sum_{j,l=1}^{N} e^{i\vec{q}\cdot(\vec{r}_j - \vec{r}_l)} \tag{3.20}$$

is the **static structure factor** that we defined in the first part of this chapter. Through some simple mathematical manipulation it is possible to show that definition 3.20 corresponds to the definition 3.3, that we recall here:

$$S(\vec{q}) = 1 + \langle c \rangle \int_V d\vec{r} e^{-i\vec{q}\cdot\vec{r}} g(\vec{r}) \tag{3.21}$$

We mention that, if needed, one can use the experimentally determined structure factor to obtain the pair correlation function, a procedure that necessarily introduces some artifacts due to the knowledge of $S(q)$ over a restricted range of wave vectors.

**Dynamic Light Scattering (DLS):** The motion of the scatterers alters the value of the scattered intensity, which exhibits temporal fluctuations:

$$I(\vec{q}, t) = AP(\vec{q})S(\vec{q}, t) = A\ P(\vec{q}) \sum_{j,l=1}^{N} e^{i\vec{q}\cdot(\vec{r}_j(t) - \vec{r}_l(t))}. \tag{3.22}$$

The lifetime of these intensity fluctuations is typically estimated by calculating the **intensity auto-correlation function**:

$$g_2(\vec{q}, t, \Delta t) = \frac{\langle I(\vec{q}, t + \Delta t) I(\vec{q}, t) \rangle}{\langle I(\vec{q}, t + \Delta t) \rangle \langle I(\vec{q}, t) \rangle} \tag{3.23}$$

that can be rewritten as

$$g_2(\vec{q}, t, \Delta t) = 1 + |g_1(\vec{q}, t, \Delta t)|^2. \tag{3.24}$$

In doing so, we have used the Siegert relation [14] to connect $g_2$ to the so-called **field auto-correlation function** $g_1$, defined as

$$g_1(\vec{q}, t, \Delta t) = \frac{\langle \vec{E}(\vec{q}, t + \Delta t) \cdot \vec{E}^*(\vec{q}, t) \rangle}{\langle |\vec{E}(\vec{q}, t)|^2 \rangle}. \tag{3.25}$$

We note that

$$f(\vec{q}, \Delta t) = \langle g_1(\vec{q}, t, \Delta t) \rangle_t. \tag{3.26}$$

where $f$ is the **normalized intermediate scattering** function 3.8, *i.e.* the Fourier transform of the van Hove distribution function 3.6. In the simple case of independent Brownian particles one has [106]

$$f(\vec{q}, \Delta t) = \exp\Big[ - \frac{\langle \Delta r^2(\Delta t) \rangle q^2)}{6} \Big] \tag{3.27}$$

but we stress that, in general, the information obtained with DLS is *collective* *i.e.* it is sensitive also to the correlated motions of different particles.

## 3.4 Differential Dynamic Microscopy (DDM)

There is a family of techniques that aim at combining microscopy and light scattering to obtain a quantitative characterization of the structural and dynamic properties of soft matter, and in particular colloids. These techniques go under the name of Digital Fourier Microscopy [49]. In this thesis we will mostly focus on Differential Dynamic Microscopy (DDM) [22], [21], a technique that obtains quantitative scattering information by analyzing the spatial Fourier modes of the intensity fluctuations that are present in a microscope image sequence. Following [49], we assume that the image formation process is linear. An image is thus expressed in terms of the sample concentration by (see also Eq.3.14 in which we have neglected the background term $I_0$):

$$I(\mathbf{x},t) = I_0 + \int dz' \int d\mathbf{x'}\ c(\mathbf{x'},z',t)K(\mathbf{x}-\mathbf{x'},z') \tag{3.28}$$

whose spatial Fourier transform is given by

$$I(\mathbf{q},t) = I_0\delta_D(\mathbf{q}) + \int dq_z\ \ c(\mathbf{q},q_z,t)K(\mathbf{q},q_z). \tag{3.29}$$

Here thanks to the property of the Fourier transform the convolution in the transverse plane $(x,y)$ becomes an algebraic product. Analogously to what defined in 3.8, we can define the **image intermediate scattering function**

$$F_i(\mathbf{q},\Delta t) = \langle I(\mathbf{q},t)\cdot I^*(\mathbf{q},\Delta t)\rangle = \int dq_z\ \ F(\mathbf{q},q_z,\Delta t)|K(\mathbf{q},q_z)|^2 \tag{3.30}$$

where $.^*$ indicates the complex conjugate, $F$ is the *sample* intermediate scattering function, and the normalized version:

$$f_i(\mathbf{q},\Delta t) = \frac{F_i(\mathbf{q},\Delta t)}{F_i(\mathbf{q},0)} = \frac{\int dq_z\ \ F(\mathbf{q},q_z,\Delta t)|K(\mathbf{q},q_z)|^2}{\int dq_z\ \ F(\mathbf{q},q_z,0)|K(\mathbf{q},q_z)|^2} \tag{3.31}$$

strictly speaking there is a difference between the intermediate scattering function of the image and the one of the sample, in particular $F_i$ is a two dimensional projection of $F$, but it has been proven [49] that in many relevant cases the axial dynamics can be neglected and so $F(\mathbf{q},q_z,\Delta t) \sim F(\mathbf{q},0,\Delta t)$. In this way, Eq.3.31 simplifies and the image intermediate scattering function is a good estimator of the intermediate scattering function of the sample

$$f_i(\mathbf{q},\Delta t) = f(\mathbf{q},\Delta t) \tag{3.32}$$

which proves that DDM extracts information analogous to DLS experiments. In practice, the image intermediate scattering function is estimated in DDM by means of the **dynamic structure function**

$$D(\mathbf{q},\Delta t) = \langle |I(\mathbf{q},t) - I(\mathbf{q},t+\Delta t)|^2\rangle_t \tag{3.33}$$

because one has:

$$\begin{aligned} D(\mathbf{q},\Delta t) &= 2\langle |I(\mathbf{q},t)|^2\rangle_t - 2\langle \mathrm{Re}[I(\mathbf{q},t)\cdot I^*(\mathbf{q},t+\Delta t)]\rangle_t \\ &= 2\langle |I(\mathbf{q},t)|^2\rangle_{\mathbf{q},t}\cdot[1-f_i(\mathbf{q},\Delta t)]. \end{aligned}$$

The dynamic structure function can be thus factorized in a static and a dynamic part

$$D(\mathbf{q},\Delta t) = T(\mathbf{q})P(\mathbf{q})S(\mathbf{q})(1-f_i(\mathbf{q},\Delta t)) = A(\mathbf{q})(1-f_i(\mathbf{q},\Delta t)) \quad (3.34)$$

where $T(\mathbf{q}) = |K(\mathbf{q})|^2$ is the microscope transfer function and, as already mentioned, $P(q)$ is the particle form factor defined in Eq.3.19 and $S(q)$ the static structure factor. We note in passing that, if the transfer function $T(\mathbf{q})$ is known, DDM can also provide static scattering information about the sample.

If we now consider the non-ideality of the detector, we can rewrite Eq.3.29 as

$$I(\mathbf{q},t) = I_0\delta_D(\mathbf{q}) + \delta S(\mathbf{q},t) + \delta N(\mathbf{q},t), \quad (3.35)$$

where we have defined $\delta s(\mathbf{q},t) = \int dq_z \;\; c(\mathbf{q},q_z,t)K(\mathbf{q},q_z)$ and added a new term $\delta N(\mathbf{q},t)$ accounting for the detection noise. The latter is a zero average term, with no spatial or temporal correlation:

$$\delta N(\mathbf{q},t)\delta N(\mathbf{q}',t') = \delta_D(t-t')\delta_D(\mathbf{q}-\mathbf{q}')\mathcal{N}.$$

Also, we assume that its fluctuations are uncorrelated with the one of the signal $\delta S$:

$$\langle \delta N(\mathbf{q},t)\delta S(\mathbf{q'},t+\tau)\rangle_t = 0.$$

Therefore, the noise enters Eq.3.34 as a $q$ and $\tau$ independent additive term:

$$D(\mathbf{q},\Delta t) = T(\mathbf{q})P(\mathbf{q})S(\mathbf{q})(1-f_i(\mathbf{q},\Delta t)) + \mathcal{N}. \quad (3.36)$$

This result is often rewritten in the literature as

$$D(\mathbf{q},\Delta t) = A(\mathbf{q})(1-f_i(\mathbf{q},\Delta t)) + B \quad (3.37)$$

where $A(\mathbf{q}) = T(\mathbf{q})P(\mathbf{q})S(\mathbf{q})$ and $B = \mathcal{N}$. In typical DDM experiments the structure function is obtained Fig.3.7 by first calculating the real space image difference $d(\mathbf{x},t,\Delta t)$, which removes the static optical background in the image what would otherwise generate unwanted signal. The two-dimensional Fourier power spectrum of the image difference is then computed

$$D(\mathbf{q},t,\Delta t) = |\mathcal{F}\{d(\mathbf{q},t,\Delta t)\}|^2.$$

If the dynamics is stationary, the only relevant temporal variable is $\Delta t$ so that one can average over $t$ to obtain

$$D(\mathbf{q},\Delta t) = \langle D(\mathbf{q},t,\Delta t)\rangle_t.$$

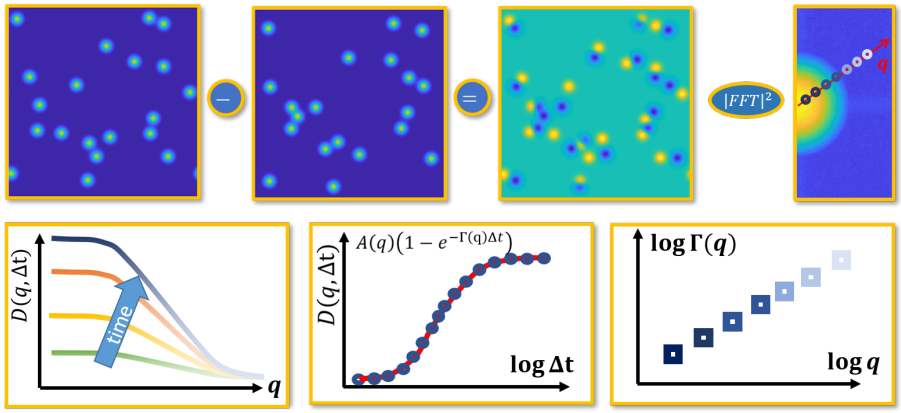


**Figure 3.7:** Schematic illustration of the DDM procedure: the structure function $D(\mathbf{q}, \Delta t)$ is built starting from the difference $d(\mathbf{x}, t, \Delta t)$ (third panel in the top row) between two images at time $t$ and $t+\Delta t$ (panels one and two), the structure function is the power spectrum of the image-difference $D(\mathbf{q}, t, \Delta t) = |\mathcal{F}\{d(x, t, \Delta t)\}|^2$ (panel four). For stationary dynamics the only relevant temporal variable is $\Delta t$ so that one can average over $t$. Bottom line: (first panel) azimuthal average of $D(q, \Delta t)$ as a function of the modulus of $\mathbf{q}$: different colors label different time delays $\Delta t$. (Second panel) structure function for a fixed $q$ as a function of $\Delta t$. The functional form depends on the dynamics of the scatterers: in diffusive case the relaxation is a simple exponential $D(q, \Delta t) = A(q)(1 - exp\{-Dq^2 t\})$. (third panel): decorrelation rate for Brownian particles $\Gamma(q) = Dq^2$.

For fixed $\Delta t$, $D(\mathbf{q}, \Delta t)$ is a function of the two-dimensional wave vector $\mathbf{q} = (q_x, q_y)$. At this stage of the analysis one has the possibility to analyze separately different directions (Fig.3.7, panel four, top line) or to perform an azimuthal average (Fig.3.7, first panel bottom line) if the dynamics is isotropic. The range of wave vectors goes from the minimum that corresponds to the spatial modulation with the largest possible spatial period $q_{min} = \frac{2\pi}{\text{image size}}$, to the maximum that corresponds to the finest possible spatial modulation $q_{max} = \frac{\pi}{\text{pixel size}}$, so that the range of available length-scales is

$$\frac{q_{max}}{q_{min}} = \frac{\text{number of pixels}}{2}.$$

Since $f_i(q, \Delta t)$ is usually a monotonically decreasing function of time, the structure function is a monotonically increasing function of time (central bottom panel). The functional form of $f_i(q, \Delta t)$ depends on the dynamics. If the scatterers are independent and their displacement probability is Gaussian, it is given by

$$f_i(q, \Delta t) = \exp\{-(q^2 \Delta r^2(\Delta t))/4\}. \tag{3.38}$$

For example, in the case of monodispersed particles freely diffusing in a Newtonian fluid, the mean square displacement reads $\Delta r^2(\Delta t)) = 4D\Delta t$

(where D is the diffusion coefficient) and $f_i(q, \Delta t)$ is a simple exponential function of $\Delta t$, with a decorrelation rate

$$\Gamma(q) = Dq^2. \tag{3.39}$$

# Chapter 4

# Novel approaches for opto-rheological experiments at the microscale

In this chapter we describe research that was carried out during this thesis work. We first (sections from 4.1 to 4.3 ) focus on the developments leading to DDM-based microrheology, which are also described in recent publications [48], [44]. In the second part of the chapter (sections from 4.5 to 4.8), we describe the methodological aspects of performing DDM during shear experiments.

## 4.1 Image windowing mitigates edge effects in DDM

As described in the previous chapter, the DDM image structure function for independent ($S(q) = 1$) Brownian particles freely diffusing in a homogeneous medium reads

$$D(q, \Delta t) = A(q)\left(1 - e^{-Dq^2\Delta t}\right) + B(q) \tag{4.1}$$

with $A(q) = T(q)P(q)$ and $B(q) = B$
In practice, the presence of spurious dynamical and statics effects due to the finite size of the image can impair to some degree the validity of Eq.4.1 for some values of $q$.

**Artifacts due to the finite image size** To demonstrate the impact of the aforementioned effects we consider a semi-diluted (0.04 volume fraction) suspension of sterically stabilized polymethylmethacrylate (PMMA) 0.5 $\mu m$ fluorescent particles in a density- and refractive-index-matching solvent [6]. The suspension is imaged by a confocal microscope equipped with a Nipkow

disk (Yokogawa), a CCD camera (QIimaging), a 100X oil disk immersion objective (Leica), and a solid-state laser source (Laserglow). Image sequences of a single plane from depth of 20 $\mu m$ from the lower coverslip are acquires at a frame rate $\Delta t_0 = 33.9$ fps.Image size is 256 x 256 pixels, with an effective pixel size of 127 $nm$. A representative frame of a movie obtained with confocal microscopy is shown in Fig.4.1, (a). By performing a DDM analysis of the movie we obtain intermediate scattering functions $f_i(q,t)$ that, when plotted as a function of the reduced variable $Dq^2\Delta t$ should collapse on a single master curve. In Fig.4.1, (c) we see that the expected collapse is observed only for some of the curves, corresponding to the lowest $q$-values. Inspection of the exponential relaxation rate $\Gamma(q)$ Fig.4.1, (d) reveals deviation from the expected scaling $\Gamma(q) = Dq^2$. In particular, we observe that:

- $\Gamma(q)$ is non monotonic
- deviations are more apparent for large values of $q$, where $\Gamma(q)$ exhibits a plateau
- the value of the plateau is close to the Brownian time $\tau_B = a^2/D$

In addition, we also observe that the static structure function shows an anomalous cross-shape pattern Fig.4.1, panel (b), a feature that is found to be particularly evident when the particles are large compared to the pixel size (data non shown).

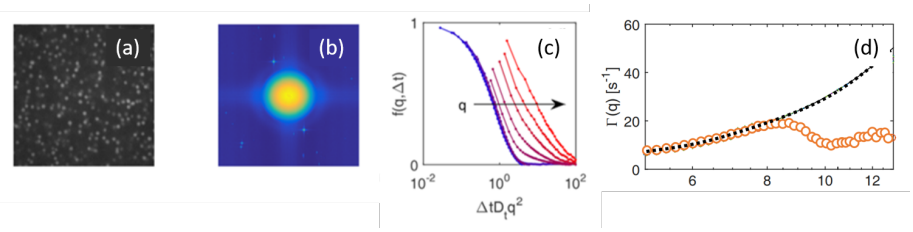


**Figure 4.1:** Panel (a) Raw confocal image of a semi-diluted (0.04 volume fraction) suspension of sterically stabilized polymethylmethacrylate (PMMA) 0.5$\mu m$ fluorescent particles in a density– and refractive-index–matching solvent. (b) Two dimensional dynamic structure function for a long decay ($t = 20s$) exhibiting a cross-shape pattern (see main text for details). (c) Rescaled intermediate scattering function the temporal variable rescaled with $Dq^2$ where $D$ is the diffusion coefficient; the $f_i$ for high qs is dominated by non diffusive decay. (d) Symbols: relaxation rate $\Gamma(q)$, black dotted line: quadratic fit. Adapted from [48]

To better understand the origin of this artifact and its consequences on the determination of the particle dynamics with DDM, we show in Fig.4.2 a sequence of numerically generated images (top row, a-d) and their Fourier power spectra (bottom row, e-h). In panels a-d we have only one particle that is positioned at different locations with respect to the image borders. We notice that, when the particle crosses the border of the image (panels c,

d), the corresponding power spectra (g, h) exhibit some streaks in the direction perpendicular to the orientation of the crossed border, as a consequence of the particle being chopped out from the images.

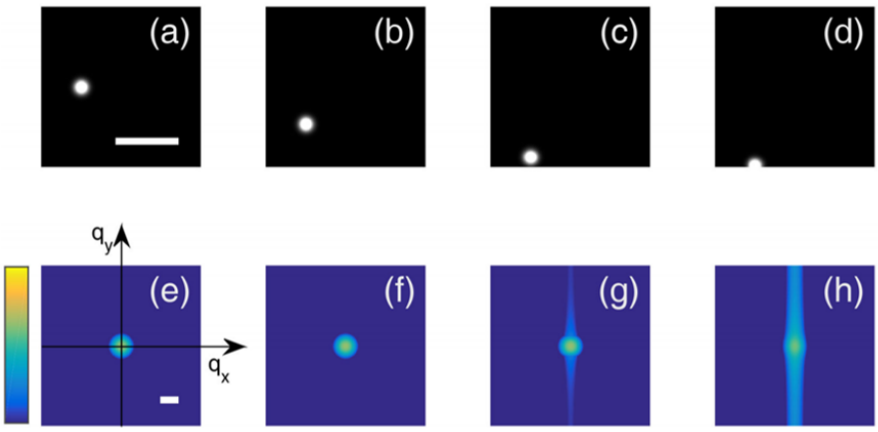


**Figure 4.2:** . Spectral leakage in DDM. A particle crossing image boundaries (top row) excites high-q wave vectors in the reconstructed Fourier spectrum (bottom row) along the direction perpendicular to the image boundary. Consequently, the characteristic dynamics associated with these events produce strong effects at large q. All images are simulated and represented using the same settings (image size: $N = 256$ pixels, effective particle radius: $\sigma_P = 10$ pixels), and Fourier spectra are represented on a logarithmic scale with the same color code. The size bar for real-space images shown in panel (a) corresponds to 100 pixels, while the size bar for Fourier-space images shown in panel (e) corresponds to $2\pi/\sigma_P$. Adapted from [48].

Interestingly, as a consequence of this edge crossing phenomenon, a particle whose power spectrum would otherwise exhibit a compact domain of existence, can create signal at larger wave-vectors, a phenomenon that goes under the name of *spectral leakage*. The relative amplitude of this signal compared to the one generated by the particle when is completely within the image boundaries is given by

$$A_R(q) = \alpha \frac{S_{border}(q)}{S_\infty(q)} \tag{4.2}$$

where $S_\infty(q)$ is the power spectrum of a particle far from the border Fig.4.2, panel(e) and (f), $S_{border}(q)$ is the power spectrum of a particle crossing the border Fig.4.2, panel (h) and $\alpha$ is the probability to find a particle within a distance $R$ from the border: for a square image of edge $L$ and particles of radius $R$

$$\alpha = \frac{(L-2R)^2}{4(L-R)\cdot R}.$$

While spectral leakage is a well known static phenomenon in signal processing, its effect on the dynamics and in particular for DDM experiments was first understood in Ref.[48], where it was shown to introduce a spurious, q-independent time-scale related to the crossing time of the image border by a particle. For Brownian particles, this time is basically the Brownian diffusion time of a particle over a distance equal to the size of its Point Spread Function.

**Image Windowing suppresses the finite size artifact -** In Ref. [48], we showed that an effective and computationally-fast way to suppress the finite-size artifact in DDM experiments is, before performing any Fourier transform operation, to multiply each image $I(\mathbf{x}, t)$ for a *window function* $W(\mathbf{x})$ that smoothly goes to zero at the images edges Fig.4.3, (a). The DDM algorithm (described in Chapter III) is then applied to a movie of apodized images:

$$I_W(\mathbf{x}, t) = W(\mathbf{x}) \cdot I(\mathbf{x}, t).$$

The results of this windowing procedure Fig.4.3 show that it suppresses almost completely the artifacts.

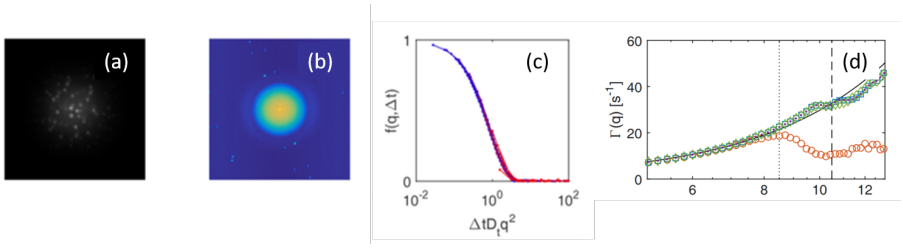


**Figure 4.3:** Results of windowing preprocessing: panel (a) apodized image $I_W(\mathbf{x}) = W(\mathbf{x})I(\mathbf{x})$; panel (b) 2D Dynamic Structure function for $\Delta t = 20s$; panel (c) rescaled intermediate scattering function; panel (d) Relaxation rate as a function of q. Red circles are obtained without the applying the windowing procedure, the other symbols correspond to different windowing function (blue square: Blackman-Harris, green diamonds: Hann, purple dots: Dolph-Chebyshev) giving remarkably similar results. The residual deviation from the $q^2$ behavior is known physical effect due to polydispersity. Adapted from [48].

In particular:

- The cross-shape pattern disappears from the 2D structure function Fig.4.3 b.
- The intermediate scattering functions nicely collapse when their temporal axis is rescaled with $Dq^2$ Fig.4.3 c.
- Different window functions give remarkably similar results (see also the caption of Fig.4.3 d).

- For large $q$, the spurious plateau is no longer observed Fig.4.3 d.

Moreover, thanks to the enlarged wave vectors range, it is now visible (in the dataset presented in this section) a residual deviation from the diffusive behavior $\Gamma(q) = q^2$: in the vicinity of $q^*$, the minimum of the static amplitude, $\Gamma(q)$ presents a swing, *i.e.* a slight speed up of the dynamics for $q > q^*$, followed by a slowing down for $q > q^*$. This effect has been predicted and observed in the context of dynamic light scattering and can be ascribed to the polydispersity of the particles [100]. Particles of different size contribute to the sample intermediate scattering function with a size-dependent scattering amplitude. In addition, they also have different form factors $P(q)$, whose minima are found for slightly different values of $q$. Close to these minima, the measured diffusion coefficient exhibits a q-dependent behavior: for small $q$, the diffusion coefficient is dominated by smaller particles, whereas the opposite holds for large $q$. Intuitively, we can say that the distribution of the minima of the particle form factors results in a way to scan the particle size distribution.

**Drawbacks of the image windowing procedure -** One drawback of the windowing procedure is that, depending on the choice of the window function, the amplitude of the signal in Fourier space may be consistently reduced. For the windowing functions that we have tested the reduction was found to be in the range $[75\%,\ 85\%]$.

A second drawback, is that multiplication with the windowing function in real space corresponds to a convolution $(*)$ with its Fourier transform in the reciprocal space, which in principle introduces correlations between different wave-vectors both for the static amplitude

$$A_W(\mathbf{q}) = 2N_P|\hat{W}(\mathbf{q})|^2 * P_\infty(\mathbf{q}) \tag{4.3}$$

and for the intermediate scattering function

$$f_W(\mathbf{q}, \Delta t) = \frac{|\hat{W}(\mathbf{q})|^2 * [f_\infty(\mathbf{q}, \Delta t)P_\infty(\mathbf{q})]}{|\hat{W}(\mathbf{q})|^2 * P_\infty(\mathbf{q})}. \tag{4.4}$$

Here $N_P$ is the average number of particles in the image, $P_\infty$ is the form factor of a particle for infinitely large sample and $|\hat{W}(\mathbf{q})|^2$ is the power spectrum of the window function.

For all the cases studied in Ref. [48] we have not observed any windowing-induced artifacts and, in general, we expect that both intensity loss and broadening will not lead to serious consequences on the mean values of $A(q)$ and $f(q, \Delta t)$, at least as far as they are smooth functions of $q$.

## 4.2 Effect of the camera exposure time in DDM experiments

As we have seen in the previous chapter, Eq.4.1 can be derived from the more general

$$D(q,\Delta t) = A(q)\Big(1 - exp\big(-q^2\langle\Delta r^2(\Delta t)\rangle/4\big)\Big) + B(q) \tag{4.5}$$

which may be inverted to estimate with DDM the mean square displacement. While the effect of exposure time in particle tracking experiments is known [104] Fig.4.7, panel (c), its impact on DDM analysis has not been studied in detail, even though encouraging steps were made in Ref. [19] for a different Digital Fourier Microscopy technique.

To evaluate such effect we start by considering the instantaneous intensity distribution $i(\mathbf{x},t)$ and its time integral over the exposure time $\tau$ *i.e.* the actual image recorded by a camera:

$$I(\mathbf{x},t) = \frac{1}{\tau}\int_t^{t+\tau} dt_1\ i(\mathbf{x},t_1). \tag{4.6}$$

The image structure function can be calculated as $D(q,\Delta t) = 2[C(q,0) - C(q,\Delta t)] + B(q)$, where we have introduced the *image correlation function* $C(q,\Delta t) = \langle I(q,\Delta t)I^*(q,0)$. The latter can be rewritten as

$$\begin{aligned} C(q,\Delta t) &= \frac{1}{\tau^2}\int_{\Delta t}^{\Delta t+\tau} dt_1 \int_0^{\tau} dt_2 \langle i(q,t_1)i^*(q,t_2)\rangle \\ &= \frac{1}{\tau^2}\int_{\Delta t}^{\Delta t+\tau} dt_1 \int_0^{\tau} dt_2\ c(q,t_1-t_2), \end{aligned} \tag{4.7}$$

where $c(q,t_1-t_2) = \langle i(q,t_1)i^*(q,t_2)\rangle$. If we assume an exponential dynamics (which holds for instance for diffusion in a Newtonian liquid) $c(q,t_1-t_2) = a(q)e^{-\Gamma(q)|t_1-t_2|}$ and we use the fact that $|t_1-t_2| > \tau$ (images are separated in time by more than the image acquisition time) we obtain:

$$C(q,\Delta t) = a(q)\Big[2\frac{\cosh(z)-1}{z^2}\Big]e^{-\Gamma(q)\Delta t} = a(q)f_1(z)e^{-\Gamma(q)\Delta t}, \tag{4.8}$$

where $z = \Gamma(q)\tau$. On the other hand,

$$C(q,0) = a(q)\Big[2\frac{e^z-1+z}{z^2}\Big] = a(q)f_0(z), \tag{4.9}$$

for which we would like to stress that, because $f_1(z) > f_0(z)$ for $z > 0$, the formal limit $C(q,\Delta t \to 0)$ does not coincide with $C(q,0)$.
Let us consider explicitly the image structure function. If $\frac{1}{2}B(q)$ is the

spectral density of the noise in one image, $D(q, \Delta t)$ can be written in the usual form

$$D(q, \Delta t) = A_{app}(q)\left[1 - e^{-\Gamma(q)\Delta t}\right] + B_{app}(q) \tag{4.10}$$

where

$$A_{app}(q) = 2a(q)f_1(z)$$

and

$$B_{app}(q) = B(q) - A_{app}(q)\Big[1 - \frac{f_0(z)}{f_1(z)}\Big].$$

Hence, in the presence of a finite exposure time the "apparent noise" $B_{app}(q)$ does not coincide with the actual noise $B(q)$. The spurious (always negative) contribution

$$-A_{app}(q)\Big[1 - \frac{f_0(z)}{f_1(z)}\Big]$$

is given by the product of $A_{app}(q)$ (which is, typically, a decreasing function on q) and the term

$$1 - \frac{f_0(z)}{f_1(z)}$$

that goes monotonically form 0 to 1 when q goes from 0 to infinity, at least as far as $\Gamma(q)$ is a monotonically increasing function of q. Overall, the spurious contribution is expected to be described by a bell-shaped function, with a (negative) amplitude proportional to the signal amplitude. We note that:

- to be able to predict the $B_{app}(q)$ we would need to know the dynamics during the acquisition time, which is typically a problem because the dynamics is what we would like to extract from the processing of the image sequences
- If the correlation function is not exponential (which is likely to be the case for non-Newtonian samples) its functional form changes upon integration Eq.4.8, so the effect is not only to affect the the amplitude and the baseline of the structure function but also to change the temporal dependence of the intermediate scattering function.

In this thesis work, this effect is experimentally kept under control by choosing an exposure time $\tau$ that is considerably smaller than the minimum time delay $\Delta t$ of interest.

## 4.3 Tracking-free extraction of the MSD from DDM analysis

In Chapter III we defined the particles mean square displacement (MSD), a quantity that is typically calculated by analyzing in direct space the particle

trajectories. It is known, however, that Dynamic Light Scattering can be used to extract the MSD [106], an alternative that may be particularly useful when the particles are too small to be tracked in direct space. In some particular cases the extraction procedure remarkably simplifies: as defined in the previous Chapter the van Hove distribution function is the Fourier transform of the displacement probability distribution $P(\Delta x, \Delta t)$. If the mono dimensional[1] $P(\Delta x; \Delta t)$(for fixed delay) is Gaussian

$$P(\Delta x, \Delta t) = \frac{1}{\sqrt{2\pi\sigma^2}} \exp\Big[-\Big(\frac{\Delta x^2}{2\sigma^2}\Big)\Big], \tag{4.11}$$

it follows that also $G_S(q; \Delta t)$ is a Gaussian, in particular

$$G_S(q, \Delta t) = \frac{1}{\sqrt{2\pi\sigma^2}} \exp\Big[-\Big(\frac{q^2 \cdot \sigma^2}{2}\Big)\Big], \tag{4.12}$$

Since for independent particles, the distinct part of the van Hove distribution function vanishes, one can obtain the MSD ($= \sigma^2$) by inversion of the *intermediate scattering function* (see Eq.3.27). Within these hypothesis this is true both in DLS and for the DDM *image intermediate scattering function* in two dimensions

$$f_i(q, \Delta t) = \exp\Big[-\frac{q^2\langle \Delta r(\Delta t)^2\rangle}{4}\Big]. \tag{4.13}$$

Let us stress that these hypothesis are not trivially satisfied, there are a number of conditions where the displacement probability distribution is not Gaussian (e.g. in glasses [24], driven or active or aging systems), but to the best of our knowledge all the conditions that break the Gaussian hypothesis also break the GSER [110], in other words the validity of GSER implies Gaussian displacements.

It must be noted that the output of the DDM analysis is not the image intermediate scattering function but the image structure function:

$$\begin{aligned} D(\mathbf{q}, \Delta t) &= \langle |I_W(q,t) - I_W(q, t+\Delta t)|^2\rangle_t \\ &= A_{app}(\mathbf{q})(1 - f_W(\mathbf{q}, \Delta t)) + B_{app}(\mathbf{q}) \end{aligned} \tag{4.14}$$

where $B_{app}$ is the apparent noise term, $A_{app}$ is the apparent static amplitude, $I_W$ is the windowed image and $f_W$ is the image intermediate scattering function after windowing[2]. Obtaining the image intermediate scattering function from the image structure function requires thus knowledge of $A(q)$ and $B$, a step for which we have devised different strategies.

[1] Two or three dimensional generalization is straightforward.

[2] From now on and in this section, we will drop the subscript $_W$ to refer to the apodized image and to the respective intermediate scattering function. Also, as explained above, we will always work in conditions for which $A_{app}(q) \simeq A(q)$ and $B_{app}(q) \simeq B$.

### 4.3.1 The fitting strategy

If the functional form of the MSD is known *a priori*, $A$ and $B$ are easily found as fitting parameters. One can thus invert $D$ and obtain Fig.4.4 the MSD

$$\langle \Delta r(\Delta t)^2 \rangle = -\frac{4}{q^2} \log\left(1 - \frac{D(q,\Delta t) - B_{fit}(q)}{A_{fit}(q)}\right). \tag{4.15}$$

This simple procedure works well for instance if the medium hosting the particles is a Newtonian liquid for which we know exactly how to model the MSD ( $\propto \Delta t$). For non-Newtonian samples, the functional form of the MSD reflects that of the linear creep compliance 3.13 that can be quite difficult to model.

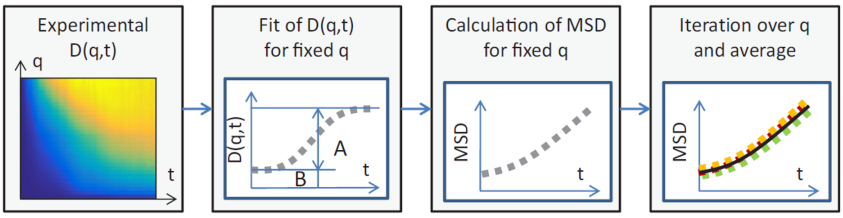


**Figure 4.4:** If the functional form of the mean square displacement is known one can try to fit the structure function, to obtain $A$ and $B$, and to invert the Structure function according to 4.15. Adapted from [44].

### 4.3.2 The asymptotic strategy

If we ignore the functional form of the MSD we can still estimate $B$ and $A(q)$ without the need to fit the structure function, provided that we perform the acquisition of a sufficiently long image sequence (to estimate $A$) at a sufficiently large frame rate (to estimate $B$). In fact, $B$ is often estimated at large $q$ where $A(q) \to 0$

$$\lim_{q\to\infty,\Delta t\to 0} D(q,\Delta t) = B$$

and $A$ can be estimated from the long time behaviour of $D$:

$$\lim_{\Delta t\to\infty} D(q,\infty) = A(q) + B.$$

In some particular cases, in which the image is strongly dominated by the signal from the particles and no other significant contributions are present, one can estimate $A(q)$ directly from the static Fourier power spectrum

$$D_0(q) = 2\langle |I(q,t)|^2 \rangle_t = A(q) + B \tag{4.16}$$

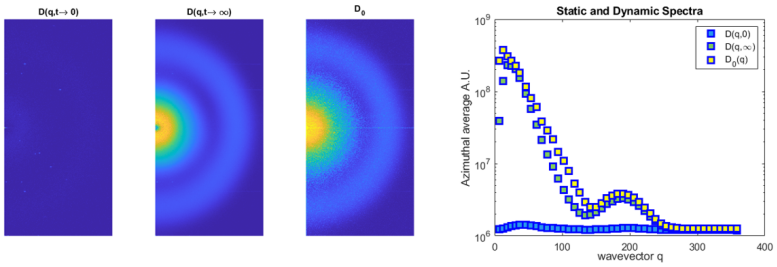


**Figure 4.5:** (a) $\lim_{\Delta t \to 0} D(\mathbf{q}, \Delta t)$ two-dimensional dynamic structure functions. (b) $\lim_{\Delta t \to \infty} D(\mathbf{q}, \Delta t)$. (c) static Fourier power spectrum $D_0(\mathbf{q})$. (d) Azimuthal averages of the images in panels a, b and c. For large $q$, all the curves plateau to the same value $B$. For smaller $q$ there are differences between the long time behavior of the dynamic structure function and $D_0(\mathbf{q})$, which are due to the presence of a static background signal in the images that does not depend on the particles under scrutiny.

Some of the possible reasons making hard to use these methods to estimate $A(q)$ are

- the presence of static background signal in the images that does not depend on the particles (e.g. dust particles on the optical surfaces, scratches, dirt,...)) Fig.4.5 d
- the dynamics occurs on time-scales that are too long compared to the duration of the experiment

We stress that the determination of $B(q)$ is also quite delicate, since small differences in its estimation takes to quite different short-time MSD.

### 4.3.3 The self consistent multi-$q$ strategy

A third approach, which is based on the assumption that we are dealing with independent particles[3], is to take advantage of the fact that in DDM experiments we have simultaneous access to a variety of $q$. We thus have several independent estimates of the MSD, one for each $q$-value, as

$$D(q, \Delta t) = A(q)\Big[1 - \exp\Big(-\frac{\langle \Delta r^2 \rangle q^2}{4}\Big)\Big] + B(q).$$

We thus devised a self-consistent procedure to iteratively estimate the values of $A(q)$ and $B(q)$ by minimizing the spread existing among all the different estimates of MSD obtained from different $q$-values. This optimization procedure is represented schematically in Fig.4.6.

[3]Extension to more general cases are discussed in [50].

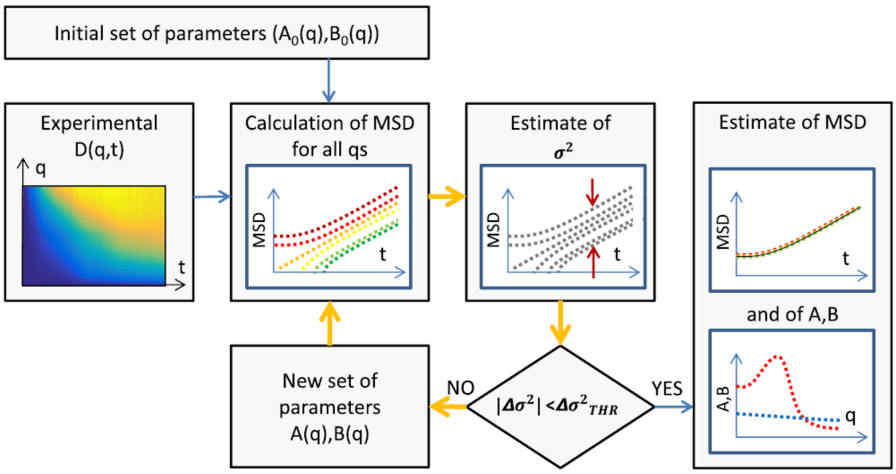


**Figure 4.6:** Schematic representation of the optimization-based DDM analysis. The procedure is based on an optimization cycle (yellow arrows), fed by the experimental image structure function $D(q, \Delta t)$ and by an initial set of parameters $(A_0(q), B_0(q))$. The object function is the dispersion $\sigma^2$ of the reconstructed mean-square displacements [see Eq.4.19]. New values of $(A(q), B(q))$ are iteratively generated in order to minimize the object function. The output of the procedure is the optimal set of parameters $(A(q), B(q))$ leading to the best estimate of MSD(t). Adapted from [44]

- One starts with a reasonable estimate of $A(q)$ and $B(q)$, obtained for instance with the fitting or with the asymptotic strategies. These starting values $A_0(q)$ and $B_0(q)$ are then used to invert the $D(q, \Delta t)$ and obtain a bundle of MSD, one for each $q$.

- From this bundle one can compute the $q$-averaged MSD

$$\overline{MSD}(\Delta t) = \langle MSD(q, \Delta t) \rangle_q \tag{4.17}$$

  and the relative spread

$$\sigma^2(\Delta t) = \sum_q |MSD(q, \Delta t) - \overline{MSD}(\Delta t)|^2 \tag{4.18}$$

  which is due to the fact that that $A_0$ and $B_0$ are not the optimal values.

- We then obtain the scalar quantity

$$\sigma^2 = \sum_{q,\Delta t} log^2 \frac{MSD(q, \Delta t)}{\overline{MSD}(\Delta t)}. \tag{4.19}$$

  as an estimator of the overall spread of the bundle.

- As a last step, we perform a numerical search for the minimum of the spread function $\sigma^2(A(q), B(q))$, which we expect to provide also the correct values of $A(q, B(q)$, under the assumption that they are the ones for which we obtain the same MSD independently on $q$.

### 4.3.4 Critical issues

For each of the three proposed strategies, the most delicate part of the inversion of the structure function to obtain the MSD lies in capturing correctly the short-time behavior *i.e.* in having a good estimate of $B(q)$, because a small error can lead to large discrepancies in the extracted MSD.

If the MSD is used in the context of microrheology this difference may

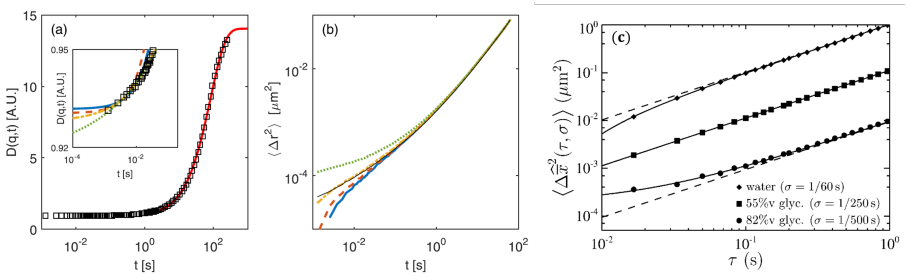


**Figure 4.7:** Panels (a) and (b): effect of the model dependent determination of the noise baseline $B(q)$ on the MSD. Panel (a) Symbols: image structure function $D(q, \Delta t)$ (for $q = 6.04 \mu m^{-1}$) obtained from DDM on $0.5 \mu m$ diameter tracers in a visco-elastic solution of PEO in water. The continuous red line is an exponential fit to the data obtained at large delay times ($\Delta t > 20 s$); this fit allows for the estimate of the plateau height $A'(q)$. Inset shows a close-up of the short time behavior of $D(q, \Delta t)$ (symbols). The data are fit with different functions, leading to different estimates of the baseline $B(q)$: linear fit over the first 10 data points (continuous blue line), linear fit over the first 5 data points (dashed orange line), fit over the first 20 data points with a function of the form $y = ax^{0.5} + b$ (dashed-dotted yellow line), and fit over the same interval with a function of the form $y = ax^{0.25} + b$ (dotted green line). Panel (b) MSD obtained from Eq.4.15 by using the amplitude $A(q) = A'(q) - B(q)$ and the noise baseline $B(q)$ obtained from the different fitting models shown in the inset of panel (a). Curves are color coded according to the fits, the black continuous line is the result of the model-free procedure described in the main text. Panel (c) MSD of diluted colloidal particles in Newtonian fluids obtained by particle tracking. The apparent deviations from a diffusive behavior are due either to a time-exposure effect (analogous to the one described in 4.2) or to a noise-induced particle localization error analogous to the baseline effect that we have in DDM experiments. Panels (a) and (b) adapted from [44], panel (c) adapted from [104].

be reflected in a both quantitative and quantitative difference in the visco-elastic moduli. In Fig.4.7 we can appreciate the dramatic effect of slightly different estimates of $B$ on the MSD at short times, extracted with DDM

(panel (a) and (b). Similar problems affect particle tracking (PT) experiments (Fig.4.7c). The effect of the detection noise in PT is known and solution are proposed in the literature [104]. In the PT case the effect of noise is appreciable, qualitatively speaking, when the particle root-MSD in one frame is small compared to accuracy in the determination of the particle position: when the *genuine* displacement between two frames is small, the presence of intensity fluctuation reflects in an apparent displacement of the center of mass

$$\langle \Delta \mathbf{r}^2_{Measured} \rangle = \langle \Delta \mathbf{r}^2_{Genuine} \rangle + \langle \Delta \mathbf{r}^2_{Noise} \rangle. \tag{4.20}$$

Without entering in a detailed description of the problem, we stress that the effect of noise in the determination of the MSD is a known problem to all the techniques and that, in general, there are two approaches to solve it:

- try to model the term $\langle \Delta \mathbf{r}^2_{Noise} \rangle$ as a function of the optical and electronical conditions
- measure the term $\langle \Delta \mathbf{r}^2_{Noise} \rangle$ (for example in Particle Tracking with immobilized particles)

Our approach based on the optimization procedure exploits the multi-q nature of DDM and is, to all effects, a novel way to get rid of noise-induced artifacts. This can be appreciated by considering the structure function

$$D(q, \Delta t) = A(q)\Big[1 - \exp\Big(-\frac{\langle \Delta r^2 \rangle q^2}{4}\Big)\Big] + B(q).$$

together with a non homogeneous MSD $\langle \Delta r^2 \rangle = \Delta r_0^2 + \Delta r^2_{hom}(\Delta t)$. By inserting the latter in Eq.4.3.4 and using a first order Taylor expansion we obtain

$$\begin{aligned} D(q, \Delta t) &= A(\mathbf{q})\Big(\frac{q^2 \Delta r^2_{hom}(\Delta t)}{4} + \frac{q^2 \Delta r_0^2}{4}\Big) + B(\mathbf{q}) \\ &= A(\mathbf{q})\frac{q^2 \Delta r^2_{hom}(\Delta t)}{4} + B'(\mathbf{q}) \end{aligned}$$

which shows how, considering a single wave vector, the effect of $\Delta r_0$ is indistinguishable from the effect of $B(q)$. On the other hand the effect of $r_0^2$ on the structure function has a strong q dependence and, if a wide range of q is considered, one should introduce a strong and systematic q dependence in $B(q)$ to "absorb" an incorrect estimate of $\Delta r_0^2$.

## 4.4 Tracking-free DDM microrheology

### 4.4.1 Part I: Translational microrheology

The self-consistent procedure presented in the previous section allows for the accurate measurement of the MSD, which is particularly relevant for

**microrheological** applications. As previously described (Chapter 3), in microrheology experiments, the MSD is connected via the Generalized Stokes Einstein Relation (GSER) Eq.3.13 to the linear creep compliance, whose functional form can be quite complex and, in general, not easy to model. The hypotheses for the validity of the GSER are:

- the medium is homogeneous on the scale of the tracer particle
- the tracer particles are monodisperse in size
- the correlation between the displacements of distinct particles is absent or negligible

If these hypotheses are satisfied, measuring the particles MSD provides an estimate for the linear creep compliance. Since in the linear regime all the rheological tests are equivalent, the linear creep compliance can be conveniently mapped onto the frequency-dependent visco-elastic storage and loss moduli $G'$ and $G''$.

### 4.4.2 Part II: Rotational microrheology

While the application of microrheology described so far was based on analyzing the translational motion of the colloidal particles, it is also possible to write a GSER involving angular displacements in place of linear displacements

$$G^*(\omega) = \frac{k_B T}{4\pi a^3 s \langle \Delta\tilde{\theta}^2(s) \rangle}\Big|_{s=i\omega}. \tag{4.21}$$

where $\langle \Delta\tilde{\theta}^2(s) \rangle$ is the Laplace transform of the **angular mean square displacement** (AMSD) $\langle \Delta\theta^2(\Delta t) \rangle$, evaluated in $s = i\omega$.
Eq.4.21 is the basis of **rotational microrheology**. With this technique the rotational motion of the particles, instead of the displacements of their center of mass, is probed. In general, the measurement with optical means of the rotational dynamics is technically more challenging than its translational counterpart and usually requires the use of specialized shape [26],[28],[23], or optically anisotropic tracers [6], [54], [45], [47]. DDM has been recently proven to be an effective tool to measure also the rotational dynamics of anisotropic colloidal particles in solution. This can be accomplished, for example, by introducing in the microscope set-up suitably oriented polarizing elements (polarized DDM or p-DDM[47].) or by adopting a dark-field imaging condition (dark-field DDM or DF-DDM [23],[12]).

In this thesis work, we show that DDM can indeed be used as a convenient and reliable tool to perform rotational microrheology experiments, as described in the following. The starting point of our rotational microrheology experiments is the theory, developed in Ref. [47], in which an expression

was obtained for the DDM image structure function extracted from image movies acquired with a suspension of optically birefringent particles placed between partially crossed polarizers[4]. One has:

$$D_P(\mathbf{q}, \Delta t) = A_P(\mathbf{q})[1 - f_P((\mathbf{q}, \Delta t))] + B_P(\mathbf{q}) \tag{4.22}$$

where the intermediate scattering function is the sum of two contributions:

$$f_P(\mathbf{q}, \Delta t) = \alpha(\mathbf{q}) f_{R,T}(\mathbf{q}, \Delta t) + [1 - \alpha(\mathbf{q})] f_T(\mathbf{q}, \Delta t) \tag{4.23}$$

and where $f_T(\mathbf{q}, \Delta t)$ is the translational intermediate scattering function 4.13, $f_R(\Delta t) = e^{-3\langle \Delta\theta^2(\Delta t)\rangle}$ is the rotational intermediate scattering function, $f_{RT} = f_R(\Delta t) f_T(\mathbf{q}, \Delta t)$, and $\alpha(\mathbf{q})$ is a weighting factor determined by the optical properties of the particles and by the angle between the polarizing elements [47].

**Isolating the rotational contribution -** To isolate from $f_P$ the contribution due to the rotational dynamics, we performed both bright-field DDM and polarized DDM (p-DDM) experiments on the same samples. For bright-field DDM we have

$$D_{BF}(\mathbf{q}, \Delta t) = A_B F(\mathbf{q})[1 - f_T((\mathbf{q}, \Delta t))] + B_{BF}(\mathbf{q}) \tag{4.24}$$

which suggests that a suitable linear combination of Eqs. 4.22 and 4.24

$$D_d(q, \Delta t) = D_P(q, \Delta t) - c(q) D_{BF}(q, \Delta t) \tag{4.25}$$

can isolate the term of interest $f_{RT}$. In particular, if the weight $c(q) = [1 - \alpha(q)]\frac{A_P(q)}{A(q)}$ is chosen[5], we obtain

$$D_d(q, \Delta t) = A_d(q)[1 - f_{RT}((q, \Delta t))] + B_d(q). \tag{4.26}$$

that, as shown in Fig.4.8, works very effectively in isolating the roto-translational term $f_{RT} = f_R(\Delta t) f_T(\mathbf{q}, \Delta t)$.
The next step of the analysis relies on the fact that for sufficiently small $q$ the translational dynamics is expected to be much slower than the rotational one and $f_{RT} \simeq f_R(\Delta t)$. This argument can be made more rigorous by noticing that

$$\ln f_{RT}(q, \Delta t) = -3\langle \theta^2(\Delta t)\rangle [1 + \epsilon(q)] \tag{4.27}$$

with

$$\epsilon(q) = \frac{\log f_{RT}(q, \Delta t)}{\log f_{RT}(q, \Delta t)} = \frac{1}{12} \frac{q^2 \langle \Delta r^2(\Delta t)\rangle}{\langle \Delta\theta^2(\Delta t)\rangle} = \frac{2}{9}(aq)^2 \tag{4.28}$$

[4] Experimental details in section 5.1.2.

[5] From a practical point of view it is easier to find the weight $c(q)$ as the number that minimizes the long time slope of the image structure function rather than through estimating $A_P(q)$ and $A(q)$ (more details can be found in the caption of Fig.4.8).

where in the last equality we exploited the GSER in its translational and rotational forms to obtain $\frac{\langle \Delta r^2(\Delta t)\rangle}{\langle \Delta\theta^2(\Delta t)\rangle} = \frac{8}{3}a^2$ where $a$ is the radius of the particles. As a result, if we restrict the analysis to a q-range where $(qa)^2 \ll 1$ we can extract the AMSD as

$$\langle \Delta\theta^2(\Delta t)\rangle \simeq -\frac{1}{3} ln f_{RT}(q, \Delta t) \tag{4.29}$$

The robustness of this approximation can be visually checked in Fig.4.8b, where all the $f_R(\Delta t)$ extracted for different q values in the range $[0.038, 1]\mu m^{-1}$ collapse on a single master curve within 1%.

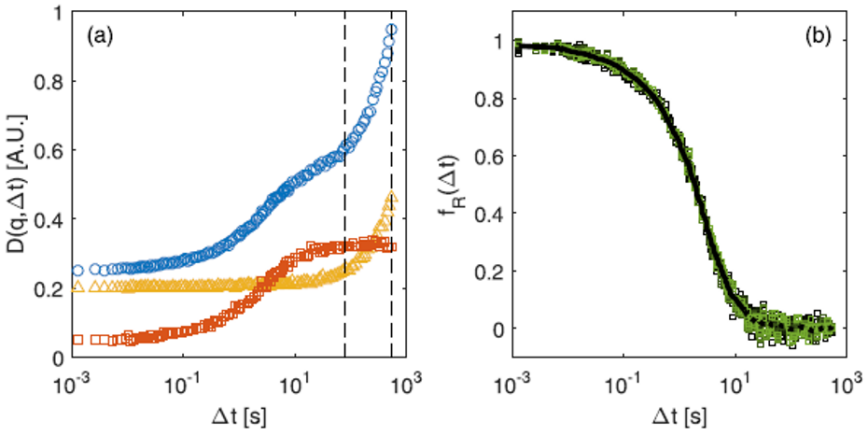


**Figure 4.8:** (a): blue symbols "polarized" structure function $D_P(q, \Delta t)$, for a fixed $q$ ( 0.94 $\mu m$), exhibiting the double decay described in the main text 4.23; yellow symbols bright field structure function; red symbols difference structure function $D_D(q, \Delta t) = D_P(q, \Delta t) - c(q)D_{BF}(q, \Delta t)$. The factor $c(q)$ is chosen to minimize the slope of $D_D(q, \Delta t)$ in the temporal window identified by the vertical dashed lines. (b) $D_D(q, \Delta t)$ for different qs $\in [0.038, 1]\mu m$. Adapted from [44].

So far we have discussed passive microrheology in the absence of external forces applied to the sample, we now turn our attention to the analysis of images during the application of external shear stresses. As already mentioned (Chapter 1), the displacement field of a sheared material (pure shear geometry) can be decomposed in the sum of an affine and a non affine components. In the combined shear+microscopy experiments that are performed in this work, the geometry is the one in of parallel sliding plates 4.9. The image plane is the (*shear*, *vorticity*) plane and the affine displacement corresponds to a rigid translation in the shear ($\hat{x}$) direction.
In the next section, we briefly present a known image correlation technique to measure global displacements, which will be used in our echo DDM experiments (see Section 4.6).

## 4.5 Global displacement detection during shear experiments

If two images differ for a global translation

$$I_1(\mathbf{x}) = I_2(\mathbf{x} + \Delta\mathbf{x}) \tag{4.30}$$

their cross correlation function

$$C(\mathbf{x}') = \sum_{\mathbf{x}} I_1(\mathbf{x}) \cdot I_2(\mathbf{x} + \mathbf{x}') \tag{4.31}$$

has a maximum in $\mathbf{x}' = \Delta\mathbf{x}$. The correlation function is easily computed exploiting the Fourier properties of the convolution product

$$C(\mathbf{x}') = \mathcal{F}^{-1}\{C(\mathbf{q})\} = \mathcal{F}^{-1}\{I_1(\mathbf{q}) \cdot I_2(\mathbf{q})\} \tag{4.32}$$

and, from the fit of the position of the peak of the cross-correlation function, one can determine $\Delta\mathbf{x}$ with a sub-pixel precision.

**Local deformation amplitude** One interesting application of this technique in the context of experiments under shear is to use it as a way to measure the shear induced displacement. As already mentioned, deviations from homogeneity in the deformation field are very likely to occur in shear experiments [77],[40],[39]. In Fig.4.9 we represent schematically the sliding plates geometry that we use in our experiments. The sample is seeded with particles (represented by blue dots). It is clear that for an applied macroscopic deformation, if the deformation field is homogeneous, the particles at different heights (in the cartoon labeled with different colors) will displace of a different amount. If the top plate displace according to an harmonic law: $\Delta x = A\sin(\omega t)$, particles with the same vertical distance from the moving plate will follow an harmonic deformation with amplitude

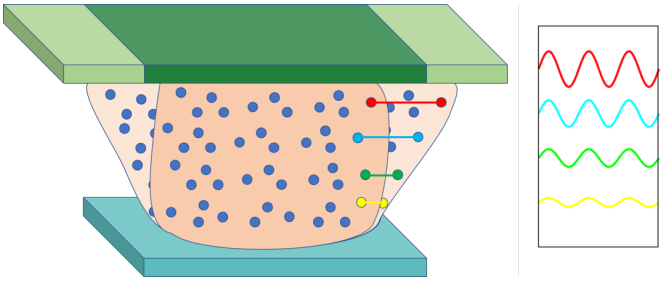

**Figure 4.9:** Cartoon of a periodically sheared sample in parallel plate geometry. The sample is seeded with tracers represented by blue dots. Tracers at different height will follow a different displacement law. To highlight it, in the cartoon, we labeled with different colors four tracers at different vertical position. The graphic on the right report the displacement law for the tracers of corresponding colors. The displacement curves have an off-set in the graphic according to their vertical position.

$\Delta x(z) = A \cdot z/H \sin(\omega t)$ (represented in the graphic Fig.4.9). In our experiments we are able to image a relatively narrow vertical portion of the sample, such that the imposed displacement appears like a global rigid displacement. We can acquire stacks of images at different height and, with the **global displacement** method, measure the deformation amplitude.

In order to apply the **global displacement** method the superposition between two images has to be good enough to have a contrasted peak in the correlation function 4.32. As rule of thumb, we consider that if the displacement between two following images is smaller than one quarter of image, the correlation function peak will still be sufficiently contrasted.

In Fig.4.10 we report an example of the described procedure for a single acquisition at a fixed vertical position. Fitting the displacement with a sinusoidal function we can measure the exact frequency of the imposed deformation[6], and the local amplitude of deformation.
If the microscope is been set to have a small focal depth[7] repeating the measurement at different heights one can extract the local amplitude and the local shear gradient with a good accuracy Fig.4.11.

## 4.6 Echo DDM

The **echo DDM approach** consists ideally in performing a DDM analysis on movies in which each frame is acquired exactly one oscillation period after the previous one. In this way, in the image difference

$$I(\mathbf{x}, t) - I(\mathbf{x}, t + nT)$$

[6] See sections 4.6.1 and 5.3.3 for an in-depth discussion.
[7] Detail of the optical settings in Chapter V.

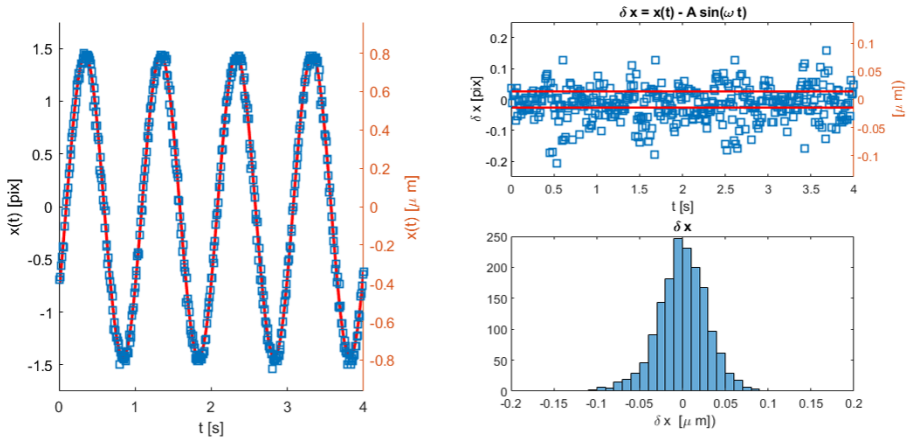


**Figure 4.10:** Main panel: shear induced global displacement measured as described in the main text. From the fit we can extract the amplitude (and compare it with the expected amplitude in absence of shear), the frequency (to synchronize deformation and acquisition 4.6.1). Top right panel: deviation from the sinusoidal fit $\delta x$. Bottom right panel: histogram for $\delta x$. The deviation from the sinusoidal fit accounts both for *localization error* and for imperfection of the imposed deformation profile.

all the reversible displacements cancel out and only plastic particle rearrangements contribute to the difference signal. However, one needs to proceed with caution to minimize the possible issues that can arise in practice.

### 4.6.1 Synchronization issues

For the success of the echo DDM approach the acquisition cycle period has to be synchronized with the deformation cycle period. If we want to characterize the dynamics over hundreds of periods the error on the period has to be small

$$\Delta T \ll \frac{T}{100},$$

simply because a mismatch of the periods of 1 part over hundred takes to a mismatch of a full period after hundred oscillations.
In Fig.4.12 we show the difference between a fully synchronized image acquisition (panel a) and two out-of-sync cases with 1 % (panel b) and 10 % (panel c) frequency mismatch. In all the three panels, the continuous blue line represent the cyclic deformation applied to the sample and the symbols represent observations with different starting points (red $t_{start} \simeq T/8$, yellow $t_{start} \simeq T/4$, violet $t_{start} \simeq T/2$ ). If $\Delta\nu \neq 0$ an apparent oscillatory displacement is observed. The period of the apparent displacement depends on the frequency mismatch. For small values of $\Delta\nu/\nu$ the apparent displacement looks like a drift at constant velocity but the amplitude and the sign

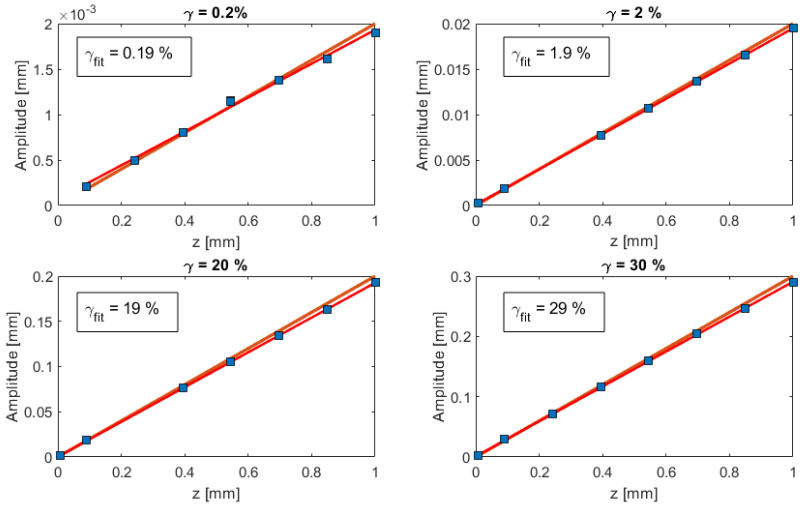


**Figure 4.11:** Vertical scan on a Sylgard gel. Symbols represent the amplitude measured by a sinusoidal fit of the displacement for fixed shearing amplitude at different vertical positions. The lines represent the expected affine behavior (dark red) and the fit with a linear non homogeneous function (light red). The agreement with the expected behaviour is satisfactory.

of the velocity depends on the starting point of the acquisition cycle. While synchronization issues are not a serious issue in echo light scattering experiments[8] [92], in a DDM experiment one should face the limitations arising from the use of detectors with a limited acquisition rate (max $\sim 1kHz$) and from the need of saving long movies acquired with very large frame rates. Our acquisition strategy consists in acquiring few images ($\sim 10$) per period with an acquisition frequency optimized to match the actual deformation frequency. The detailed aspects of the frequency matching (synchronization) protocol are described in 5.3.3. Here it suffices to say that our procedure leads to a typical residual frequency difference of $\Delta\nu/\nu \lessapprox 10^{-4}$. This value, however small it may seem, causes an apparent drift with a phase dependent velocity in the echo movies, the removal of which requires a successive registration process.

### 4.6.2 Image registration

An accurate image registration procedure requires that the main signal in the images arises from the sample. Since this is not always true in microscopy

[8] Light scattering detectors are so fast to allow the acquisition of the scattered intensity with a rate ($1MHz$) way larger than the deformation frequency ($\sim 70Hz$), which enables *a-posteriori* frequency matching

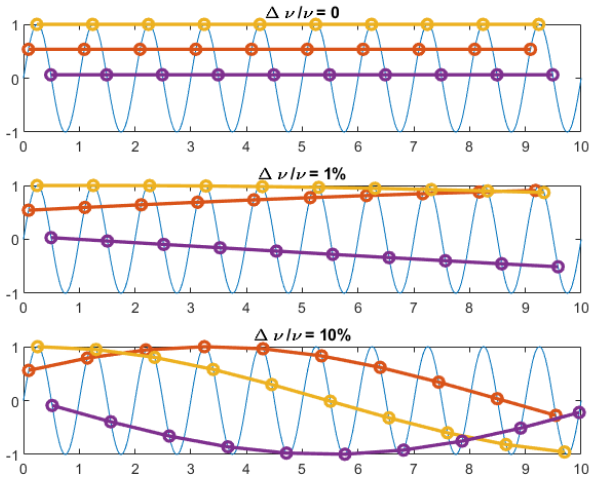


**Figure 4.12:** Effect of a frequency mismatch between a cyclic sample deformation and a cyclic image acquisition with the same frequency (a), with 1 % mismatch (b) and with 10 % mismatch (c). The blue line represents the position of the sample as a function of time, the symbols represent observation with a period $\nu_{acq} = \nu_{def} - \Delta\nu$, for different starting points: red $t_{start} \simeq T/8$, yellow $t_{start} \simeq T/4$, violet $t_{start} \simeq T/2$.

experiments, we need a pre-processing step to **remove the static background**. Since we acquire roughly ten images per period, if the affine shear induced displacement is large enough we can find the static background by averaging all the images acquired within a period

$$B(x) = \langle I(x,t) \rangle_{\varphi}. \tag{4.33}$$

When non affine dynamics is also observed, the accuracy of the background characterization is increased by averaging on several periods. If the optical conditions are unchanged the same background images can be used for different acquisitions.

Once the so-obtained background is subtracted, we proceed in measuring the apparent global displacement. The temporal variable can be conveniently expressed in terms of the number of periods $n$ and of the initial phase $\varphi$

$$t = nT + \varphi$$

and, from this point on, we will consider the series of images with different $\varphi$ as if they were different replicas of the same experiment

$$I(t) = I(nT + \varphi) = I_{\varphi}(n) \quad \varphi \in (1, N_{\varphi})$$

**Global displacement detection -** The global displacement is measured with the image correlation algorithm just described in 4.5. If the rigid translation is combined with a rearrangement the contrast and the sharpness of the correlation function peak diminish [27]. In our case, it is sufficient that the correlation peak survives one deformation cycle. The fulfilment of this requirement depends, of course, on the sample and on the deformation amplitude. In most of our experiments the condition is satisfied. For some experiments at high shear amplitude ($\gamma \sim 100\%$) and with weak particles' contrast (polystyrene particles $r \simeq 250$ nm, magnification 20X) the procedure failed.
For a fixed phase $\varphi$, we compute the series of displacements between images

$$\Delta\mathbf{x}_\varphi(n) = \Delta\mathbf{x}\{I_\varphi(n+1); I_\varphi(n)\} \tag{4.34}$$

which we can use (Fig.4.13) for feeding the registration algorithm for each phase-dependent image stack $I_\varphi(\mathbf{x})$ with the suitable displacement before computing the image structure functions.

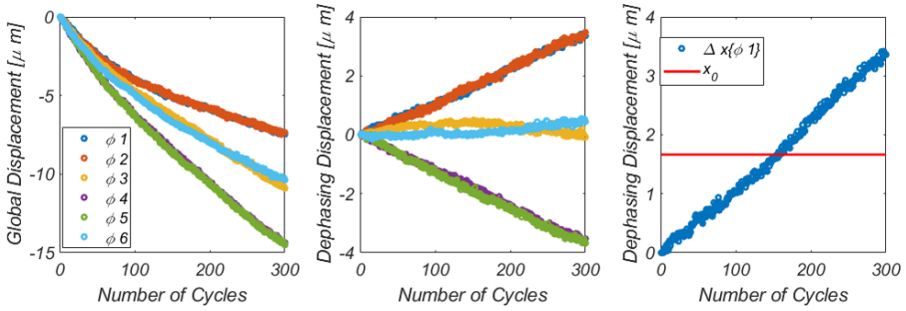


**Figure 4.13:** Fisrt panel: displacement with respect to the first image of the stack $I_\phi$ for different phases $\phi$ (labeled by the colors). The total displacement is a superposition of a global (phase independent) drift plus a phase dependent apparent displacement (second panel). Third panel: $\Delta x_{\phi=1}$, to maximize the overlap all the images of this stack are registered with respect to an intermediate position $x_0 = \Delta x(N_{max})/2$.

**Registration -** Each image stack is registered with respect to the position $x_0 = \Delta x(N_{max})/2$ (Fig.4.13 c), to maximize the overlap region between images. This precaution is particularly relevant when the displacements are large compared to the image size ($\Delta x \sim \frac{1}{4}$Image Size).

The sub-pixel registration is implemented in the Fourier space by multiplying the image to be registered with the translation kernel

$$K_{l,m}(\Delta x, \Delta y) = exp(i\delta) \cdot exp\Big(i2\pi(l\Delta x + m\Delta y)\Big) \tag{4.35}$$

where the phase constant is $\delta = \pi(\Delta x + \Delta y) - \lfloor(\Delta x + \Delta y)\rfloor$ and where $\lfloor x \rfloor$ indicates the integer part of $x$.

An *inverse transform* is then performed and the translated image is *cropped* to get rid of the artifacts arising from the periodicity of the Fast Fourier Transform algorithm (Fig.4.14). For all our experiments, we cropped

**Figure 4.14:** An image translated of $\Delta\mathbf{x}$ (red arrow), *via* the method described in the main text. Notice the artifact due to the periodic boundary conditions of the Fourier transform: the portion of image that *exits* from the right and the bottom *enters* from the left and the top.

the 512 x 512 pixels images down to 384 x 384 pixels. Of course, this poses an upper limit to the apparent image drift caused by synchronization issues. This limit was strictly enforced in our analysis by rejecting all the temporal delays for which the corresponding image displacement was larger than 128 *pix*. Retrospectively, we found that for all the cases in which rejection occurred, the particle dynamics of interest took place on time scales that were way shorter than the time delay of the rejected images.

## 4.7 $q$-resolved dynamic susceptibility $\chi_4(q,\tau)$

We present here a brief description of a novel technique to measure the q-resolved dynamic susceptibility from a series of microscopy images [91]. The algorithm was tested on a quasi-2D dense colloidal suspension in the vicinity of the glass transition. The same sample has been characterized in Ref. [89] with a different method and it was shown to display a marked dynamical heterogeneity (DH) .

$\chi_4^0$, the dynamic susceptibility, is generally defined as the second central moment of a dynamic observable (or order parameter) $s$

$$\chi_4^0 = \langle s^2 \rangle - \langle s \rangle^2. \tag{4.36}$$

In our case the dynamic observable is $d$, whose temporal average gives the dynamic structure function:

$$D(\mathbf{q}, t) = \langle d(\mathbf{q}, t, \tau) \rangle_t \tag{4.37}$$

where $d$ is the power spectrum of the difference of a pair of images.
Dynamical heterogeneity emerges in the correlation of wave vectors with the same modulus and different directions. While on the single wave vector DH are not apparent, it becomes evident when we study the temporal distribution of the azimuthal average of the two point structure function:

$$d(q, t, \tau) = \langle d(\mathbf{q}, t, \tau) \rangle_{|\mathbf{q}|=q}. \tag{4.38}$$

The structure function for the single wave vector for independent Brownian particles has the following property:

$$\langle d(\mathbf{q}, t, \tau)^2 \rangle_t = 2 \langle d(\mathbf{q}, t, \tau) \rangle_t^2. \tag{4.39}$$

It follows that when we consider the distribution of the azimuthally averaged structure function $d(q, t, \tau)$ its fluctuation will be reduced in reason of the number of independent variables involved in the azimuthal average:

$$\chi_4^0(q, \tau) = \langle d(q, t, \tau)^2 \rangle_t - \langle d(q, t, \tau) \rangle_t^2 = (1/N_q) \langle d(q, t, \tau) \rangle_t^2 \tag{4.40}$$

where $N_q$ is the number of *independent* wave vectors used in the azimuthal average.
For systems presenting DH the dynamic heterogeneity is modified in

$$\chi_4^0 = \langle d(\mathbf{q}, t, \tau)^2 \rangle_t - \langle d(\mathbf{q}, t, \tau) \rangle_t^2 = \chi_\infty (1/N_q) \langle d(\mathbf{q}, t, \tau) \rangle_t^2 \tag{4.41}$$

with $\chi_\infty < 1$.
If, on top of this, an additional time-dependent contribution to the dynamic susceptibility is present, we can highlight it by subtracting to the dynamic susceptibility $\chi_4^0$ the part proportional to the square of the structure function. We define $\chi_4$ as :

$$\chi_4(q, \tau) = \chi_4^0(q, \tau) - \chi_\infty / N_q \langle d(\mathbf{q}, t, \tau) \rangle_t^2. \tag{4.42}$$

The so-defined dynamic susceptibility is expected to have a peak at the relaxation time, and the height of the peak is expect to be proportional to the *fraction* of particles involved in the collective rearrangement. The edge effect presented in section 4.1 adds a spurious decay that would impair the analysis. We mitigate this effect by applying a windowing procedure [48]. As anticipated multiplication for the window function in the real space introduces correlations among different wave vectors in the structure function. We can include this effect in $N_q$ Eq.4.40. This will introduce a difficulty in the prediction of the dynamic susceptibility $\chi_4^0$ that will not depend only on

$\chi_\infty$ and on trivial geometrical factors. As a consequence we will estimate the ratio $\chi_\infty/N_q$ from the ratio between the second and the first moment of the structure function:

$$\frac{\langle d(q,t,\tau)^2\rangle_t}{\langle d(q,t,\tau)\rangle_t^2} = \alpha(q) = 1 + \chi_\infty(q)/N_q.$$

We tested our algorithm on a dataset that is known to present DH [89]. Experimental images were obtained in previous experiments [90], aimed at investigating single particle motion in glass formers with particle tracking. Quasi-2D hard-sphere-like colloidal suspensions at different area fractions $\phi$ were obtained by using a 50:50 binary mixture of silica beads dispersed in water. Surfactant (Triton X-100 0.2% v/v) was added to the solution to avoid van der Waals-induced particle sticking. Large and small beads diameters measure $d_l = 3.16\mu m$ and $d_s = 2.31\mu m$, respectively, resulting in a 1.4 ratio, which prevents crystallization. The experiments are performed in condition of thermodynamic equilibrium. The dataset we studied is at area fraction $\phi = 0.77$, below the estimated glass transition $\phi = 0.80$-$0.81$ for this system. In Fig.4.15 we show the second central moment $\chi_4^0(q,\tau)$ rescaled with $\alpha$ and the square of the first one $d1(q,\tau)$[9] properly normalized.
Given that the leading contribute in $d_2$ is $\propto d_1^2$ we fit both these functions with the same functional model $a\{1 - exp[-(\Gamma t)^s]\}$ to find a good approximation of $\alpha$. We use alpha to obtain the DS $\chi_4$:

$$\chi_4 = \chi_4^0 - (1-\alpha)d_1^2 \tag{4.43}$$

This is reported as a black line in figure 4.15 (to have it on the same scale of the structure functions we multiply it for a factor 50). In panel top right we report $1 - \alpha(q) = \chi_\infty/N_q$. As expected $\chi_4$ has a peak in correspondence of the relaxation time, and goes to zero for longer times. In the top right panel we report the ratio $\chi_\infty/N_q$ (we can't estimate the values of $N_q$ and $\chi_\infty$ separately). This object is remarkably q independent. The value of the maximum is reported in the second panel from the top. The red full symbols correspond to the values of the q plotted in the bigger panel. The maximum shows oscillation in q. The origin of such oscillation is, to the best of our knowledge, still unknown.

## 4.8 Activity Maps

To investigate the spatial and temporal heterogeneity of the dynamics we built **activity maps**

$$M_0(\mathbf{x},t) = |I(\mathbf{x},t) - I(\mathbf{x},t+T)|^2 \tag{4.44}$$

[9] We are here assuming that the noise contribution is negligible. This assumption is delicate since noise and signal couples in higher order moments of the structure function.

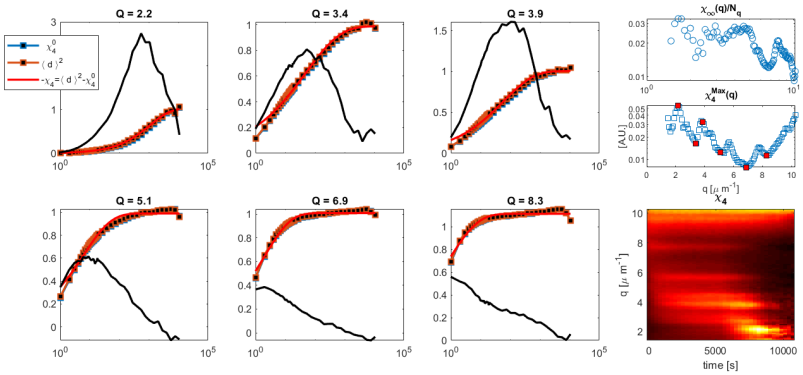


**Figure 4.15:** $q$-dependent dynamic susceptibility in a quasi 2D dense colloidal suspension. In first six panels on the left: rescaled dynamic susceptibility: $\chi_0/(1-\alpha)$ (blue squares), square of the structure function:$(D(q,\Delta t))^2$ (red squares), rescaled dynamic susceptibility $50 \cdot \chi_4$ (black lines). Each panel corresponds to a different wave-vector $Q$, as indicated in the title (units $= 1/\mu m$). Right top panel: scaling factor $\chi_\infty/N_q$. Right central panel: $\chi_4$ peak height. Red symbols identify the wave-vectors reported in the six panels on the right. Right bottom panel: $\chi_4(q,\Delta t)$.

which were successively binned in such a way that each bin of the binned activity map

$$M(\mathbf{X},t) = M(l,m,t) = \sum_{i,j=0:n_B-1} M_0(l \cdot n_B + i, m \cdot n_B + j) \tag{4.45}$$

contained some particles. In Eq.4.45, $n_B$ is the dimension of the new bin, $N_{pix}$ the number of pixel of the original image and we have $l, m$ going from one to $N_{pix}/n_B$. If the particles displacements between two cycle events are small compared to their size, $M(\mathbf{X},\mathbf{t})$ is an image where the intensity within a bin is proportional to the MSD of the particles contained in that bin [13] Fig.4.16.

We report in Fig.4.18, some typical activity maps for a sample sheared at different amplitudes (increasing from left to right) in the non linear regime. Already from visual inspection of the activity maps, it appears how the presence of active regions within the sample can be clearly spotted.
Once the activity map $M(\mathbf{x},t)$ is available, one can define several quantities. Some typical examples are provided below.

**Average activity** By performing a spatio-temporal averaging one can quantify the average activity

$$\mathcal{A}(\gamma_0) = \langle M(\mathbf{x},t)\rangle_{\mathbf{x},t} \tag{4.46}$$

associated with a certain shearing amplitude, which can be used, for instance, to single out the microscopic signature of plasticity (Fig.4.17).

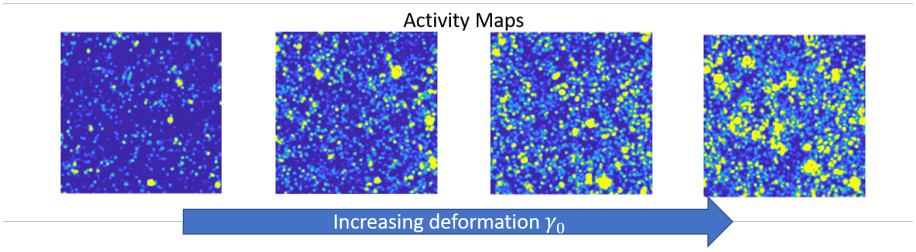


**Figure 4.16:** Activity maps as defined in the main text for a Yield Stress Fluid (Carbopol) sheared with increasing (from left to right) deformation amplitude in the non linear regime. The activity increases as a function of $\gamma$ and spatial heterogeneity is apparent.

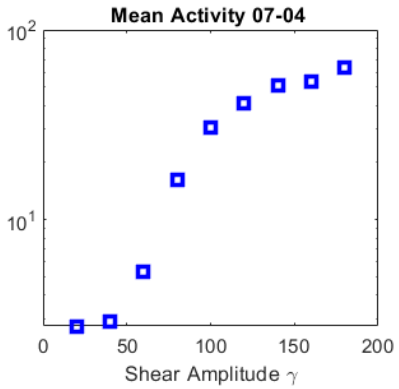


**Figure 4.17:** Mean Activity $\mathcal{A}(\gamma_0)$ for an Yield Stress Fluid (Carbopol).

**Size and connectivity properties of the active zones** By setting a threshold above which a site is considered active one can learn much about the resulting spatial distribution, dimension and connectivity of the active sites. We report in Fig.4.18 typical results of this analysis in a simple Yield Stress Fluid (*Carbopol* see Chapter V for details).

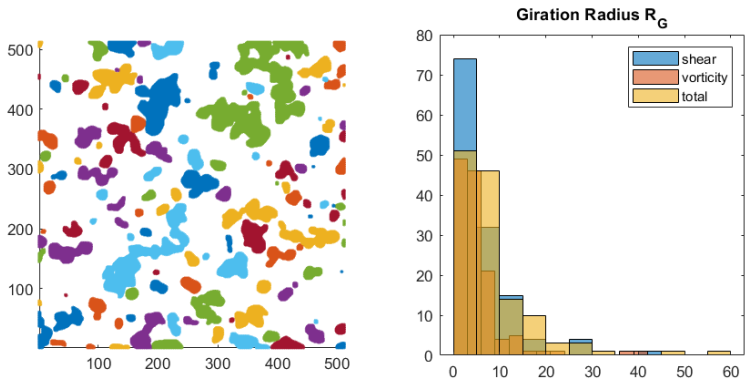


**Figure 4.18:** Left panel: active sites in a periodically sheared simple Yield Stress Fluid with an amplitude $\gamma = 40\%$. Neighbouring active sites are considered belonging to the same active zone and labeled with the same color. Right panel: histogram for the gyration radius of the active zones in the shear direction (blue columns) , vorticity direction (red), average (yellow).

# Chapter 5

# Experimental

## 5.1 Sample preparation

### 5.1.1 Newtonian liquids: water/glycerol mixtures

By mixing water and glycerol in different amounts we obtain Newtonian liquids spanning roughly three decades in viscosity $\eta \in (0.001, 1.4) Pa\ s$. In Table 5.1, we report some properties of interest for the four mixtures that we used in this work. Of particular interest is the expected viscosities at 22° [25], together with their uncertainties. The large uncertainty in the viscosity of the sample with the largest glycerol concentration is due to (i) the sensitivity of the glycerol/water viscosity to small concentration uncertainties and (ii) the large uncertainty in concentration arising from the known tendency of glycerol to adsorb water from the atmosphere.

**Tracers -** For water-based samples we employ polystyrene latex beads as tracers. For microrheological experiments we used Sigma Aldrich *LB5* (solid content 10%) particles (nominal diameter 0.45-0.47 $\mu m$), whose radius was measured with DDM to be $a_5 \simeq 223$ nm.

| c ($g/w\ wt/wt$) | $\eta$ (mPa s) at 22° | $\phi_{tr}$ (-)) |
|---|---|---|
| 0 | $0.914 \pm 0.01$ | 0.075% |
| 48.8% | $4.9 \pm 0.05$ | 0.14% |
| 82.7% | $69.2 \pm 0.7$ | 0.18% |
| 97.5% | $702 \pm 50$ | 0.2% |

**Table 5.1:** Properties of the water/glycerol mixtures used as control Newtonian liquids. From left to right: glycerol concentration, sample viscosity, volume fraction of the tracers.

### 5.1.2 Viscoelastic samples: PEO aqueous solutions

A polymer solution in the *semidilute* regime is a good reference viscoelastic sample. The semidilute regime is defined in terms of the *overlap concentration* $c^*$. To evaluate the latter, we need to consider that, in dilute conditions, linear polymers in good solvents assume a coil configuration with a gyration radius approximately scaling as a power law

$$R_G = aM_w^{3/5} \tag{5.1}$$

of the polymer molecular weight $M_w$, in our case $M_w = 2 \cdot 10^6 Da$, where $a$ is a constant that depends on the chemical details of the monomer and on the flexibility of the polymer chain. For Polyethylene Oxide (PEO) $a = 0.215\text{Å}/kDa$ [34]. The overlap density is defined as

$$c^* = \frac{N}{V} = \left(\frac{4}{3}\pi R_G^3\right)^{-1} \tag{5.2}$$

corresponding to the situation where the sum of the volumes occupied by spheres of radius $R_G$ is equal to the available volume:

$$N\ \frac{4}{3}\pi R_G^3 = V.$$

While for polymer concentrations below $c^*$ the individual polymer chains do not feel each other too much, for $c > c^*$, *i.e.* in the **semi-dilute** regime, chains strongly interact with each other and are strongly compressed, which gives rise to a macroscopic elastic behaviour at a short time scale after the material is macroscopically deformed. Indeed, waiting long enough, the stored elastic energy can relax, as the chains are free to slide one onto another, and the sample exhibits a viscous behaviour. In essence, this is the behaviour of a viscoelastic liquid.
One sample property that is worth knowing for microrheology experiments is the typical mesh size $\xi$ that characterizes the temporary network formed by the polymer coils. One has [34]

$$\xi \simeq R(c/c^*)^{-3/4}.$$

where $R$ is the radius of the polymer in unperturbed state which highlights the fact that $\xi$ decreases monotonically with the polymer concentration. In this work we used a concentration 2% wt/wt (corresponding to $c/c^* \simeq 22$) that provides a mesh size $\xi \sim 10$ nm.

**Tracers -** The beads were purchased from Sigma Aldrich with the part numbers LB1 (nominal diameter 0.10˘0.12 $\mu m$, solid content 10%) and LB5 (nominal diameter 0.45˘0.47 $\mu m$, solid content 10%). The bead sizes were also tested with DDM and were found to be equal to $0.112 \pm 0.002$ $\mu m$

and $0.445 \pm 0.005$ $\mu m$ for the LB1 and LB5 samples, respectively. the final concentration of tracer beads was $(1.00 \pm 0.05)10^{-3}$ wt/wt. To ensure multiple scattering for the DWS experiment we used LB5 particles at $(1.00 \pm 0.05)10^{2}$wt/wt. For the p-DDM experiment we used spherical colloidal particles with a polymerized nematic liquid-crystal core, whose birefringence makes the particles optically anisotropic, with a uniaxial symmetry [54], [45], [82], [41]. The concentration of optically anisotropic tracers was $(1.8 \pm 0.2)10^{3}$ wt/wt. The diameter of the tracers ($0.22 \pm 0.03$ $\mu m$) was determined by measuring with bright-field DDM the translational diffusion coefficient of a diluted dispersion in pure water. The tracers are dispersed in the sample and mixed with the help of a spatula and a vortex mixer. The air bubbles, incorporated during tracers dispersion, are expelled trough centrifugation.

**Sample loading and sealing -** At the end of the preparation procedure, the sample is loaded into a transparent glass capillary with rectangular cross-section of internal dimensions: $10 \times 2 \times 0.1$ mm. After sample filling is completed, the capillary is sealed with a UV-reacting glue. During the exposure of the capillary to UV radiation, the central part of the capillary is covered with an aluminium foil in order to protect the polymer form radiation damages.

### 5.1.3 Elastomeric solid: Sylgard

*Sylgard 184* (Dow Corning) is a cross-linked transparent silicon elastomer. We chose it as a model system to test the shear cell, in particular for the validation of the vertical scan procedure and for the validation of Echo DDM in the purely elastic regime. The sample is obtained mixing a *base* element (silicon oil) with a *cross-linking agent*. After mixing the two elements, solidification occurs in few hours, the exact value depending on the sample temperature [111].

**Tracers -** Before adding the cross-linking agent, we disperse in the base PMMA particles of radius $a \simeq 500$ nm. Once the particles are homogeneously dispersed in the base we add the curing agent in a ratio of $1/60\frac{wt}{wt}$. We then mix with the help of a vortex mixer, centrifuge to get rid of air bubbles, and we pour the (still liquid) sample on the bottom slide of the shear cell. We then lower the top slide until contact with the sample is reached. After 48 h the system is solidified and firmly attached to the glass slides.

### 5.1.4 Simple yield stress fluids: Carbopol microgels

The Simple Yield Stress Fluid we use in this work is a microgel-based *soft-glass* known with the commercial name of *Carbopol* (Lubrizol). *Carbopol*

is widely used as thickener in industrial applications (e.g. hair gels) and is often used as a model system for the study of the yielding transition because it is perfectly transparent and exhibits reproducible flow properties. The solid behaviour is essentially given by a jamming mechanism, and not by irreversible cross linking between the different microgel particles. The system is very easy to flow and the transition is reversible: when the flow is stopped the mechanical solid properties are rapidly recovered. *Carbopol* exists in several types, all sharing similar composition. In this work, we use *Carbopol 971 P NF*.

**Sample preparation -** *Carbopol 971 P NF* is sold as a water-soluble powder. We disperse the powder in filtered Milli-Q water in a 0.5% wt/wt ratio. The resulting dispersion is gently stirred until the powder is dissolved and an homogeneous state is reached, whose pH is strongly acidic. To neutralize the pH of the dispersion, we add during stirring few drops (of the order of tens of *microliters* over 10 ml) of NaOH $10M$. When the pH is raised, the polymeric microgels swell and the effective volume fraction increases reaching a jammed state. We leave the system to equilibrate few hours and we check the pH. The procedure is repeated until a neutral pH is reached.

**Tracers -** Once the system equilibrates, we take a small amount of sample ($0.5\ ml$) and we add the desired quantity of tracers (final volume fraction $\phi = 0.03\%$). We disperse the particles using a vortex mixer and we get rid of the bubble by centrifuging it. Previous studies on similar systems showed that the size of the microgels is quite polydispersed and the average radius is of the order of magnitude of few microns. We thus disperse tracers of different sizes with the idea of probing length scale both smaller and bigger than the material characteristic structural lenght-scale. The following radii were used:

- $a_1 = 28\ nm$ LB1 (Sigma Aldrich)
- $a_2 = 1\ \mu m$
- $a_3 = 2.5\ \mu m$ (Microparticles)

**Sample loading and sealing -** Once the sample is seeded with tracers, with the help of a spatula we smear it on the bottom slide of the shear cell. To avoid evaporation we surround the perimeter of the sample with a fluorinated oil (*Solvay Fomblin Y25*).

### 5.1.5 Depletion gels: PMMA suspensions with added polybutadine

A class of reference system, widely studied from theoretical, simulation and experimental points of view are colloidal gels obtained with hard-sphere particles interacting via short-range, depletion-induced interaction. A widespread experimental realization of such gel is obtained with PMMA particles in a suitable solvent. The appeal of the system is the high control that one can achieve on the *starting condition*

1. Particles are synthesized with high control of the size distribution
2. In the absence of polymers, the particles interacts via a hard-sphere potential
3. Adding the polymer turns on an attractive short-range interaction, with tunable range and intensity
4. the colloidal particles are easily fluorescently labeled and the system can be studied with confocal microscopy even at high density
5. for PMMA particles a density and refractive index matching solvent exists
6. out-of-equilibrium systems with short range interaction are easier to simulate and have a rich phase behaviour than their long-range counterparts

Even though the starting conditions and the interactions are under good experimental control, the result in terms of mechanical properties, and in particular the yielding behaviour of hard sphere depletion gels, is quite complex: these gels are typically thixotropic, they exhibit shear banding and shear history dependence [65].
In this work, we are interested in studying the yielding of high density gels with volume fraction $\phi \simeq 40\%$. The experiment presented in Sect.6.5 are on gels obtained with colloids of size $R \simeq 170\ nm$. To avoid multiple scattering at this volume fraction we need to keep the refractive index mismatch between the particles and the solvent at $\Delta n \sim 0.01$. *Decalin* and *cycloheptylbromide* (CHB7) combined in the right proportions accurately matches the PMMA refractive index and density, but CHB7 reacts with oxygen and so the properties of the system change quickly if the sample is not perfectly sealed. *Squalene* is another organic solvent that almost perfectly matches the refractive index of PMMA and does not evaporate or react with elements in the atmosphere. Adding a minor percentage of *Octadecene* ($\sim 20 - 30\%$) we can take the system to the desired refractive index mismatch.
Our PMMA particles are synthesized by Mr. Manuel Alejandro Escobedo

Sanchez, currently a PhD student at HHU Dusseldorf (Prof. Stefan U. Egelhaaf lab). The particles are shipped in a mixture of *Decalin*, *hexane* and other organic solvents. The preparation procedure requires three washings in hexane and five in the final solvent: either *Decalin*, good for storage, or *squalene* for final use. For each washing, we start with a sample at $\phi \sim 30\%$, we centrifuge it until it separates in a solvent phase and a random close packing phase. We remove the solvent and we replace it with new solvent. We ridisperse the particles. The time required for a complete washing is variable and depends on the particle size, the particle-solvent density mismatch, the solvent viscosity, and the particles-solvent affinity.
Once a sample with the desired properties is obtained, gelation is induced with a depletion mechanism by using the short linear polymer Polybutadine average hydrodinamic radius $R_{PB} = (20 \pm 5)nm$. The size of the polymer was checked by DLS. A similar system was already studied under shear with DWS [69].

## 5.2 The optical setup

### 5.2.1 Microscopes: Nikon Ti-S and Ti-E

The imaging instruments used in this work are both inverted microscopes: *Nikon Eclipse Ti-S* and *Nikon Eclipse Ti-E*. Both microscopes models have

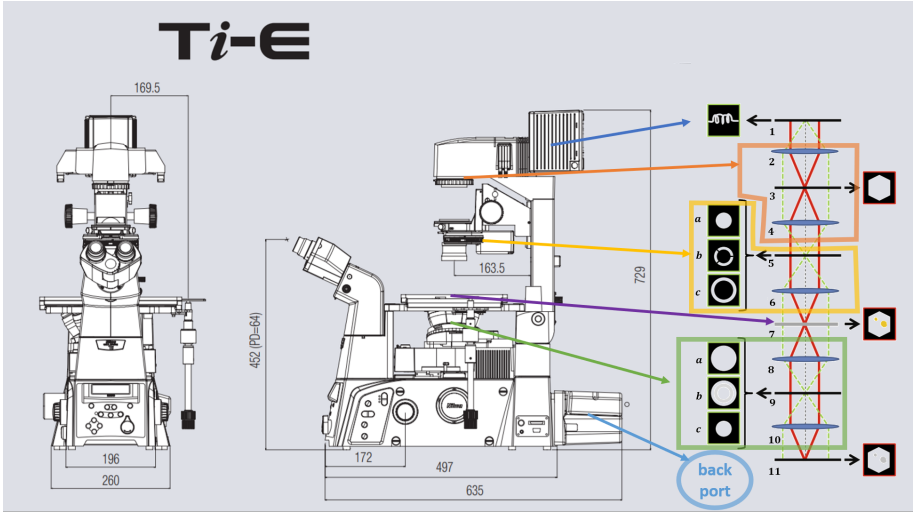


**Figure 5.1:** Front sight, side sight and optical scheme of a Nikon Ti-E inverted microscope. Lamp (1), collimating lens (2,4), field diaphragm (3), aperture diaphragm (5), condenser (6), object plane (7), objective (8,9,10), camera sensor (11). Microscope Nikon, optical scheme adapted from [49].

two illumination ports (one on the top) Fig. 5.1 1. for: bright field, polarized microscopy, phase contrast. The back port is used in this work for: reflection illumination and laser-based alignment system of the shear cell.

When the condition of the Koehler illumination is realized we have two series of conjugated planes Fig. 5.1: $(1, 5, 9)$ are the first set of planes, conjugated with the source and $(3, 7, 11)$ are the second set of planes conjugated with the object. Moreover the field impinging on the second set of planes is the Fourier transform of the first set.

In the Ti-S model, the position of the objectives is controlled by a mechanical double wheel, a coarse wheel, and a fine graduated wheel with $10\mu$m spaced ticks. The vertical position of the objectives is locked mechanically. Compared to the S-model, the E-model has some additional features, among which we mention the following:

- the position of the objectives is controlled electronically
- a feedback-based positioning system (Perfect Focus) is available that

| Aperture Diaphragm | Spatial Coherence | Focal Depth | Transmitted Power | Image Definition | q-range (fixed $I_0$) |
|---|---|---|---|---|---|
| **Closed** | Maximized | Max | Min | Min | Max |
| **Open** | Minimized | Min | Max | Max | Min |

**Table 5.2:** Summary of the effect of varying the size of the aperture diapraghm in a microscope under Kohler illumination conditions

maintains fixed the vertical position of the image plane

- the microscope is installed on an optical table, with a pneumatic system for vibrations' isolation and damping.

**Bright Field microscopy -** The Koehler configuration allows to tune the spatial coherence of the illumination and, as a consequence, the focal depth: when the aperture diaphragm Fig. 5.1 (5.a) is ideally shrunk to a point, the light field impinging on the objective plane is a plane wave with perfect spatial coherence; *viceversa*, when the aperture diaphragm is fully open we have a continuous superposition of plane waves propagating within an extended range of azimuthal angle $\theta$ with respect to the optical axis, each one of them having no prescribed phase relation with the others. In the latter condition the spatial coherence is thus minimized. As also summarized in Table 5.2, increasing the spatial coherence comes at the expense of image intensity because of the reduced apparent size of the light source. For this reason, a compromise needs to be found that changes from experiment to experiments. As a general rule we use the following criteria:

- the power of the lamp is generally kept at its maximum value, also because its emission spectrum depends on the current flowing in the lamp
- once the objective and the frame rate are fixed, we fix the exposure time. A conservative choice for the maximum exposure time is that it is at least a factor of ten smaller than the time between successive frames *i.e.*
$$\tau_{exp} \leq \frac{1}{10}\Delta t_0$$
- if strictly needed, we increase the counts on the detector by opening the aperture diaphragm
- for experiments under shear, where different planes possibly have different local shear and thus different dynamics, we also tune the aperture diapraghm to obtain the desired focal depth (see Table 5.2)

As a final remark, we note that for bright field microscopy experiments the image is formed from the interference of the transmitted light ("local oscillator") and the field scattered from the sample:

$$E(x) = E_0 + E_S(x) \tag{5.3}$$

$$I(x) = I_0 + 2\mathcal{R}e\{E_0 \cdot E_S^*(x)\} + |E_S(x)|^2. \tag{5.4}$$

As long as the optical density of the sample is such to ensure a single scattering regime, the $|E_S(x)|^2$ term is negligible and the image formation process is linear

$$I(x) \simeq I_0 + 2\mathcal{R}e\{E_0 \cdot E_S^*(x)\}, \tag{5.5}$$

which means that the DDM technique can correctly probe the sample dynamics [46].

**Polarized microscopy -** Polarized microscopy is implemented by introducing a polarizer, typically between the condenser and the aperture diaphragm Fig. 5.1 (4-5), and an analyzer between the objective (9) and the sensor plane (11). Partially-crossed polaryzers ($\beta \simeq 75°$) allow to be sensitive to birefringence maintaining the linearity of the image formation process (see Eq. 5.5).

**Reflection and Fluorescence microscopy -** In some cases, for instance when the microscope is coupled to a commercial rheometer, it is used in reflection mode, since only one optical access is possible. In other cases, the signal of interest comes from the fluorescent emission of suitable flurophores. In these configurations, the optical scheme is slightly different from the bright-field one: light is sent onto the sample and collected from the same side, which is typically done through:

- a beam splitter in the case of reflection
- a beam splitter coupled with a dichroic mirror plus a filter in the case of fluorescence.

While fluorescence offers the appealing advantage of filtering out all the unwanted contributions in the image, the fluorescent signal is normally low, which requires relatively long exposure times that are not compatible with our willingness to study fast dynamics under shear. For this reason we do not present data obtained in fluorescence microscopy.

**Microscope objectives -** For our aims, the most important features that identify an objective are the **magnification**, the **numerical aperture** (NA), the **working distance**. We report in the following table some

| Series | Magnification | Numerical Aperture | Working distance |
|---|---|---|---|
| PlanFLuor | 20x | 0.75 | 0.35 mm |
| ELWD | 20x | 0.40 | 11.0 mm |
| SLWD | 20x | 0.35 | 20.5 mm |

**Table 5.3:** Typical properties of some Nikon objectives used in this work

examples of different Nikon objectives with fixed magnification and different working distances, and numerical apertures:

The numerical aperture quantifies the angular acceptance of the objective and (together with the numerical aperture of the condenser) sets the optical resolution of the imaging system: a higher numerical aperture allows a higher resolution[1]. Even though a high resolution is generally desirable, in the experiments under shear also the access to different vertical planes is important, and also the cell has a certain size, this is why we prefer to use long working distance objectives.

**Perfect Focus -** The Ti-E microscope is equipped with an active system that stabilizes the position of the focal plane even for long ($\sim$ hours) acquisitions. This system provided by Nikon is called *Perfect Focus*. The principle of the system is to monitor the distance from a reference interface Fig. 5.2. If, for any reason (thermal drift, vibration, electronic drift of the objective positioning system, *etc.*), the distance between the reference surface and the objective changes, the position of the objective is automatically adjusted to reset the initial distance.

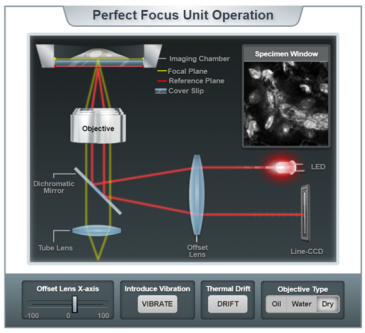


**Figure 5.2:** Scheme of Perfect Focus System. The position of the led spot on the sensor depends on the distance between the objective and the reference plane. A feedback loop resets the position of the objective in order to keep constant the position of the spot . Adapted from [96].

[1] NA $= n \sin\theta_{acc}$, $tan\theta_{acc} = \frac{D}{\mathrm{WD}}$, where $n$ is the refractive index of the medium, $\theta_{acc}$ is the objective's acceptance angle, $D$ is the diameter of the lens, and WD is the working distance.

### 5.2.2 Orca Hamamatsu camera

*Orca Hamamatsu V3* CMOS is a scientific CMOS (sCMOS) camera, whose main characteristics are:

- resolution 2048 x2048 pixels
- peak quantum efficiency 82% (@560$nm$)
- dynamic range: 37 000
- digital output depth: 16-bit
- max acquisition rate full frame: 100 fps
- max acquisition rate 256x 2048: 800 fps
- pixel size (6.5 $\mu m$)$^2$
- on-board binning: x2, x4
- cooling options: air (fan) or water (pump)
- computer interface: Camera Link

For extremely accurate measurements of the *MSD*, the camera cooling is switched from air to water since the fan, when spinning, introduces a small a coherent vibration with frequency $\nu_{vib} = 110\ Hz$. The amplitude of the vibration is likely to depend on the characteristics of the optical systems, such as the magnification. To give an example, the root-*MSD* induced by the vibration with a high numerical aperture (1.15) 40x objective is of the order of $\sim 10^{-2}\mu m$.

The camera is controlled with a software from Hamamatsu, and the output is a series of images that we save in a lossless TIFF format or, occasionally, in a proprietary Hamamatsu format.

### 5.2.3 Prosilica GX 1050 camera

The camera coupled with the shear cell is a CCD *Prosilica GX 1050* Gigabit Ethernet camera with:

- resolution 1024 x 1024 pixels
- peak quantum efficiency 44%
- max acquisition rate full frame: 112 fps
- pixel size (5.5 $\mu m$)$^2$

- computer interface: Gigabit Ethernet

The camera is controlled with a custom-developed *Labview VI*, the output is a single RAW file. When acquiring at full frame and at maximum frame rate ($100fps$) some frames are affected by an artifact: the image presents some horizontal black stripes. The stacks affected by this artifacts are pre-processed, to exclude from the rest of the analysis all the corrupted images.

### 5.2.4 Parameters optimization for microrheology

We suggest some guidelines for the choice of the experimental parameters for a DDM based microrheological characterization such as particle size, magnification, frame rate etc.

**Acquisition rate $f$-** The acquisition rate and measurement duration fix the range of tested frequency for the viscoelastic moduli. If one wants to characterize the material's response in the range of frequency $\Omega$, the acquisition rate $f$ and the duration of the measurement $D$ should be chosen in such a way that:

$$10/D < \Omega < f \tag{5.6}$$

The maximum acquisition frequency is dictated by the camera. In this work $f_{\max} = 1kHz$, nowadays extremely fast cameras reach $1GHz$[109]. Two or more acquisitions with different frame rates can be merged to efficiently widen the temporal range.

**particle size $a$-** Since the $MSD \propto 1/a$ the use of small particles enhance the dynamic signal. The use of small particles as tracers mitigates also sedimentation effect. At the same time the particles must feel an homogeneous environment so they have to be bigger than material's constituents $\xi$(e.g. in a polymeric network bigger than the mesh size)

$$\xi < a. \tag{5.7}$$

**Magnification $M$ -** Given the material, the time range and the particle size using the GSER 3.13 we can have a rough idea of the $MSD(t)$. The objective magnification and image size should be chosen in such a way to include the interval $\mathcal{M} = [MSD(t_0), MSD(D)]$:

$$\mathrm{pix}_{im}/10 < \mathcal{M} < N_{\mathrm{pix}} \cdot \mathrm{pix}_{im} \tag{5.8}$$

where with $\mathrm{pix}_{im}$ we indicate the dimension of the pixel in the image, related to the physical size of the sensor $\mathrm{pix}_{phys}$ by :

$$\mathrm{pix}_{im} = \mathrm{pix}_{phys}/M, \tag{5.9}$$

and $N_{\mathrm{pix}}$ is the number of pixel on an image line.

**Summary of experimental parameters and comparison with existing techniques** It is useful at this stage to briefly compare the key experimental parameters of DDM-microrheology and echo-DDM with the available alternative techniques. Such comparison is presented in Table 5.4 and 5.5, respectively. We note that using samples different from the ones studied here may bring-in other effects (e.g. slip or need to use tracers with different size) that may change or limit some of these parameter ranges.

| **Techniques** | MSD $[\mu m]$ | t [s] | $\phi_{Tr}$ |
|---|---|---|---|
| DWS-$\mu$r | $(3-30)\cdot 10^{-3}$ | $10^{-6}-1$ | 1% |
| DDM-$\mu$r | $0.01-1$ | $10^{-3}-100$ | 0.01% |

**Table 5.4:** DDM-microrheology vs DWS-microrheology

| **Techniques** | $\Lambda$ $[\mu m]$ | $\nu$ [Hz] | Gap [mm] |
|---|---|---|---|
| Echo-DDM[2]2 | $0.5-50$ | $0.5-2$ | $0.5-2$ |
| Echo-DWS [69] | 0.3 | $10-70$ | 0.3 |
| Echo-Xray [101] | $0.03-0.2$ | 0.25 | 0.5 |
| Echo-DLS [112] | $1.5-63$ | 0.04 | 1.5 |

**Table 5.5:** Echo-DDM vs other echo techniques

## 5.3 Shear Cell

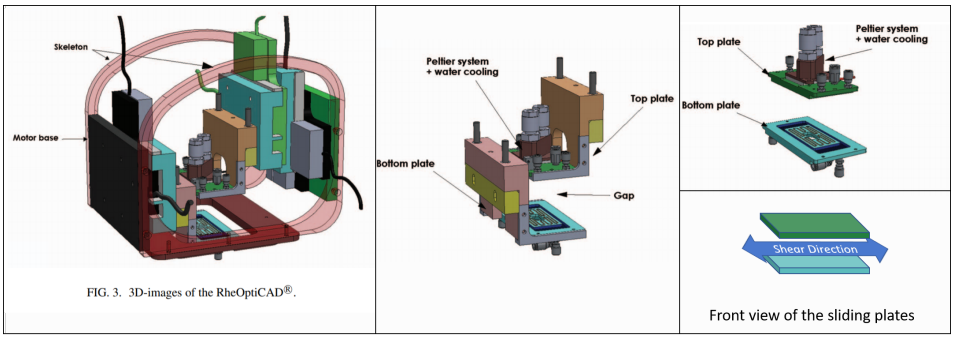


**Figure 5.3:** Progressive explosion of the shear cell. Left Panel: whole cell, The skeleton is screwed on the optical table. Central panel: top and bottom motors and plates. Right top panel: top and bottom plates. The glass slides are attached to the plates with a vacuum pump system. The inlets for the vacuum circuit hoses are visible in gray. Right bottom: shear axis. Adapted from [17].

We use a *RheOptiCAD* strain controlled shear cell mounted on the stage of the inverted Nikon Ti-S microscope. The cell produces a parallel sliding

[2]This work.

plate deformation geometry, the slides are standard microscope slides previously cut with a diamond glass cutter. The position along one horizontal direction is controlled by piezoelectic transducers. The control software allows the imposition of a desired deformation profile with the following options:

- step strain $\Delta x$ of the top and/or of the bottom plate
- constant strain rate $v$ of the top and/or the bottom plate
- oscillation of amplitude $\Delta x_0$, frequency $f$ of the top or the bottom plate

The **gap** (*i.e.* the distance between the two slides) can be set in the approximate range

$$h \in [100\mu m, 2mm],$$

where the lower boundary is given by the precision of alignment of the plates, and the upper one by the presence of the microscope condenser Fig. 5.1 (elements 5 and 6). If the observation are carried out in reflection, so that the condenser is unnecessary, the upper bound becomes $\sim 5$ cm.

The **amplitude range** is

$$\Delta x \in [1\ \mu m, 32\ mm].$$

The **frequency range** is

$$f \in [0.01,\ 10]\ Hz.$$

Typical values for our experiments are: $gap = 500\ \mu m$, $\Delta x \in [10\ \mu m,\ 1.5\ mm]$, frequency $f \in [0.5, 2]\ Hz$.

### 5.3.1 Alignment of the cell plates

One of the most critical part of the experiments is the alignment of the cell plates: the plates need to be parallel and aligned with the shear axis. If the alignment is not good enough, the deformation field is a composition of the desired *pure shear* profile with a compression-dilatation cycle.

The alignment steps are the following:

1. **plate-plate distance calibration**. Once the glass slides are mounted on the cell the distance between the plates is calibrated with a sensor Fig. 5.5.

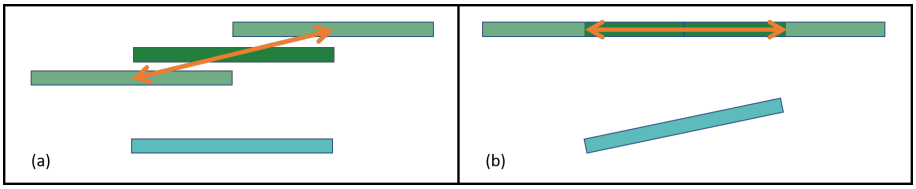


**Figure 5.4:** Panel (a) the two plates of the shear cell are parallel but not aligned with the shear direction. Panel (b) the top plate is aligned with the shear direction but the bottom plate is not parallel to the top plate. In both situation a dilatation-compression cycles combines with the shear cycle.

2. **alignment of the top plate with the shear direction**. To align the top plate with the shear direction we focus on the bottom surface of the top slide (either in a reflection illumination mode or in bright field with reduced spatial coherence). With the shear cell software, we move the top slide along the shear direction to the extremes $\pm 3\ mm$. We adjust the tilt of the top slide in order to maintain the bottom surface in focus when is moved along the shear axis. The accuracy reached with this procedure is limited by the *slides planarity* and the accuracy of the *plates tilting and locking* mechanisms. The resulting accuracy is
$$\delta\theta_{hor} \lesssim 2 \cdot 10^{-3}\ rad = 2\ \mu m/mm. \tag{5.10}$$

3. **parallelization of the bottom plate to the top one**. To align the bottom slide parallel to the top one, we use an interferometric technique. The microscope is mounted on an optical table. On the optical table a laser beam is aligned and expanded to a diameter $D \sim 0.5\ cm$. The beam is shined on the slides from the back port of the microscope without passing trough any objective. The interference pattern of the waves reflected by the two slides is observed on the camera sensor. If the slides are tilted of an angle $\theta_X$ a stripes pattern is observed, and the spacing between the intensity minima $\kappa_x$ is related to the tilt angle by
$$\kappa_x \sin(\theta_x) = \lambda_{laser}. \tag{5.11}$$
By adjusting the angle of the bottom plate we aim at maximizing the spatial period of the interference pattern until it exceeds the sensor size
$$\kappa_x > \ sensor\ size\ = 1\ mm, \tag{5.12}$$
which means that
$$\theta_x < \frac{\lambda_{laser}}{\kappa_x} \simeq 10^{-3}\ rad. \tag{5.13}$$
The argument is valid for both the shear and the vorticity directions.

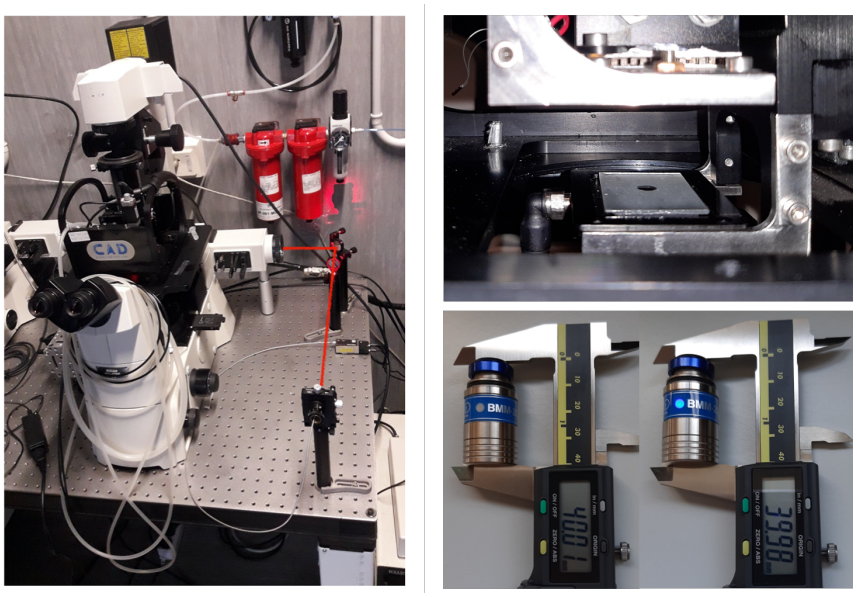

**Figure 5.5:** Left panel: picture of the shear cell mounted on the Nikon Ti microscope, with the alignment system. The collimated laser beam enters the microscope from the back door and reaches the glass slide through the same optical system used to do observation in reflection, without any objective. Right top panel: picture of the shear cell's glass plates. Right bottom panel: sensor used for gap calibration.

4. **repetition of the distance calibration**. During the parallelization we lose control of the vertical distance so that another distance calibration is required.

### 5.3.2 Choice of the glass slides

**Thickness -** The glass slide chosen for these experiments are 1 $mm$ thick slides. With thinner slides ($150\mu m$) we could have used higher numerical aperture (and thus lower working distance) objectives but the slide locking system (vacuum pump) bends thin slides impairing the parallelization procedure.

**Roughness -** In shear rheology the roughness of the geometries plays a crucial role, but we need optical access to the sample so in our experiments the confining surface (or at least part of it) has to be transparent.
The strategy we have adopted is to sandblast the slides a part for a small window ($\mathcal{O} \sim 1mm^0$) in correspondence with the observation and the illumination positions.
In our case we can tolerate *some* slip with no direct effect on the experiment as long as we are able to measure the local deformation profile $\Delta x(\gamma_0, z)$ Fig. 5.7.

### 5.3.3 Synchronization

Another crucial issue is the synchronization between the deformation frequency and the acquisition frequency, as we found that the **actual frequency** of the oscillation $\nu_{act}$ does not correspond to the nominal one $\nu$ set by the shear cell control software. In particular, $\nu_{act}$ **depends on the deformation amplitude**. At the same time we have to consider the constraints of the image acquisition frequency $f$: the acquisition software does not control explicitly the acquisition frequency but the time delay between frames $\Delta t_0 \ : \ f = 1/\Delta t_0$, with an accuracy $a_\tau = 0.01ms$. Since we want to correlate images with a delay of hundreds of cycles even a mismatch of one part over thousand in the periods takes to sensible systematic errors and requires a frequency calibration protocol.

The frequency calibration has been performed for a nominal frequency $\nu = 1\ Hz$ in a range of amplitudes $\Delta x \in [10,\ 1000]\ \mu m$ as follows:

1. **measure of the actual frequency as a function of the deformation amplitude** $\nu_A(\gamma)$. The position of the moving slide is imaged with at a high frame rate and the stack of images is analyzed with the cross-correlation algorithm for global displacement detection. The displacement profile is fitted with a sinusoidal function. In this way, we estimate both the actual amplitude and the frequency of the oscillation. We also check that for a fixed deformation amplitude the actual frequency does not depend on the camera acquisition rate, which means that we can assume that the timing of the acquisition software is reliable.

2. **search for the minimum discrepancy with the possible acquisition frequencies** Once we have carefully characterized the deformation frequency $\nu_A(\gamma)$, we have to find the most closely matching acquisition frequency $f$. In principle we could just take $f$ given by

$$1/f = \tau = round(1/\nu_A,\ 0.01\ ms), \tag{5.14}$$

which leads to a rounding error

$$e_\tau = abs(1/\nu_A - \tau) \tag{5.15}$$

but we want to acquire more than one image per period. Since the exact number of images per period $n_P$ is not constrained, we chose it as the number in the range $n_P \in [4,\ 20]$ that minimizes the rounding error $e_{tau}$:

$$e_{\tau_{n_p}} = \frac{1}{\nu_A} - n_p \cdot round\Big(\frac{1}{n_p \nu_A},\ 0.01\ ms\Big). \tag{5.16}$$

| $\Delta x$ | 10 | 20 | 50 | 100 | 200 | 300 | 330 |
|---|---|---|---|---|---|---|---|
| $n_p$ | 4 | 8 | 8 | 8 | 5 | 6 | 5 |
| $\tau$ | 248.41 | 125.1 | 125.08 | 125.02 | 199.9 | 166.69 | 200.01 |

| $\Delta x$ | 380 | 400 | 500 | 600 | 700 | 800 | 900 | 1000 |
|---|---|---|---|---|---|---|---|---|
| $n_p$ | 8 | 8 | 5 | 7 | 7 | 6 | 7 | 5 |
| $\tau$ | 125 | 124.97 | 200 | 142.84 | 142.84 | 166.65 | 142.86 | 200 |

**Table 5.6:** Synchronization parameters (measured frequency, number of images per period, and delay) for the image acquisition during oscillatory shear with nominal frequency $\nu = 1\ Hz$ in a range of amplitudes $\Delta x \in [10,\ 1000]\ \mu m$

so that the frequency selection process flow is $\nu_A \rightarrow n_p \rightarrow f$.
We report in Fig. 5.6 the measured frequency as function of the amplitude, and in Table 5.6 number of images per period and delays obtained with oscillatory shear deformation at nominal frequency of 1 Hz.

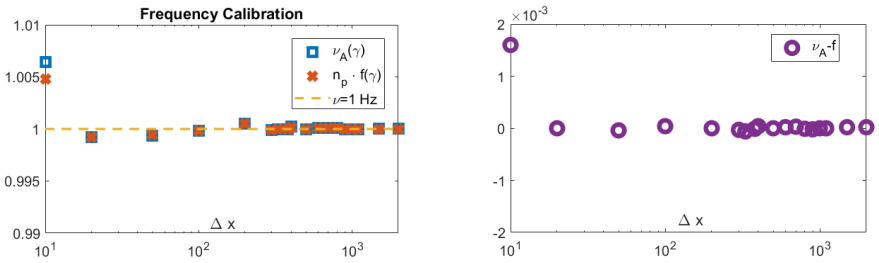


**Figure 5.6:** Left panel: measured frequency as a function of the shearing amplitude $\nu_A(\gamma)$, optimized acquisition frequency times number of images per period $n_p \cdot f(\gamma)$. Right panel: $\nu_A(\gamma) - n_p \cdot f(\gamma)$

### 5.3.4 Validation of the shear amplitude profile along the optical axis

To check the correct behaviour of the cell during shear applaiction we use an elastomer, described in [Section: 5.1.3], that exhibits an elastic behavior up to relatively high shear strain without slip.

For the measurements, we first open the aperture diaphragm and we use a 20x objective, to have a small focal depth and thus a better resolution along the optical axis $z$. For a fixed deformation amplitude, we acquire stacks of images at high frame rate and at different focal depths, from the fixed (bottom) plate to the moving (top) one. Following the procedure described in [Section: 4.5] we measured the deformation amplitude at different heights. From the measurement at different heights one can extract the local amplitude and the local shear gradient with a good accuracy Fig. 4.11. One controls the vertical position of the objective, that does not correspond to the position of the focal plane. To a vertical displacement $\Delta z_{obj}$ corresponds

a vertical displacement $\Delta z_{focal}$:

$$\Delta z_{focal} = n_{sample} \Delta z_{obj} \tag{5.17}$$

where $n_{sample}$ is the sample refractive index. In practice, if the gap is known with a good precision, and if the working distance is sufficient to observe the top plate, one can deduce the $n_{samp}$ as $gap_{imposed}/gap_{apparent}$ where $gap_{apparent} = z_{obj}(topslide) - z_{obj}(bottomslide)$.

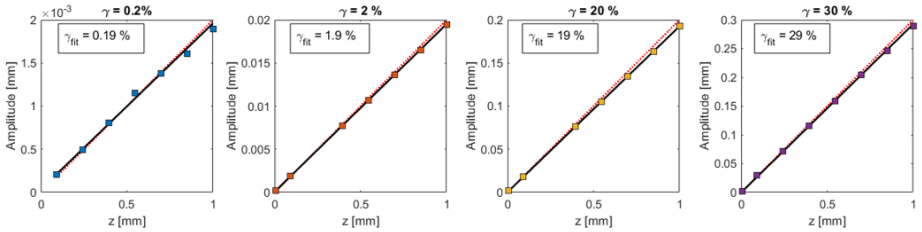


**Figure 5.7:** Results of a vertical scan on a Sylgard gel during the application of a controlled shear amplitude. Symbols represent the amplitude measured by a sinusoidal fit of the displacement for fixed shearing amplitude at different vertical positions. The lines represent the expected affine behavior (dotted red) and the fit with a linear non homogeneous function (black). The agreement with the expected behaviour is satisfactory.

We find that the shear amplitude is slightly reduced with respect to the expected behavior ($\gamma_m \simeq 0.95 \cdot \gamma_I$ ), the deviation being compatible with either a small amount of slip or a small error in the imposed amplitude.

### 5.3.5 PT Displacement probability distribution

The following experiments are meant to be compared with the Particle Tracking (PT) experiments under shear on Carbopol. In particular we are interested in the characterization of the displacement probability distribution, and on its agreement with Gaussian distribution. In this experiment we track particles of 2 $\mu m$ diameter diffusing in water, that are expected to follow a Gaussian displacement probability distribution:

$$P(\Delta x) = \frac{1}{\sqrt{\pi \sigma^2}} \Big[ ] \exp\Big( - \frac{\Delta x^2}{2\sigma^2} \Big) \Big], \tag{5.18}$$

any deviation is to attribute to experimental limits.

The experimental setup is the same of the experiments under shear. The objective is a

$$\text{magnification} = 20\text{X} \qquad \text{NA} = 0.45$$

(CFI S Plan Fluor ELWD 20XC), and the camera is the ProSilica described in 5.2.3, the acquisition rate is $f = 100$ fps. The PT analysis was conducted by using a customized version of the MATLAB code script made

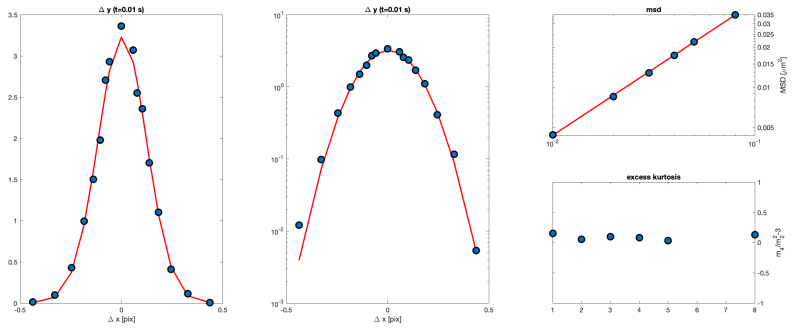


**Figure 5.8:** Left panel: displacement probability distribution $P(\Delta x, \Delta t = 0.01s)$ of colloidal tracers in water obtained from particle tracking (symbols). The red line is the best fitting curve to the data with a Gaussian model. Central panel: same as the left panel, represented on a semi logarithmic scale. Right top panel: width of $P(\Delta x, \Delta t)$ as function of the delay time $\Delta t$, corresponding to the particle MSD (symbols). The red line is a linear fit to the data. Right bottom panel: Excess kurtosis:$\frac{m_4}{m_2^2} - 3$, where $m_n$ is the $n$-th central moment of the distribution. It is expected to be zero for a Gaussian distribution.

freely available by the group of Maria Kilfoil at UMass [60] The agreement of the displacement probability distribution with a Gaussian is good Fig.5.8 (left panel in double linear scale, and central panel in semi logarithmic scale). The width of the distribution (MSD) scales linearly with time Fig.5.8 (top right panel), and the excess kurtosis of the distribution :$\frac{m_4}{m_2^2} - 3$, (where $m_n$ is the $n$-th central moment of the distribution) is close to zero, as expected for a Gaussian distribution.

# Chapter 6

# Results

## 6.1 Newtonian fluid

We present here results on the microrheological characterization of the Newtonian samples described in section5.1.1. Microscopy measurements performed on each sample are analyzed with different approaches, the outputs of which are critically compared.

**Experimental details -** All the experiments presented in this section here are performed on a Nikon Ti-E inverted microscope equipped with a $40X$ water immersion objective ($NA = 1.15$) and a liquid-cooled digital camera (Hamamatsu Orca Flash 4.0 v2). In all measurements (with the only exception of the one performed on pure water) the structure functions are obtained by combining two acquisitions taken at different frame rates: $f_1 = 777$ Hz and $f_2 = 10$ Hz. We employ polystyrene latex beads as tracers. For microrheological experiments we used Sigma Aldrich *LB5* particles (nominal diameter 0.45-0.47 $\mu m$), whose radius was measured with DDM to be $a_5 \simeq 223$ nm at a concentration $\phi_{tr} \in [0.075, 0.2]\%$, depending on the sample.

### 6.1.1 Fitting-based DDM microrheology

A first strategy to obtain the mean square displacement (MSD) of the tracer particles consists in fitting the dynamic structure function at a given wave-vector $q$ with a simple exponential function

$$D(q, \Delta t) = A(q)\big(1 - e^{-\Gamma(q)\Delta t}\big) + B(q). \tag{6.1}$$

The fit enables estimating the amplitude $A(q)$ and the noise term $B(q)$, that can be used to invert $D(q, \Delta t)$, according to Eq.6.1, providing an estimate of the MSD for each wave-vector. The best estimate of the MSD is then obtained as an average over all probed wave-vectors. The results of this procedure are shown as colored symbols in the first panel of Fig.6.1. In the same

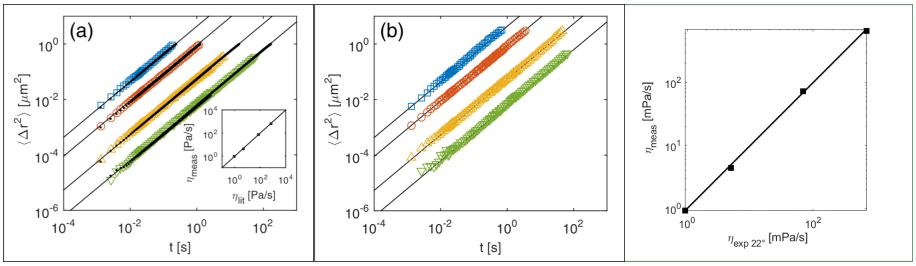


**Figure 6.1:** Fist panel: MSD obtained from fitting-based DDM (colored symbols), black lines are linear homogeneous fits, black dots are MSD measured with PT and corrected for the localization error by subtracting a suitable constant value to the raw MSD. Second panel: MSD obtained from the self consistent procedure, symbols as in the first panel. Third panel: measured versus expected viscosity, the symbols are experimental data and the line is the identity $y = x$.

panel, black dots represent the MSD obtained from particle tracking (PT) on the same image sequences. It is worth noticing that in particle tracking the localization error gives a significant contribution for the samples with the slower dynamics. As a consequence, a correction must be applied, by subtracting a suitable constant value to the MSD. The DDM fitting-based procedure, implicitly apply a similar correction, by incorporating the localization error in the noise baseline $B(q)$, as discussed in more detail in Sect.4.3. As it can be appreciated from the figure, the agreement between the results of fitting-based DDM and PT is excellent.

### 6.1.2 Optimization-based DDM microrheology

A second strategy to extract the MSD of the tracers from DDM analysis is the optimization-based, self-consistent procedure described in detail in Sect.4.3. As it can be appreciated from Fig.6.1b, the MSDs obtained with this method show the expected linear dependence on time and are in excellent agreement with the ones obtained with the fitting-based approach described in the previous subsection. Of note, the optimization-based procedure enables extracting meaningful information also at very low wave-vectors, even below $3\mu m^{-1}$, where the fitting-based approach does not converge. From a linear fit of the MSD: $\langle \Delta r^2(\Delta t) \rangle = 4D\Delta t$ we can obtain an estimate of the diffusion coefficient $D$ of the tracers. Finally, by means of the Stokes-Einstein relation (Eq.3.11), we extract the viscosity (Fig.6.1, third panel). The values obtained for the viscosity: $\eta_{meas} = 0.92 \pm 0.03$, $4.4 \pm 0.2$, $73 \pm 3$, $633 \pm 40$ $mPas$ are in very good agreement with the expected values based on literature data: $\eta_{lit} = 0.914 \pm 0.01$, $4.9 \pm 0.05$, $69.2 \pm 0.7$, $702 \pm 50$ $mPas$, [25]. The relatively large error on the last value (corresponding to the 97.5% glycerol sample) is mainly due to the uncertainty in the sample starting

purity.

## 6.2 Visco-elastic fluid

### 6.2.1 Optimization-based DDM: translational and rotational microrheology

We make use of the optimization-based approach to DDM microrheology for characterizing a model viscoelastic material, a case where the functional form of the MSD of the embedded tracers is not known *a priori*.
As described in more detail in Sect.5.1.2, the sample is a solution of PEO at a weight concentration $c_{wt} = 2\%$, much larger than the overlap concentration $c^*$: $c \simeq 22\ c^*$. To perform translational microrheology we use LB5 tracers (radius $a \simeq 223nm$) and LB1 tracers (radius $a \simeq 55nm$) at volume fraction $c_T = (1.00 \pm 0.05)10^{-3}$, imaged in bright-field. In the rotational microrheology experiments, we use spherical colloidal particles, with a polymerized nematic liquid-crystal core, whose birefringence makes them optically anisotropic, with a uniaxial symmetry [54] [45], [82], [41]. These particles were studied both in bright field and between partially-crossed-polarizers. The particles are prepared and purified according to the protocols described in detail in Refs. [82] [16]. After dilution, the concentration of optically anisotropic tracers was $(1.8 \pm 0.2)10^{-3}$ wt/wt. The diameter of the tracers $(0.22 \pm 0.03\mu m)$ was determined by measuring with bright-field DDM the translational diffusion coefficient of a diluted dispersion in pure water. In all cases, the tracers are larger than the mesh size of the hosting material. As a consequence, we can model the interaction of the particle with the fluid as with an homogeneous medium. We thus expect that the motion of the tracers with different sizes reflects the same mechanical properties.
The experiments were performed with a $40X$ dry objective NA = 0.6 (CFi S Plan Fluor ELWD). Also in this case we combined two acquisitions with different frame rates ($f_1 = 777$ Hz and $f_2 = 10$ Hz) to probe the dynamics of the tracer over a wider temporal range. In Fig.6.2(a) we report the MSD of LB5 particles (blue circles) and of LB1 particles (orange triangles). The LB5 data are analyzed also with PT; the obtained MSD is also shown as black dots. The agreement between the MSD obtained from optimization-based DDM and from PT is very satisfactory. It is worth noticing that that PT results have been corrected for the localization error by subtracting a suitable constant value to the raw MSD, while this correction is not needed for the MSD obtained from DDM thanks to the self-consistent procedure. For the smaller particles PT is not feasible, as the contrast associated with a single tracer is too small, as it can be appreciated in the upper inset image of Fig.6.2(a).
In Fig.6.2 (d) the angular mean square displacement (AMSD) obtained with birefringent particles is also shown. The optical contrast of the subdiffrac-

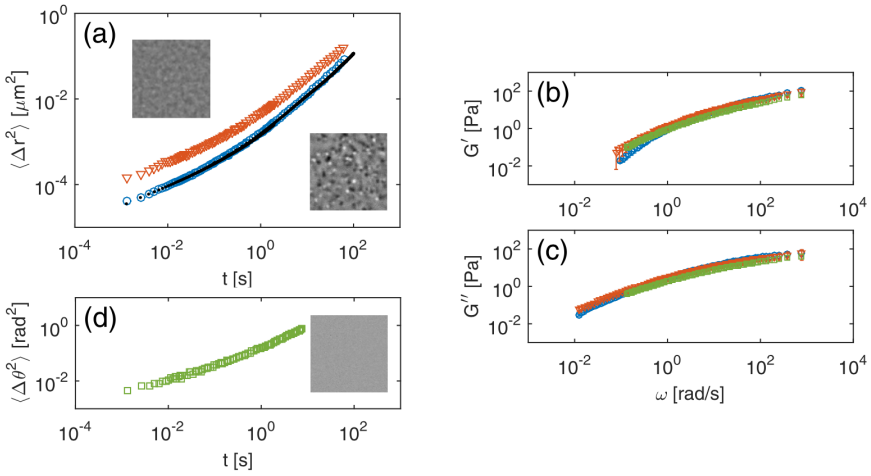


**Figure 6.2:** (a) Large symbols: MSDs obtained from the optimization-based DDM procedure described in Sect.4.3.3 using LB1 particles (orange triangles) and LB5 particles (blue circles), respectively. Black dots: same quantity obtained from PT analysis for the sample with LB5 tracers. The small insets show representative images of the two samples: the one loaded with LB1 particles (upper-left corner) and the one loaded with LB5 tracers (lower-right corner), respectively. In both cases the image size corresponds to 20.8 $\mu m$. (d) Symbols: angular MSD measured with DDM. Inset: representative bright-field image of the sample loaded with the birefringent particles. (b) Comparison of the storage modulus $G'$ estimated with DDM microrheology using LB1 tracers (orange triangles), LB5 tracers (blue circles), and optically anisotropic tracers (green squares), respectively. (c) Same as (b) for the loss modulus $G''$.

tion birefringent tracer particles used in these experiments is extremely low. This fact, combined with the intrinsic fluctuation in the particle's intensity due to their rotational dynamics, made PT absolutely impossible in this case.

Using generalized Stokes-Einstein relations we can use the MSD and the AMSD obtained with different tracers to estimate the frequency-dependent dynamical modulus of the PEO solution. As it can be appreciated from Fig.6.2, the self-consistency of the obtained results for both the storage modulus $G'$ and the loss modulus $G''$ is encouraging, the last step for the validation of DDM microrheology is the comparison with conventional rheological and micro-rheological methods.

**DWS -** DWS microrheology experiments were performed on the same polymer solution with a higher tracer particles concentration $\phi = 1\%$, chosen to

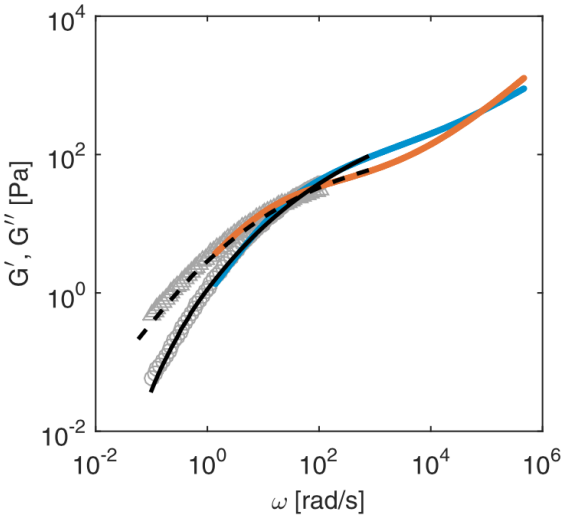


**Figure 6.3:** Storage and loss modulus of a viscoelastic fluid (a $2\%wt/wt$ solution of PEO in water) measured with different techniques: black lines, DDM microrheology (dashed $G''$, continuous $G'$), grey symbols, shear rheology (triangles $G''$), colored continuous lines, DWS microrheology (orange $G''$).

ensure multiple scattering [80]. In the limit of multiple scattering the autocorrelation function of the scattering intensity is given by

$$\int_0^\infty P(s) \exp\left[-\frac{k^2}{3}\langle \Delta r^2(\tau)\rangle \frac{s}{l^*}\right] ds \tag{6.2}$$

where $k = 2\pi n/\lambda$ is the wave vector of light with wavelength $\lambda$ (in our experiment $687nm$) incident on a medium with refractive index $n$. $P(s)$ is the scattering-geometry-dependent relative probability distribution of photon path lengths $s$ inside the medium and $l^*$ is the transport mean free path, which quantifies the distance that a photon has to travel inside the sample before loosing memory of its original direction. $l^*$ is measured from the transmittance and for our sample is $l^* = 256 \pm 5\ \mu m$. For our experiments we used the commercial instrument DWS Rheolab (LSInstruments, Fribourg, Switzerland), a compact stand-alone optical microrheometer that is based on DWS. The sample was hosted in a cuvette of thickness $L = 2\ mm$. Measurements were performed in transmission geometry with a duration of 3000 $s$ each. The instruments directly provides the MSD of the tracer particles (in the time range $1.38\ \mu s - 0.71\ s$), a fit of it, and the moduli Fig.6.4.

**Bulk Rheology -** For the standard bulk characterization of the viscoelastic moduli we used a commercial rheometer (Anton Paar MCR502) equipped with a cone and plate geometry (radius = 25 mm, cone angle = 1°). We

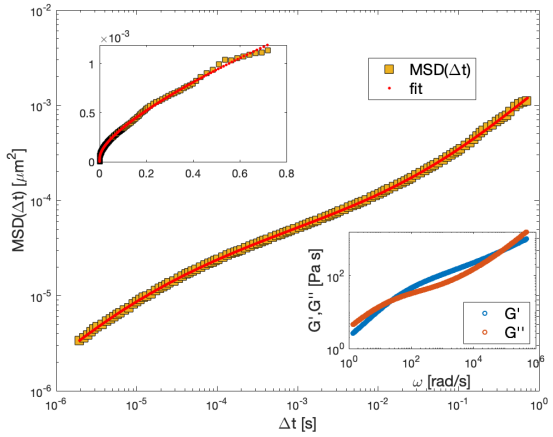


**Figure 6.4:** Main panel: MSD($\Delta t$) measured with DWS Rheolab for the viscoelastic fluid described in the main text (PEO in water concentration $2\% wt/wt$), the yellow squares are raw data and the red dots are the polynomial fit provided by the instrument. In the top left inset the same as in the main panel in linear scale. In the bottom right inset the viscoelastic moduli (same as Fig.6.3).

applied an oscillatory strain with strain amplitude of 5%, small enough to be in the linear region, and angular frequency in the range $[0.1, 100] rad/s$. The experiments were performed in the temperature range $T = 20 - 25°C$, observing no relevant temperature dependence. To avoid evaporation during measurement we used a solvent trap.

In Fig.6.3 we show $G'$ and $G''$ measured with an oscillatory, strain-controlled rheometer, with Diffusive Wave Spectroscopy microrheology and DDM microrheology. While different techniques cover different frequency ranges, in the overlap regions, the moduli estimated with different techniques are in very good agreement.

## 6.3 Simple yield stress fluid

As a first example of yield stress fluid (YSF), we consider an aqueous suspension of microgel particles (Carbopol[1]). Simple YSFs are, by definition, non-thyxotropic, meaning that their response depends only on the instantaneous shear state, with negligible memory of the shear history. This property makes simple YSFs the ideal model system, in terms of reproducibility and control of the experimental conditions, to approach the study of yielding. In the literature there is an open discussion about the yielding behaviour of Carbopol, if it has to be considered as a simple YSF or a thixotropic one [37]. We will show to what extent it can be considered a simple YSF in Sect. 6.3.2 and Sect. 6.3.2. On the other hand it must be noted that from the microstructural point of view Carbopol is not an ideal system, it is a commercial system and its size distribution is broad and not perfectly controlled.
The reason for the choice of this sample as the starting one is found in its simple rheological behaviour and in its transparency which allow to seed the material with monodipersed particles and study their shear induce dynamics as described below in Sect.6.3.3.

In this section, the results of a thorough rheological[2] and microscopic characterization of this sample will be presented.

### 6.3.1 Linear rheology

In order to probe the frequency-dependent linear response of the sample, we performed a number of dynamic frequency sweep (DFS) tests. The left panel of Fig.6.5 shows four repetitions of a DFS test performed in the linear regime at shear amplitude $\gamma = 1\%$. As expected, the linear properties are well reproducible. In the whole explored frequency range the storage modulus ($G'$) is larger than the loss modulus ($G''$), as expected for a yield stress fluid. The value of $G' \simeq 40Pa$ is weakly dependent on the frequency. In the top right panel the ratio between $G''$ and $G'$ is reported, while in the panel below the phase lag $\delta$ (see subsection2.3.1) is shown. $\delta$ is commonly used to quantify the resemblance of the material to an ideal solid ($\delta = 0$, red line in Fig.6.5 bottom right), or to an ideal liquid ($\delta = \pi/2$, blue line). The stronger indication that the linear response of the material under study is substantially solid-like comes from the fact that, since $G'(\omega) > G''(\omega)$, one cannot identify any finite relaxation time $\tau_R$ in the low frequency region. As

[1] Details on sample preparation can be found in section5.1.4)

[2] Some of the rheological measurements described in this section have been performed in collaboration with Mr. Mohandas and Prof. George Petekidis (Material Science department, Crete University) and Dr. Giuliano Zanchetta (BIOMETRA department, University of Milan).

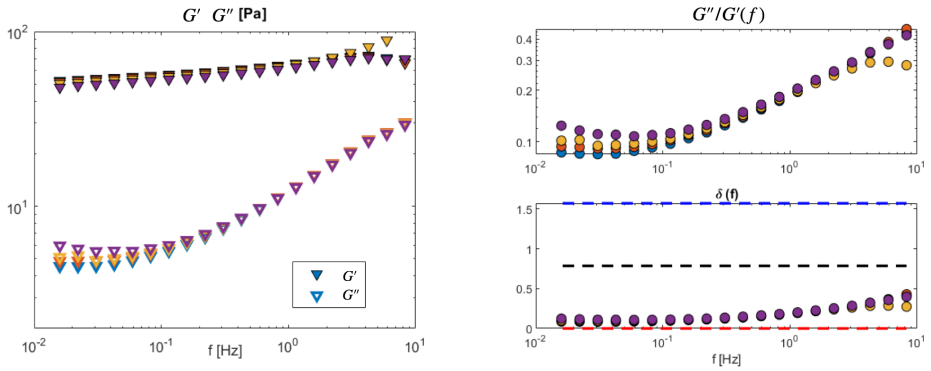


**Figure 6.5:** Left Panel: frequency-dependent storage modulus $G'$ (full symbols) and loss modulus $G''$ (empty symbols) obtained from repeated DFS test. Right top panel: ratio $G''/G'$ between the viscous and the elastic modulus. Right bottom panel: phase lag $\delta = \arctan\left(\frac{G''}{G'}\right)$ (symbols), dashed lines mark the values of $\delta$ expected for an ideal solid (red line), an ideal liquid (blue line), and for a material where $G' = G''$ (black line), respectively.

a consequence, in a linear creep test the sample is never expected to flow, even for very long times.

### 6.3.2 Non-linear rheology: LAOS

**First harmonic moduli -** A first characterization of the non-linear mechanical response of the sample can be obtained by monitoring the first harmonic of the viscoelastic moduli during a large amplitude oscillatory shear (LAOS) test (see Fig.6.6, where full symbols correspond to the storage modulus while open symbols to the loss modulus). The test is repeated two times: the first time by increasing the strain amplitude (blue symbols in Fig.6.6), and the second one by decreasing the amplitude (red symbols).

While the two measurements of the loss modulus superimpose almost perfectly, the estimate of the storage modulus obtained with increasing amplitude is appreciably larger (of about 20%) than the one obtained with decreasing amplitude. Although this discrepancy is not a large, it appears to be a quite robust feature, as it is consistently observed for all investigated frequencies. It's tempting to interpret this behaviour as a transient "weakening" of the elastic response of material caused by the exposure at large amplitude deformations. It would be interesting to investigate more in-depth this phenomenology and to understand the microscopic counterpart of this behaviour. Some preliminary result along this line is presented in the second part of this section.

The linear regime extends up to $\gamma_P \simeq 1\%$, where the loss modulus starts to increase smoothly, it reaches its maximum around $\gamma_M \simeq 50\%$, and than

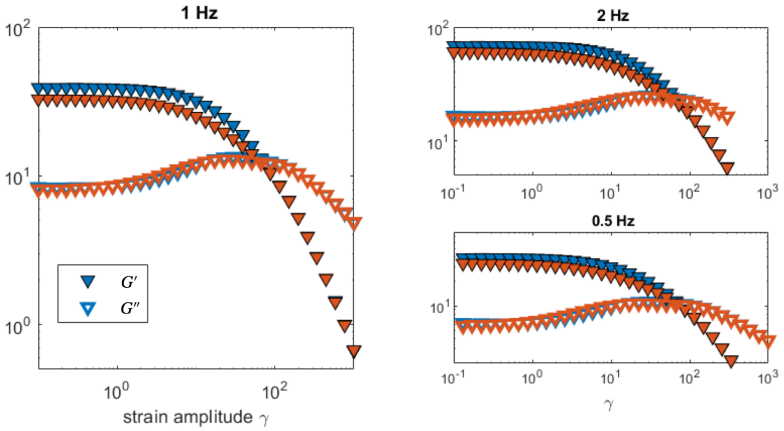


**Figure 6.6:** First harmonic of the storage modulus (full symbols) and of the loss modulus (empty symbols) moduli obtained during a LAOS test. The test is repeated twice: with increasing shear amplitude (blue symbols) and with decreasing shear amplitude (red symbols). Each panel corresponds to the same test, performed at a different frequency, as indicated in the title. Results obtained at different frequencies share the same qualitative features.

starts to decrease. At $\gamma_{c.o.} \simeq 66\%$ the two moduli crosses. While in the linear spectrum the frequency where $G'$ and $G''$ crosses has a precise meaning this is not the same for the crossover point in the amplitude sweep since the value of the modulus for a single frequency is not enough to describe the response of the system.

**Dynamic time sweep -** In order to obtain a direct measurement of the time needed to reach a stationary condition under non-linear forcing, we impose on the sample a periodic deformation with fixed amplitude for 600 s, while monitoring the first harmonic of $G'$ and $G''$. During this interval of time the storage modulus is essentially constant, while the loss modulus, although its overall variation is moderate (less then 10%), seems to show a systematic evolution over time, that is well captured by the phenomenological relation

$$G = G_\infty + \Delta G / t^\alpha. \tag{6.3}$$

Under the hypothesis that Eq.6.3 provides a faithful description on the evolution of each viscoelastic modulus even for very long times, fitting Eq.6.3 to the data enables predicting the asymptotic value that would be eventually reached in a prolonged experiment.

We repeated the test at different amplitudes, obtaining results similar to the ones obtained from the LAOS experiments described in previous paragraph (Fig:6.7). We fit both the storage and the loss modulus with Eq.6.3

and we report both the starting values and the asymptotic values estimated from the fit (last column). As it can be appreciated from the figure, starting and asymptotic values are almost indistinguishable for the storage modulus, while a small but systematic difference (of about 10%) is observed for the loss modulus.

We conclude that the loss modulus seems to slowly decrease over time and that, as a consequence, the value of the loss modulus obtained in a short experiment may differ (a few percent) from the stationary value. On the other hand we expect that the shape of the amplitude sweep will not change much if we consider the starting values of the moduli instead of their asymptotic values, since the evolution process is quite similar for different amplitudes.

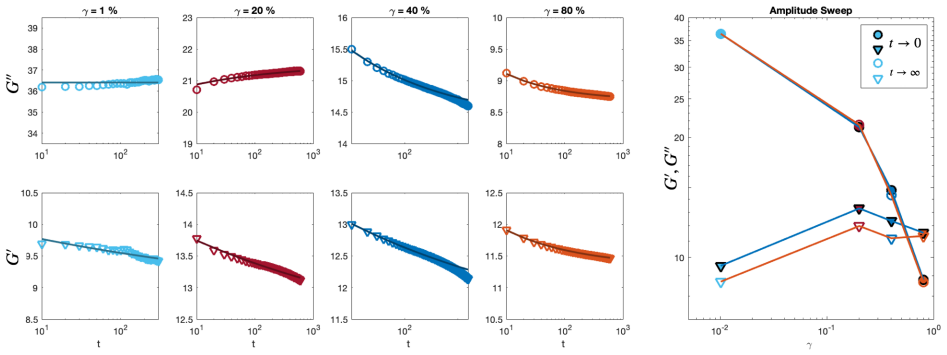


**Figure 6.7:** Storage modulus (first row) and loss modulus (second row) for different amplitudes as function of time during a dynamic time sweep test performed at frequency $\nu = 1$ Hz and amplitudes $\gamma = 1\%, 20\%, 40\%, 80\%$. The continuous lines are best fitting curves to the data with the model in Eq.6.3. In the last column $G'$ and $G''$ are plotted as function of the shear amplitude. The starting values correspond to full symbols, the asymptotic values to empty symbols.

**Lissajous plots -** Compared to the relatively simple tests described in previous paragraphs, the study of the Lissajous plots recorded during a strain-controlled LAOS test enable accessing a richer and more complete information on the mechanical response of the sample. Typical curves are shown in Fig.6.8. In the first row the normalized stress $\sigma/\sigma_0$ is plotted against the normalized strain amplitude $\gamma/\gamma_0$, while in the second row $\sigma/\sigma_0$ is plotted as function of the normalized strain rate $\dot{\gamma}/\dot{\gamma}_0$. Form left to right the strain amplitude increases from 1% to 400%. The red line represents the result of the fit with a linear response model

$$\sigma(t) = a\ sin(xt + \delta). \tag{6.4}$$

As anticipated in the second chapter (Sect.2.3.1), the area enclosed by the $\sigma(\gamma)$ curve equals the dissipated work per unit volume per cycle $W_D$.

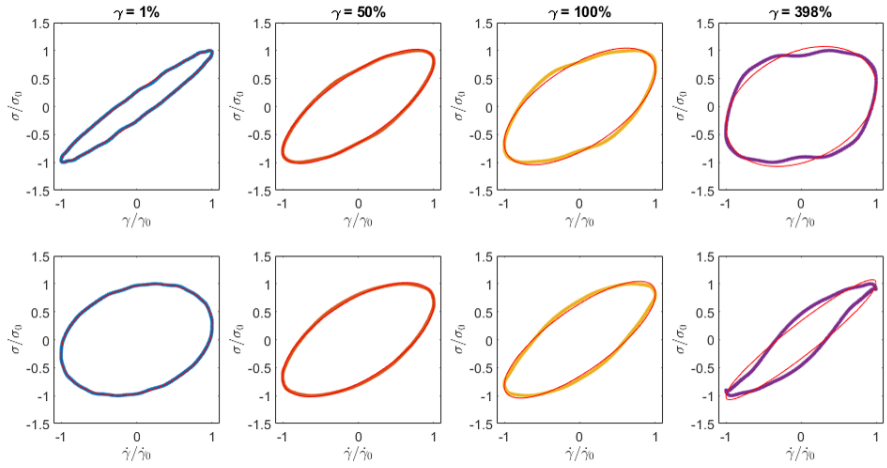


**Figure 6.8:** Lissajous Figures obtained from strain-controlled LAOS tests on the Carbopol sample. In the first row the normalized instantaneous stress as function of the instantaneous normalized strain $\sigma(\gamma/\gamma_0)/\sigma_0$ is shown for different amplitudes. In the second row the normalized stress as function of the normalized strain rate $\sigma(\dot{\gamma}/\dot{\gamma}_0)/\sigma_0$ is reported. Red lines are best fitting curves with the linear response model in Eq.6.4.

In particular, when the stress-deformation relation is described by Eq.6.4, $W_D = \pi\sigma_0\gamma_0 \sin(\delta)$, where $\delta = \arctan(G''/G')$. We can clearly see that from $\gamma = 1\%$ to $50\%$, the shape of the Lissajous plots changes appreciably. In particular the area enclosed in the $\sigma(\gamma/\gamma_0)/\sigma_0$ curves increases and so does $\delta$. This indicates that the material is becoming more liquid-like upon increasing shear amplitude. We also observe that even when the response of the material is no longer linear, the stress-deformation relation still remains approximately harmonic. Clear signs of non-harmonicity become apparent only for $\gamma \geq 100\%$.
From the fit shown in Fig.6.8 we can extract the first harmonic of the viscoelastic moduli. From the integral we can also measure $W_D$ and its elastic analog $W_E$ that we can use to define some non-linear moduli $G'^{NL}$, $G''^{NL}$ according to equations2.36. Even in the regime where the response is not harmonic the difference between the linear and the non-linear moduli are very small, reflecting the fact the area enclosed by the fitting curve differ from the one enclosed by the data by less than 1% (data not shown).
From these tests we learn that at all the explored amplitudes the first harmonics of the viscoelastic moduli give a quite faithful representation of the *period-averaged*. Moreover also the *in-cycle* response is faithfully represented by the first harmonic of the viscoelastic moduli up to $\gamma \sim 100\%$.

One of the main limits that LAOS suffers is the difficulty in the phys-

ical interpretation of its outcome. In particular non-harmonicity can be interpreted as a dependence of the material response on the phase of the deformation cycle [103]. In other words the rheological state of the system is not well defined but oscillates between different states. Concepts like the mechanical relaxation spectrum or the creep compliance of these rheological "states" are not well defined. But when the system's response at a given shear amplitude $\gamma$ is described by a single (phase independent) value of the dynamic modulus, we can assume that its response is the same in every phase of the deformation cycles. As a consequence, we can still regard at it as a well-defined material, different from the material at rest, if we are in the non-linear regime, but still a single, well-defined material.
For such system, in a well defined shear state, we can conceive a mechanical relaxation spectrum or equivalently a linear creep compliance. This system will be liquid or solid depending on the presence, or not, of a relaxation time [74].
In a superposition rheology experiment [116] the system is taken out of its linear condition with the application of a *large* deformation $\gamma$, and the *linear* response of the *sheared* material is tested superposing to it a small test perturbation $\gamma'$. With similar idea we turn to the microscopic dynamics: we expect that if the sheared system is in a fluid state, *i.e.* has a relaxation time in its spectrum, tracers dispersed in the material will undergo a free dynamics, and *viceversa*, if the sheared system is in a solid state tracers will be bounded to their original position.

### 6.3.3 Microscopy experiments

The experiments described in the rest of this section are performed on the shear cell already described in5.3, mounted on top of an inverted microscope, equipped with a $20X$ objective ($NA = 0.45$) and a CCD camera (Prosilica GX 1050 5.2.3). The resulting pixel size is $d_{pix} = 0.55\ \mu m$. The experimental protocols are described in detail5.3.4,4.8,4.6.

### 6.3.4 Deformation profile

As a first step, we perform an accurate characterization of the local deformation profile of the sample under shear, as explained in detail in5.3.4. Before and after each Echo experiment we measure the deformation amplitude on the plane $z_0$ imaged during the Echo experiment, and on two neighbouring planes $(z-)$ and $(z+)$ located 40 $\mu m$ below and 40 $\mu m$ above the Echo image plane, respectively (Fig.6.9). In all cases, we find no appreciable variations in the deformation profile before and after the Echo experiment. For a given

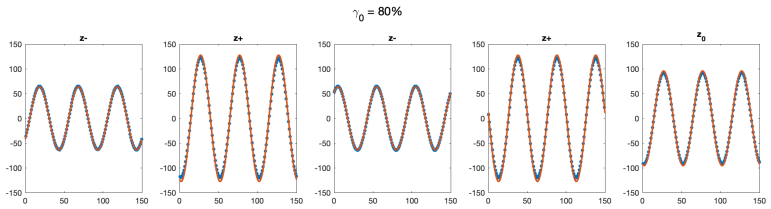


**Figure 6.9:** Experimentally measured displacement (blue circles) and expected displacement (red line) on different planes: 40 $\mu m$ below the plane imaged in EchoDDM experiments (first and third panels), 40 $\mu m$ above the plane imaged in EchoDDM (second and fourth) and on the same plane imaged in EchoDDM (fifth panel). Measurements are performed both before (first and second panels) and after (third to fifth panels) the execution of an EchoDMM experiment. The imposed shear amplitude is $\gamma_0 = 80\%$.

strain amplitude $\gamma_0$, the deformation amplitude $A^*(z;\gamma_0)$ on each plane is measured by fitting the observed displacement as a function of time with an harmonic function, as shown in Fig.6.9. The typical reconstructed local deformation profile (reported in Fig.6.10), although in fair agreement with the expected $\gamma_0 z/h$ behaviour, is better described in terms of a non-homogeneous linear function. This behaviour can be probably explained by the presence of some slip at the boundaries.
The slope of the non-homogeneous linear function fitting the experimental points provides a good estimate for the actual local strain $\gamma$ on the considered plane. The outcome of this calibration procedure is twofold:

- first of all, we checked that in the proximity of $z_0$ (the plane imaged during Echo experiments) the deformation profile is, to a good approximation, linear. This ensures that the optical signal collected during

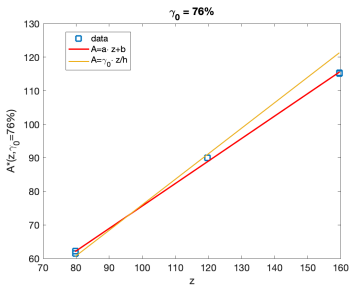


**Figure 6.10:** Measured deformation amplitude as a function of the height $z$ for a fixed deformation amplitude $\gamma_0 = 76\%$ (symbols). The red line is a non-homogeneous linear fit, the yellow line corresponds to the expected displacement amplitude, based on the nominal imposed strain amplitude.

an Echo experiment originates from planes where the deformation field is homogeneous.

- secondly, we can directly measure the actual value of the deformation $\gamma(\gamma_0)$ experienced by the sample, that we can use to compare microscopic and macroscopic mechanical behaviour.

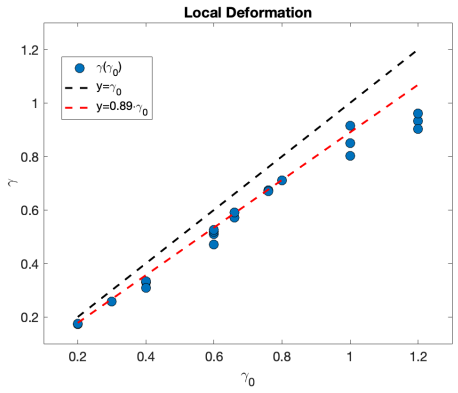


**Figure 6.11:** Experimentally determined deformation gradient $\gamma = \partial_z A^*$ in the vicinity of the plane imaged in EchoDDM experiments plotted as function of the nominal shear amplitude $\gamma_0$ (symbols). The actual deformation is approximately 90% of the imposed one up to $\gamma_0 = 100\%$.

### 6.3.5 Activity maps

Visual inspection of the images collected during a typical Echo experiment with $2\mu m$ diameter tracers reveals a marked spatial heterogeneity in the behaviour of the tracer particles across the the sample. An effective way to highlight these spatially heterogeneous particle displacements, is to consider "activity maps" obtained according to Eq.4.44 that we report here for clarity:

$$\mathcal{M}(\mathbf{x}, t) = |I_r(\mathbf{x}, t) - I_r(\mathbf{x}, t + T)|^2$$

where $I_r$ the registered image at time $t$ and $T$ is the oscillation period.

**Mean activity $\mathcal{A}(\gamma_0)$ -** A first quantitative indicator of the sample dynamics is provided the mean value of the activity maps per cycle or **mean activity**:

$$\mathcal{A}(\gamma_0) = \langle \mathcal{M}(\mathbf{x}, t) \rangle_{\mathbf{x},t}$$

From Fig.6.12 we can clearly see that the microscopic dynamics changes drastically above $\gamma \sim 50\%$. The good collapse of curves obtained at different frequencies indicates the mean activity induced during a deformation cycle is almost independent on the frequency of the deformation.

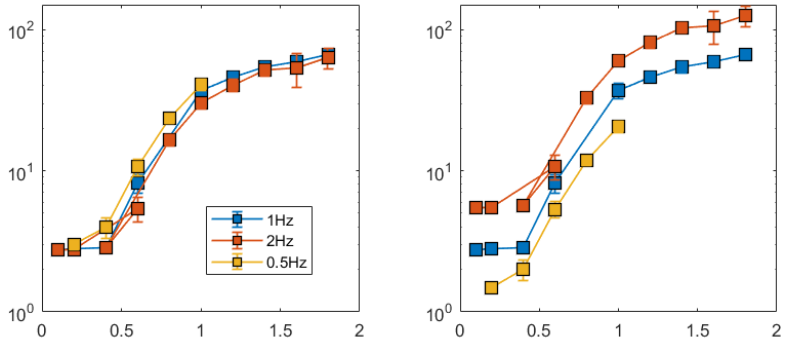


**Figure 6.12:** Mean activity $\mathcal{A}(\gamma_0) = \langle M(\mathbf{x}, t) \rangle_{\mathbf{x},t}$ obtained from Echo experiments on the Carbopol sample seeded with $2\mu m$ diameter tracers. Different symbols correspond to tests performed with different shear frequencies. In the right Panel the mean activity per unit time (*i.e.* the mean activity multiplied by the shear frequency) is shown.

**Statistical analysis of the activity maps -** A more detailed understanding of the shear-induced dynamics can be obtained by considering the intensity histogram of activity maps Fig.6.13, second panel. We recall that, as far as the particle displacements are small compared to their size, the average intensity in given portion of the activity map is proportional to the mean square displacement of the particles comprised within that portion.

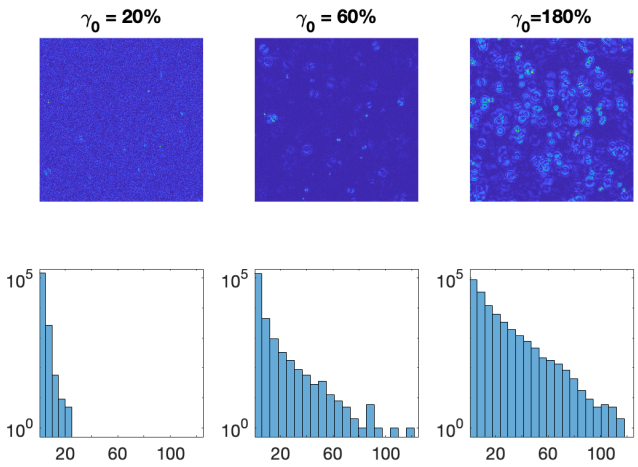


**Figure 6.13:** Top row: representative activity maps $\mathcal{M}(\mathbf{x}, t)$ obtained from Echo experiments on the Carbopol sample seeded with $2\mu m$ diameter tracers at different shear amplitudes. Bottom row: intensity histogram. As long as the displacements are small compared to the size of the particle image, the local intensity is approximately proportional to the MSD.

Inspection of the intensity histograms at different amplitudes suggests to introduce two thresholds: one to separate the signal due to genuine displacements from the noise, and another one to identify very large displacements. We make use of these two thresholds to simplify our activity maps to "three levels maps". The discretization is done at the original resolution and each pixel is associated to one of the three categories: "noise", "normally active", "super active". Since the average particle-particle distance is tipically way larger than the pixel size we introduce a spatial binning of the maps in order to have at least one particle in every site. The resulting site or "meta-pixel" is $(8.8\mu m)^2$ (Fig.6.14). A site is labeled as "super-active" if it has at least one super-active pixel inside, as "noise" if it contains no active pixels, as "active" otherwise.

As it is clear from visual inspection of the maps, activity tends to be spatially correlated (Fig.6.14, central and right panels) and the characteristic size of these active regions tends to increase with the shear amplitude. To make this observation more quantitative, we identify in each map groups of adjacent active sites, that we refer to as active clusters. The characteristic size of the active clusters can be captured by considering their gyration radius, while the presence of highly connected (possibly system-spanning) active cluster is monitored by considering the gyration radius of the largest cluster in each map. In Fig.6.15 we show the value of the mean gyration radius and the (time averaged) maximum gyration radius for different shear

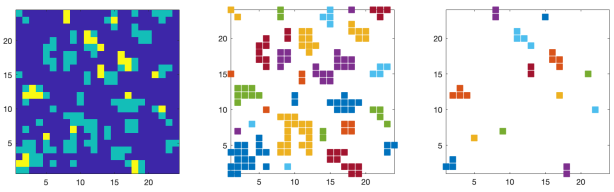

**Figure 6.14:** Left panel: binned version of a "three levels map" obtained from Echo experiments on the Carbopol sample seeded with $2\mu m$ diameter tracers at shear amplitude $\gamma_0 = 60\%$. described in main text. If inside a given bin there are no active pixels the site is considered "inactive" (blue), if there is at least one active pixel the site is considered "active" (green), if there is at least one "super mobile" pixel the site is "super active" (yellow). Central panel: connected regions of "normally active" site, shown with different colors. Left panel: connected regions of "super active" sites, shown with different colors.

amplitudes:

$$\text{Mean } R_G = \langle R_G(t,n)\rangle_{t,n} \qquad \text{Max } R_G = \langle \text{Max}_n\{R_G(t,n)\}\rangle_t$$

where $n$ labels the different clusters in the same map, $\langle ...\rangle$ the averages on time or on the distribution, and $\text{Max}_n\{...\}$ the maximum on the distribution of the clusters for a fixed frame. In the third panel of Fig.6.15 we report the active sites as function of the shear amplitude (left panel), the radius of the larger cluster (central panel) and the fraction of active sites (right panel), the blue symbols correspond to the "active" sites and the red to the "super-active" ones. The indicators of the "normally-active" sites reaches a plateau

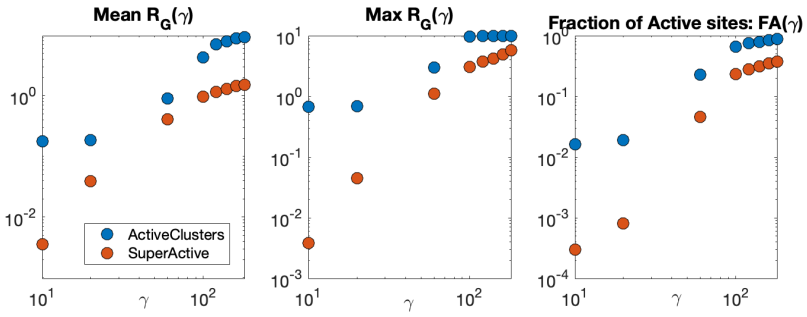


**Figure 6.15:** Spatial statistics of the binned "three levels activity maps" obtained from Echo experiments on the Carbopol sample seeded with $2\mu m$ diameter tracers at different shear amplitudes. Blue symbols correspond to "active" sites, while red symbols indicates "super active" sites (see main text for details). Left panel: mean gyration radius of the connected active domains as function of the shear amplitude. Central Panel: maximum gyration radius of a connected active domain. Right panel: fraction of active sites.

for small shear amplitudes, while the same indicators for the "super-active"

sites, homogeneously go to zero. Around $\gamma = 80\%$ the normally active cluster percolates: all the normally active sites are connected in a unique cluster.

For the same experiments we report in Fig.6.16 the distribution of the activity time $\tau_{Act}$ measured as the number of successive frames for which a given site is continuously active. We find a very broad distribution of activity times. The mean time $\langle \tau_{Act} \rangle$ (third panel) is quite small compared to the duration of the experiments, indicating that the large majority of activity events are quite ephemeral and only a small number of sites remain active for a long time.

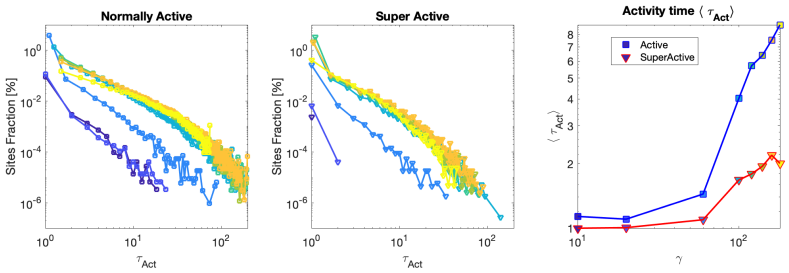


**Figure 6.16:** Left panel: frequency distribution of the activity duration for "normal activity". Central panel: histogram of the activity duration for "super activity". The colors corresponds to different amplitudes going from 10% (blue) to 180% (yellow). Right panel: mean duration of an activity burst for mobile (squares with blue line) and "super-mobile" bins (triangles with red line).

### 6.3.6 EchoDDM

EchoDDM experiments were performed using particles of three different radii: LB5, $a_1 = 250$ nm, PS2, $a_2 = 1\ \mu m$, PS5 $a_3 = 2.5\ \mu m$, at a concentration $\phi_{tr} = 0.03\%$.

#### Echo dynamics for PS2 particles

The majority of the experiments presented in this work are performed with PS2 particles, as they realize a very good compromise between different needs. On one hand, they are larger than the mesh size of the material, and thus they exhibit almost no thermal dynamics at rest. On the other hand, they are not so large to generate multiple scattering even when seeded at relatively high density. Finally, since their size is close to the expected average size of the microgels particles, we can assume that their dynamics somehow mimics the intrinsic one of the microgel particles.

Dynamic structure functions are normalized according to the following procedure. The noise term is estimated (separately for each phase) as the high-$q$ limit, short-$\Delta t$ limit of the image structure function

$$B = \lim_{\Delta t \to 0; q \to \infty} D(q, \Delta t), \tag{6.5}$$

while the amplitude is estimated from $D_0(q)$

$$A(q) = 2 \cdot D_0(q) - B. \tag{6.6}$$

where $D_0$ is calculated as the power spectrum of single images after background subtraction, as described in4.6.2.

#### Dynamics at rest

Before applying any shear we characterize the spontaneous dynamics of the tracer particles. From visual inspection of a typical image sequence of the sample at rest (2000 frames at 5 fps) it is not easy to spot any particle displacement, apart for a slow global drift due to the fact that the sample is not laterally confined.
To minimize potential spurious effects, image sequences acquired in the absence of shear are analyzed with the same protocol used for acquisitions under shear, consisting in the following sequential steps: background subtraction, registration (to remove potential drifts), DDM analysis. Moreover, in order to further reduce the effect of residual drifts, we decided to restrict our attention to **q**-values comprised within a small cone (of aperture $\theta_w = 11°$) along the direction with the slower dynamics.

While the normalized structure functions exhibit negligible temporal dependence in the accessible time window, their amplitude displays a rather clean quadratic dependence on the wave vector $q$, as shown in Fig.6.17. This be-

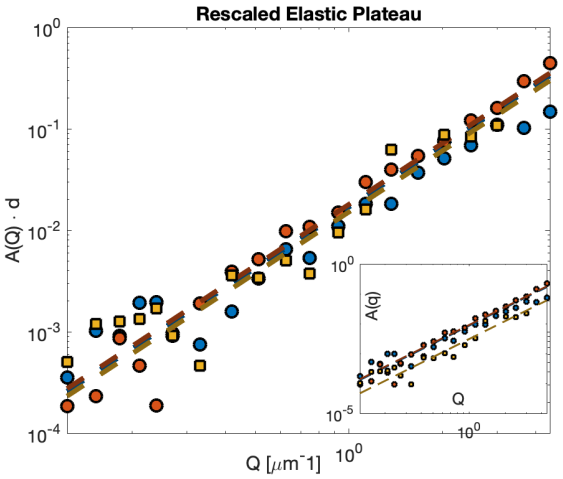


**Figure 6.17:** Dynamics in the absence of shear for 2 $\mu m$ (circles) and 5$\mu m$ (squares) particles dispersed in a Carbopol sample. Main Panel: Amplitude of the normalized structure functions rescaled with the tracers diameter $A(Q) \cdot d$ as a function of $q$. Dashed lines are best fitting curves to the data with a quadratic homogeneous function. Inset: Amplitude of the normalized structure functions $A(Q)$.

haviour is compatible with a restricted dynamics, occurring at time scales shorter than the sampling time. In other words, if we assume that the tracers undergo a fast bounded motion of mean squared amplitude $\Delta r_0^2$ with $\Delta r_0 \ll 1/q$ the structure function is given by

$$D(q,t) = \frac{\Delta r_0^2}{4} q^2.$$

If we now rescale the amplitude of the structure function with the particle diameter, we observe a good collapse all curves (compare main panel and inset in Fig.6.17), suggesting that $\Delta r_0^2$ is inversely proportional to the particles diameter. This would be in agreement with the prediction of the generalized Stokes Einstein Relation Eq.3.13 for a particle trapped in an elastic matrix. Unfortunately, if we try to estimate an elastic modulus from $\Delta r_0^2$ we get

$$G' \simeq 0.02 Pa,$$

a value which is order of magnitude smaller than the expected elastic modulus of this material ($\sim 40 Pa$)6.3.1. We can give this result two possible interpretations:

- the tracers display a bounded motion of amplitude $\Delta r_0^2$, because the material is not homogeneous on the length scales of the tracers
- the value $\Delta r_0^2$ corresponds to a *localization error*, possibly influenced from a mechanical instability of the system and set a limit to the sensitivity of our experiment.

Although the scaling with the tracer size points in the direction of the first interpretation, we note that the plateau value for the MSD of $2\mu m$ particles is $r_0^2 \simeq 0.0025\ \mu m^2$, corresponding to a typical displacement of about of one tenth of pixel, well below the experimental sensitivity. This probably makes the second hypothesis the most plausible.

It is useful to extract a sensitivity threshold also in terms of diffusion coefficient. To this aim we apply the same fitting procedure that we will use to analyze data under shear: we fit the dynamics structure functions with an exponential decay with fixed noise (6.5) and amplitude (6.6)

$$D(q, \Delta t) = A(q)\{1 - exp[-\Gamma(q)\Delta t]\}$$

where the rate $\Gamma(q)$ is the only free parameter. We force a fit with a diffusive decay $\Gamma(q) = Dq^2$ and we extract an apparent diffusion coefficient:

$$D_{S.T.} \simeq 4 \cdot 10^{-7} \mu m^2/s. \tag{6.7}$$

this value sets a lower bound for the determination detection of a diffusion coefficient in this working conditions.

### Dynamics under shear

For instrumental reasons the length of each acquisition is limited to $\sim 400$ oscillations. To minimize potential spurious effects due synchronization or registration issues, we decided to restrict our attention to **q**-values comprised within a small cone (of aperture $\theta_w = 11^\circ$ ) along the vorticity direction. Representative Echo dynamic structure functions, obtained at relatively high shear amplitude ($\gamma_0 = 80\%$), at a single phase $\varphi$, are shown in Fig.6.18 for different wave vectors in the range ($q \in [0.09, 3.3]\mu m^{-1}$). As it can be appreciated from the figure, the experimental curves are not particularly "clean". This is at least in part due to the fact that the relaxation dynamics is usually very slow compared to the experimental time window and this necessarily limits the statistical accuracy. Moreover, the quality of this kind of data is strictly dependent on the mechanical stability of the experimental set-up. Since the sample is subjected to a large macroscopic deformation, even small synchronization or image registration errors can have a strong impact on the Echo dynamics. A natural strategy to obtain "cleaner" dynamic structure functions could be to perform an average over different realization of the

same experiments. However, since the overall quality of the data collected in a single experiment is usually good enough to reliably extract the relevant dynamic parameters *via* the curve fitting procedure described in detail in the next paragraph, we decided to average the results obtained from different experiments only at a later stage of the analysis process. In order to

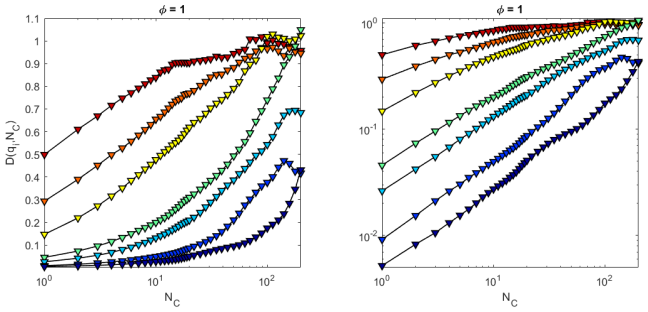


**Figure 6.18:** EchoDDM normalized dynamic structure functions for the Carbopol sample seed with PS2 tracers under shear ($\gamma_0 = 80\%$). In the two panels we report the same functions in semilogarithmic scale (left panel) and in double lograithmic scale (right panel). Colors of the symbols go from blue (small wave vectors) to red (large wave vectors). The range of wave vectors is $q \in [0.09, 3.3]\mu m^{-1}$. Time (in the horizontal axis) is measured in terms of number of cycles.

estimate a characteristic relaxation rate $\Gamma(q)$ for each wave-vector $q$, with fit a generalized exponential model to our data.
To facilitate the convergence of the fit, we adopt a model with fixed stretching exponent $\beta$:

$$D_{N,\varphi}(q, \Delta t) = 1 - \exp\big[-(\Gamma(q)\Delta t)^{\beta}\big]. \tag{6.8}$$

The subscript $N$ indicates that the structure function is normalized, and the subscript $\varphi$ indicates that each phase is analyzed separately. In the following we will omit $\varphi$ for a lighter notation.

**Errors -** Error bars are computed as the sum of two contributions: one associated with the uncertainty on the *bare* structure function $\sigma_D$, and one due to the uncertainty on the normalization $\sigma_N$

$$\sigma = \sqrt{\sigma_D^2 + \sigma_N^2}. \tag{6.9}$$

$\sigma_D$ is the standard deviation on the angular average of $D(\vec{q}, t)$: the one dimensional structure function in the vorticity direction is estimated with an angular average on an window of width $\theta_w = 11°$.
$\sigma_N$ is the propagation of the error in the determination of the baseline and the amplitude $\sigma_B, \sigma_A$ on the normalized structure function:

$$\sigma_N = \sqrt{\Big(\frac{\partial D_N}{\partial B}\sigma_B\Big)^2 + \Big(\frac{\partial D_N}{\partial A}\sigma_A\Big)^2}. \tag{6.10}$$

**Stretching exponent optimization -** To choose the best stretching exponent we followed this procedure:

- we fit $D_N(q_i, \Delta t)$ with a stretched exponential function with fixed exponent $\beta$, for some wave vectors $\{q_i\}$, sampled with a logarithmic spacing in the range of interest $[0.09, 3.3]$ $\mu m^{-1}$.
- We compute the weighed residuals

$$r(\beta) = \sum_{q_i,t} |D(q, \Delta t) - f(\beta, q, \Delta t)|^2 w(q, \Delta t) \tag{6.11}$$

  where $f(\beta, q, \Delta t)$ is the best fitting curve and the weights are given by $w(q, \Delta t) = 1/\sigma^2(q, \Delta t)$ (6.9).
- We repeat the procedure for different values of $\beta$. We find that the function $r(\beta)$ always show a well-defined minimum in the range $[0.3, 1]$ and it is nicely fitted with a parabola $r(\beta) = a + b(\beta - \beta_{min})^2$ (see Fig.6.19).
- We use $\beta_{min}$ as the fixed stretching exponent and we use the model in Eq.6.8 to fit all the structure functions for all $q$- and $\varphi$-values.

As it can be appreciated from Fig.6.19, the best exponent $\beta_{min}$ does not depend on the phase. Representative examples of the resulting best fitting

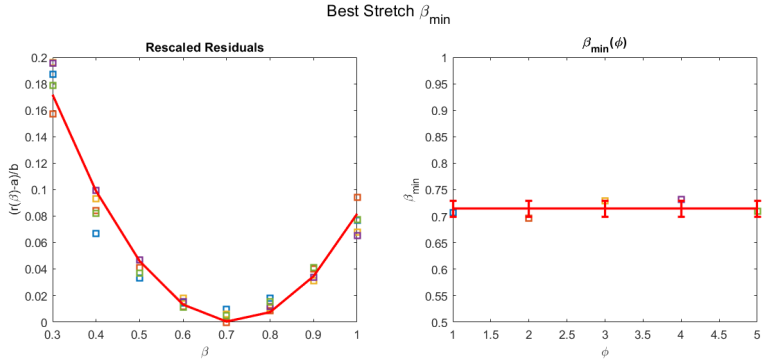


**Figure 6.19:** Optimization procedure for the selection of the exponent of the stretched exponential fitting model. Left panel: rescaled residuals $\frac{r(\beta)-a}{b}$. Different colors corresponds to different phases of the deformation cycle. $a$ and $b$ are phase-dependent parameters obtained from a parabolic fit of the residuals. Right panel: $\beta - value\langle\beta_{min}\rangle_\phi$ minimizing the residuals for the different phases.

curves are shown in Fig.6.20. From the fit we extract the $q$-dependent relaxation rate $\Gamma(q)$. The scaling, in this regime, is diffusive-like, as shown in Fig.6.21.

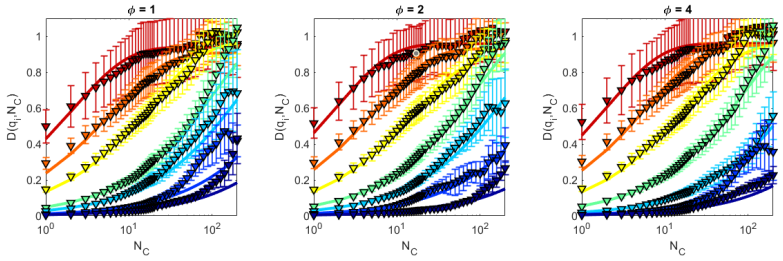


**Figure 6.20:** Representative EchoDDM dynamic structure functions. Color code as in6.18. Different panels correspond to different deformation phases. The error bars are obtained as explained in the main text. Continuous lines are best fitting curve with a stretched exponential model with fixed stretching exponent $\beta$.

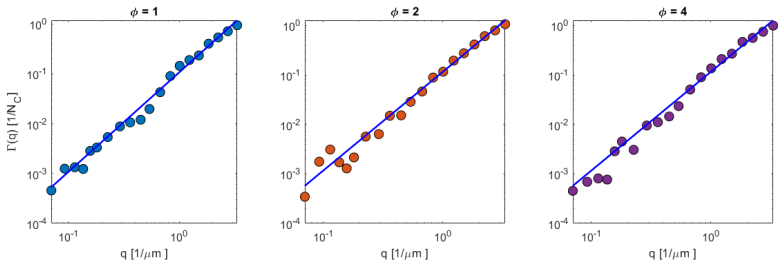


**Figure 6.21:** $q$-dependent relaxation rate $\Gamma(q)$ extracted from a stretched exponential fit of the dynamic structure function shown in Fig.6.20. Continuous lines are quadratic best fitting curves $f = D_E q^2$, providing an estimate of the effective diffusion coefficient $D_E$.

**On the fitting model -** Before moving to the presentation of the rest of the results, we would like to discuss in more detail some of the assumptions behind the adopted fitting model.

- We assume that the dynamic structure functions always decorrelate completely, with a single characteristic relaxation time. This is equivalent to assume that, at least for long times, all the particles are free to move at least over a length scale $\sim 2\pi/q$. This assumption is compatible with our data, as we don't find evidence of any plateau below 1 in the dynamic structure functions. On the other hand, the dynamics is often so slow that a complete decorrelation cannot be clearly observed for all $q$-values. In those cases, we cannot exclude that a plateau could actually exist, well outside the accessible time window.

- We assume a stretched exponential relaxation of the dynamic structure function, with the same stretching exponent for all the wave-vectors. This is compatible with a heterogeneous dynamics and a broad distribution of relaxation times.

In the following we will discuss the results of the EchoDDM experiments

in non-linear conditions for the different particle sizes.

### Shear-induced diffusion of PS2 tracers

The first set of data that we discuss are from experiments performed on a sample seeded with PS2 particles, according to the following protocol: the sample is not pre-sheared, the shear amplitude is increased at steps of $\Delta\gamma_0 \sim 10\%$ in the range $\gamma_0 \in [2\%, 180\%]$.

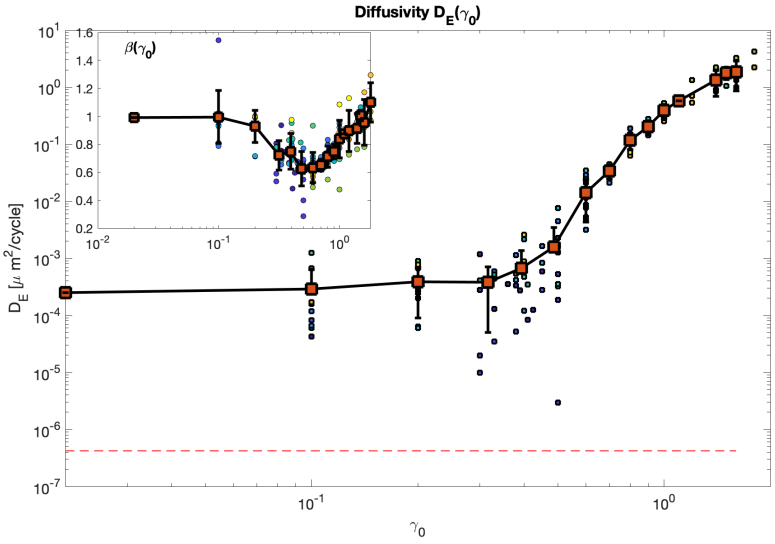


**Figure 6.22:** Main Panel: Effective diffusion coefficient as function of the imposed shear amplitude $\gamma_0$ for the Carbopol sample seeded with $2\mu m$ tracers, as obtained from EchoDDM analysis. Each one of the smaller symbols corresponds to the effective diffusion coefficient obtained from a single experiment at a given $\gamma_0$ (calculated as average over different phases of the deformation cycle). Red squares correspond the average values on different experiments with the same imposed amplitude. The red dashed line marks the estimated diffusion coefficient sensitivity threshold defined in Sect.6.7. Inset: stretching exponent $\beta(\gamma_0)$, color code as in the main panel.

In the main panel of Fig.6.22 we report the shear-induced diffusion coefficient measured in $\mu m^2$/cycle for different shearing amplitudes $\gamma_0$. The horizontal red line corresponds to our estimated sensitivity threshold. Under shear in the non-linear regime, we measure a shear-induced diffusivity which is well above the sensitivity threshold.

- The dynamic transition appears to be quite sharp: is not emerging continuously from the sensitivity limit.
- For intermediate shearing amplitudes $\gamma_0 \in (2, 30)\%$ the average value of the diffusion coefficient $\overline{D}_E(\gamma_0)$ is roughly constant, while, for $\gamma_0 >$

30%, $\overline{D}_E(\gamma_0)$ starts rapidly increasing going from $\mathcal{O}(10^{-4}\mu m^2/cycle)$ to $\mathcal{O}(1\mu m^2/cycle)$.

The stretching exponent is (almost) always smaller than one. For increasing $\gamma_0$, the average stretching exponent $\overline{\beta}(\gamma_0)$ decreases, reaches a minimum around $\gamma_0 = 60\%$ and starts then increasing again.
It seems reasonable to attribute the minimum of $\beta$ to a state of maximal heterogeneity of the dynamics. Consistently, for the same shear amplitude the dispersion of $D_E$ is quite large and the worst reproducibility is observed around $\gamma_0 \simeq 40\% - 50\%$

**Determination of the yielding threshold -** The determination of the threshold above which a plastic activity is observed is delicate. The longest delay that we consider is 100 cycles, the wave vector that has a relaxation time of 100 cycles when $D_E = 10^{-4}\mu m^2$/cycle is $q = 10\mu m^{-1}$. This value is out of our range. A representative wave-vector well within our experimental range is $q = 1\mu m^{-1}$: the longest delay that we can observe is just one hundredth of its estimated relaxation time.

**Dependence on the shear history -** The experiments presented in the previous paragraph clearly demonstrate a sharp increase of the effective diffusivity around $\gamma_0 \simeq 40\%$. To better investigate this transition, we performed new experiments where the shear amplitude is increased more gradually than in the previously discussed tests. Although these experiments turned out to

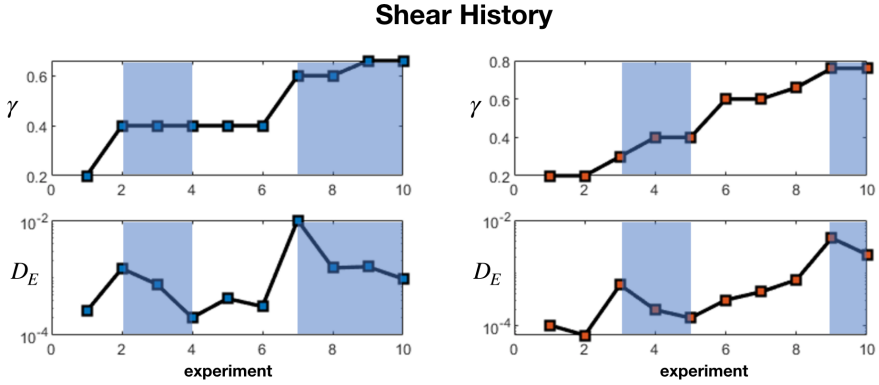


**Figure 6.23:** Effect of shear history. In the top row we report the temporal sequence of shear amplitudes imposed on the sample. Each point corresponds to an EchoDDM experiment of duration 500 s. In the bottom row the report the corresponding measured effective diffusion coefficient. Shaded areas highlight those experiment in which for a constant (or increasing) shear amplitude a decreasing diffusion coefficient is observed.

be not very helpful in locating with higher precision the transition point,

they point to some interesting consideration. In particular, we observed a marked variability in the tracers diffusivity in repeated experiments at fixed shear amplitude, as well as the presence of history-dependent effects. In Fig.6.23 in the top panel we plot the temporal progression of the imposed deformation amplitudes and in the bottom one the corresponding diffusion coefficient. While the shear amplitude is a monotonic function of time, the diffusivity is not. The effect is not completely unexpected: it is known that some time is required to reach a stationary condition, especially in the proximity of the yielding point. We have seen earlier in this section that the mechanical moduli show some evolution6.3.2, but the magnitude of the microscopic effect is surprising large if compared to a modest change in the mechanical moduli.

To clarify these unexpected results we decided to complement our EchoDDM analysis with a more standard, real-space based particle tracking analysis of the same image sequences.

**Particle Tracking: probability distribution function of tracer displacements**

In Fig.6.24 a typical outcome of a particle tracking (PT) analysis on a sample seeded with PS2 tracer, sheared at $\gamma_0 = 66\%$ is shown. While on a double linear scale the probability distribution function (PDF) of particle displacements seems to be well approximated by a Gaussian distribution, by representing the same data on a semi-logarithmic scale we can appreciate that the tails of the distribution are markedly "fatter" than expected for a Gaussian distribution. In particular, we find that the tails are well described in terms of quasi-exponential function $f(\Delta y) = exp(-(|\Delta y/\sigma|)^{\alpha})$, with $\alpha \simeq 1$[3].

To monitor the temporal evolution of the PDF we compute the MSD as a function of the delay time, whose behaviour is found to be well described in terms of an asymptotic power law (Fig.6.25 left panel). By repeating the same analysis for different shear amplitudes (Fig.6.25, right panel), we observe that the shear-induced motility depends drastically on the shear amplitude (data are color-labeled from blue at low amplitude, to red at large amplitudes). We also observe that the scaling exponent of the MSD changes from one experiment to another. To rationalize this behavior we plot the MSD at delay $\Delta t = 1$ cycle as function of the shear amplitude $\gamma_0$ (Fig.6.26, left column top panel), and the corresponding power law exponent $\alpha$ (Fig.6.26, left column bottom panel). The data display a certain dispersion but the general trend for both the MSD and the scaling exponent $\alpha$ is that of a strong increase with $\gamma_0$. The fact that the functional form of the

[3]This resembles a universal feature of the dynamics at rest of glassy systems [24].

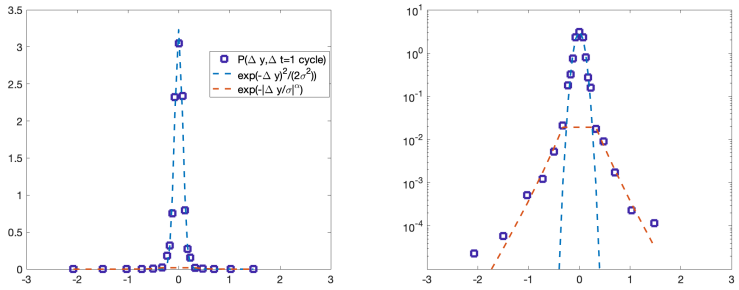


**Figure 6.24:** Probability distribution of tracer displacements measured with a particle tracking during an Echo experiment with 2 $\mu m$ particles dispersed in *Carbopol*. The sample is sheared with a nominal amplitude $\gamma_0 = 66\%$. In the two panels the same distribution is shown on a linear scale (left) and on a semilogarithmic scale (right). Dashed lines are best fitting curves with a Gaussian (blue) and a stretched exponential function (red), respectively.

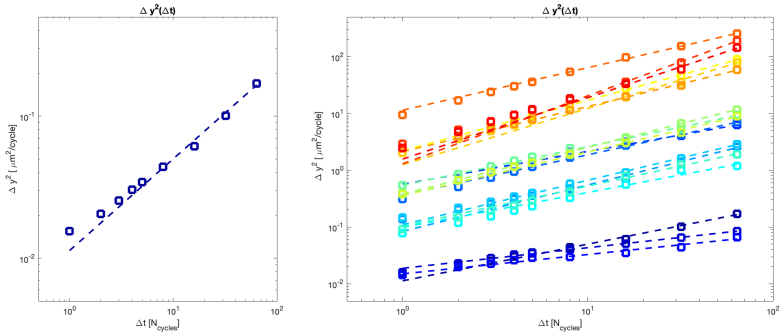


**Figure 6.25:** Power law scaling of the MSD measured with particle tracking for $\gamma_0 = 66\%$ (left panel), for shear amplitudes going from 40% to 120% (right panel). Dashed lines are fit with power laws. The values of the exponent as function of the amplitude in Fig.6.26 bottom left panel.

displacement PDF changes for different delays - probably due to the presence of two distinct families of particles with different dynamics - complicates the interpretation of the MSD scaling exponent. Further discussion of the temporal scaling of the MSD is postponed to Sect.6.3.6.
To clarify the origin of the non-monotonicity of $\Delta y^2(\gamma_0)$ we plot $\Delta y^2(\Delta t = 1)$ as function of the progressive number of the measurement (right column, central panel in Fig.6.26). In the top panel of the same column we plot the temporal sequence of imposed shear amplitudes (shear history), and in the bottom panel the power law exponent $\alpha$ as function of the progressive number of the measurement. We can clearly see that, upon repetition of the experiment at a fixed shear amplitude, a systematic slowing down of the dynamics is observed. This is the same qualitative behaviour observed in EchoDDM experiments. To obtain a more quantitative comparison we

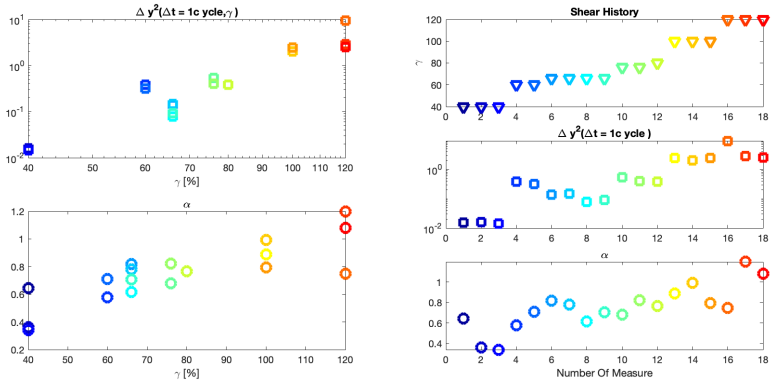


**Figure 6.26:** Particle tracking analysis of shear-induced dynamics in a Carbopol sample seeded with 2 $\mu m$ diameter tracers. Left top panel: MSD in the vorticity direction at delay $\Delta t = 1$ cycle as function of the shear amplitude. Left bottom panel: exponent $\alpha$ describing the scaling of the MSD as function of time plotted as function of $\gamma_0$ (see main text for details). Right upper panel: temporal sequence of the imposed shear amplitudes. Right central panel: temporal sequence of the value of the MSD for delay equal to one cycle. Right bottom panel: temporal sequence of the power law exponent $\alpha$.

adopt the following procedure: we fit the long time mean square displacement in the vorticity direction with a diffusive model: $\Delta y^2(\Delta t) = 2D\Delta t$ and we compare the extracted diffusion coefficient with the one extracted from EchoDDM Fig.6.27, right panel. The correlation between the effective diffusivity estimated with DDM and PT is not perfect but is good enough to corroborate the idea that the observed shear history dependence is a genuine physical effect.

The non perfect agreement between the diffusion coefficient extracted with DDM and PT might be due to the fact that the microscopic dynamics of the sample appears strongly heterogeneous. As a consequence, the function MSD($\Delta t$) is a useful yet not complete indicator of the dynamics and different averaging strategy may lead to different results.
This can be appreciated in Fig.6.27. In the right panel the diffusion coefficient is extracted from the MSD determined directly as the second moment of the displacement distribution. To obtain the results in the left panel we first compute the displacements' cumulative distribution function (CDF) for a fixed time delay; we then fit it with an error function[4]

$$\mathrm{CDF}(\Delta x; \Delta t) = 0.5 + 0.5\ \mathrm{erf}\Big(\frac{\Delta x - \Delta x_0}{\sqrt{2}\cdot\sigma}\Big) \tag{6.12}$$

to extract the MSD($\Delta t$) $= \sigma^2$; as a last step, we fit the MSD($\Delta t$) with a diffusive law do extract the diffusion coefficient.

[4]Corresponding to a Gaussian PDF.

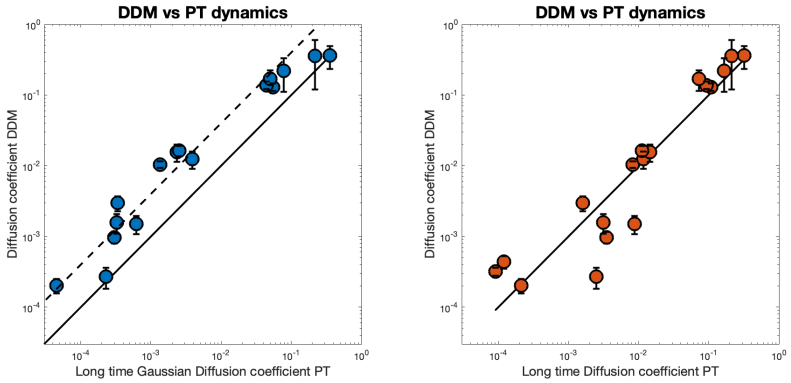


**Figure 6.27:** Comparison of the diffusion coefficient estimated with particle tracking and with DDM for the experiments presented in this section6.26. In the left panel the PT Diffusion coefficient is estimated fitting the displacement CDF with an error function, corresponding to Gaussian hypothesis for Gaussian displacements PDF. In the right panel the PT MSD is computed without the assumpion of a model for the CDF. In both panels the continuous black line corresponds to the identity, the dashed line in the left panel corresponds to $y = 4 \cdot x$.

With both strategies, the correlation of the PT diffusion coefficient with the DDM diffusion coefficient is strong. However, in the first case (right panel) we have $D_{\mathrm{PT}} \simeq D_{\mathrm{DDM}}$, whereas in the second (left panel): $D_{\mathrm{PT}} \simeq (1/4)D_{DDM}$.

It is quite natural to wonder if a stricter correspondence links the dynamical quantities measured in direct (PT) and in reciprocal space (DDM). At the same time, we know that the non-Gaussianity of the displacements' PDF complicates this comparison. We briefly present some attempts to answer this question.

**Sub-diffusive MSD model -** We can hypothesize that the non perfect correspondence between PT and DDM is due to an inadequate modeling of the MSD. To test this hypothesis we try to use a more general model . As shown in Fig.6.25 the MSD follows a power law dependence on the lag time

$$\mathrm{MSD}(\Delta t) = 2A \cdot (\Delta t)^{\alpha} \tag{6.13}$$

where we call $A$ "motility" (if $\alpha = 1$ $A$ is a Diffusion coefficient, if $\alpha = 2$ $A$ is proportional to the velocity squared). For Gaussian displacements' PDF

the resulting structure function[5] is:

$$\begin{aligned} D(q,\Delta t) &= 1 - exp\{-q^2 \cdot \mathrm{MSD}(\Delta t)/2\} \\ &= 1 - exp\{-q^2 \cdot A(\Delta t)^\alpha/2\} \\ &= 1 - exp\{-(A^{1/\alpha}q^{2/\alpha}\Delta t)^\alpha\} \\ &= 1 - exp\{-(\Gamma(q)\Delta t)^\beta\} \end{aligned} \tag{6.14}$$

*i.e.* a stretched (if $\alpha < 1$) exponential decay with a stretching exponent $\beta$, equal to the power law exponent of the MSD

$$\beta = \alpha \tag{6.15}$$

and the relaxation rate

$$\Gamma(q) = A^{1/\alpha}q^{2/\alpha} = Bq^\delta, \tag{6.16}$$

from Eq.6.16, $B$ is connected to the above defined motility by

$$B = A^{1/\alpha}, \tag{6.17}$$

and the q-scaling exponent

$$\delta = 2/\alpha. \tag{6.18}$$

In Fig.6.28 we report the comparisons between the parameters extracted via PT and DDM. The PT data are again treated according to the procedure described before (blue symbols are obtained through a Gaussian modeling of the PDF), and the dashed black lines always represent the expected relation in the Gaussian case. In the top left panel we plot $\alpha(\beta)$ (expected to be equal in the Gaussian displacement case). In the bottom left $\alpha(\delta)$. In the right panel the motility $A^{1/\alpha}(B)$. Concerning the exponents $\alpha, \beta, \delta$, left column's plots show that they are quite clearly correlated, but their relation seems to depart from what expected in the Gaussian case. The "motility" measured in PT and DDM also correlates strongly but again their correlation does not agree with the Gaussian case prediction.
We conclude that even a more general assumption on the MSD ($MSD \propto (\Delta t)^\alpha$) does not increase the quality of the agreement between DDM and PT as compared to the previous modeling (diffusive dynamics Fig.6.27).

**Statistical samples difference -** As anticipated, the difference is easily explained with the non-Gaussianity of the displacements' PDF, but this may not be the only reason: an additional ingredient to this discrepancy may be found in the difference between the PT and DDM samples. To check this hypothesis we use the PT trajectories to produce synthetic movies to

[5] In one dimension, with straightforward generalization to two or three dimensions.

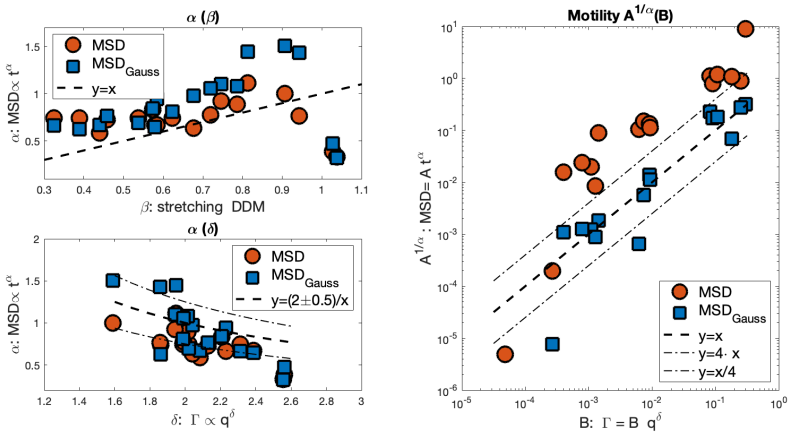


**Figure 6.28:** Test of the hypothesis of Gaussian sub-diffusive behaviour. As explained in detail in the main text, assuming $MSD(\Delta t) = 2A\Delta t^{\alpha}$ implies a stretched exponential decay for the structure functions: $D(q, \Delta t) = 1 - exp\{-(\Gamma(q)\Delta t)^{\beta}\}$, with $\beta = \alpha$ (top left panel), the relaxation rate scaling as $\Gamma = B \cdot q^{\delta}$, with $\delta = 2/\alpha$ (bottom left panel), and $B = A^{1/\alpha}$ (right panel).

which we apply the DDM processing. We eventually compare the structure functions of the synthetic data to the one obtained by the raw data.
A representative example of this comparison is shown in Fig.6.29, the one-dimensional structure functions $D(q, \Delta t)$ are represented for different wave vectors in different panels. In general at the higher qs the two methods agree, and at low qs the raw DDM structure function (diamonds) are always slower than the one obtained from the synthetic movies (stars). In this case there is no underlying hypothesis of Gaussianity, thus the difference in the normalized structure functions probably suggests that the statistical samples are different or, in other words, the particles considered in PT are different from the the one considered in DDM.

### Shear-induced diffusion of SP5 particles

Similar experiments were performed with particles of different dimensions. The comparison of the shear-induced diffusion for particles of different sizes can help us in understanding more deeply the microscopic counterpart of the shear-induced fluidization. EchoDDM analysis reveals that the applied shear induces an effective diffusive dynamics also on these bigger particles. In Fig.6.30 we report the averaged stretching exponent and the effective diffusion coefficient as function of the strain amplitude $\gamma_0$. The observed behaviour is qualitatively similar to the one observed in experiments with SP2 particles. In particular, the stretching exponent $\beta(\gamma_0)$ displays a minimum and the effective diffusion coefficient increases sharply for $\gamma_0 > 50\%$. At fixed $\gamma_0$ the diffusivity of SP5 particles seems to be systematically slower

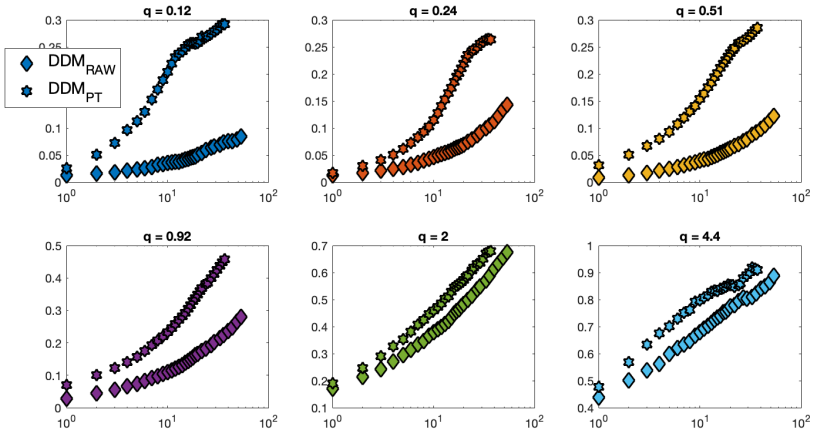


**Figure 6.29:** Comparison of the structure functions obtained from raw data (diamonds) and from synthetic movies (stars) created from the PT trajectories. In both cases we consider the wave vector q in the vorticity direction. Different panels correspond to different moduli of the wave vector (value reported in the panels' titles in $[\mu m^{-1}]$. In both cases the structure functions are normalized following the same procedure.

that the one of SP2 particles, but the difference falls within the range of sample-to-sample variability.

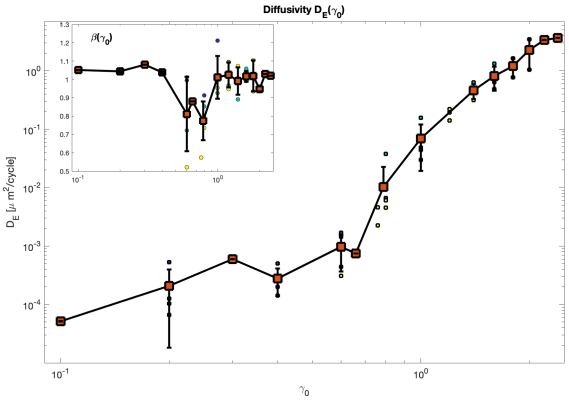


**Figure 6.30:** Main Panel: effective diffusion coefficient as function of the imposed shear amplitude $\gamma_0$ for Carbopol sample ($c = 0.5\%$) seeded with 5 $\mu m$ tracers, as obtained from EchoDDM analysis. Each one of the smaller symbols corresponds to the effective diffusion coefficient obtained from a single experiment at a given $\gamma_0$ (calculated as average over different phases of the deformation cycle). Red squares correspond the average values on different experiments with the same imposed amplitude. Inset: stretching exponent $\beta(\gamma_0)$, color code as in the main panel.

### Shear-induced diffusion of LB5 particles

The behaviour is qualitatively different for particles of smaller size (LB5, radius 250 $\mu m$). In this case, on the scale of the particle size, we cannot longer assume that our Carbopol sample behaves like an homogeneous material. This is made immediately apparent by the fact that even at rest some of the tracer particles show a constrained ("caged") diffusive motion. This in-cage diffusion is observed also for sheared samples (at least for intermediate shear amplitudes). The effect of the applied shear is to introduce a second relaxation mechanism that superimpose to the in-cage diffusive dynamics.
Ideally, we would like to determine simultaneously and independently these two dynamic behaviour, but the complexity of the microscopic dynamics, the critical mechanical stability of the experimental setup and the sample-to-sample variability make the task quite difficult.
A "zeroth order approach", in the absence of a complete fitting model, is to fit the structure functions with a single decay with the same stretching exponent for all wave-vectors. Then we fit the relaxation time as function of $q$ with a diffusive scaling, obtaining an effective diffusion coefficient $D_E$, that we use as rough indicator of how the tracer mobility depends on the strain amplitude $\gamma_0$ (see Fig.6.31).

The characterizing traits of the results obtained with this approach are following:

- There is a marked sample-to-sample variability. This could be a consequence of the fact that the length scales over which the sample is

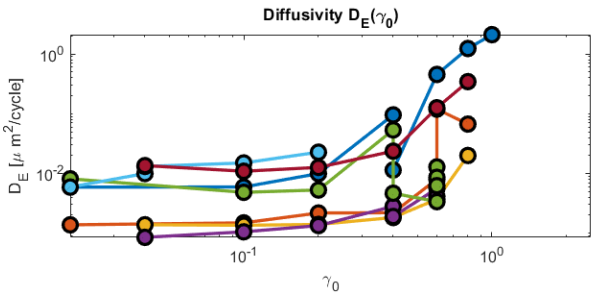


**Figure 6.31:** Effective diffusion coefficient of the LB5 tracers dispersed in *Carbopol*, extracted from the fit of the structure functions with a single decay as explained in the main text. Each color corresponds to an independent experimental run.

probed are more heterogeneous.

- The overall behaviour of $D_E(\gamma_0)$ has some distinctive features:
  - on a wide regime of shear amplitudes ($0.1 \leq \gamma_0 < 40\%$) the effective diffusion $D_E$ is essentially flat
  - the relaxation dynamics speed up for $\gamma_0 \geq 40\%$, but the increase of $D_E$ as a function of $\gamma_0$ is slower compared to what observed for larger tracers.

We also note that the range of shear amplitudes that can be probed in the experiments performed with LB5 tracers is narrower compared to the one of previously presented experiments. This is dictated by the fact that, for large shear amplitudes, the registration procedure tends to fail[6].

An alternative approach to obtain a quantitative information on the sample dynamics is to invert the structure functions to directly obtain, with a procedure similar to the one used in DDM microrheology (4.3.3), the MSD of the particles. This would enable bypassing the problem of identifying *a priori* a suitable functional form of the MSD. To do so, we exploit the fact that, even if the displacement probability distribution is not Gaussian, in the low-$q$ limit the following identity is expected to hold [35]

$$D_N(q,t) \simeq 1 - \exp(-\langle \Delta r^2 \rangle q^2/4). \tag{6.19}$$

If we perform the inversion by using a constant $B$-value obtained as the high-$q$ limit of $D$ (see Eq.6.5) and the amplitude $A(q)$ obtained from the statics (see Eq.6.6), we find systematical differences between the MSD extracted at different $q$ -values in the range $[0.23, 3]\mu m^{-1}$. This could indicate

[6] This is likely associated to the contrast of the image cross-correlation function that is smaller for smaller particles.

that the values of $A$ and $B$, obtained with the aforementioned procedure, are not accurate enough. On the other hand, if we apply the self-consistent inversion algorithm described earlier in Sect.4.3.3, the results are not fully satisfactory as they show a marked dependence on the specific choice of $q$-range over which the optimization procedure is performed.
To solve this issue, we identify a reasonable $q$-range $[0.23, 1.9]\mu m^{-1}$ that we hold fixed for all the experiments. The qualitative criteria used for the choice of the range are: the q values should not be too high, since Eq.6.19 is valid at low qs, at the same time the range has to be wide in order to make robust the self-consistent inversion procedure. In Fig.6.32 we report the resulting MSD extracted from a single sample sheared at increasing amplitude. Error bars correspond to the standard deviation of the MSD obtained at different phases of the deformation cycle. The red lines are a best fitting curves to the data with a simple linear model $\langle \Delta r^2 \rangle = 4D_E t + \Delta r_0^2$, where the non-homogeneous term $\Delta r_0^2$ accounts for the constrained, short-time dynamics of the tracers and can be identify as a sort of "effective cage size".

The described approach enables extracting an effective diffusivity, whose

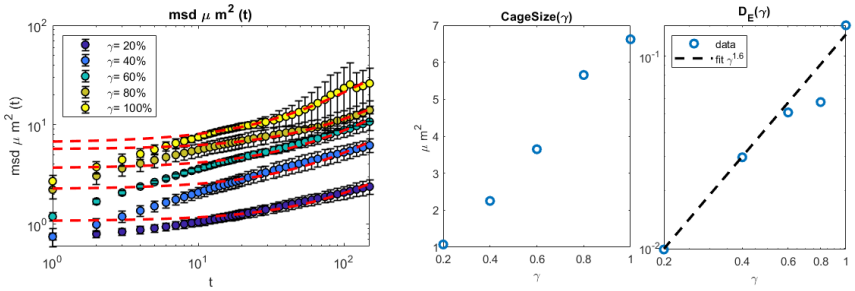


**Figure 6.32:** From left to right: MSD, estimated cage size and effective diffusion coefficient measured through self-consistent inversion of the structure functions. Data are obtained from a sequence of experiments with 0.5 $\mu m$ tracers in *Carbopol* sheared at increasing amplitude.

rapid increase with $\gamma_0$ clearly outlines the effect of the shear in accelerating the microscopic dynamics. Applying the same treatment to all the collected data confirms a strong sample to sample variability. The average on a subset of four experiments is reported in Fig.6.33.

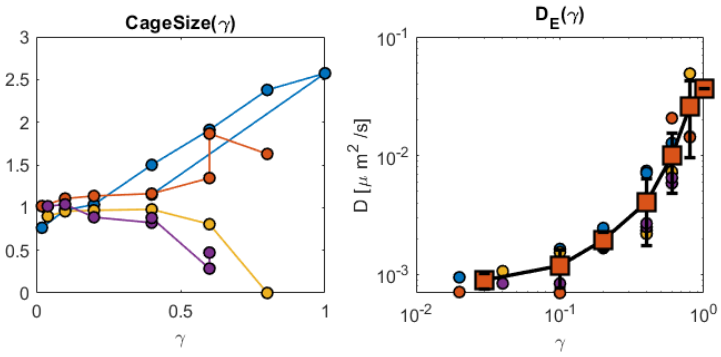


**Figure 6.33:** From left to right: cage size $[\mu m]$ and diffusion coefficient for all the experiments performed on the Carbopol sample seeded with $0.5\mu m$ tracers. The red squares are the average over different experiments with same imposed shear amplitude.

### Dependence of the shear-induced effective diffusivity on tracer size and shear frequency

In previous paragraphs we described in some detail the different methods used to extract a dynamic information from EchoDDM experiments performed with tracers of different size. Here, we give an overview of all the results collected so far, trying to learn something about the physical mechanism ruling the shear-induced diffusion. In particular, we want to understand how far can be pushed the analogy between the yielding (or yielded) material and a liquid. We start discussing the effect that the imposition of a large shear deformation can have on the sample (and so on the tracer mobility). The effect is at least twofold:

1. to modify the structure of the material and its mechanical properties
2. to inject mechanical energy in the system.

Of course, in YSF the two mechanism occur at the same time. Nevertheless, we can think at two idealized scenarios where only one of the two effects is present.

1. **The "melting scenario" -** In this picture the effect of shear is only to decrease the viscosity of the sample, and thus to facilitate and speed-up Brownian diffusion.

2. **The "plastic scenario" -** in this picture, the material behaves like a granular (non-Brownian) system where the tracer dynamics is directly induced by shear: the source of the energy is the mechanically dissipated energy.

One strategy to decide which of the two scenarios is the most plausible one, is to perform tests at different frequencies. Let us consider two identical samples, deformed with the same shear amplitude but with different frequency. If the first mechanism is the dominant one, we expect to observe during a prescribed time interval the same characteristic tracer displacement in the two sample. In the second scenario, instead, we expect the characteristic tracer displacement *per cycle* to be the same for the two samples.

If, as in the present case, the shear-induced motion is diffusive-like, we can define an effective diffusion coefficent $D_T(\gamma, \nu)$ as the MSD of the tracers *per unit time* and an effective diffusion coefficent $D_C(\gamma, \nu)$ as the MSD of the tracers *per cycle*. If the first scenario is the correct one, we do expect to measure the same value of $D_T$ across experiments performed at different frequency $\nu$ (*i.e.* $D_T(\gamma, \nu)$ does not really depends on $\nu$) , while in the second scenario is $D_C$ to remain unchanged (*i.e.* $D_C(\gamma, \nu)$ does not really depend on $\nu$).

In the following, we will test the consistency of these two competing scenarios comparing experiments performed at different frequencies. For each value of $\gamma$ we calculate the relative spread $\sigma_T(\gamma)/\overline{D_T}(\gamma)$, and $\sigma_C(\gamma)/\overline{D_C}(\gamma)$ where $\overline{D_{T,C}}(\gamma) = \langle D_{T,C}(\gamma, \nu)\rangle_\nu$ and

$$\sigma^2_{T,C} = \Sigma_\nu \frac{\left(D_{T,C}(\nu) - \overline{D_{T,C}}\right)^2}{n_\nu}.$$

For the PS2 diameter particles if we apply this strategy to the whole dataset we observe no particular trend as function of $\gamma$, the small difference between $\sigma_T(\gamma)/\overline{D_T}(\gamma)$ and $\sigma_C(\gamma)/\overline{D_C}(\gamma)$ being completely overcome by the large intrinsic variability between different experiment. In order to reduce such variability, we limit the analysis to only one sample that (in the very same day) was sheared at different frequency. Under these conditions, it is possible to observe a crossover between two regimes: for large shear amplitudes ($\gamma > 80\%$) $D_C$ displays the weaker frequency dependence, while for smaller amplitude ($20\% < \gamma < 80\%$), $D_T$ seems to be the more conserved indicator of the tracer dynamics.

A qualitatively similar behavior is observed also in the experiments performed with 5 $\mu m$ diameter Fig.6.35 and 0.5 $\mu m$ particles Fig.6.36. In the latter case the rescaling with time is the more appropriate for $\gamma < 40\%$. At higher shear amplitude we find a better agreement when data are rescaled with the number of cycles.

To summarize this part we can say that, for all the tested tracers' sizes, the shear-induced diffusion is better described in terms of the "viscous scenario" for small and intermediate values of $\gamma$, while the "plastic scenario" seems to hold for higher shear amplitudes.

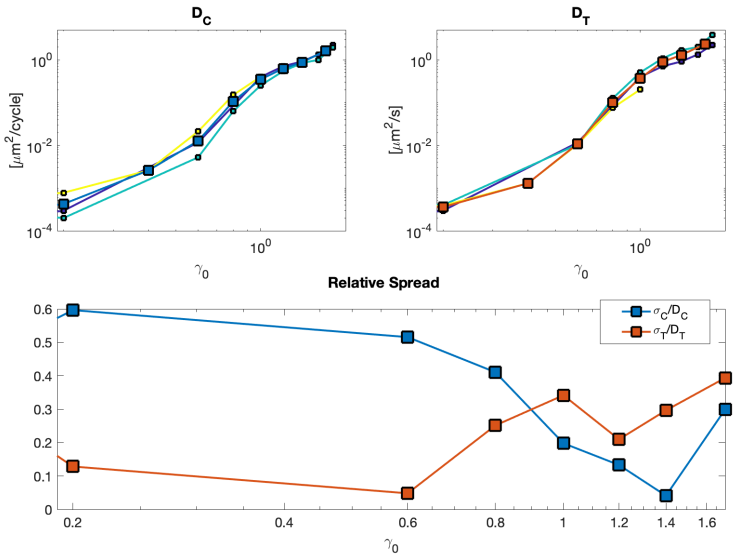


**Figure 6.34:** Effective diffusion coefficient for 2 $\mu m$ tracers in Carbopol obtained from selected experiments, all performed with a similar shear protocol, at different frequencies: (0.5, 1, 2) $Hz$. Top left panel: effective diffusion coefficient $D_C$, calculated adopting the period of the deformation cycle as a time unit. The top right panel: frequency-corrected effective diffusion coefficient $D_T = \nu D_C$. Bottom panel: relative spread among experiments with the same amplitude and different frequency for $D_C$ (blue symbols), and $D_T$ (red symbols).

We now try to combine and compare results obtained with particles of different sizes (see Fig.6.37). Again, we test two competing options:

- the effective diffusion coefficient depends on the tracer size as prescribed by the Stokes-Einstein relation (as it could be expected in the "melting scenario", where the yielded material behaves like an ordinary liquid)
- the effective diffusion coefficient is size-independent (as it could be expected in the "plastic scenario")

As it can be appreciated from the figure, the overlap between curves obtained with tracers of different sizes is generally improved upon rescaling with the size. In this region there is a strong analogy with the microscopic dynamics in a liquid:

$$D \propto 1/a$$

The fact that the dynamics is diffusive suggests that the "kicks" that promote the stochastic motions of the tracers occur on length-scales way smaller than the particles. Brownian diffusion comes from a balance between temporally and spatially uncorrelated thermal kicks and viscous drag (which is

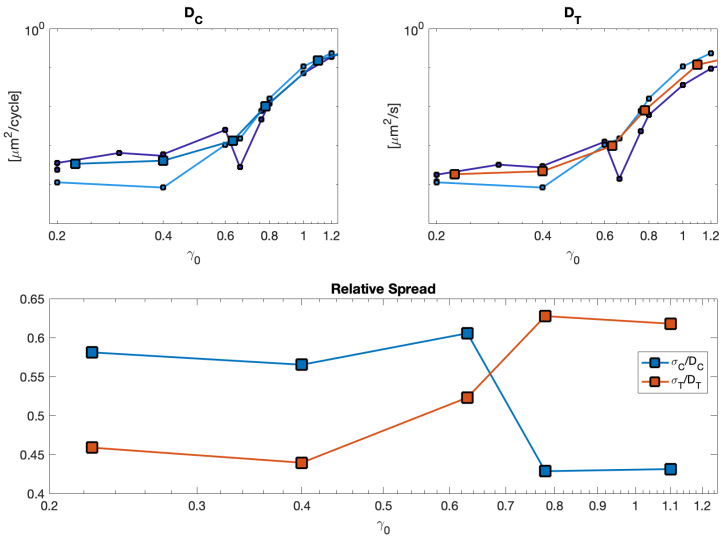


**Figure 6.35:** Effective diffusion coefficient for 2 $\mu m$ tracers in Carbopol obtained from selected experiments, all performed with a similar shear protocol, at different frequencies: (0.5, 1, 2) $Hz$. Top left panel: effective diffusion coefficient $D_C$, calculated adopting the period of the deformation cycle as a time unit. The top right panel: frequency-corrected effective diffusion coefficient $D_T = \nu D_C$. Bottom panel: relative spread among experiments with the same amplitude and different frequency for $D_C$ (blue symbols), and $D_T$ (red symbols).

proportional to the section of the particle and its velocity). The validity a similar $D \propto 1/a$ scaling suggests that a similar balance could occur also in shear induced diffusion.

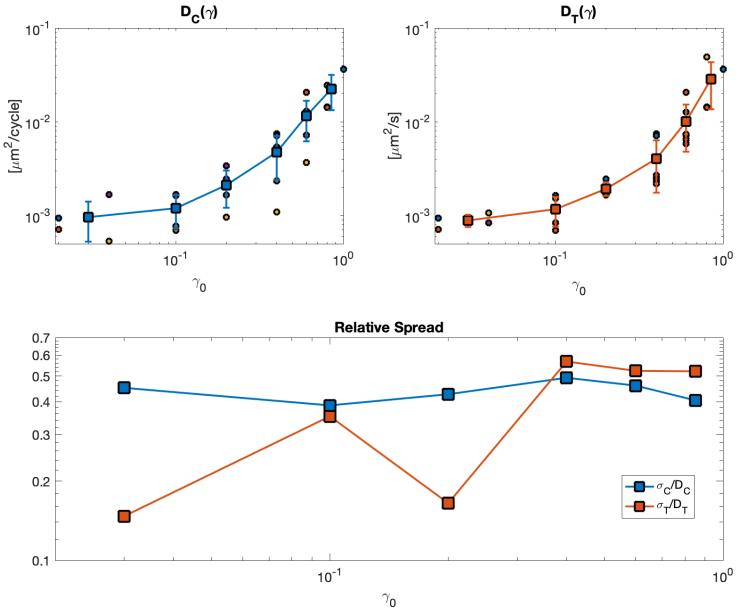


**Figure 6.36:** Effective diffusion coefficient for 0.5 $\mu m$ tracers in Carbopol obtained from selected experiments, all performed with a similar shear protocol, at different frequencies: (0.5, 1, 2) $Hz$. Top left panel: effective diffusion coefficient $D_C$, calculated adopting the period of the deformation cycle as a time unit. The top right panel: frequency-corrected effective diffusion coefficient $D_T = \nu D_C$. Bottom panel: relative spread among experiments with the same amplitude and different frequency for $D_C$ (blue symbols), and $D_T$ (red symbols).

### 6.3.7 Microgels concentration dependence

In addition to the microgel sample with polymer concentration $c_1 = 0.5\%$ wt, we also studied two samples with $c_2 = 2\%$ wt and $c_3 = 5\%$ wt. We first determined their rheological properties with linear ($\gamma = 1\%$) frequency sweeps (Fig.6.38, left panel) and amplitude sweeps (Fig.6.38, right panel), by using rheometry. The three yield stress fluids exhibit very similar linear properties: applying a multiplicative rescaling with the low frequency value of $G'(c)$ (reported in the inset of the left panel of Fig.6.38) the linear moduli overlap fairly well.

EchoDDM experiments on the same samples show that the relaxation rate at a representative wave vector $q = 1\ \mu m^{-1}$ Fig.6.39 changes drastically with the microgels concentration, the dynamics becoming slower for increasing polymer concentration.

Interestingly, this observation seems to correlate with the non-linear rheological properties of the materials that we can extract, for instance, by determining the value of $\gamma$ at the crossover point (marked by red edge circles

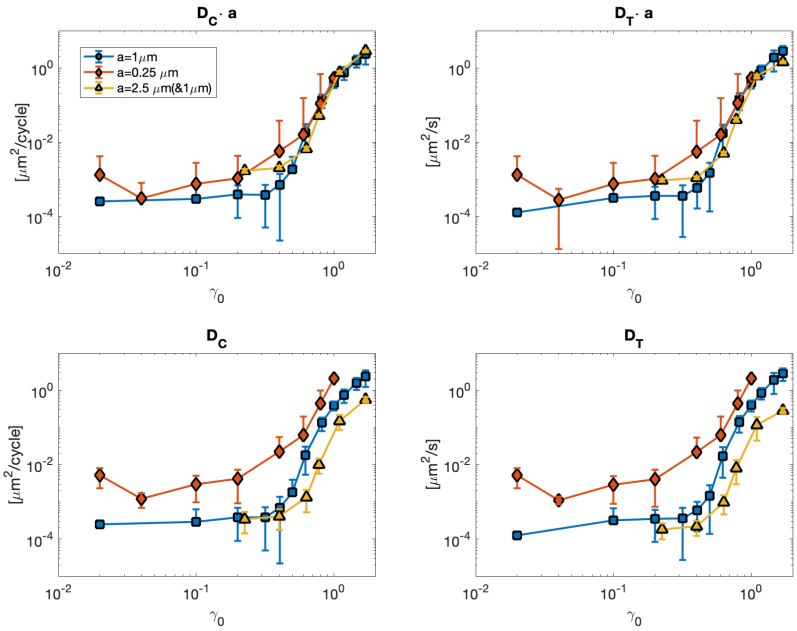


**Figure 6.37:** Shear-induced effective diffusion coefficient of tracers of different sizes (2 $\mu m$ - blue symbols, 0.5 $\mu m$ - red symbols, 5 $\mu m$ - yellow symbols) in Carbopol. In the panels on the left the effective diffusion coefficient $D_C$ is calculated adopting the period of the deformation cycle as a time unit, while on the right panels the frequency-corrected effective diffusion coefficient $D_T = \nu D_C$ in shown. In the panels on the top the vertical axis is scaled with the the particle radius $a$, while in the bottom panels it is not.

in Fig.6.38). The crossover amplitude $\gamma_c$ increases with the concentration (inset of the right panel in Fig.6.38), which indicates that a stronger material is obtained for increasing polymer concentration. These preliminary findings are very encouraging and further work along this direction will be needed to make a more deep connection.

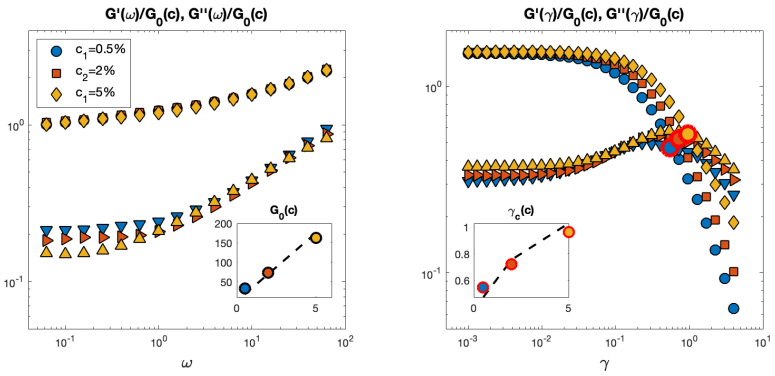


**Figure 6.38:** Left panel: frequency sweep $G', G''(\omega)$ for different polymer concentrations, $c_1 = 0.5\%$ blue symbols, $c_2 = 2\%$ red symbols, $c_3 = 5\%$ yellow symbols. Both the moduli are rescaled with $G_0(c)$ the low frequency value of $G'$. Inset $G_0(c)$, the black dashed line is a linear homogeneous fit. Right panel: amplitude sweep $G', G''(\gamma)$ for different polymer concentrations, symbols as in the left panel. Both moduli are rescaled with $G_0(c)$. The crossover point has been marked with a red edge circle, the stain value of the crossover point is reported in the inset as function of the concentration. The black line is $\propto c^{1/3}$ and serves as guideline for the eyes.

### 6.3.8 $q$-resolved dynamical susceptibility analysis

We try to apply our $q$-resolved dynamic heterogeneity approach to the sample under shear. The output of this procedure on a typical experiment is reported in Fig..:6.40. To try to overcome the data noise we bin together different wave vectors and to average together the results of different experiments. Unfortunately no clear signature of DH is observed. Probably this is mainly due to the relatively small number of particles present in the field of view, and the limited number of images per measure (compared to [90]).

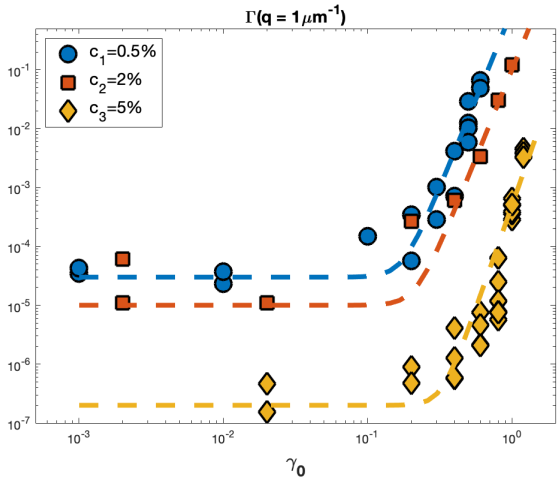


**Figure 6.39:** Relaxation rate at a reference wave vector $q = 1\mu m^{-1}$ oriented in the vorticity direction, for different concentrations (colors as in 6.38) as function of the imposed shear amplitude $\gamma_0$ (not corrected for possible slip or other non affine phenomena). The dashed lines are guidelines for the eyes.

## 6.4 On the connection between macroscopic and microscopic yielding

We review now altogether the results obtained for this sample with different macroscopic and microscopic techniques.

From linear rheology we learn that this sample, at rest has a solid-like behaviour, since the frequency sweep reveals the absence of a relaxation time at small frequency. This characterization can be translated in a linear creep compliance that reaches a plateau.
In the amplitude sweep, around $\gamma_P = 1\%$ $G''$ starts to increase smoothly, it reaches its maximum around $\gamma_M = 50\%$, from that point decreases again smoothly and it crosses $G'$ around $\gamma_{c.o.} = 70\%$.

From Lissajous plots emerge that in all the explored region the first harmonics of the non-linear viscoelastic moduli is a good approximation of the system period average response. In other words the higher harmonics contributions to the stress are always small. Moreover up to $\gamma \sim 100\%$ the mechanical response appears as homogeneous during the cycle.

These mechanical tests reveal the onset of plasticity but are not sufficient to place the *yielding point*: the shear amplitude at which the system transit from a solid-like to a liquid-like behavior. If we want to know if the sheared material is in a fluid or in a solid state we need to know if

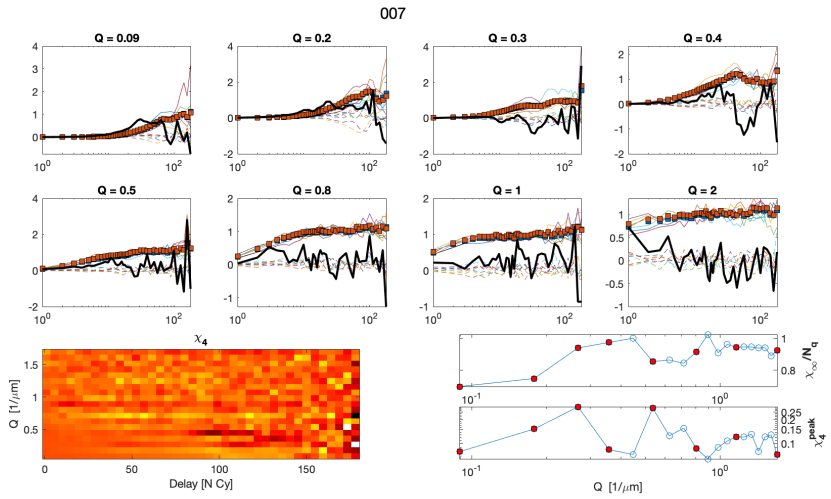


**Figure 6.40:** $q$-dependent dynamic susceptibility of a soft colloidal glass (Carbopol) under shear. First and second rows: rescaled dynamic susceptibility: $\chi_0/(1-\alpha)$ (blue squares), square of the structure function $(D(q,\Delta t))^2$ (red squares), rescaled dynamic susceptibility $10 \cdot \chi_4$ (black lines). Each panel corresponds to a different wave-vector $Q$, as indicated in the title (units $= 1/\mu m$). Left bottom panel: $\chi_4(q,\Delta t)$. Right bottom panels, form top to bottom: scaling factor $\chi_\infty/N_q$ and $\chi_4$ peak height. Red symbols identify the wave-vectors reported in the eighth panels on the top.

the mechanical response has a relaxation time : a frequency $\omega_R$ so that for $\omega < \omega_R$ $G'(\omega;\gamma) < G''(\omega;\gamma)$, or equivalently the linear creep compliance of the sheared material $J(t) \propto t$ for $t > t_R$. In this context we can interpret the crossover point ($G'(\gamma) > G''(\gamma)$ for $\gamma > \gamma_{c.o.}$) as the point at which the relaxation time becomes equal to the shearing period. As a consequence the yielding point is expected to lay in $\gamma_P\gamma < \gamma_{c.o.}$.

Activity maps reveals the presence of plastic rearrangements for shear amplitude in the non-linear region. The activity is spatially heterogeneous and correlated on areas way larger than the typical displacements of the particles[7]. The size of connected active regions grows for $\gamma > 20\%$ and invades the FOV at $\gamma = 100\%$.
Also the microscopic evidence of plastic activity is not a sufficient sign for yielding: to discriminate a flowing from a non-flowing material we need information on the extent of the constituents rearrangements, and in particular we want to know if neighbours position exchanges are allowed. This has not to happen necessarily during one cycle, it may involve several cycles.

[7]The displacements detectable with this method is of the order of the PSF $\sim 1\mu m$.

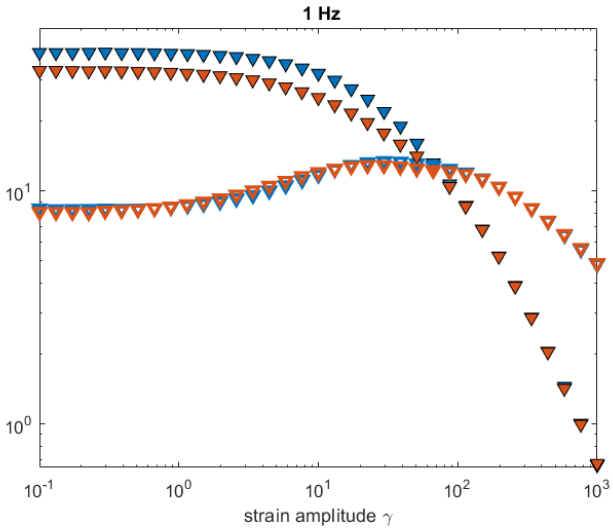


**Figure 6.41:** Dynamic Amplitude Sweep at 1 Hz on Carbopol at a polymer concentration $c = 0.5\%$, full (empty) symbols are $G'$ ($G''$). Blue symbols data are acquired for increasing shear amplitude $\gamma = 0.1\% \rightarrow 1000\%$.

This information comes from EchoDDM experiments Fig.6.42. For shear amplitudes $\gamma \geq 2\%$ the dynamics is sensibly enhanced with respect to the rest condition. The dynamics is compatible with a diffusive behavior, but because of the temporal limits of the acquisition is not clear whether the observed diffusion is a caged diffusion or a free diffusion.
To distinguish the two we introduce a threshold that accounts for the limited temporal window.

We will consider a sample to be fluidized if rearrangements of the order of the material constituents' average diameter are observed within our experimental time window: $\Delta y^2(\Delta T = 100 \text{ cycles}) \sim 1\mu m$. The effective diffusion coefficient associated to this threshold is

$$D_{Tr} \simeq 5 \cdot 10^{-3} \mu m/\text{cycle}$$

This condition is realized around $\gamma_0 \simeq 50\% - 60\%$, that accounting for the slip corresponds to $\gamma \simeq 45\% - 55\%$.
We observe that this value is a reasonable value for the yield stain since it lays in the non-linear regime and before the crossover point.

The fact that the diffusion coefficient measured with tracers particles with different sizes ($d \in [0.5\mu m, 5\mu m]$) nicely collapse when rescaled with the particle radius encourages the parallelism between the sheared solid and a liquid at rest[8].

[8]We can take this as the microscopic analogy to the elliptic Lissajous plots. This is no more than an analogy and the statement is not a rigorous since the conditions that gives the observed outcomes for the two tests are different.

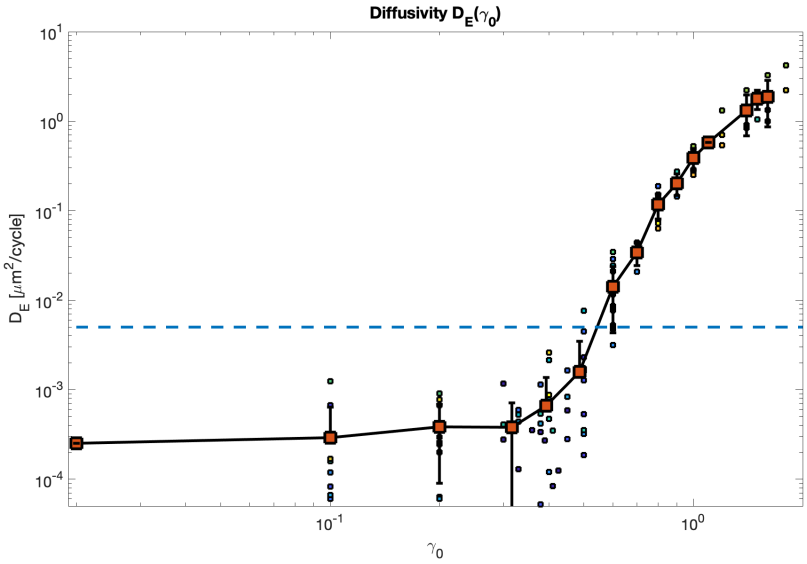


**Figure 6.42:** Shear induced diffusion coefficient for 2 diameter tracers in Carbopol $c = 0.5\%$ as function of the imposed deformation amplitude $\gamma_0$. The blue dashed line is the threshold $D_{Tr}$ determined as explained in the main text.

The tests at different frequencies suggest that below a threshold $\gamma_T$ the effect of the shear on the particles diffusion is comparable to a change in the material effective viscosity (what we referred to as a "melting" effect), while above $\gamma_T$ the shear do not only affect the effective viscosity: the diffusivity is also affected by the rate of deformation that gives the rate of energy furnished to the system ("plastic picture"). The value of the threshold probably suffers the sample to sample variability and further tests should be done to clarify this point. $\gamma_T^{0.5\mu m} \sim 40\%$, $\gamma_T^{2\mu m} \sim 90\%$, $\gamma_T^{2\mu m} \sim 70\%$.
Further tests both mechanical and microscopical are required to verify this view.

In the intermediate regime the sample has a quite stable mechanical response, a careful time sweep show a small but continuous evolution of the response moduli. The decrease of the loss modulus and an essentially constant storage modulus indicates that the material evolves toward a less and less dissipative material. The microscopic counterpart is a decrease of the rearranging dynamics. The EchoDDM experiments are much more sensitive to this evolution than the mechanical moduli: the measured effective diffusion coefficient for repeated tests at fixed amplitudes has a decrease up to one order of magnitude, while the corresponding decrease of the loss modulus is of the order of ten percent.
As a consequence we can interpret the decrease of the diffusion coefficient for fixed deformation amplitude and therefore source of signal in Echo ex-

periments. which is a source of optical signal This fact indicated that the plastic dynamics is probably mainly associated with the slow evolution of the system rather than to the stationary plastic activity. This distinction, that turns out to be particularly relevant for this system, is probably important in general.

## 6.5 Thixotropic Yield Stress Fluid

In this section we present preliminary results from experiments performed on depletion gels. The aim is to extend our experimental approach to samples with a more precise control of the microscopic state, mainly in terms of size distribution of the colloidal particles and interaction potential. An interesting additional feature of our sample of choice (a PMMA colloidal gel) is that, with a suitable selection of the solvent, it is possible to obtain information on its structural and dynamical properties by measuring the light scattered by the material itself, without the need of introducing external tracers (see Sect.5.1.5 for more details on the sample). The preliminary results presented here regard: the characterization of the vertical deformation profile, the study of the microscopic dynamics trough EchoDDM experiments, observation on the formation of shear induced structural anisotropy.

### Vertical Deformation Profile

As a preliminary test, we checked that the linearity of the deformation profile experienced by the sample when loaded in our shear cell. As it can be appre-

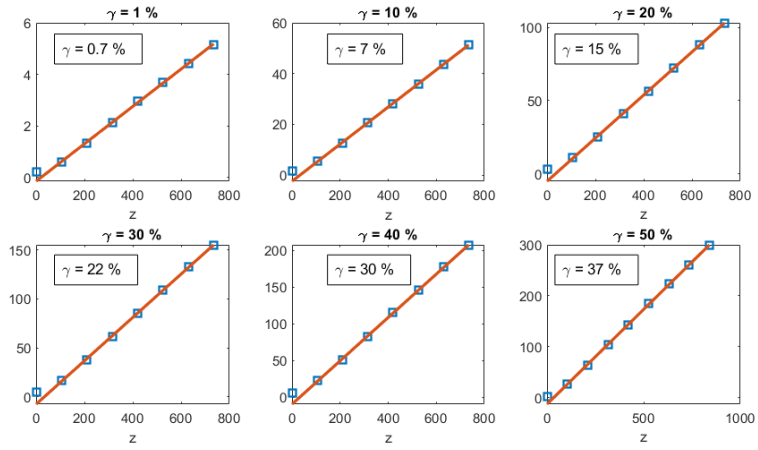


**Figure 6.43:** Amplitude of the deformation as function of the distance from the bottom plane $z$ for different shear amplitudes $\gamma$, as indicated in the title of each panel. Red lines are best fitting curves with a linear homogeneous model. The resulting effective shear amplitude is reported in the box inside each panel.

ciated from Fig.6.43, the deformation profile follows a good linear scaling, at least far enough from the boundaries. The slip is considerably stronger than in Carbopol: the actual deformation in the central part of the cell is reduced approximately by 30% with respect to the nominally imposed one.

### Dynamics

The experiments presented in the following were performed with a 40X objective, NA = 0.6 with maximized spatial coherence of the light source5.2.1. The preliminary results obtained from EchoDDM on the PMMA gel are rather puzzling. The observed dynamics is very slow, at least if compared to the one detected in similar experiments performed on the Carbopol sample. This is quite surprising, especially considering that the colloidal gel is much more fragile than Carbopol. In Fig.6.44 we report the dynamic structure structure factors for shear amplitude $\gamma_0 = 20\%$, for wave-vectors in the range $q \in [0.65, 6.5]\mu m^{-1}$ (colors going from blue to yellow). In all

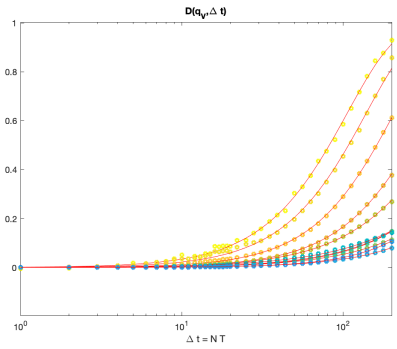


**Figure 6.44:** Structure functions for shear amplitude $\gamma = 20\%$, wave vectors go from $0.65\mu m^{-1}$ to $6.5\mu m^{-1}$ (colors going from blue to yellow). The continuous red lines are fit with compressed exponential.

cases, the dynamic structure functions are well described in terms of a single compressed exponential relaxation

$$D(q, \Delta t) = 1 - exp\big( - (\Delta t \Gamma(q))^{\alpha}\big)$$

with $\alpha \simeq 2$. The $q$-dependence of the relaxation rate follows a ballistic scaling $\Gamma(q) \propto q$ (Fig.6.45).
First of all we notice that the observed behaviour is not compatible with the expected shear induced diffusion [69], but the most surprising feature is the small dependence on the shear amplitude Fig.6.45.
A crucial difference between the work of Ref. [69], that used DWS coupled to LAOS to highlighting the presence of shear induced plastic dynamics, and our experiments is the range of length-scales. In their work they are sensitive to displacements of the order of the particle radius ($l_{DWS} \sim R = 137nm$), and in this experimental condition thermal agitation leads to (at least partial) decorrelation of the signal. In our experiments the maximum wave vector with a good signal is $q = 6.5\mu m^{-1}$ corresponding to $l_{DDM} \sim 6R \sim 1\mu m$ and the sole thermal agitation do not produce any appreciable signal decorrelation. From the inspection of the registered movies the speckle pattern

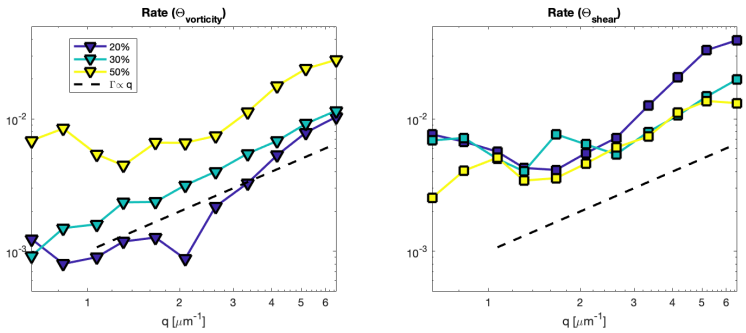


**Figure 6.45:** Relaxation rate as function of the wave vector for structure functions along the vorticity direction, for different shearing amplitudes, the black line indicate the ballistic scaling $\Gamma \propto q$. Second panel, the same as the fist but in the shear direction.

produced by the sample do not show appreciable reconfiguration, our interpretation is that the plastic dynamics occurs at scales that do not contribute sensitively to out signal. In the image sequence the most apparent dynamics is a slow compression in the vorticity direction and an expansion in the shear direction and this effect, dominates over the microscopic mechanism reported in the literature that is slower at the considered length scales.

### Static spectral features

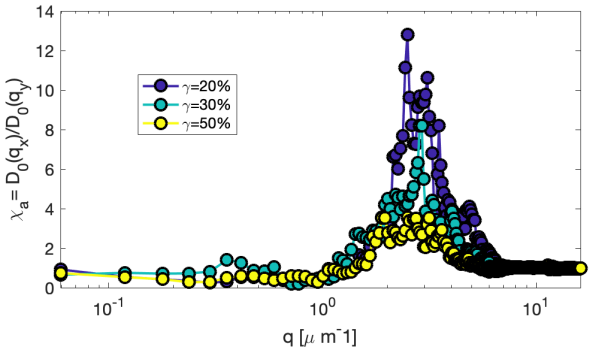


**Figure 6.46:** $\chi_a(q) = D_0(q_{shear})/D_0(q_{vort})$: Ratio between the image power spectrum along the shear direction and the vorticity direction. $\chi_a(q)$ has a peak around $q \sim 3\mu m^{-1}$, whose amplitude diminish at high shear amplitudes.

Interestingly, we observed the emergence of a shear-induced structural anisotropy in the sample. We calculate the image power spectrum $D_0(\mathbf{q}) = \langle |I(\mathbf{q},t)|^2 \rangle_t$ and we consider the ratio between the power spectrum in the shear and in the vorticity directions: $\chi_a(q) = D_0(q_{shear})/D_0(q_{vort})$. In this way, the effect of microscope transfer function is removed and we end up with

an unbiased indicator of the anistoropy. In the case of an isotropic structure $\chi_a \sim 1$, while the emergence of a peak at $q \sim 3\mu m^{-1}$ indicates the presence of structures with a characteristic length scale $\Lambda \sim 2\mu m$, elongated along the vorticity direction. As it can be appreciated in Fig.6.46, the maximum of this effect is observed for $\gamma_0 = 20\%$ and when the shear is increased the anisotropy decreases.

### Summary of the subsection

We showed that the system, with appropriate refractive index mismatch, has enough contrast to apply the cross-correlation algorithm for global displacement detection and that with our apparatus we can produce an homogeneous and controlled deformation field Fig.6.43.
The analysis of the static spectrum shows the presence of shear induced structural anisotropy.
The structure functions exhibit a slow dynamics even when the system is sheared well above its yielding point, this is probably explained by the range of inspected length scales that do not superimpose with the one explored in previous studies.
The resolution of the optical setup can't be increased much. But we can obtain an equivalent result using bigger colloids since we expect the shear induced displacements to scale with the size of the material building blocks.

# Chapter 7

# Conclusions

### The context

In this thesis, we investigated the relation between the mechanical properties of a material and the state of its microscopic constituents, with a particular focus on the yielding transition in soft materials. Yielding represents one of the key modes of mechanical failure and characterizes the mechanical response of a wide class of materials, from metals to polymers, from biological tissues to emulsions. Despite being a complex phenomenon, encompassing a wide range of length- and time-scales [51], [101], [15], yielding is characterized by an associated phenomenology that displays a number of universal features, that are largely material-independent [83], [10].

It is this universality that makes soft materials very convenient model systems for understanding yielding: on one hand, they usually display a structural organization at length scales that can be probed by means of optical techniques; on the other hand, as they are "soft", it is very easy to obtain large deformations or induce yielding even upon the application of moderate forces.

Experimentally, the greatest challenge of a multi-scale (from micro to macro) study of yielding in soft materials lies in imposing a macroscopic deformation on a soft sample while monitoring the microscopic degrees of freedom. Characterization of the microscopic states through far field scattering techniques suffers from lack of spatial resolution, as the output of these experiments typically represent a spatial average performed over a large (and possibly heterogeneous) volume. At the same time, imaging techniques usually suffer from poor statistics, since usually a better spatial resolution comes at the expense of the extension of the field of view.

The possibility to combine a good spatial resolution and a statistically robust characterization is crucial in the study of a complex phenomenon, that has an intrinsic stochastic nature, a considerable sample to sample variability and a strong sensitivity to spatial heterogeneity.

**Our methodological contribution**

Here we have developed an integrated approach (rheology protocol and image analysis) to study the microscopic dynamics of soft materials, both at rest and under oscillatory shear strain. All the techniques and methods that we have refined provide a quantitative characterization of the statics (e.g. spatial arrangement and positional correlation,...) and dynamics (e.g. relaxation of density modes, determination of particle trajectories, dynamical activity,...) of the soft material under scrutiny. Most of the proposed tools pivot around Differential Dynamic Microscopy that combines the experimental setup of optical microscopy with an image processing aimed at extracting scattering-like information about the sample at different wavevectors.

Two basic methodological advances obtained in this work, which were succesfully applied to samples at rest and under shear, include

- **Image Windowing** - A pre-processing step for DDM analysis aimed at removing artifacts due to the image finite size. This tool revealed to be essential to extract the correct dynamics over a larger wave-vector range, as detailed in the associated peer-reviewed article [48].
- **DDM-$\mu$rheology** - Microrheology is a family of techniques aimed at characterising the linear mechanical properties of a material *via* the measurement of the MSD of embedded micrometric tracers . The most diffuse route to microrheology is particle tracking, that requires to individually identify the tracers and their trajectories. We have shown how DDM can be used to obtain the same information, under a wide range imaging conditions. More details are available also in the published peer-reviewed article [44].

To study the dynamics under shear, we used a large amplitude oscillatory shear (LAOS) approach, applied to simple yield stress fluids. This choice was motivated by the fact that in LAOS experiments, simple yield stress fluids reach a stationary condition even in the non-linear regime. The so-obtained stationary state allows for a statistically significant characterization of the microscopic state. To achieve this goal we have acted along two main lines:

- we have **developed an echo-DDM approach** to monitor and quantify the shear-induced dynamics at different wave-vectors: images of the sample are acquired with a frame rate equal to the deformation rate, in order to be sensible only to irreversible plastic rearrangements.
- we have **monitored intermittency and heterogeneity of the shear-induced dynamics** by computing *activity maps* (in direct space) and *q-resolved dynamic susceptibility* $\chi_4(q, \Delta t)$ (in reciprocal space) to go beyond average quantities like the intermediate scattering function or the particle MSD.

### Results on the physics of yielding

LAOS experiments with the simple yield stress fluid (*Carbopol 971 P NF*) provided interesting results on the physics behind the yielding transition.

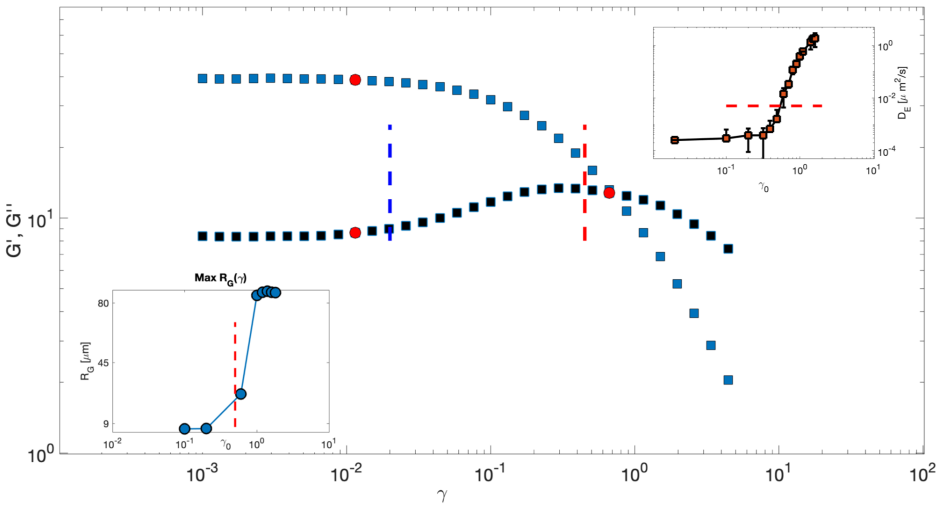


**Figure 7.1: Main Panel:** Storage modulus $G'$ (blue squares) and loss modulus $G''$ (black squares) for a LAOS test on *Carbopol*. The white circles marks the onset of non-linearity. The red circle marks the crossover point where $G' = G''$ ($\gamma = 66\%$). The dashed red line marks the upper limit of the yielding point according to EchoDDM results ($\gamma = 45\%$). **Top right inset:** shear induced diffusion coefficient measured with EchoDDM for tracers with radius $a = 1\mu m$. The red dashed line marks the limit above which the shear induced diffusion lead to rearrangements of the order of the microgels' average size within the observation time. The corresponding amplitude is reported on the main panel and on the other inset. **Bottom left inset:** gyration radius $R_G$ of the largest active zone observed for a given shear amplitude for tracers with radius $a = 1\mu m$. The drastic increase of $R_G$ occurs for a critical strain amplitude value that is in agreements with the one found with EchoDDM.

Through the study of Lissajous plots we have shown that in the yielding regime the mechanical response of the material is *non-linear* but yet *harmonic*, that is, accurately described in terms of phase-independent viscoelastic moduli $G''$ (loss modulus) and $G'$ (storage modulus), respectively. This property allows to treat the sample in the non-linear regime as an "effective viscoelastic material", with distinct mechanical properties from the sample at rest. In other words, it should be conceptually feasible to study the *linear* response of the shared material to small harmonic perturbations *superimposed on the LAOS*, obtaining an effective frequency-dependent dynamic modulus. According to basic concepts of linear rheology, whether this effective dynamic modulus presents or not a relaxation time provides a

criterion to discriminate a solid-like to a liquid-like behaviour [74].

In this context, with the additional hypothesis that the storage and loss moduli crosses each other once (if ever), we can thus interpret the crossover point where $G'' = G'$ (occurring for $\gamma_{c.o.} = 66\%$, and marked by a red circle in Fig. 7.1) as the point at which the relaxation time becomes equal to the shearing period. As a consequence, under the hypothesis that the relaxation time monotonically decreases with the shear amplitude, we expect the yielding point to be located at $\gamma < \gamma_{c.o.}$.

As our experimental setup did not allow a direct measurement of the linear response of the sheared material, we probed the state of the shared material *via* microscopy observations of the spontaneous dynamics of embedded tracer particles.

EchoDDM measurements highlighted the presence of plastic dynamics: in the high-$q$ limit we found a diffusive scaling of the relaxation rate with the wavevector, with an effective diffusion coefficient which is strongly dependent on the shear amplitude (Fig. 7.1 inset top right corner).

Experiments with tracers of different sizes show that the shear-induced diffusion coefficient is inversely proportional to the particle radius, in analogy with the Stokes-Einstein relation. The validity of this scaling law is intriguing and opens to the possibility of pushing even further the analogy between a yielding material and viscoelastic material at rest.

Because of limits imposed by our setup on the duration of the experiments, we are not always able to unambiguously discriminate between free and constrained diffusion, so that the presence of a diffusive dynamics on small spatial length scales should not be necessarily interpreted as a proxy for the "fluidization" of the sample. We could instead consider "fluidized" a sample where the effective diffusion coefficient $D$ is such to allow a particle with the typical size of a microgel ($r \sim 1\mu m$) to displace by an amount comparable with its own size within the duration of the experiment. This operative criterion defines a threshold $D_T$ for the effective diffusion coefficient (marked by the red line in Fig. 7.1 inset top right corner)

$$\langle \Delta y^2 \rangle (\Delta t = 100s) = (1\mu m)^2 = 2D_T \cdot 100s.$$

By applying this criterion we obtain $\gamma_Y \sim 45\%$, which is within the nonlinear regime identified in LAOS experiments, but below the crossover point, consistently with the picture described before.

### Perspectives and open questions on yielding

The approach proposed in this work enables one overcoming some of the key experimental limitations in the study of soft yield-stress materials. For this reason it should be applied to other systems to understand the generality of the observed behaviour and possibly new aspects of the shear-induced dy-

namics.

One of the open issues remains the exact location of the yielding threshold. Our experiments provides an upper boundary, but further investigation and longer measurements are needed to increase the precision in locating the transition point. Also, the comparison with *ad hoc* mechanical tests aimed at measuring the linear response to small perturbation in the non-linear regime[1] will be key to validate the consistency of the proposed scenario and the identified yielding criterion.

We suggest that the proposed scenario for the yielding transition in simple YSF under LAOS forcing could provide an ideal starting point also for understanding more complex non-linear and non-stationary phenomena linked to yielding. For this reason the very next steps for the follow-up to this work is the application of this method to other simple YSF.

This work includes also a first body of preliminary results on a different sample: a depletion gel. In particular, we showed that we can impose a controlled homogeneous deformation profile. Unfortunately, EchoDDM experiments on this sample didn't provide fully satisfactory results. In particular, the genuine dynamic signal originated from shear-induced plastic rearrangement in the sample was almost completely buried by the spurious effects (large-scale drifts or flows) due to the unstable confinement of the sample. Beside optimizing the experimental set-up, a possible strategy to improve the quality of the optical signal could be to study gels formed by larger colloidal particles. This should increase the "effective resolution" of the experiment. In fact, we expect the amplitude of shear-induced displacements to scale with the particle size, which is the only relevant length-scale in the system.

### Methodological perspectives

The self-consistent approach developed for the DDM-$\mu$rheology is applicable also outside of the context of microrheology: it is a promising tool for a more accurate characterization of the colloids dynamics.

Given the close analogy that we have drawn between sheared samples and viscoelastic materials, valid both at the macroscopic (as shown by Lissajous plots), and at microscopic level (as suggested by the validity of the scaling of the diffusion coefficient with the particle size) we believe that the application of microrheological methods to sheared samples could provide interesting information. In particular, we think that DDM-$\mu$rheology could be the ideal tool to extract the MSD of tracers embedded in a sheared sample

[1] For example the so-called superposition rheology [116].

and to ectract *via* a suitable GSER an effective dynamic modulus.

Another interesting development is to apply the DDM analysis to characterize the in-cycle dynamics. This is expected to be particularly interesting for intermediate shear amplitudes, *i.e.* in the non-linear regime, below the yielding point. Methods to decouple affine and non affine displacements have been recently proposed [3], but, to the best of our knowledge, they have not been applied yet to yielding systems.

# Outlook

In this work we studied the microscopic motility transition induced by periodic shear in a soft glass. In Fig.7.2 (left panel) we show the effective diffusion coefficient as a function of the shear amplitude. Interestingly a similar be-

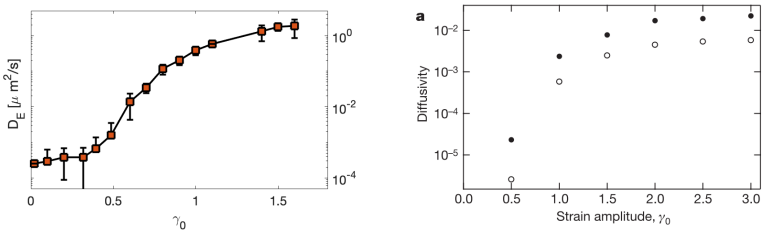


**Figure 7.2:** Left panel: shear-induced diffusion coefficient measured with EchoDDM for tracers with radius $a = 1\mu m$. Right panel: shear-induced self diffusion coefficient for a system of non-brownian hard spheres with radius $a = 230\mu m$ at a volume fraction $\phi = 40\%$ in the shear (fulled symbols) and vorticity (empty symbols) directions, Adapted from [97]. Both graphs are in log-linear scale.

haviour was observed, years ago, in quite different systems under oscillatory shear [97]. Pine and coworkers showed that non-brownian particles dispersed in a newtonian fluid undergo a similar reversible to irreversible transition. The core of the experiment was the measurement of particles' displacements after an integer number of cycles, similarly to the experiments presented in Sect. 4.6 (echo) in this work. In the irreversible state the non-browinan particles exhibit a shear induced diffusive dynamics. In Fig.7.2 (right panel) we reproduce their plot of the shear-induced diffusion coefficient as a function of the shear amplitude.
In their experiment the system is always in the low Reynolds number regime, and thus the flow is governed by Stokes equations that are deterministic and reversible[71]. The onset of diffusion for non-brownian particles was recognised as the transition from a deterministic to a chaotic state. Their aim was to show the transition for a deterministic evolution to a chaotic one. They suggest that chaos is introduced in the system as the amplification of small

perturbations due to the presence of the particles[2], consistently with the fact that the threshold for the onset of the irreversibility strongly decreases with the colloids' volume fraction.

In our experiments we think that the transition is due to the breakage and formation of new links, nevertheless the resemblance of the graphs for the shear-induced diffusion coefficient $D(\gamma)$ is impressive and intriguing, and make us wonder what is the origin of the similarity.

During the writing of this manuscript, an insightful work was published on the transition from reversible to irreversible state in periodically sheared colloidal suspensions [33]. In this work the authors simulate soft non-brownian particles, at different concentration, under periodical shear, spanning different particle volume fractions both below (similar to Ref. [97]), and above the jamming density (similar to this work). At every concentration they observe a sharp transition in the particles' motility, with the MSD abruptly passing from a reversible state (MSD small and constant) to a diffusive state (MSD $\propto t$). The value of the threshold amplitude depends on the volume fraction but quite surprisingly no discontinuity is observed across the jamming transition Fig.7.4. From our point of view this work provides a bridge

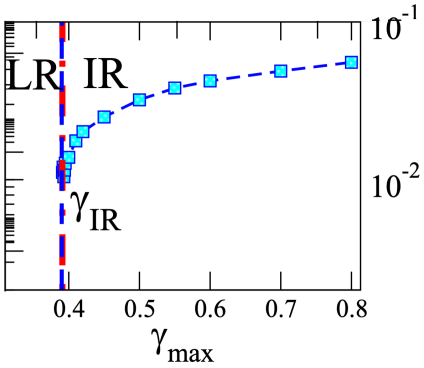


**Figure 7.3:** Shear-induce diffusion coefficient as a function of the shear amplitude. The graph is for volume fraction $\phi = 0.627$, below jamming transition, qualitatively similar result are observed irrespectively of the volume fraction. Adapted from [33].

from the Pine's case study to the one studied in this (and others) works. The similarity of the transition irrespecively of the density pushes to study in deep the ultimate origin of the phenomenon.

[2] "the large number of interacting particles may be responsible".

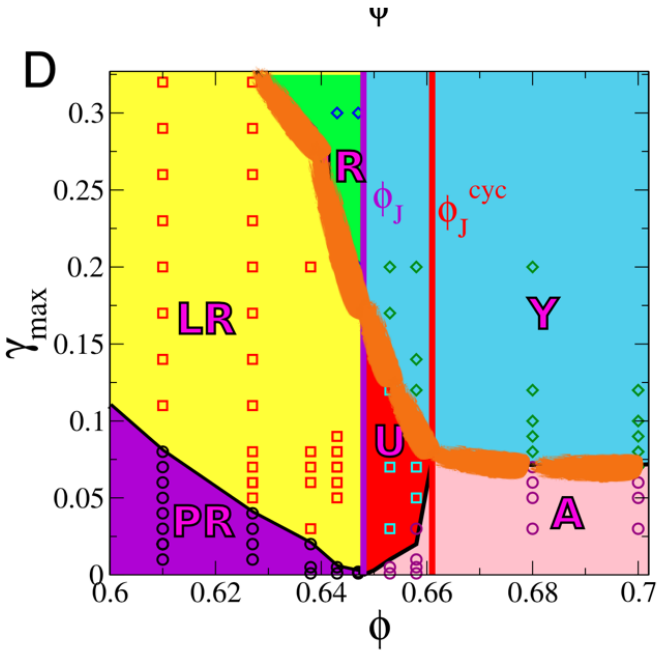


**Figure 7.4:** Phase Diagram deformation amplitude - density ($\gamma - \phi$), the orange line (added) separate reversible (below) from irreversible (above) states. The purple vertical line marks the jamming density.

# Bibliography


[1] Stefano Aime. "Dynamic failure precursors in soft materials". unpublished thesis. PhD thesis. Université de Montpellier, 2017.

[2] Stefano Aime and Luca Cipelletti. "Probing shear-induced rearrangements in Fourier space. I. Dynamic light scattering". In: *Soft matter* 15.2 (2019), pp. 200–212.

[3] Stefano Aime and Luca Cipelletti. "Probing shear-induced rearrangements in Fourier space. II. Differential dynamic microscopy". In: *Soft matter* 15.2 (2019), pp. 213–226.

[4] Stefano Aime, Laurence Ramos, and Luca Cipelletti. "Microscopic dynamics and failure precursors of a gel under mechanical load". In: *Proceedings of the National Academy of Sciences* 115.14 (2018), pp. 3587–3592.

[5] Stefano Aime et al. "A stress-controlled shear cell for small-angle light scattering and microscopy". In: *Review of Scientific Instruments* 87.12 (2016), p. 123907.

[6] Efrén Andablo-Reyes, Pedro Dıaz-Leyva, and José Luis Arauz-Lara. "Microrheology from rotational diffusion of colloidal particles". In: *Physical review letters* 94.10 (2005), p. 106001.

[7] Sho Asakura and Fumio Oosawa. "Interaction between particles suspended in solutions of macromolecules". In: *Journal of polymer science* 33.126 (1958), pp. 183–192.

[8] Pierre Ballesta et al. "Slip and flow of hard-sphere colloidal glasses". In: *Physical Review Letters* 101.25 (2008), p. 258301.

[9] Pierre Ballesta et al. "Slip of gels in colloid–polymer mixtures under shear". In: *Soft Matter* 9.12 (2013), pp. 3237–3245.

[10] Howard A Barnes. "The yield stress—a review or '$\pi\alpha\nu\tau\alpha\ \rho\varepsilon\iota$'—everything flows?" In: *Journal of Non-Newtonian Fluid Mechanics* 81.1-2 (1999), pp. 133–178.

[11] OH Basquin. "The exponential law of endurance tests". In: *Proc Am Soc Test Mater.* Vol. 10. 1910, pp. 625–630.

[12] Todd M. Squires Bayles Alexandra V. and Matthew E. Helgeson. "Probe microrheology withous particle tracking by differential dynamic microscopy". In: *Rheologica Acta* (2017).

[13] Steven S. Beauchemin and John L. Barron. "The computation of optical flow". In: *ACM computing surveys (CSUR)* 27.3 (1995), pp. 433–466.

[14] Bruce J Berne and Robert Pecora. *Dynamic light scattering: with applications to chemistry, biology, and physics*. Courier Corporation, 2000.

[15] R Besseling et al. "Three-dimensional imaging of colloidal glasses under steady shear". In: *Physical review letters* 99.2 (2007), p. 028301.

[16] Jerome Bibette. "Depletion interactions and fractionated crystallization for polydisperse emulsion purification". In: *Journal of colloid and interface science* 147.2 (1991), pp. 474–478.

[17] Jean-Baptiste Boitte et al. "A novel rheo-optical device for studying complex fluids in a double shear plate geometry". In: *Review of Scientific Instruments* 84.1 (2013), p. 013709.

[18] J-P Bouchaud and E Pitard. "Anomalous dynamical light scattering in soft glassy gels". In: *The European Physical Journal E* 6.3 (2001), pp. 231–236.

[19] Doriano Brogioli et al. "Nano-particle characterization by using Exposure Time Dependent Spectrum and scattering in the near field methods: how to get fast dynamics with low-speed CCD camera". In: *Optics express* 16.25 (2008), pp. 20272–20282.

[20] Francois Caton and Christophe Baravian. "Plastic behavior of some yield stress fluids: from creep to long-time yield". In: *Rheologica Acta* 47.5-6 (2008), pp. 601–607.

[21] Roberto Cerbino and Pietro Cicuta. "Perspective: differential dynamic microscopy extracts multi-scale activity in complex fluids and biological systems". In: *The Journal of chemical physics* 147.11 (2017), p. 110901.

[22] Roberto Cerbino and Veronique Trappe. "Differential dynamic microscopy: probing wave vector dependent dynamics with a microscope". In: *Physical review letters* 100.18 (2008), p. 188102.

[23] Roberto Cerbino et al. "Dark field differential dynamic microscopy enables accurate characterization of the roto-translational dynamics of bacteria and colloidal clusters". In: *Journal of Physics: Condensed Matter* 30.2 (2017), p. 025901.

[24] Pinaki Chaudhuri, Ludovic Berthier, and Walter Kob. "Universal nature of particle displacements close to glass and jamming transitions". In: *Physical review letters* 99.6 (2007), p. 060604.

[25] Nian-Sheng Cheng. "Formula for the viscosity of a glycerol- water mixture". In: *Industrial & engineering chemistry research* 47.9 (2008), pp. 3285–3288.

[26] Z Cheng and Thomas G Mason. "Rotational diffusion microrheology". In: *Physical review letters* (2003).

[27] Luca Cipelletti et al. "Simultaneous measurement of the microscopic dynamics and the mesoscopic displacement field in soft systems by speckle imaging". In: *Optics express* 21.19 (2013), pp. 22353–22366.

[28] Rémy Colin et al. "Rotational microrheology of Maxwell fluids using micron-sized wires". In: *Soft Matter* 10.8 (2014), pp. 1167–1173.

[29] Philippe Coussot. *Rheometry of pastes, suspensions, and granular materials: applications in industry and environment*. John Wiley & Sons, 2005.

[30] Philippe Coussot et al. "Aging and solid or liquid behavior in pastes". In: *Journal of Rheology* 50.6 (2006), pp. 975–994.

[31] Philippe Coussot et al. "Viscosity bifurcation in thixotropic, yielding fluids". In: *Journal of rheology* 46.3 (2002), pp. 573–589.

[32] John C. Crocker and David G. Grier. "Methods of digital video microscopy for colloidal studies". In: *Journal of colloid and interface science* (1996), pp. 298–310.

[33] Pallabi Das, HA Vinutha, and Srikanth Sastry. "Unified phase diagram of reversible–irreversible, jamming, and yielding transitions in cyclically sheared soft-sphere packings". In: *Proceedings of the National Academy of Sciences* 117.19 (2020), pp. 10203–10209.

[34] Bivash R Dasgupta et al. "Microrheology of polyethylene oxide using diffusing wave spectroscopy and single scattering". In: *Physical Review E* 65.5 (2002), p. 051505.

[35] Jan KG Dhont. *An introduction to dynamics of colloids*. Elsevier, 1996.

[36] Maureen Dinkgreve et al. "On different ways of measuring "the" yield stress". In: *Journal of non-Newtonian fluid mechanics* 238 (2016), pp. 233–241.

[37] M Dinkgreve et al. "Carbopol: From a simple to a thixotropic yield stress fluid". In: *Journal of Rheology* 62.3 (2018), pp. 773–780.

[38] Anthony D Dinsmore et al. "Three-dimensional confocal microscopy of colloids". In: *Applied optics* 40.24 (2001), pp. 4152–4159.

[39] Thibaut Divoux, Catherine Barentin, and Sébastien Manneville. "From stress-induced fluidization processes to Herschel-Bulkley behaviour in simple yield stress fluids". In: *Soft Matter* 7.18 (2011), pp. 8409–8418.

[40] Thibaut Divoux et al. "Transient shear banding in a simple yield stress fluid". In: *Physical review letters* 104.20 (2010), p. 208301.

[41] Pedro Dıaz-Leyva, Elıas Perez, and José Luis Arauz-Lara. "Dynamic light scattering by optically anisotropic colloidal particles in polyacrylamide gels". In: *The Journal of chemical physics* 121.18 (2004), pp. 9103–9110.

[42] *DLS*. https://lsinstruments.ch/en/technology/dynamic-light-scattering-dls.

[43] Gavin J Donley et al. "Time-resolved dynamics of the yielding transition in soft materials". In: *Journal of Non-Newtonian Fluid Mechanics* 264 (2019), pp. 117–134.

[44] Paolo Edera et al. "Differential dynamic microscopy microrheology of soft materials: A tracking-free determination of the frequency-dependent loss and storage moduli". In: *Physical Review Materials* 1.7 (2017), p. 073804.

[45] Manuel A Escobedo-Sánchez et al. "Study of translational and rotational dynamics of birefringent colloidal particles by depolarized light scattering in the far-and near-field regimes". In: *The Journal of chemical physics* 143.4 (2015), p. 044902.

[46] Fabio Giavazzi and Roberto Cerbino. "Digital Fourier microscopy for soft matter dynamics". In: *Journal of Optics* 16.8 (2014), p. 083001.

[47] Fabio Giavazzi, Catalina Haro-Pérez, and Roberto Cerbino. "Simultaneous characterization of rotational and translational diffusion of optically anisotropic particles by optical microscopy". In: *Journal of Physics: Condensed Matter* 28.19 (2016), p. 195201.

[48] Fabio Giavazzi et al. "Image windowing mitigates edge effects in Differential Dynamic Microscopy". In: *The European Physical Journal E* 40.11 (2017), p. 97.

[49] Fabio Giavazzi et al. "Scattering information obtained by optical microscopy: differential dynamic microscopy and beyond". In: *Physical Review E* 80.3 (2009), p. 031403.

[50] Fabio Giavazzi et al. "Tracking-free determination of single-cell displacements and division rates in confluent monolayers". In: *Frontiers in Physics* 6 (2018), p. 120.

[51] Thomas Gibaud et al. "Multiple yielding processes in a colloidal gel under large amplitude oscillatory stress". In: *Soft Matter* 12.6 (2016), pp. 1701–1712.

[52] Nicoletta Gnan and Emanuela Zaccarelli. “The microscopic role of deformation in the dynamics of soft colloids”. In: *Nature Physics* (2019), p. 1.

[53] Rim Harich et al. “Gravitational collapse of depletion-induced colloidal gels”. In: *Soft Matter* 12.19 (2016), pp. 4300–4308.

[54] Catalina Haro-Pérez et al. “Microrheology of viscoelastic fluids containing light-scattering inclusions”. In: *Physical Review E* 75.4 (2007), p. 041505.

[55] P Hébraud et al. “Yielding and rearrangements in disordered emulsions”. In: *Physical Review Letters* 78.24 (1997), p. 4657.

[56] Michiel Hermes and Paul S Clegg. “Yielding and flow of concentrated Pickering emulsions”. In: *Soft Matter* 9.31 (2013), pp. 7568–7575.

[57] Reinhard Höhler, Sylvie Cohen-Addad, and Hussein Hoballah. “Periodic nonlinear bubble motion in aqueous foam under oscillating shear strain”. In: *Physical review letters* 79.6 (1997), p. 1154.

[58] Kyu Hyun et al. “A review of nonlinear oscillatory shear tests: Analysis and application of large amplitude oscillatory shear (LAOS)”. In: *Progress in Polymer Science* 36.12 (2011), pp. 1697–1753.

[59] Liesbeth Janssen. “Mode-coupling theory of the glass transition: A primer”. In: *Frontiers in Physics* 6 (2018), p. 97.

[60] *KilfoilWebPage*. https://www.physics.umass.edu/people/maria-kilfoil.

[61] Elizabeth D Knowlton, David J Pine, and Luca Cipelletti. “A microscopic view of the yielding transition in concentrated emulsions”. In: *Soft Matter* 10.36 (2014), pp. 6931–6940.

[62] Juha Koivisto et al. “Predicting sample lifetimes in creep fracture of heterogeneous materials”. In: *Physical Review E* 94.2 (2016), p. 023002.

[63] Jarosław Korus et al. “The impact of resistant starch on characteristics of gluten-free dough and bread”. In: *Food Hydrocolloids* 23.3 (2009), pp. 988–995.

[64] Nick Koumakis and George Petekidis. “Two step yielding in attractive colloids: transition from gels to attractive glasses”. In: *Soft Matter* 7.6 (2011), pp. 2456–2470.

[65] Nick Koumakis et al. “Tuning colloidal gels by shear”. In: *Soft Matter* 11.23 (2015), pp. 4640–4648.

[66] Nick Koumakis et al. “Yielding of hard-sphere glasses during start-up shear”. In: *Physical review letters* 108.9 (2012), p. 098303.

[67] Ferenc Kun et al. “Universality behind Basquin’s law of fatigue”. In: *Physical review letters* 100.9 (2008), p. 094301.

[68] Ronald Lambourne and TA Strivens. *Paint and surface coatings: theory and practice*. Elsevier, 1999.

[69] Marco Laurati, SU Egelhaaf, and George Petekidis. "Plastic rearrangements in colloidal gels investigated by LAOS and LS-Echo". In: *Journal of Rheology* 58.5 (2014), pp. 1395–1417.

[70] Marco Laurati et al. "Long-lived neighbors determine the rheological response of glasses". In: *Physical review letters* 118.1 (2017), p. 018002.

[71] L Gary Leal. *Laminar flow and convective transport processes: scaling principles and asymptotic analysis*. Butterworth-Heinemann Boston: 1992.

[72] Peter J Lu. "Confocal scanning optical microscopy and nanotechnology". In: *Handbook of Microscopy for Nanotechnology*. Springer, 2005, pp. 3–24.

[73] Peter J Lu et al. "Gelation of particles with short-range attraction". In: *Nature* 453.7194 (2008), p. 499.

[74] Christopher W Macosko and Ronald G Larson. *Rheology: principles, measurements, and applications*. Vch New York, 1994.

[75] Vikas Mahto and VP Sharma. "Rheological study of a water based oil well drilling fluid". In: *Journal of Petroleum Science and Engineering* 45.1-2 (2004), pp. 123–128.

[76] Alexander Ya Malkin and Avraam I Isayev. *Rheology: concepts, methods, and applications*. Elsevier, 2017.

[77] Sébastien Manneville, Lydiane Bécu, and Annie Colin. "High-frequency ultrasonic speckle velocimetry in sheared complex fluids". In: *The European Physical Journal-Applied Physics* 28.3 (2004), pp. 361–373.

[78] Thomas G Mason, J Bibette, and David A Weitz. "Yielding and flow of monodisperse emulsions". In: *Journal of Colloid and Interface Science* 179.2 (1996), pp. 439–448.

[79] Thomas G Mason, Hu Gang, and David A Weitz. "Rheology of complex fluids measured by dynamic light scattering". In: *Journal of Molecular Structure* 383.1-3 (1996), pp. 81–90.

[80] Thomas G Mason and David A Weitz. "Optical measurements of frequency-dependent linear viscoelastic moduli of complex fluids". In: *Physical review letters* 74.7 (1995), p. 1250.

[81] Jeffrey J McGuire, Margaret S Boettcher, and Thomas H Jordan. "Foreshock sequences and short-term earthquake predictability on East Pacific Rise transform faults". In: *Nature* 434.7032 (2005), p. 457.

[82] Alenka Mertelj et al. "Rotational diffusion in a bistable potential". In: *EPL (Europhysics Letters)* 59.3 (2002), p. 337.

[83] Carmen Miguel and Miguel Rubi. *Jamming, yielding, and irreversible deformation in condensed matter*. Vol. 688. Springer, 2006.

[84] Kunimasa Miyazaki, David R Reichman, and Ryoichi Yamamoto. "Supercooled liquids under shear: Theory and simulation". In: *Physical Review E* 70.1 (2004), p. 011501.

[85] Esmaeel Moghimi et al. "Colloidal gels tuned by oscillatory shear". In: *Soft Matter* 13.12 (2017), pp. 2371–2383.

[86] Marie-Hélène Nadal and Philippe Le Poac. "Continuous model for the shear modulus as a function of pressure and temperature up to the melting point: analysis and ultrasonic validation". In: *Journal of applied physics* (2003).

[87] Guillaume Ovarlez and Sarah Hormozi. *Lectures on Visco-Plastic Fluid Mechanics*. Springer, 2019.

[88] José Paredes, Noushine Shahidzadeh-Bonn, and Daniel Bonn. "Shear banding in thixotropic and normal emulsions". In: *Journal of Physics: Condensed Matter* 23.28 (2011), p. 284116.

[89] Raffaele Pastore, Giuseppe Pesce, and Marco Caggioni. "Differential Variance Analysis: a direct method to quantify and visualize dynamic heterogeneities". In: *Scientific reports* 7 (2017), p. 43496.

[90] Raffaele Pastore et al. "Connecting short and long time dynamics in hard-sphere-like colloidal glasses". In: *Soft Matter* 11.3 (2015), pp. 622–626.

[91] Raffaele Pastore et al. "Multi-scale heterogeneous dynamics in glassy suspensions". In: (in preparation).

[92] George Petekidis, A Moussaid, and PN Pusey. "Rearrangements in hard-sphere glasses under oscillatory shear strain". In: *physical review E* 66.5 (2002), p. 051402.

[93] George Petekidis, Dimitris Vlassopoulos, and Peter N Pusey. "Yielding and flow of colloidal glasses". In: *Faraday discussions* 123 (2003), pp. 287–302.

[94] George Petekidis, Dimitris Vlassopoulos, and PN Pusey. "Yielding and flow of sheared colloidal glasses". In: *Journal of Physics: Condensed Matter* 16.38 (2004), S3955.

[95] George Petekidis et al. "Shear-induced yielding and ordering in concentrated particle suspensions". In: *Physica A: Statistical Mechanics and its Applications* 306 (2002), pp. 334–342.

[96] *PFS*. https://www.microscopyu.com/tutorials/the-nikon-perfect-focus-system-pfs.

[97] David J Pine et al. "Chaos and threshold for irreversibility in sheared suspensions". In: *Nature* 438.7070 (2005), pp. 997–1000.

[98] DJ Pine et al. “Diffusing wave spectroscopy”. In: *Physical review letters* 60.12 (1988), p. 1134.

[99] PN Pusey, AD Pirie, and WCK Poon. “Dynamics of colloid-polymer mixtures”. In: *Physica A: Statistical Mechanics and its Applications* 201.1-3 (1993), pp. 322–331.

[100] PN Pusey and W Van Megen. “Detection of small polydispersities by photon correlation spectroscopy”. In: *The Journal of chemical physics* 80.8 (1984), pp. 3513–3520.

[101] Michael C Rogers et al. “Echoes in x-ray speckles track nanometer-scale plastic events in colloidal gels under shear”. In: *Physical Review E* 90.6 (2014), p. 062310.

[102] Michael C Rogers et al. “Microscopic signatures of yielding in concentrated nanoemulsions under large-amplitude oscillatory shear”. In: *Physical Review Materials* 2.9 (2018), p. 095601.

[103] Simon A Rogers. “In search of physical meaning: Defining transient parameters for nonlinear viscoelasticity”. In: *Rheologica Acta* 56.5 (2017), pp. 501–525.

[104] Thierry Savin and Patrick S Doyle. “Static and dynamic errors in particle tracking microrheology”. In: *Biophysical journal* 88.1 (2005), pp. 623–638.

[105] Shibu Saw, Sneha Abraham, and Peter Harrowell. “Nonaffine displacements and the nonlinear response of a strained amorphous solid”. In: *Physical Review E* 94.2 (2016), p. 022606.

[106] Wolfgang Schärtl. *Light scattering from polymer solutions and nanoparticle dispersions*. Springer Science Business Media, 2007.

[107] T Sentjabrskaja et al. “Creep and flow of glasses: Strain response linked to the spatial distribution of dynamical heterogeneities”. In: *Scientific reports* 5 (2015), p. 11884.

[108] Peter Sollich et al. “Rheology of soft glassy materials”. In: *Physical review letters* 78.10 (1997), p. 2020.

[109] *Specialised Imaging*. https://www.specialised-imaging.com/products/framing-cameras/simx.

[110] Todd M Squires and Thomas G Mason. “Fluid mechanics of microrheology”. In: *Annual review of fluid mechanics* 42 (2010), pp. 413–438.

[111] *sylgard*. https://www.dow.com/content/dam/dcc/documents/en-us/productdatasheet/11/11-31/11-3184-sylgard-184-elastomer.pdf?iframe=true.

[112] Elisa Tamborini, Luca Cipelletti, and Laurence Ramos. “Plasticity of a colloidal polycrystal under cyclic shear”. In: *Physical review letters* 113.7 (2014), p. 078301.

[113] Geoffrey Howarth Tattersall and Phillip FG Banfill. *The rheology of fresh concrete*. Monograph. 1983.

[114] PT Tokumaru and PE Dimotakis. "Image correlation velocimetry". In: *Experiments in Fluids* 19.1 (1995), pp. 1–15.

[115] Zsigmond Varga, Gang Wang, and James Swan. "The hydrodynamics of colloidal gelation". In: *Soft Matter* 11.46 (2015), pp. 9009–9019.

[116] Jan Vermant et al. "Orthogonal versus parallel superposition measurements". In: *Journal of non-newtonian fluid mechanics* 79.2-3 (1998), pp. 173–189.

[117] Alessio Zaccone, Jamie R Blundell, and Eugene M Terentjev. "Network disorder and nonaffine deformations in marginal solids". In: *Physical Review B* 84.17 (2011), p. 174119.